RHODES UNIVERSITY

Where Leaders Learn

Petrogenetic implications for the Merensky Reef: A platinum-group element distribution study from wide-reef facies in the western Bushveld Complex, RSA

A thesis submitted in fulfilment of the requirements of the degree of

Master of Science

at

Rhodes University

by

Savvas Anthony Largatzis

Submitted in February 2016

Department of Geology, Rhodes University

South Africa

Supervisor: Prof. Stephen Prevec

DECLARATION

I declare that this thesis, titled "Petrogenetic implications for the Merensky Reef: A platinum-group element distribution study from wide-reef facies in the western Bushveld Complex, RSA", is my own work, and information from other publications is adequately referenced. It is being submitted in fulfilment for the Master of Science degree in the Department of Geology, Rhodes University.

SAVVAS ANTHONY LARGATZIS

Name of candidate

Signature

Signed on 12th day of FEBRUARY 2016.

Acknowledgments

First and foremost I would like to extend my gratitude to my supervisor Prof. Steve Prevec. Steve, thanks for always having the time to assist me and guide me. Your advice and comments were always appreciated and this thesis could not have been completed without your help.

The author is grateful for the financial assistance provided by the Ada and Bertie Levenstein Bursary, without which, the completion of this degree would not have been possible. Words cannot express how grateful I am for having had this opportunity.

I would also like to thank Glencore, and in particular Pieter-Jan Gräbe, for their generosity in providing the sample material for this study.

Andrea King, Thulani and Chris are thanked for their assistance in preparing the thin sections required for this study.

Dr. Gabi Costin and T.P. are thanked for their assistance during EPMA and their knowledge and guidance when required.

To room 21 and the rest of my department colleagues, thanks for making this year memorable and for all the laughs in the tea room.

My deepest gratitude belongs to my friends, family and my girlfriend. Thank you for the encouragement, support and patience you have given me over the course of this year.

Abstract

Despite decades of research and its economic importance, the formation of the Merensky Reef still remains controversial. This study reports on the distribution of platinum-group elements within wide-reef facies in an attempt to identify petrogenetic controls in the formation of the Merensky Reef. Wide-reef Merensky was sampled from Eland Platinum Mines in the western Bushveld. Macroscopic investigation of the drillcore identified a basal chromitite stringer overlying an anorthositic footwall. The reef comprised a pyroxenite unit while the hangingwall comprised noritic, leuconoritic and anorthositic units (upwards the stratigraphy). Furthermore, an anorthositic seam was identified within the pyroxenite reef, near the top of the unit. Ophitic textures of orthopyroxene oikocrysts comprising inclusions of plagioclase chadacrysts suggest that the crystallization of plagioclase preceded the crystallization of orthopyroxene. Furthermore, plagioclase and orthopyroxene were shown to be in mineral disequilibrium with one another. Pervasive hydrous alteration features throughout the Merensky Reef suggest late stage deuteric alteration.

Mineral chemistry of plagioclase cores recorded ranges for An content in the Merensky Reef as follows: An_{72-79} in the anorthositic footwall, An_{71-77} in the chromitite stringer, An_{45-78} in the pyroxenite reef unit, An_{47-73} in the anorthosite reef unit, An_{72-76} in the norite hangingwall, An_{75-77} in the leuconorite hangingwall and An_{72-77} in the anorthosite hangingwall. This suggest that the reef units were more evolved than the footwall and hangingwall units. Furthermore, plagioclase showed reverse zoning in the anorthosite footwall unit while normal zoning was identified in the anorthosite reef unit. This suggested that the footwall unit underwent reheating and re-equilibration with a hotter, more primitive magma (also evident in recrystallization textures) while the anorthositic reef unit cooled relatively slowly and interstitial plagioclase present within this unit equilibrated with a trapped, more evolved liquid.

The pyroxenite reef unit shows enrichment in incompatible elements and corresponding negative Eu anomalies, indicating the presence of trapped liquids. Cu, Ni and S concentrations remained low throughout the reef with the exception of a peak underlying the anorthositic seam and further enrichment underlying this peak. Platinum-group element geochemistry identified two major peaks: an upper peak which coincided with the peaks for Cu, Ni and S, and showed preferential enrichment in Pd and Au relative to other PGE, and a lower peak which coincided with the presence of chromitite and showed the preferential enrichment of Os, Ir, Ru, Rh and Pt relative to Pd, Au, Cu and Ni. The formation of the lower peak was consistent with a model involving the co-precipitation of chromite and PGE clusters (as PGM) while the upper peak was attributed to a model involving the collection of PGE by an immiscible sulphide liquid. Moreover, high Cu/Pd and Pt/Pd ratios in the lower pyroxenite unit indicated a process

involving sulphide fractional segregation and scavenging while the inverse, present within the upper pyroxenite unit, suggested a more dynamic system involving the introduction of PGE-undepleted magma and S during simultaneous sulphide precipitation. Furthermore, a separation of PPGE peaks from IPGE peaks was observed within the pyroxenite unit, indicating a different partitioning behaviour between PPGE and IPGE. The separation of these peaks is attributed to a sulphide liquid fractionation model while depletion haloes occurring in the proximity of the main PGE peaks was suggested to form through an Ostwald-ripening type mechanism.

The results of this study are consistent with a model for the formation of the Merensky Reef involving a combination of geochemical processes, including sulphide segregation and fractionation, as well as multiple replenishments of magma.

List of Terms

1. **Andesine** – An endmember of the plagioclase feldspar solid solution series. It comprises 30 – 50 % An.
2. **Anorthite** – An endmember of the plagioclase feldspar solid solution series. It comprises 90 – 100 % An.
3. **Anorthosite** – An intrusive igneous rock, which is coarsely grained and primarily composed of calcium-rich plagioclase feldspar.
4. **Bytownite** – An endmember of the plagioclase feldspar solid solution series. It comprises 70 – 90 % An.
5. **Chromitite -** A rock composed primarily of the mineral chromite.
6. **Conduit -** A passage through which magma traverses.
7. **Crossed Nicols –** The orientation of two nicol prisms so that their transmitted planes for plane-polarized light are at right angles to one another. Thus, no light is reflected to the observer but instead interferes with minerals on a microscopic stage.
8. **Disseminated** – The scattering of fine-grained ore minerals throughout a rock.
9. **The 'Downers'** – A school of thought who primarily consider PGE-mineralised reefs to form by the downward settling of PGE in sulphides.
10. **Dunite –** An ultrabasic, coarse grained, igneous rock consisting mainly of olivine.
11. **Exsolution -** The processes through which a solid solution homogenous phase separates into two separate constituents during cooling. This process is done without the addition or removal of material.
12. **Harzburgite -** An igneous plutonic rock, belonging to the peridotite group, composed primarily of olivine and orthopyroxene.
13. **High Field Strength Elements** – Elements whose ions are small in radius but contain a high cationic charge.
14. **Intercumulus –** Intergranular crystals that formed in a cumulate rock from intercumulus liquid (i.e. the trapping of magma melt during crystal accumulation).
15. **Intracratonic –** Within a craton.
16. **Labradorite -** An endmember of the plagioclase feldspar solid solution series. It comprises 50 – 70 % An.
17. **Large-Ion Lithophile Element** – Trace elements which have a large ionic radius to charge ratio.

18. **Oikocrysts** – Anhedral crystals which enclose smaller subhedral chadacrysts.
19. **Ophitic -** An igneous texture in which pyroxene oikocrysts enclose plagioclase chadacrysts. This is thus a particular type of poikilitic texture.
20. **PGE –** Platinum-group elements comprise a group of six elements which are some of the rarest and most precious of metals on Earth. The six chemical elements belonging to this group are palladium (Pd), platinum (Pt), rhodium (Rh), osmium (Os), iridium (Ir), and ruthenium, (Ru).
21. **Plane polarized light –** Light whose electric field oscillates in just one plane perpendicular to the plane of propagation.
22. **Poikilitic –** An igneous texture in which small, randomly orientated crystals are enclosed in larger crystals of another mineral.
23. **Rare-Earth Elements** – A series of metallic elements comprising the 15 lanthanides, scandium and yttrium. The group may be further subdivided into the **Light Rare-Earth Elements (LREE)** and the **Heavy Rare-Earth Elements (HREE).**
24. **Sericitic Alteration –** Alteration of plagioclase feldspar to form a fine-grained white mica called sericite.
25. **The 'Uppers'** - A school of thought who primarily consider PGE-mineralised reefs to form by the upwards scavenging of PGE by late aqueous phases.

List of Abbreviations

1. Ab – Albite
2. An – Anorthite
3. Ap – Apatite
4. BC – Bushveld Complex
5. BIC – Bushveld Igneous Complex
6. BMS - Base Metal Sulphides
7. BSE – Back-Scattered Electrons
8. Bt – Biotite
9. Ccp – Chalcopyrite
10. Chl – Chlorite
11. Chr – Chromite
12. Cpx – Clinopyroxene
13. CZ – Critical Zone
14. En – Enstatite
15. Fs – Fosterite
16. FW – Footwall
17. Hbl – Hornblende
18. HFSE – High Field Strength Elements
19. HH-XRF – Hand-Held X-Ray Fluorescence
20. HREE – Heavy Rare Earth Elements
21. HW – Hangingwall
22. ICP-MS – Inductively Coupled Plasma – Mass Spectroscopy
23. Ilm – Ilmenite
24. Iss - Intermediate Solid Solution
25. IPGE – Ir-Group PGE
26. LCZ – Lower Critical Zone
27. LILE – Large-Ion Lithophile Element
28. LGS – Lebowa Granite Suite
29. LOD – Limits of Detection
30. LREE – Light Rare Earth Elements
31. LZ – Lower Zone
32. MCU – Merensky Cyclic Unit
33. Mg# - Magnesium Number
34. MgZ – Marginal Zone
35. Mss - Monosulphide Solid Solution
36. MR – Merensky Reef
37. Ms – Muscovite
38. MZ – Main Zone
39. Ol – Olivine
40. Opx – Orthopyroxene
41. Or – Orthoclase
42. PGE – Platinum-Group Elements
43. PGM – Platinum- Group Minerals
44. PPGE – Pd-Group PGE
45. Pl – Plagioclase
46. Pn – Pentlandite
47. Po – Pyrrhotite
48. ppb – Parts per billion
49. PPL – Plane Polarized Light
50. ppm – Parts per million
51. Py – Pyrite
52. Pyrr – Pyrrhotite
53. Qtz – Quartz
54. REE – Rare Earth Elements
55. RGS – Rashoop Granophyre Suite
56. RL – Reflected Light
57. RLS – Rustenburg Layered Suite
58. RSD – Relative Standard Deviation
59. Rt – Rutile
60. Sp – Sphalerite
61. Srp – Serpentine
62. UCZ – Upper Critical Zone
63. WDS – Wavelength-Dispersive Spectroscopy
64. Wt – Weight
65. Wo – Wollastonite
66. XPL – Crossed Polarized Light
67. XRF – X-Ray Fluorescence

Table of Contents

List of Figures

List of Tables

Chapter 1. Introduction

The Bushveld Complex (BC) is a layered ultramafic to mafic igneous intrusion and is the largest of its kind on Earth (Harris *et al*., 2005). Research done on this deposit has been pivotal in shaping the field of igneous petrology and has aided scientists in understanding and revising basic aspects and models regarding magmatic differentiation (Mathez, 1995). Furthermore, the BC is arguably the most important economic deposit on Earth and comprises the world's largest reserves of platinum group elements (PGE; Pt, Pd, Ru, Rh, Os and Ir), chromium, magnetite and vanadium, as well as significant reserves of copper, nickel, tin and gold (Wilson and Chunnett, 2006; Maier *et al*., 2013).

The Merensky Reef, which is hosted within the Critical Zone of the BC, is an economic PGE-bearing metalliferous reef that divides the mostly ultramafic Critical Zone from the overlying, more noritic Main Zone (Wilson and Chunnett, 2006). The enrichment of PGE in such stratiform Merensky-type ore horizons is a relatively poorly understood process despite decades of research (Ballhaus and Sylvester, 2000; Wilson and Chunnett, 2006). Three popular models have emerged for the origins of such reefs: 1) primary magmatic processes involving the settling of PGE within sulphides (Campbell *et al*., 1983); 2) upward migration of PGE and sulphides via a late percolating vapour (Boudreau, 2008); 3) injection of a crystal slurry, sourced from a staging chamber, as a sill (Eales and Costin, 2012).

Previous studies have shown that in the Merensky Reef, sulphides host the majority of PGM species (Vermaak and Hendriks, 1976; Barnes and Maier, 2002b). The most common base metal sulphides in the Merensky Reef are pyrrhotite, chalcopyrite, pentlandite and pyrite (Vermaak and Hendriks, 1976). However, there is also a suggestion that chromite may act as potential host for PGE (Hiemstra, 1979; Latypov *et al*., 2013). The control of PGE-partitioning within the Merensky Reef still remains controversial despite strong interest in recent years.

In this study, the distribution of PGE are used as a tool for evaluating the genetic processes which led to the formation of the Merensky Reef. This is done in combination with a critical

reassessment of existing models which is required in testing their applicability to the Merensky Reef.

Previous investigations into the PGE distribution of the Merensky Reef have been focussed on narrow or normal Merensky facies. According to Cawthorn (2002; 2010), Wilson and Chunnett (2006) and Mitchell and Scoon (2007) these facies result in PGE distributions, and other vertical patterns, so condensed that researchers are unable to properly decipher magmatic events. In this study, a wider reef facies was adopted to allow for broader PGE distributions and ultimately a better interpretation of the magmatic events which transpired in the Merensky Reef. Access to 16.48 metres of drill core was kindly granted by Glencore Operations. This drillcore comes from their Eland Platinum mine in the Western Bushveld. In total, 28 closely spaced samples were analysed using high-precision analytical methods in order to determine the distribution of PGE, major elements, trace elements and mineral chemistry.

1.1. Applications of Chromium and Platinum-Group Elements

1.1.1. Chromium

Chromium is a metallic element which belongs to Group VIA of the transition metals (ICDA, 2015). The element was first discovered in 1797 by Louis-Nicholas Vauquelin who was experimenting with the mineral crocoite (PbCrO4) (ICDA, 2015). Chromium is extractable from chromite ore which occurs within mafic-ultramafic layered intrusions. Typically, chromium is used in the development of metal alloys within the metallurgical industry due to the characteristic properties of the element (ICDA, 2015). These properties include hardness, a high melting point, strength and resistance to temperature, corrosion and wear (ICDA, 2015). Chromium is also actively used within foundry sands, plating of metals, leather tanning, paints and as catalysts (ICDA, 2015). According to the USGS (2015), Kazakhstan and South Africa contain the largest reserves of chromium in the world (Fig. 1.1.1). In 2014, South Africa recorded a higher mine production of chromium than any other country in the world (USGS, 2015). Although China contains no significant chromium reserves, the country's considerable industrial output of stainless steel means that it is the world's leading chromium-consuming country (USGS, 2015).

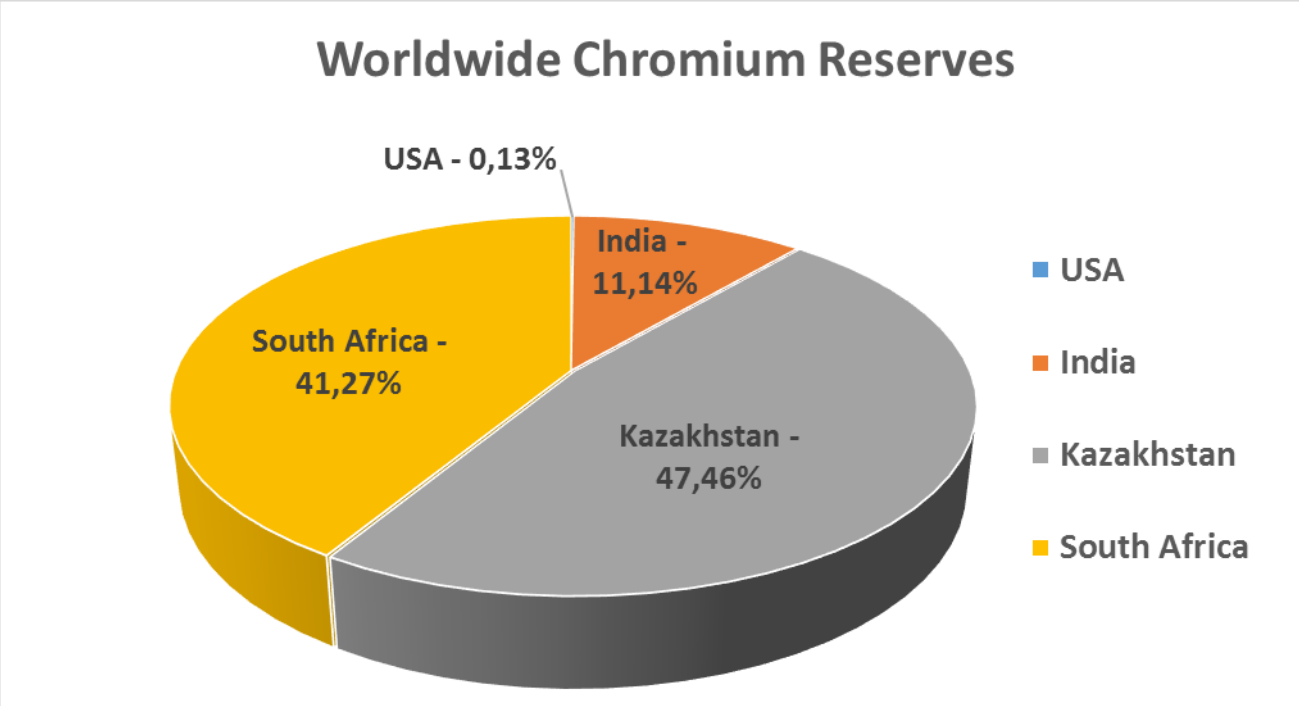

Figure 1.1.1. The world's reserves of chromium. Kazakhstan and South Africa contain the largest chromium resource reserves and production in the world. Data according to USGS (2015).

1.1.2. Platinum-Group Elements

Platinum-group elements (PGE), also referred to as platinum-group metals, comprise 6 elements (Fig. 1.1.2). The group comprises osmium (Os), iridium (Ir), ruthenium (Ru), rhodium (Rh), platinum (Pt) and palladium (Pd), in order of decreasing melting point (Barnes et al., 1985). PGE are found within the Group VIII transition series of the Periodic Table and all elements show similar chemical and physical properties (Table 1.1.1) (Bell, 2015). Some of the chemical and physical properties of PGE include high density, high melting points and thermal and electrical conductivity (Bell, 2015). According to Barnes *et al*. (1985), these siderophile elements may be subdivided into 2 groups: Pd-group PGE (PPGE; Pd, Pt and Rh) and Ir-group PGE (IPGE; Ru, Os and Ir) on the basis of their refractory properties. Over the past 2 decades, with developing technology, the importance of these metals has risen. This is particularly true because of their use in major industrial processes such as catalysts in petroleum processing (Bell, 2015). Other applications of PGE include their use in automotive catalysts for reducing pollution, as electrical components in computer hardware and as jewelery (USGS, 2004).

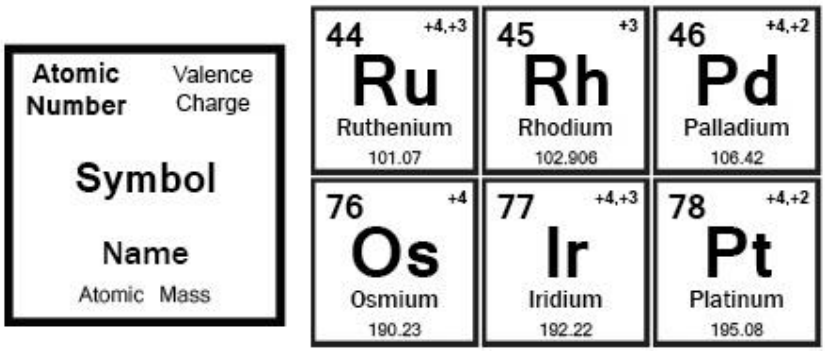

Figure 1.1.2. Platinum-group element chemistry as displayed on the Periodic Table. Properties shown include atomic number, valency, charge, symbol and atomic mass. Figure adapted from Helmenstine (2015).

According to the USGS (2015), South Africa dominates PGE resource reserves in the world with an estimated 95.5 % (Fig. 1.1.3). The largest economically mineable reserve located in South Africa is hosted within the largest ultramafic-mafic igneous deposit in the world, the Bushveld Igneous Complex (BIC). These PGE are specifically concentrated in stratiform reefs (such as the Merensky Reef, UG2 and Platreef). Other notable PGE-bearing deposits on Earth include the Noril'sk deposit in Russia and the Stillwater Complex in the USA (Barnes *et al*., 1985).

Table 1.1.1. Chemical and physical properties of PGE. Table from Bell (2015).

	Platinum	Palladium	Rhodium	Iridium	Ruthenium	Osmium
Chemical Symbol	**Pt**	**Pd**	**Rh**	**Ir**	**Ru**	**Os**
Density (g/cm3)	**21.45**	**12.02**	**12.41**	**22.65**	**12.45**	**22.61**
Melting point (°C)	**1,769**	**1,554**	**1,966**	**2,443**	**2,310**	**3,045**
Electrical resistivity (microhm.cm at 0°C)	**9.85**	**9.93**	**4.33**	**4.71**	**6.80**	**8.12**
Thermal conductivity (watts/metre/°C)	**73**	**76**	**150**	**148**	**105**	**87**

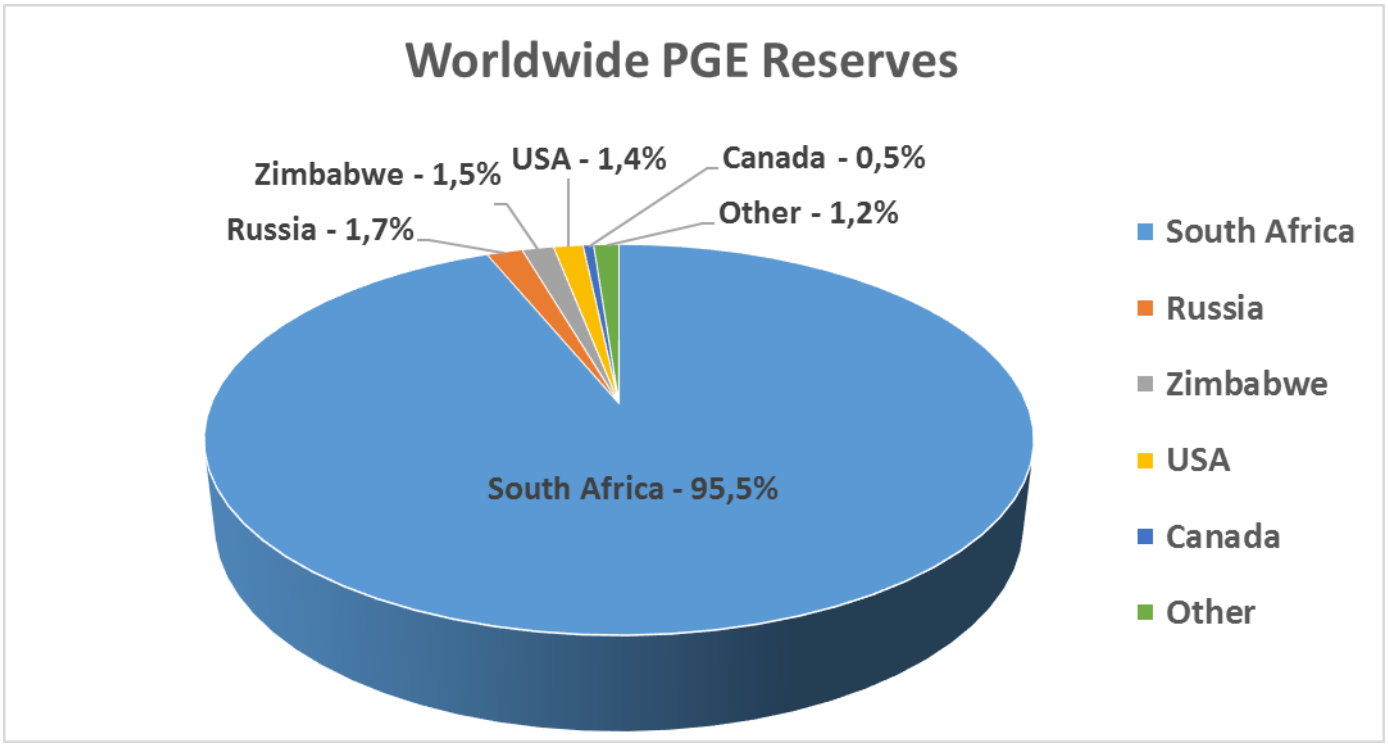

Figure 1.1.3. The world's reserves of PGE. South Africa contains the largest PGE resource reserves and production in the world, with Russia and Zimbabwe coming in at 2nd and 3rd, respectively. Data according to USGS (2015).

1.2. Aims and Objectives of this Study

The chief aim of this study is to improve understanding and to provide constraints on the genesis of the Merensky Reef. One tool for evaluating these processes includes an analysis of the vertical distribution of PGE though a section of the Merensky Reef. In order to intepret and produce clear PGE distribution patterns, the use of a wider reef facies (from the Eland Platinum mines in the Western Bushveld) will be adopted for this investigation. In addition to the analysis of the distribution of PGE in the Merensky Reef, current models for the formation of PGE-mineralised reefs will also be critically assessed and evaluated.

To supplement the PGE data, rock and mineral chemistry data will be used in further constraining the petrogensis of the Merensky Reef and its PGE distributions. This will be done using the following techniques: ICP-MS for an analysis of trace elements, XRF for an analysis of major elements, fire assay for an analysis of PGE, EPMA for analysis of mineral chemistry and petrography for mineral and textural identification. One of the aims of this study is that if constraints on the formation of the Merensky Reef can be made, then the concepts can be applied to other metalliferous (PGE-bearing) reefs.

In combination to analysing the PGE distribution of the Merensky Reef, the study will also investigate the control of PGE-paritioning in the Merensky Reef (specifically the role of chromite and sulphide in controlling the PGE distribution).

Furthermore, findings obtained through an investigation conducted on similar rocks, i.e., borehole ELF-393, identified a separation of IPGE (Ir, Os, Ru; as well as Rh) and PPGE (Pt and Pd) peaks (Largatzis, 2014). To the authors knowledge, this separation of IPGE and PPGE peaks has never before been documented in the Bushveld Complex and thus this thesis also serves as foundation to explore this phenomenom further.

1.3. Outline of the Thesis

This thesis is subdivided into 7 major chapters. Chapter 1 provides a brief introduction to the thesis, as well as the chief aims and objectives of the study. Furthemore, the chapter provides details on the uses of PGE and chromium and gives an estimate into their reserves within the Bushveld Complex. Chapter 2 comprises the general geology and stratigraphy of the Bushveld Complex, and specifically the Merensky Reef, and introduces current models for PGE mineralisation, the formation of chromitite and ultimately the formation of economic, PGE-bearing reefs. The methodology and techniques used in this study are provided in Chapter 3. Chapter 4 comprises results from this study, i.e., macroscopic results, petrography, mineral chemistry, trace elements, major elements and PGE data and distributions. An interpretation into these results is discussed in Chapter 5 and a conclusion of the findings of this study are provided in Chapter 6. Appendices have also been included in this study, in which analytical data are summarised.

Chapter 2. Geological Setting

2.1. Regional Geology and Stratigraphy of the Bushveld Complex

Collectively, the Bushveld Complex (Fig. 2.1.1) covers an area of approximately 65,000 km^2 and has been considered to be the intrusive equivalent of a continental flood basalt province (Cawthorn and Walraven, 1998; Harris *et al*., 2005). On a regional basis, the BC comprises 5 main lobes (also referred to as limbs): the eastern lobe, the western lobe, the northern lobe, the southeastern lobe and the far western lobe (Wilson and Chunnett, 2006). All lobes, except the southeastern lobe, outcrop on the surface and are essentially made up of the same stratigraphic succession of units, excluding the far western lobe which shows some variation (Cawthorn and Walraven, 1998; Wilson and Chunnett, 2006). A study by Webb *et al*. (2004), who conducted gravitational modelling on the BC, suggested that the eastern and western lobes are interconnected beneath the surface. Given the size of the BC its origin has been linked to a mantle plume source (Cawthorn and Walraven, 1998).

The deposit has been dated to ~ 2.05 Ga (i.e., Paleoproterozoic) where magmas intruded into the early Proterozoic Transvaal Supergroup, situated within the Kaapvaal Craton (Wilson and Chunnett, 2006; Maier *et al*., 2013). These country rocks comprise a thick package of intracratonic clastic and chemical sediments, predominantly conglomerates, shales, quartzites and minor mafic volcanic rocks (Cawthorn and Walraven, 1998; Barnes and Maier, 2002b). The BC comprises three distinctive suites of plutonic rocks, namely the mafic-ultramafic Rustenburg Layered Suite (RLS), the Rashoop Granophyre Suite (RGS) and the Lebowa Granite Suite (LGS) (Harne & Von Gruenewaldt, 1995). The RLS is the most important suite for the purpose of this study and thus will be the only suite discussed from here onwards.

The RLS comprises 5 distinct zones (Fig. 2.1.2), namely the Marginal Zone (MgZ), the Lower Zone (LZ), the Critical Zone (CZ), the Main Zone (MZ) and the Upper Zone (UZ) (Cawthorn and Walraven, 1998). Collectively these zones make up a stratigraphic thickness of approximately 7 to 8 km (Eales *et al*., 1990; Barnes & Maier, 2002b). However, the stratigraphic thickness may vary from limb to limb. For instance, the western and eastern limbs (which are relatively similar) are much thicker than the northern limb, which is only around 3 to 5 km thick (Barnes & Maier, 2002b).

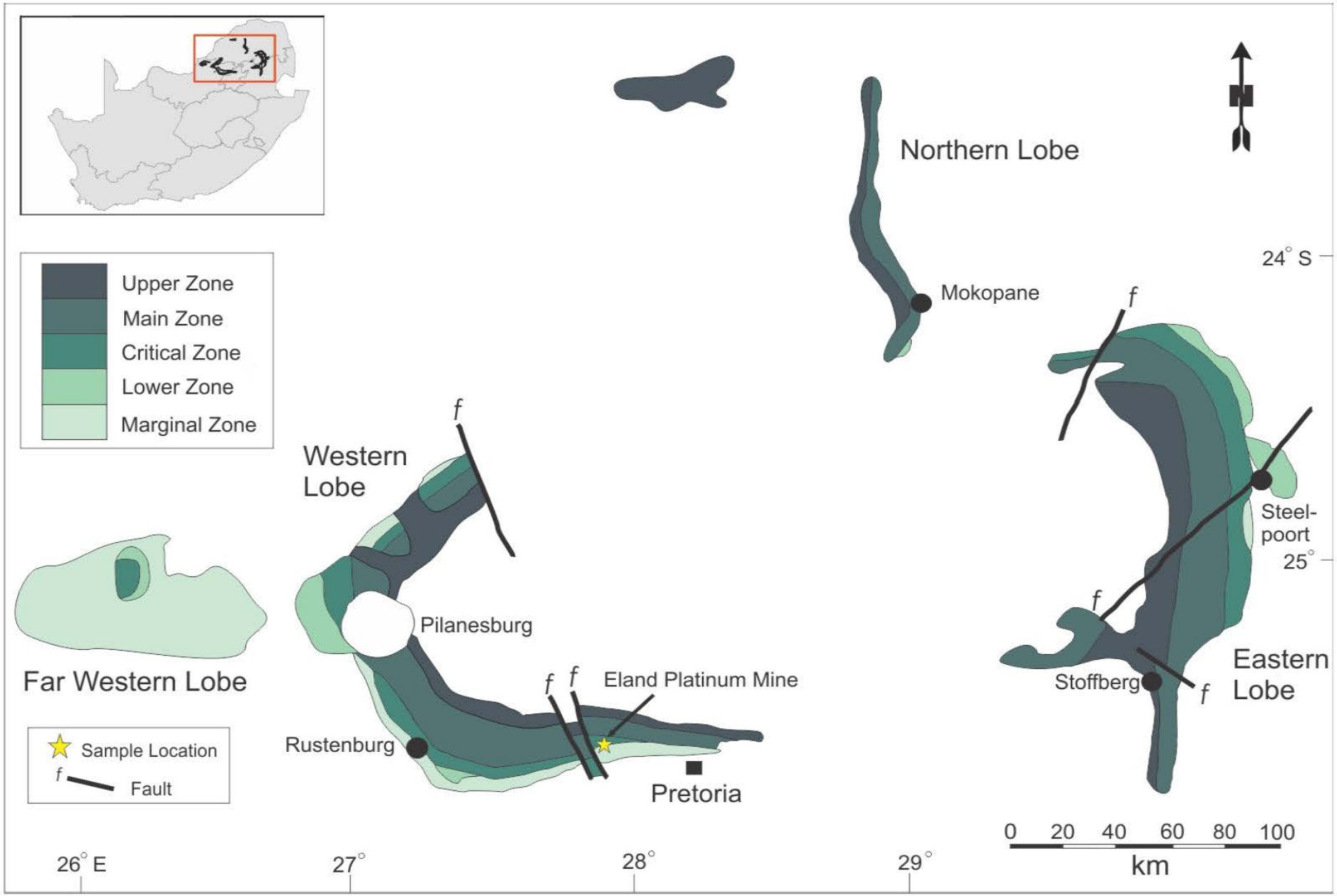

Figure 2.1.1. The Bushveld Igneous Complex. Image modified from Cawthorn and Webb (2013) and MINXCON (2009).

The Critical Zone is generally subdivided into the Lower Critical Zone (LCZ) and the Upper Critical Zone (UCZ) by the appearance of cumulus plagioclase which occurs at the base of the UCZ (Barnes & Maier, 2002b). The CZ is remarkable in that it contains regular layering in the form of 8 cyclic units which each comprise chromitites, pyroxenites, dunites, harzburgites, norites and anorthosites (Eales *et al*., 1990).

Wilson and Chunnett (2006) described the term 'reef' as an important economic zone (in terms of payable metal values) typically hosted within plagioclase-pyroxenite. Within the BC a number of reefs may be found, all within the Critical Zone (with the exception of the Platreef), namely the UG2 reef, the Merensky Reef, the Bastard Reef, and the Pseudo reefs (Barnes & Maier, 2002b). Arguably, the most economically important reef present in the BC is the Merensky Reef (MR). Typically, the Merensky Reef package (Fig. 2.1.2) comprises an anorthositic footwall, overlain by feldspathic pyroxenitic pegmatoid which is bounded by two chromitites, in which pyroxenite overlies the upper chromitite and is in turn overlain by norite and anorthosite (making up the hangingwall) (Cawthorn and Boerst, 2006). The stratigraphic succession from the basal chromitite to the top of the hangingwall anorthosite is referred to as the Merensky Cyclic Unit (MCU) (Cawthorn and Boerst, 2006; Wilson & Chunnett, 2006). The Merensky Reef is remarkable and world-class in that it contains up to 10 g/t PGE and is traceable for 300 km's from the western limb to the eastern limb (Schouwstra *et al*., 2000; Seabrook *et al*., 2005).

Three types of metalliferous, PGE-hosting reefs have been recognised (Fig. 2.1.3) in layered mafic-ultramafic intrusions (Wilson and Chunnett, 2006; Latypov *et al*., 2013). In the first PGE-deposit type, massive chromitite seams control disseminated sulphides (Latypov *et al*., 2013). This example is observed in the Rum, Stillwater and Bushveld Complexes. The second PGE-deposit type, as exhibited in the Merensky Reef, involves disseminated sulphides being associated with chromitite seams (Latypov *et al*., 2013). However, this relationship has been shown to not be spatially-exclusive, in that sulphides can also occur in the rock units both immediately above and below the chromitite seams (Latypov *et al*., 2013). The third and final PGE-deposit type involves a chromitite-free scenario in which disseminated sulphides occur within silicate rocks (Latypov *et al*., 2013). Examples for this type include the Munni Munni intrusion, the Skaergaard intrusion, the J-M reef of the Stillwater Complex and the Great Dyke (Latypov *et al*., 2013).

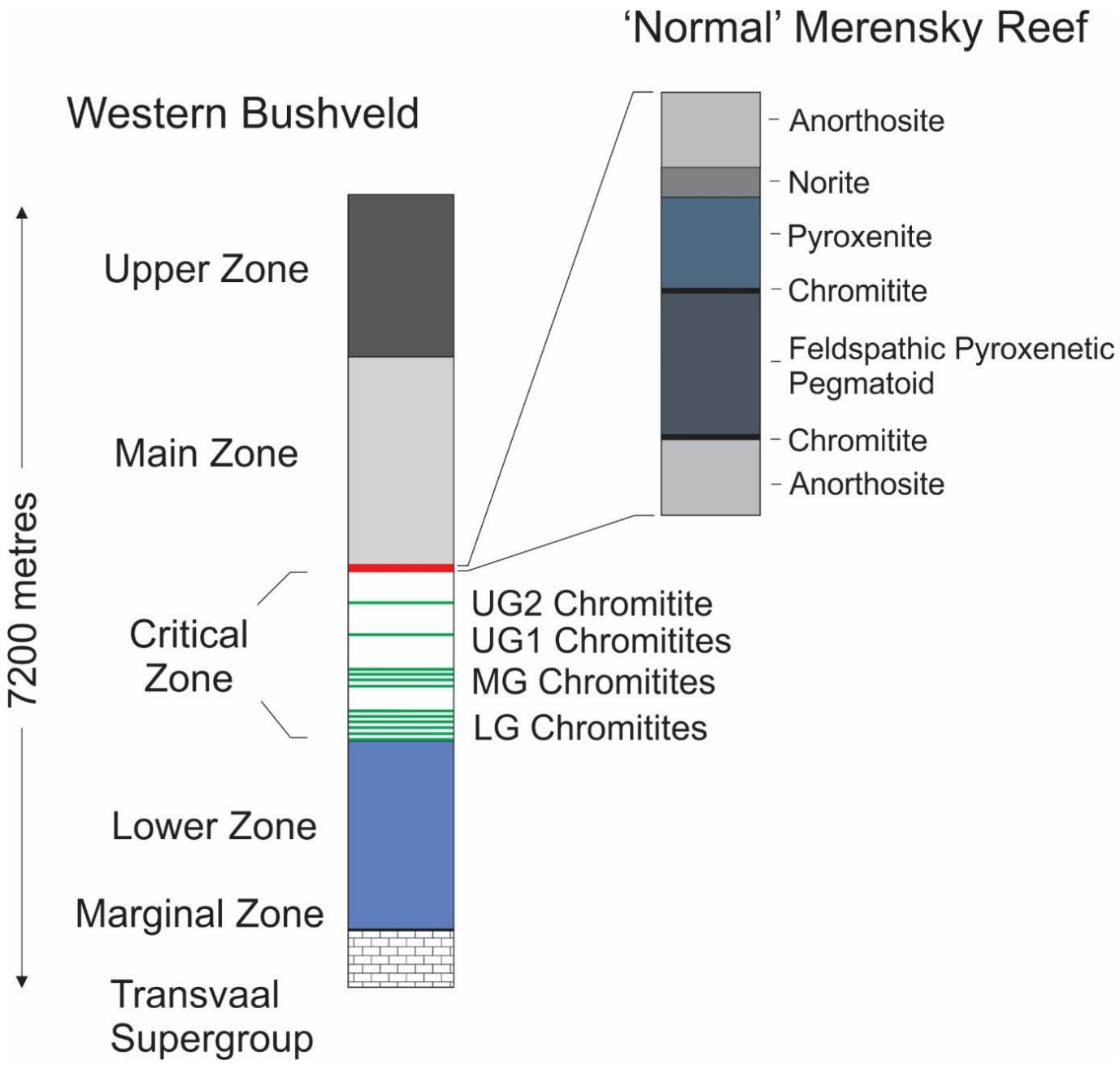

Figure 2.1.2. The stratigraphy of the Bushveld Complex and the Merensky Reef. Image adapted and modified from Cawthorn and Boerst (2006) and Yudovskaya *et al*. (2011).

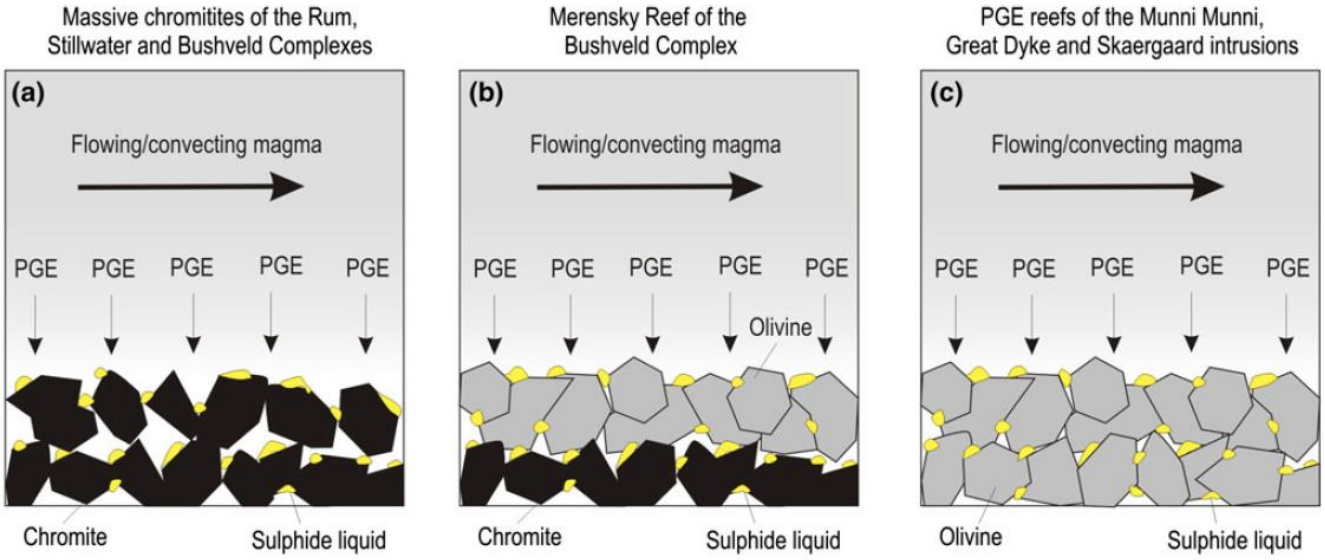

Figure 2.1.3. The three PGE-deposit types occurring in layered intrusions: 1) chromitite controls disseminated sulphide (e.g., The Bushveld Complex); 2) chromitite is associated with disseminated sulphide but does not control its occurrence (e.g., Merensky Reef); 3) disseminated sulphides occur but chromitite is absent (e.g., Munni Munni intrusion). Image adapted from Latypov *et al*. (2013).

2.2. Models for Chromitite Formation and PGE Mineralisation

2.2.1. Models for the Formation of Chromitite

Chromitites of the Bushveld Complex have received worldwide attention. This is because these chromitite layers (Fig. 2.1.4) can be traced over hundreds of km's along strike in both the eastern and western lobes of the Bushveld Complex and are associated with significant PGE mineralisation (Maier *et al*., 2013). Within the BC, up to 14 major seams are recognised (LG1-7, MG1-4 and UG1-3), however, their also exist many thinner layers which may bifurcate and merge with the major seams (Maier *et al*., 2013). The contacts of these seams with their silicate host rocks are sharp and PGE tend to be concentrated at the chromitite seam margins (such is the case for the UG2) (Maier *et al*., 2013).

Figure 2.1.4. Chromitite layering within the UG1 footwall at Dwars River. Image from Maier *et al*. (2013).

Magma Mixing

Arguably the most popular model for the formation of chromitite is the elegant magma-mixing model presented by Irvine (1975; 1977) from his work on the Muskox Intrusion. In this model, injections of primitive magma mix with the more evolved resident magma, within a magma chamber, to result in chromium supersaturation. While this model is largely accepted, e.g., explaining for the occurrence of nucleated chromite, it is also agreed upon that some additional processes to this model are required to account for the chromium budget problem that Eales (2000) first highlighted. The occurrence of chromitite with various host lithologies, such as anorthosites, pyroxenites, norites and mafic pegmatites, suggest that the lithology does not play a major role in controlling chromitite formation (Eales, 2000). Maier *et al.* (2013) also argued that constant proportions and compositions of mixing end-members is required to explain for the formation of laterally continuous chromitite layers seen in the BC. However, such a process seems difficult to envisage.

Pressure Change

Cameron (1980) and Lipin (1993) both suggested that pressure may be an important controlling factor in oxide formation, where stability fields may be shifted through pressure changes.

Pressure changes occurring in a magma chamber would also be able to explain the lateral extensiveness seen in chromitites today (Maier *et al*., 2013). However, because the model leaves behind no effect in the magmatic system, with only the order of crystallization of minerals being preserved, it is a difficult model to test and therefore significant experimental work has yet to be conducted (Cawthorn, 2010; Maier *et al*., 2013).

Crustal Contamination

Crustal contamination as a control on chromitite formation was first introduced by Irvine (1975), but later rejected by Irvine (1977) two years later. His explanation follows that any granitic melt added (e.g., from the Rooiberg felsites) would also contain alkalis which have the effect of shifting the olivine-orthopyroxene reaction to the SiO_2 apex on the ternary diagram (Irvine, 1977). Thus to move the reaction off the cotectic, geologically improbable amounts of crustal rock would be required (Irvine, 1977).

Injection of a Chromite Slurry

To overcome the problem of the chromium budget in the LZ and CZ, Eales (2000) suggested that chromite had to have been formed in some deeper magma chamber, i.e., a staging chamber, and later introduced to the system, via conduits, as chromite microphenocrysts (Eales, 2000). Eales and Costin (2012) estimated that the mixing of komatiitic melts with 20 to 30 % of crustal melts would be sufficient in creating a heterogeneous (liquid and crystal) system in such a staging chamber. One problem that is difficult to resolve with this model is that a dense chromite slurry might be expected to settle close to the site of entry and with increased distance away from the entry site the chromite slurry would be expected to thin dramatically (Cawthorn, 2010). This is particularly important given the lateral extent of the uniform chromitite layers seen in the BC.

2.2.2. Models for PGE Mineralisation

The association of PGE with chromitite in the BC is so remarkable that even the thinnest chromitite stringers contain elevated PGE grades (Maier *et al*., 2013). It is also important to

note that the platinum-group minerals (PGM) found in the RLS are generally associated with base metal sulphides (Kinloch, 1982).

Sulphide Association

It has been suggested that because PGM are so closely associated with sulphides, such as in the Merensky Reef, that a sulphide liquid was the principal phase in collecting the PGE (+Au, Ni and Cu) (Barnes & Maier, 2002b). In this model, a fractionating body of magma may reach sulphide saturation and thus form an immiscible sulphide liquid which is exsolved from the silicate magma (Campbell *et al*., 1983; Naldrett, 1999; Barnes & Maier, 2002b). Two popular methods in which a magma may become saturated in sulphide liquid is: 1) through assimilation of wall rocks or erosion of the roof of the magma chamber (Kruger and Schoenberg, 1998; Naldrett, 1999) and/or 2) magma mixing between the resident magma and the new injected magma (Campbell *et al*., 1983; Barnes & Maier, 2002b). However, the ability of magma mixing to produce sulphide oversaturation on its own was questioned by Cawthorn (2002) and Seabrook *et al*. (2005) who argued that additional processes are required. PGE (+Au, Ni and Cu), which have very high sulphide/silicate partition coefficients, are collected by the immiscible sulphide droplets (Barnes & Maier, 2002b). This collection process may be enhanced through the amount of time the sulphide droplets interact with the silicate magma and the turbulence within the system (Naldrett, 1997; 1999). With time the sulphide droplets, now rich in PGE, Au, Cu and Ni, settle onto the magma pile and form metalliferous reefs (Campbell *et al*., 1983; Naldrett, 1999).

Chromite Association

Some authors (e.g., Hiemstra, 1979; Latypov *et al*., 2013) have speculated that chromite may act as a potential host for PGE. Vermaak and Hendriks (1976) noted cases where sulphides occur within chromites, specifically in the Merensky Reef. In this model, the ability of sulphides to settle down and form metalliferous reefs (e.g., in the UG2) has been questioned (Hiemstra, 1979). It was suggested that because sulphide droplets have a greater tendency to wet chromite grains, compared to silicate grains, that sulphide droplets will nucleate onto *in situ* chromite grains, thus causing them to stick, and will settle down together (Hiemstra, 1979;

Latypov *et al*., 2012). However, Hiemstra (1979) questioned why some chromitite layers contain 'normal' concentrations of PGE compared to those with elevated PGE concentrations.

PGE Clusters

Tredoux *et al*. (1995) provided a model for PGE mineralisation (Fig. 2.1.5) which does not involve processes such as sulphide saturation, magma mixing and changes in pressure. In the model presented, PGE (which occur as metal clusters; about 10 - 100 atoms per cluster) are stabilized by surface adsorption with either sulphur or iron. Essentially, these clusters pre-concentrate the PGE. The IPGE (Ir, Os and Ru) which are heavier than PPGE (Pd, Rh and Pt) should have a greater chance of forming clusters and therefore chromitites should be enriched in Os, Ir and Ru. Following a sulphur-rich pathway the PGE clusters will associate with the sulphide melt and likely form PGE-sulphide complexes (e.g., tellurides, antimonides, arsenides and alloys). However, if the PGE clusters occur in a sulphur-poor environment the clusters will remain within the silicate melt and eventually merge to form PGE alloys which may act as nucleation sites for oxide and silicate minerals (e.g., chromites and olivines). One problem with this model is that a magma needs to be saturated in PGM, however, PGE are generally only present in ppb concentrations (Mathez, 1999).

2.2.3. A Discrepancy in Models for the Formation of both PGE and Chromitite

In reviewing models for the formation of PGE and chromitites, which commonly occur together (as in the Merensky Reef), it is clear that there is a discrepancy in their respective genetic models. As explained above, chromitite formation is generally attributed to magma mixing (Irvine, 1975; 1977) and not crustal contamination, as explained by Irvine (1977). However, the formation of sulphides, and ultimately PGE mineralisation, is considered to be the result of crustal contamination (Naldrett, 1997; 1999) and not through magma mixing (Cawthorn, 2002; Seabrook *et al*., 2005). Thus a reappraisal of genetic models is required to clear any confusion surrounding the formation of these deposits which are so intimately associated.

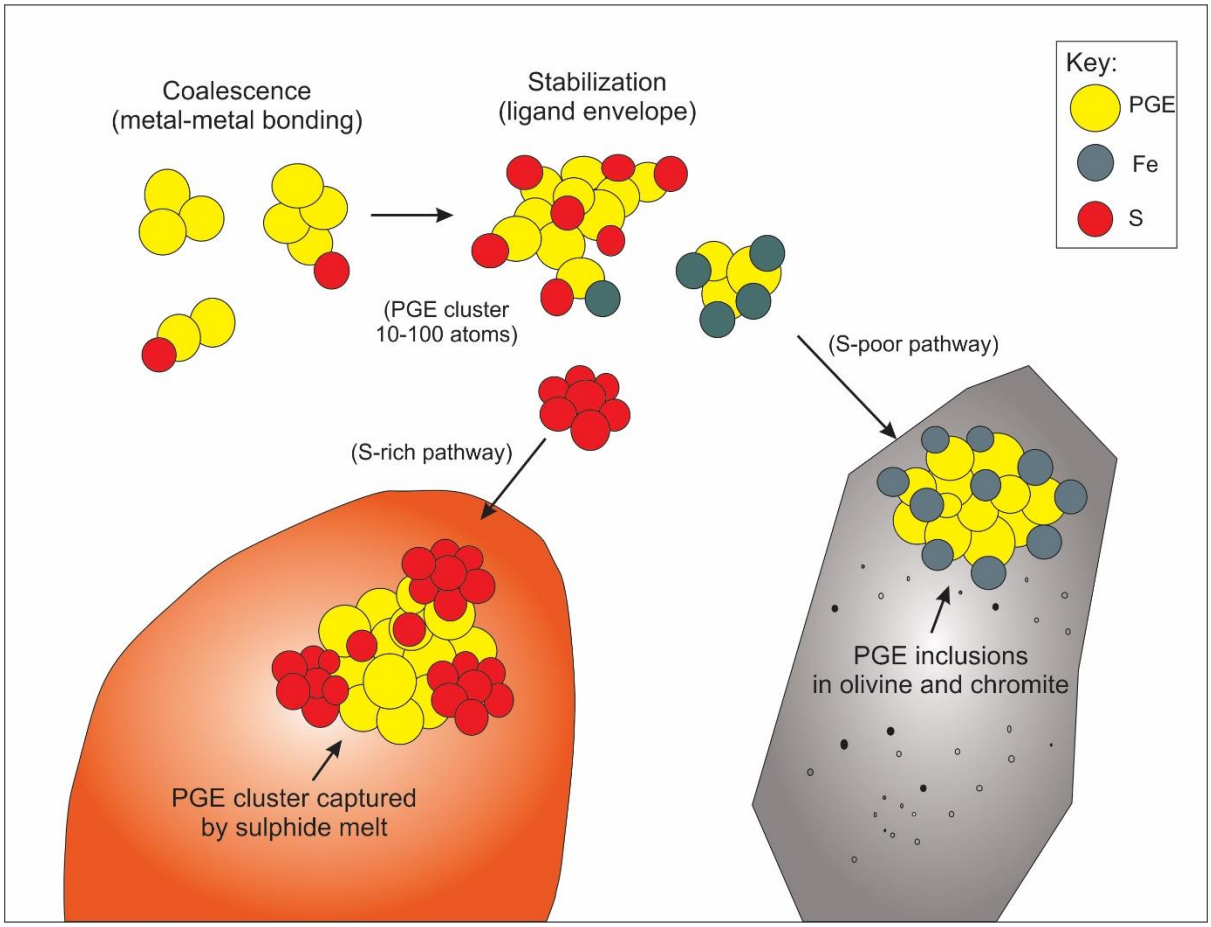

Figure 2.1.5. PGE cluster as a model for PGE mineralisation (as proposed by Tredoux *et al*., 1995). Two possible pathways are presented: 1) S-rich pathway and 2) S-poor pathway. Image modified after Robb (2005).

2.3. Models for the Formation of Metalliferous (PGE) Reefs

Various hypotheses have been proposed for the formation of metalliferous (PGE-bearing) reefs, and in particular the Merensky Reef, which will be evaluated below. Essentially two schools of thought currently dominate ideas for the presence of PGE in sulphides, and ultimately the formation of these metalliferous reefs.

2.3.1. The Downward Accumulation of PGE-bearing Sulphide Melts

The first group, referred to as the 'Downers' (Fig. 2.2.1), believe that primary magmatic processes such as magma mixing, crustal contamination and gravitational crystal settling are responsible for formation of these reefs. Variations of the Downers model exist in explaining the source of sulphide immiscibility, which hosts the abnormally high concentrations of PGE

compared to other magmatic sulphide ores, but the end result is ultimately the same (Campbell *et al*., 1983; Cawthorn, 2010). In a summary of the model proposed by Campbell *et al*. (1983), an immiscible sulphide liquid is created by magma mixing of a new primitive magma and the resident evolved magma in the chamber. PGE, present within the silicate melt, have extremely high partition coefficients with regard to sulphide and are effectively captured by the sulphide melt droplets. With time, these PGE-bearing sulphide droplets will settle upon a cumulus pile to produce a metalliferous ore horizon. There are various flaws in this model, as pointed out by Nicholson and Mathez (1991) who suggested that the model has difficulty in explaining the presence of the pegmatoid and the high abundance of PGE associated with this unit.

2.3.2. The Upward Infiltration of Fluid

This opposing group, referred to as the 'Uppers' (Fig. 2.2.1), believe that present day concentrations of PGE in reefs may be attributed to their transportation and migration within an aqueous fluid (Nicholson and Mathez, 1991). Following the model presented by Boudreau and Meurer (1999), a Cl-rich intercumulus fluid percolates upward, through the cumulus pile, and dissolves any PGE and sulphide present. Upon meeting a layer of crystal mush, where the intercumulus fluid was undersaturated, the fluid (along with sulphur and PGE) is redissolved into the interstitial silicate liquid and reprecipitates as BMS. The high fluid content of the magma would also act as a flux, in which remelting would ultimately lead to the formation of a coarse grained pegmatite, e.g., as seen in the MR. Nicholson and Mathez (1991) suggested that a hydration-melting front could account for the formation of the Merensky Reef (this model is presented in figure 2.2.2).

Evidence for the upward infiltration of late magmatic/hydrothermal fluids includes the presence of the pegmatoidal unit of the MR, the enrichment in Rare Earth Elements (REE) in the pyroxenes of the MR and the Cl-rich nature of apatites within the reef (Maier, 2005). However, as argued by Cawthorn (2010), the model presented by Boudreau (2008) requires that the PGE mineralisation be entirely associated with the pegmatitic zone. This is not always the case as PGE mineralisation is commonly associated with the chromitite stringers (Cawthorn, 2010). Furthermore, some MR facies which contain elevated PGE grades do not

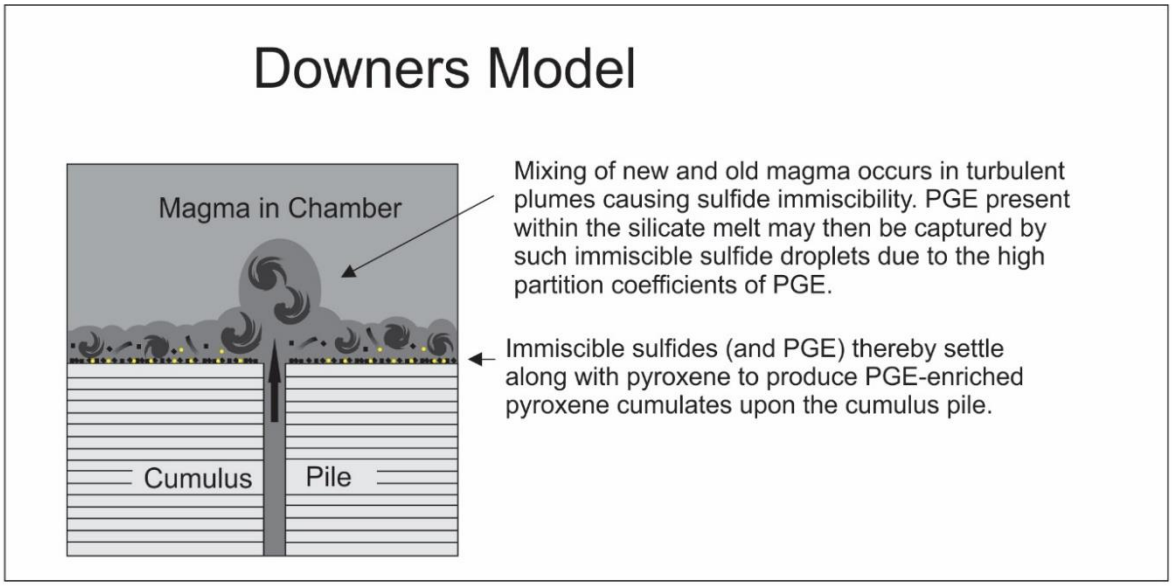

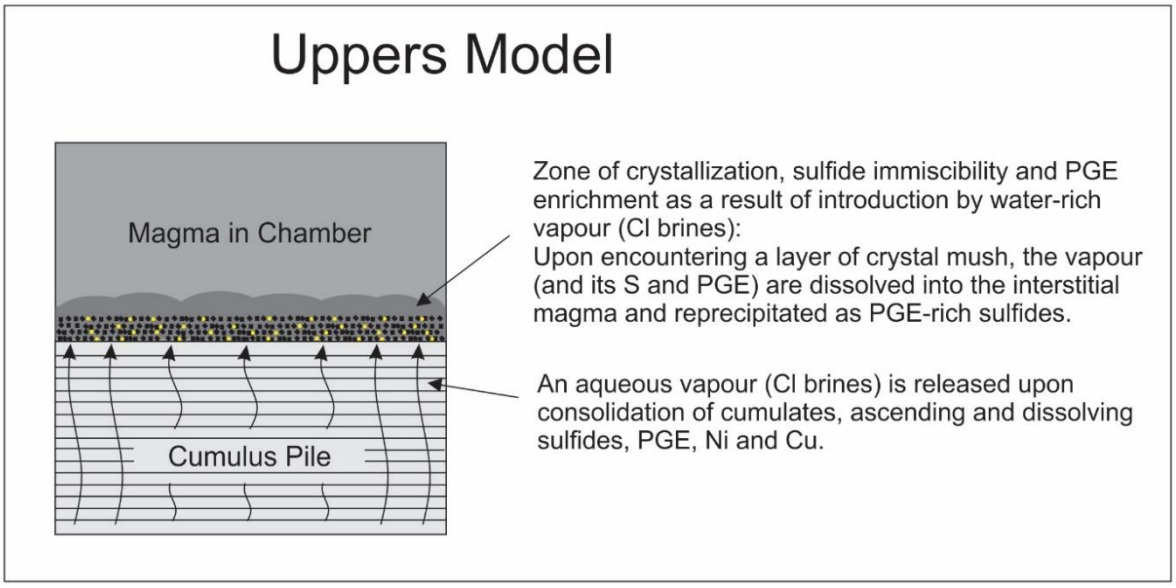

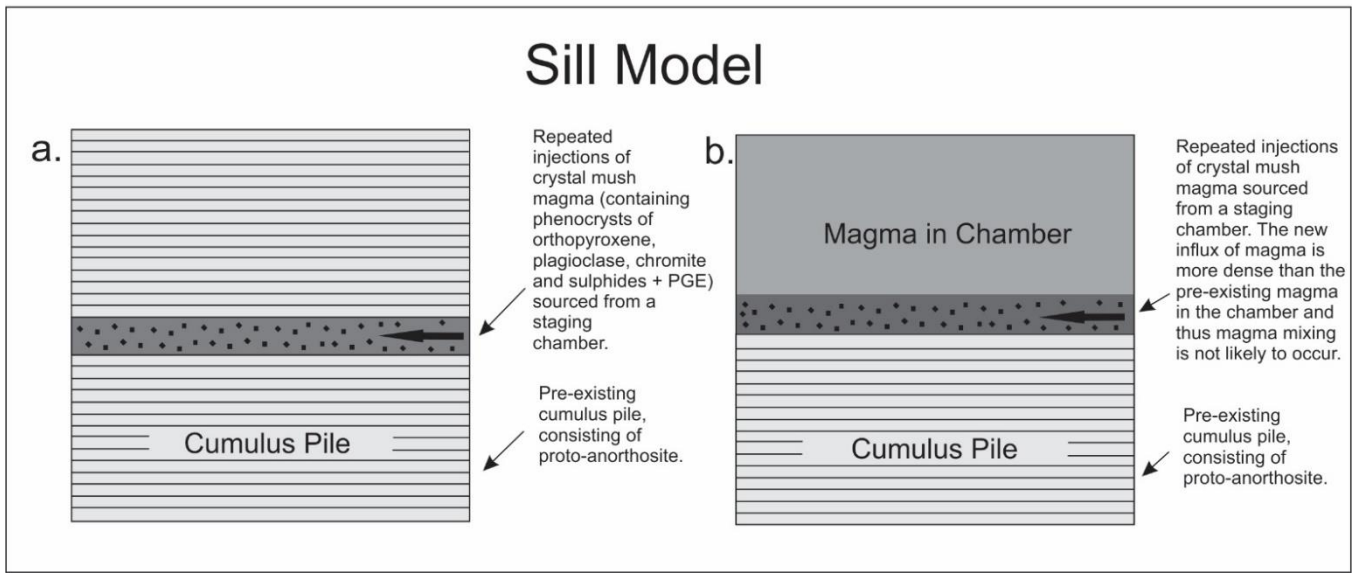

Figure 2.2.1. The 3 most popular models for the formation of metalliferous (PGE-bearing) reefs. Campbell *et al*. (1983); Boudreau (2008); Eales (2000); Marsh (1996). Image modified after Naldrett *et al*. (2009).

have a pegmatitic unit and thus this unit does not appear to be a controlling factor in PGE distribution. Furthermore, the model suggest that rocks below the reefs should be highly depleted in PGE, but often there is no evidence of such PGE depletion in the rocks below the reefs (Barnes and Maier, 1999; Maier, 2005). Maier (2005) suggested that most of the evidence and features used to support this model can equally be explained by magmatic processes (Barnes and Maier, 2002b).

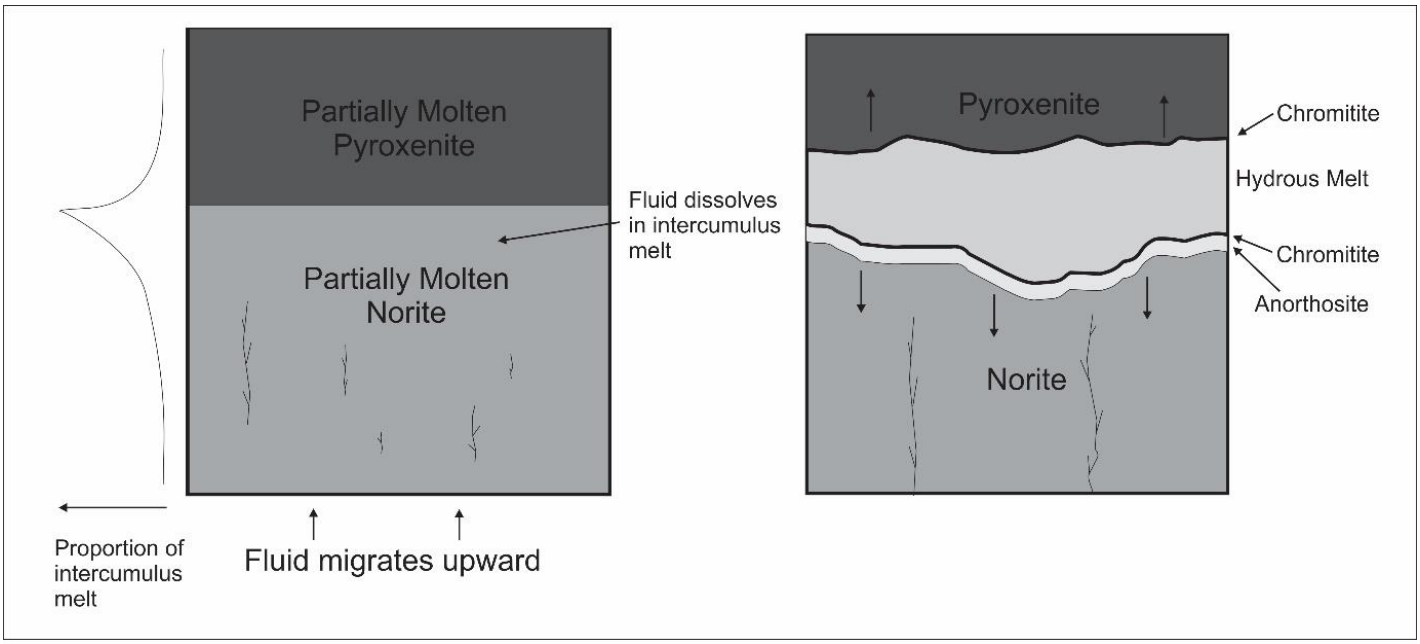

Figure 2.2.2. The role of upwards migrating fluids for the development of the Merensky Reef. In this model, presented by Nicholson and Mathez (1991), upwards migrating fluids traverse through fractures within partially molten norite. Thereafter, these fluids concentrate in a melt-rich zone, as indicated by the proportion of intercumulus melt shown on the left, due to a lack fractures within this zone. A resultant hydration front travelling into the overlying pyroxenite will form a chromitite seam while a hydration front travelling into the underlying norite will form an anorthosite and chromitite seam.

2.3.3. The lateral Injection of a Crystal-rich Slurry

Following on from the Eales (2000) and Eales and Costin (2012) chromite slurry injection model, a model involving the injection of a crystal slurry (Fig. 2.2.1) as a sill has been proposed for the Merensky Reef and other metalliferous reefs (Mitchell and Scoon, 2007; Kruger, 2010). The concept and properties of phenocryst-rich magmas is drawn from Marsh (1996). The model requires that magma, ascending through a mush column (Fig. 2.2.3), migrates through

conduits and inherits crystals from earlier crystallization events which may differ from one another as a result of their own local physical and chemical conditions. For example, as depicted in figure 2.2.3, pressure variations, as a result of stratigraphic depth, may influence the local crystallization conditions, i.e., pre-crystallized olivine within the deepest portions of the magmatic system. This column of magma is in itself flow sorted (i.e., differentiated) as a result of gravity and grain dispersive pressures and thus a stream of fairly sorted phenocrysts may be delivered to any filling magma chamber (Marsh, 1996). This sorting, as suggested by Marsh (1996), depends on differences in the hydraulic properties between the liquid and crystals, as well as the time available for sorting. The intensity and volume of delivered phenocrysts depends on the magma path and its interaction with these pre-existing crystals (Marsh, 1996). Furthermore, as suggested by Marsh (1996), the actual magmatic system may be a tall stack of interconnected sills within the lithosphere.

This model provides an explanation to many problems that the previous two models have difficulty in answering. For example, the chromium budget problem (as suggested by Eales, 2000) is resolved by the introduction of chromite microphenocrysts sourced from a staging chamber. Furthermore, elevated PGE grades can be explained by the upgrading of sulphide melts within a conduit as proposed by Maier *et al*. (2001). In this model, sulphide droplets are carried by an initial surge of magma and deposited within widened parts of a conduit to form ‘proto-ore’ (Fig. 2.2.4A). Thereafter, continued surges of magma, which are undepleted, may upgrade previously accumulated sulphide melts in PGE, Cu and Ni and reprecipitate these sulphide melts further down the conduit (Fig. 2.2.4B). During the first stage it is possible that sulphide melts may be injected into the floor and thus these proto-ores would remain shielded from upgrading during subsequent surges. However, Maier *et al*. (2001) has questioned the model’s applicability to the BC as the entire LZ and CZ have been shown to be PGE-enriched (thus making it unlikely that sulphides equilibrated with the magmas responsible for these two zones).

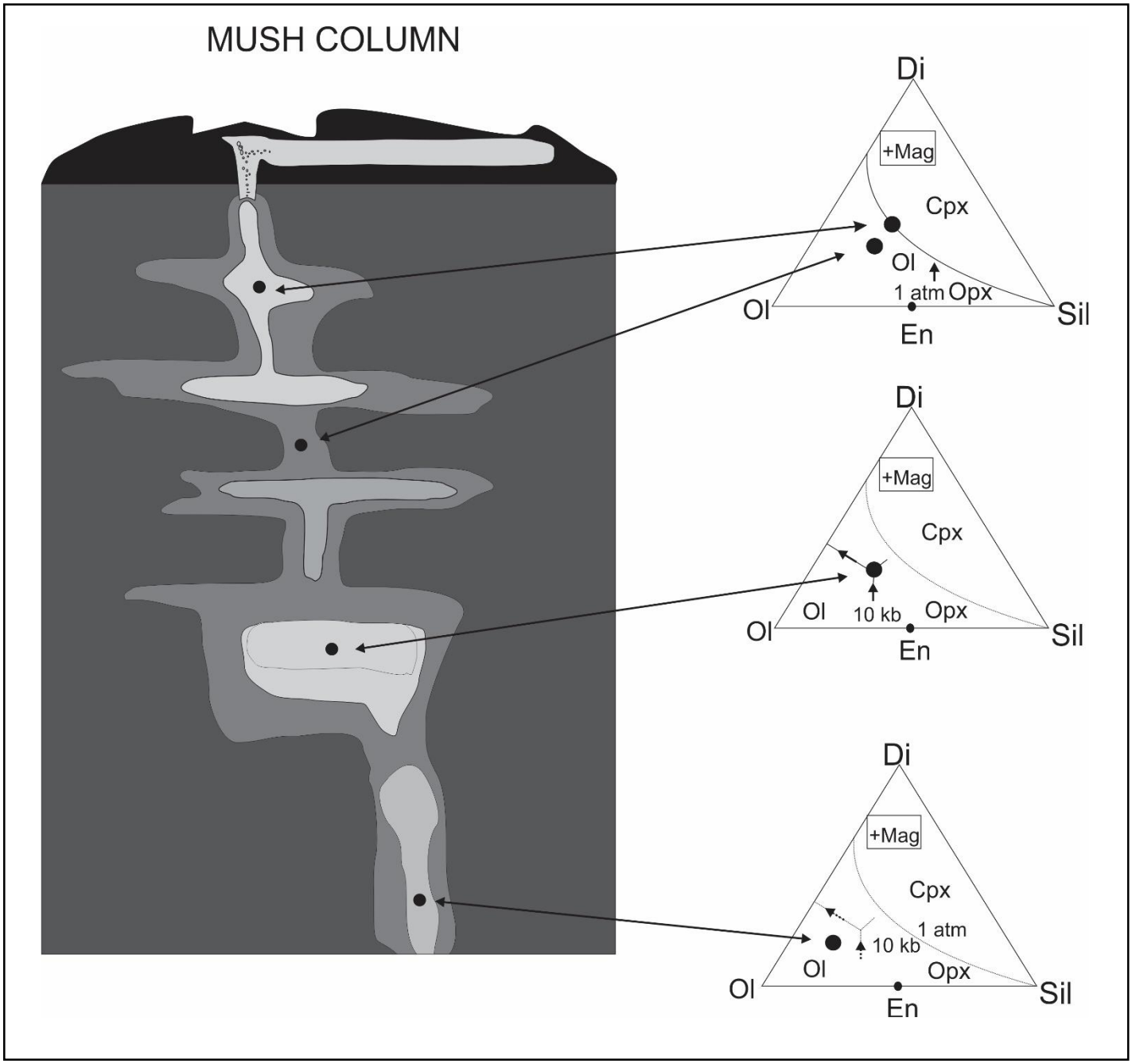

Figure 2.2.3. A schematic diagram illustrating a crystal mush column. Within this magmatic system, comprising stacked sills which are interconnected by conduits, are various local crystallization environments which are pressure-dependent. The system describes how magma, migrating through these conduits, may inherit and transport pre-crystallized phenocrysts to a filling magma chamber. Image adapted and modified from Marsh (1996).

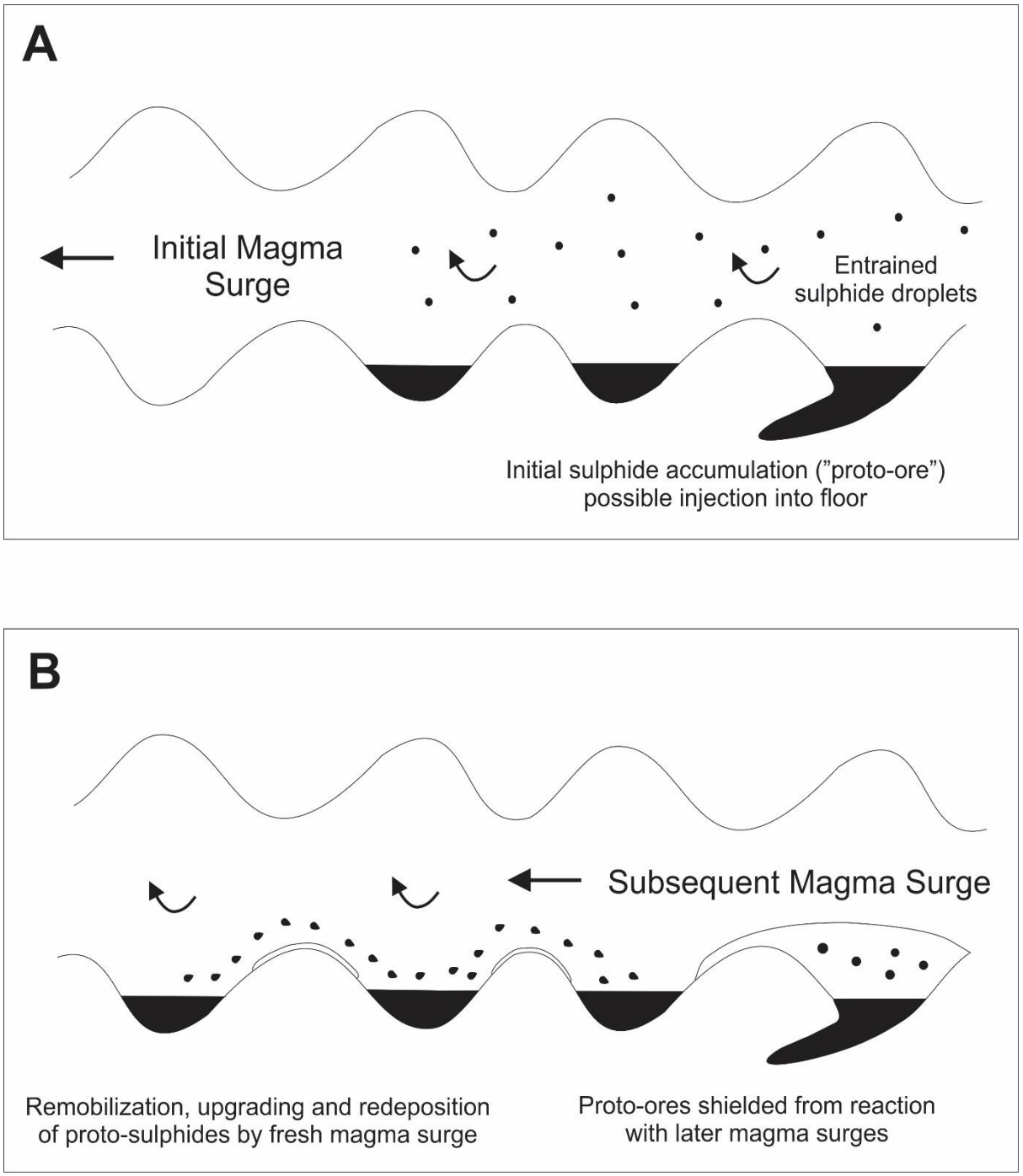

Figure 2.2.4. A schematic diagram illustrating a conduit system (Maier *et al*., 2001). A) An initial surge of magma, carrying entrained sulphide droplets, migrates through a conduit and deposits the sulphides in wider parts of the conduit, and in some cases these sulphides are injected into the floor to form "proto-ore". B) Subsequent surges of undepleted magma may uncover previously accumulated sulphides and upgrade them in Ni, Cu and PGE and redeposit them further downstream. However, sulphides which were previously injected into the floor of the conduit may remain shielded from further upgrading. Image modified after Maier *et al.* (2001).

2.4. Previous Research on the Merensky Reef and its PGE Distribution

The Bushveld Complex is the largest layered intrusion on the planet, containing various world class reserves (PGE, chromium, vanadium and magnetite to name a few). Evidently, a vast database of literature exists on this deposit and in particular the Merensky Reef. Yet mechanisms for the formation of the Merensky Reef still remain controversial despite decades of research (Wilson and Chunnett, 2006).

An early paper by Vermaak and Hendriks (1976) provided a detailed review of the mineralogy, and in particular the precious metals, of the Merensky Reef. Typically, the MR comprises cumulate orthopyroxene and olivine while plagioclase and clinopyroxene are postcumulus (i.e., interstitial). Hydrous minerals such as biotite, phlogopite, hornblende and muscovite occur as accessory minerals along with quartz, tourmaline, zircon and calcite. Chromite, magnetite, rutile, ilmenite and various base metal sulphides (BMS; such as pyrrhotite, chalcopyrite, pyrite, pentlandite and cubanite) generally make up the rest of the primary mineralogy. Barnes and Maier (2002b) noted that despite a modal proportion of 1 - 5 % for the BMS, these disseminated to net-textured sulphides host the majority of the precious metals occurring in the MR. This suggest that the precursor to the sulphide and PGE phases must have been extremely enriched in PGE (Ballhaus and Sylvester, 2000). Vermaak and Hendriks (1976) identified precious metals comprising, predominantly, braggite, laurite, cooperite, minor sperrylite and Pt-Fe alloys. Schoenberg *et al*. (1999) recorded other occurrences of PGM within chromite lattices and in cumulus chromite.

Various facies for the Merensky Reef have been documented (historically by Wagner, 1929) which may influence PGE distribution. Cawthorn (2010) provided detailed illustrations of the MR for contact/thin reef, pegmatitic pyroxenite reef and thick/wide reef. Cawthorn (2002; 2010) and Mitchell and Scoon (2007) also suggested that there are problems in using thin or normal (e.g., pegmatitic pyroxenite) facies in an attempt to decipher magmatic events due to compaction. Instead, they refer the reader to the use of a wider reef facies (such as thick reef) in understanding these events, which is in agreement with the suggestions of Wilson and Chunnett (2006). Viljoen (1999) noted that the pyroxenite unit, between the two chromitites, varies in thickness from about 10 cm (e.g., contact reef from the Impala mine area) up to 14 metres thick (e.g., wide reef from Brits area). Viljoen (1999) also showed that the pegmatoidal

texture, as in normal Merensky facies, is less pronounced in the wider reef facies and may be completely absent in some cases (Fig. 2.3.1).

In terms of PGE distribution, Cawthorn (2012) noted that PGE in the MR are irregularly distributed through the vertical section. Typically, contact or thin reef facies contain mineralisation within the anorthosite underlying the lower chromitite unit and within pyroxenite layers of the main reef (Cawthorn, 2012). In addition to this, Viljoen (1999) suggested that PGE mineralisation (primarily Pt+Pd) greater than 2 g/t may be found in the norite overlying the upper chromitite. In facies where the reef is wider, a double peak PGE distribution is evident, though the mineralisation tends to track the upper chromitite giving a mineralisation style known as 'top loaded' (Viljoen, 1999; Cawthorn, 2012). Barnes and Maier (2002b) proposed that the thickness of the pyroxenite unit within the MR is inversely proportional to the grade of ore. For example, Viljoen (1999) showed that where the thickness of this unit is greater than 3 metres the package, typically, is not economical to mine.

Barnes and Maier (2002b) showed that mantle-normalised PGE diagrams for the MR footwall norite and anorthosite show a pattern of slight enrichment of PGE relative to Ni and Cu, while the reef exhibits a pattern of strongly enriched PGE relative to Ni and Cu. Furthermore, the MR hangingwall pyroxenites and norites show a pattern of steady enrichment from Ni to Pt and a general flatness from Pt to Pd.

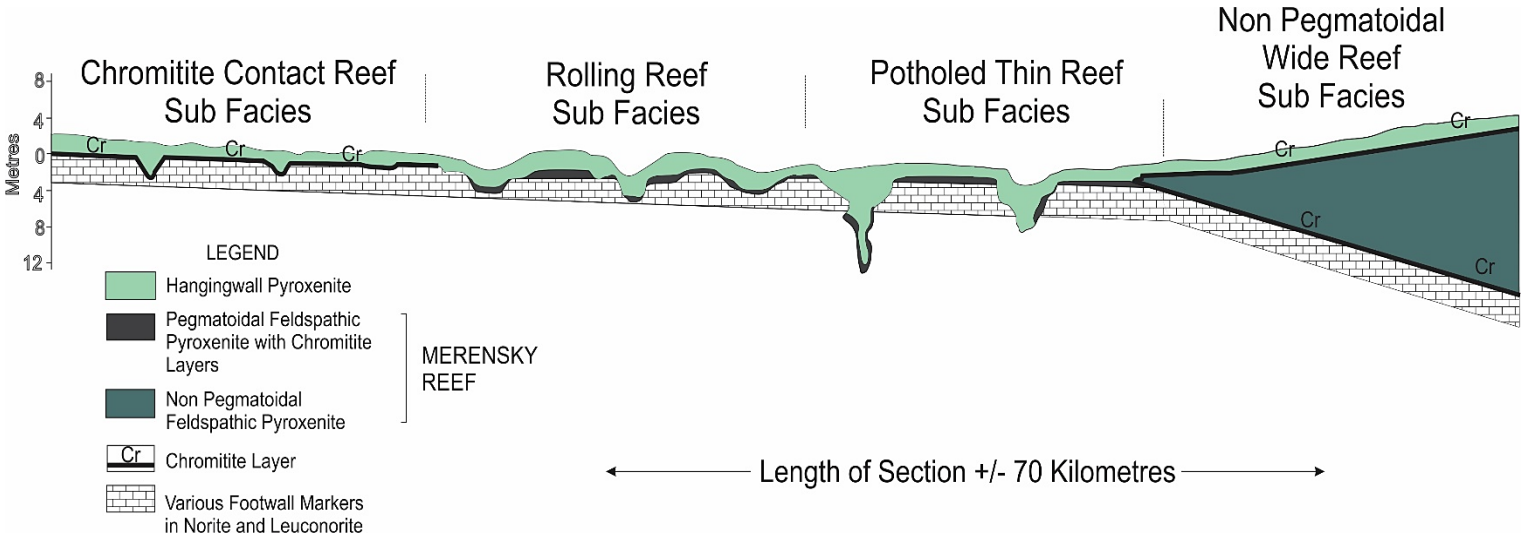

Figure 2.3.1. Schematic diagram of the geology of the various types of Merensky Reef facies. Image modified after Viljoen (1999).

Chapter 3. Materials and Methodology

3.1. Sampling

Access to core yards and sample material at Eland Platinum Mines (Fig. 3.1.1) was kindly granted by Glencore. The drillcore obtained for this study, borehole ELF-395, was sampled approximately 5 metres into the bottom section of the hangingwall and 3 metres into the top section of the footwall. In total 16.48 metres of drill core was made available for the purpose of this study.

3.1.1. Sampling Strategy

Wide-reef Merensky facies was targeted for this study as previous investigations (e.g., Barnes and Maier, 2002a; Wilson and Chunnett, 2006) into PGE distribution have been hindered by the compression of PGE-peaks associated with narrower economic reef facies. Furthermore, as suggested by Wilson and Chunnett (2006), whole core was targeted to ensure that sufficient sample material was available for analysis while still maintaining representative fine-scale intervals. Thus, the use of a wider reef facies, as well as access to whole-core as opposed to more commonly used half- and quarter-core, is intended to facilitate detection of small scale variations in PGE abundances. On this premise, ELF-395 was chosen and sampled much like ELF-393, which was used in a previous study (Largatzis, 2014). One noteworthy difference between boreholes ELF-395 and ELF-393 is that borehole ELF-393 contained no chromitite stringers whereas borehole ELF-395 does contain a thin chromitite stringer at the contact of the base of the reef and the underlying footwall rocks. This is significant in that insights may thus be gained into the control of PGE-partitioning in the Merensky Reef, and specifically the role of chromite in controlling PGE distribution.

3.1.2. Sample Preparation

The drillcore was transported to the Geology Department at Rhodes University, Grahamstown, for use of their in-house sample preparation and analytical facilities. Once core logging was completed, 28 samples were taken from various representative depths from borehole ELF-395 for thin section preparation (Table 3.1.1). Sampling for thin-section preparation targeted changes in lithology and textures, as well as across contacts (e.g., across the chromitite stringer at the base of the reef) and in particular where separation of PGE peaks was previously

identified in borehole ELF-393. Both normal, i.e., uncovered, and polished thin sections (for analysis of mineral chemistry) were prepared. Using 2.0 cm intervals, at their respective depths (Table 3.1.1), 29 samples were prepared for rock crushing. Each sample was placed into a manganese-steel vessel (Fig. 3.1.2C), which in turn was placed into a Herzog swing mill (Fig 3.1.2E). Each sample was set to run for approximately 3 minutes until ground into a fine powder (< 400 mesh). In between samples, the manganese-steel vessel was cleaned thoroughly with soap and distilled water and dried using acetone and compressed air. Quartzite blanks between samples were avoided to minimise SiO_2 contamination and the samples were crushed in order of broadly increasing expected PGE content, by lithology (i.e., anorthositic samples followed by more ultramafic samples). Rocks abundant in sulphides were crushed last to limit sulphide contamination. Contamination by the vessel itself is possible and thus the composition of the vessel was noted: 2.00 % manganese, 0.90 % carbon, 0.30 % phosphorus and 0.20 % silica.

3.2. Analytical Methods

3.2.1. Petrography

Normal and polished thin sections were investigated for textural features, petrographic description and mineral identification, paragenetic sequences and mineral-mineral relationships. Polished thin sections were investigated under reflected light (RL) while normal thin sections were examined under transmitted light in plane-polarized light (PPL) and cross-polarized light (XPL). Modal analyses of minerals present within each sample were calculated quantitatively via a James Swift Point Counter. Petrography was done on a Leica DM EP microscope (Fig. 3.1.2A) and photomicrographs were captured through an EC 3 high-resolution digital camera attachment which were then analysed and processed on the Leica Application Suite software.

3.2.2. Mineral Chemistry

16 polished thin sections were analysed for their mineral chemistry and composition to provide detailed context to the PGE variation. In particular, pyroxenes, plagioclases, sulphides, oxides, micas and PGM (to identify partitioning preferences) were examined. Furthermore, back-scattered electron (BSE) images and wavelength-dispersive spectroscopy (WDS) elemental

distribution maps were produced. Mineral chemistry was done at the Geology Department, Rhodes University, using the Jeol JXA 8230 Superprobe (Fig 3.1.2D). Using 4 WD spectrometers, analytical conditions were set to the following: an acceleration voltage of 15 kV, a probe current of 0.2 nA, a 10 second peak counting time and a 5 second background counting time. A range of 98.5 to 101.5 wt. % was set as the requirement for the totals of all minerals when calculating ternary plots or evaluating data, i.e., to avoid poor and misleading data.

Table 3.1.1. Samples taken from borehole ELF-395 for thin section preparation and for powders. The lithological unit, stratigraphic height and thin section type are also given. Abbreviations are as follows: AnMo - mottled anorthosite, AnSp – spotted anorthosite, LuNo – leuconorite, No – norite, Px – pyroxenite, An – anorthosite, Chr – chromitite. *Note sample MR-09b was prepared for rock crushing only and not as a thin section.

Sample	Unit	Stratigraphic Height (m)	Thin Section Type
MR-01	AnMo	55.07	Normal
MR-02	AnMo	55.31	Polished
MR-03	AnSp	56.09	Normal
MR-04	AnSp	56.38	Polished
MR-05	AnSp	56.89	Normal
MR-06	LuNo	57.05	Polished
MR-07	No	57.27	Polished
MR-08	Px	57.8	Polished
MR-09a	An	57.97	Polished
*MR-09b	An	58.01	*
MR-10	Px	58.04	Polished
MR-11	Px	58.13	Polished
MR-12	Px	58.88	Normal
MR-13	Px	59.6	Polished
MR-14	Px	60.43	Normal
MR-15	Px	62.48	Normal
MR-16	Px	63.3	Polished
MR-17	Px	63.95	Normal
MR-18	Px	65.5	Normal
MR-19	Px	66.63	Polished
MR-20	Px	67.63	Normal
MR-21	Px	68.14	Polished
MR-22	Px	68.61	Polished
MR-23	Chr	68.64	Polished
MR-24	AnMo	68.68	Polished
MR-25	AnMo	68.79	Polished
MR-26	AnMo	69	Normal
MR-27	AnMo	70.73	Normal
MR-28	AnMo	71.17	Normal

Figure 3.1.1. Satellite image of Eland Platinum mine, in the western Bushveld, where borehole ELF-395 was drilled. Image obtained from Google Earth.

3.2.3. Platinum-Group Elements

Samples were weighed to 25 g and the powders were packaged and transported to UQAC, Chicoutimi, Canada, for PGE analysis by fire assay followed by ICP-MS analysis. The technique used is described in Savard *et al*. (2010). The following isotopes were analysed: ^{99}Ru, ^{103}Rh, ^{105}Pd, ^{190}Os, ^{193}Ir, ^{195}Pt and ^{197}Au. Detection limits for the respective PGE (+ Au) are given in Table 3.1.2.

Table 3.1.2. Limits of detection for PGE and Au in borehole ELF-395. Units in ppb.

Element	Ru	Rh	Pd	Os	Ir	Pt	Au
Limits of Detection (LOD)	0.120	0.082	0.471	0.065	0.025	0.084	0.484

3.2.4. Major Elements

To determine whole-rock major element oxide content, samples were weighed to 5 g and sent to the Ministry of Northern Development and Mines (MNDM) Geoscience Laboratories (Geo Labs) in Sudbury, Canada, for major element analysis by X-ray fluorescence (XRF) (using Geolabs method code XRF-M01). Samples were analysed for the following major element oxides: TiO_2, CaO, Fe_2O_3, MnO, K_2O, Al_2O_3, Cr_2O_3, P_2O_5, SiO_2, MgO and Na_2O. Co, Ni, Cu and S were measured using a hand-held XRF machine (HH-XRF). However, certain samples could not be analysed for Ni, Cu and Co because of lower detection limits. Instead, data for these respective elements were used from the trace element (ICP-MS) results. S (measured using the HH-XRF) was included in this study to compare trends to Ni, Cu and the PGE.

3.2.5. Trace Elements

Samples were weighed to 5 g and sent to the MNDM Geoscience Laboratories in Sudbury, Canada, for trace element analysis by Inductively Coupled Plasma - Mass Spectrometry (ICP-MS) (using Geolabs method code IMC-100). Trace element data for borehole ELF-393, which was analysed under the same analytical conditions, is also included in this thesis.

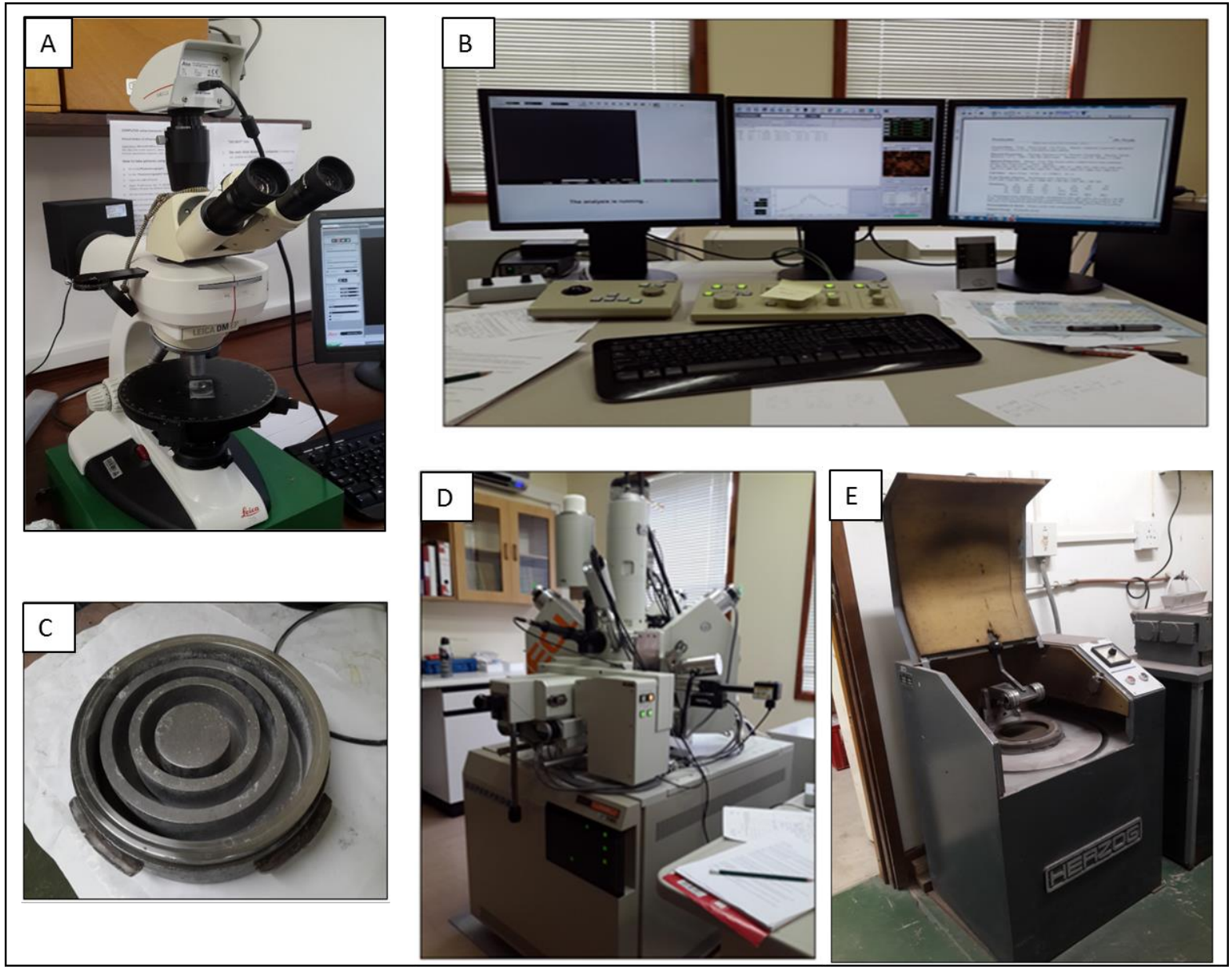

Figure 3.1.2. Rhodes University's in-house sample preparation and analytical equipment. **A)** A Leica DM EP microscope used during petrography. **B**) Desktop and monitors used in mineral compositional analysis. **C**) Manganese-steel vessel used to grind rock into powder. **D)** The Jeol JXA 8230 Superprobe. **E)** The Herzog swing mill into which the Mn-vessel is placed.

Chapter 4. Results

4.1. Macroscopic Results

Borehole ELF-395 (Fig. 4.1.2), representing the wide-reef Merensky facies, is approximately 16.48 metres in length. A core log of the borehole is provided in figure 4.1.3. The footwall rocks comprise a 2.74 metre anorthosite (Fig. 4.1.2) that is mottled in texture and comprises substantial chloritisation. Fractures and veins are common and are associated with the chloritisation. Interstitial pyroxene in this unit occurs as 2 cm irregular grains and in a 10:90 % ratio with cumulus plagioclase.

In sharp contact with the anorthosite footwall is a 3 mm chromitite stringer (Fig. 4.1.1A). Overlying the chromitite stringer, and in sharp contact with it, is a pyroxenite unit (Fig. 4.1.2) which makes up the bulk of the reef (i.e., 10.60 metres in length). Typically, pyroxene occurs as 3 mm grains, however, grains of up to 5 mm in size are also present. Sulphides are abundant throughout this unit and occur as disseminated ± 2 mm grains. The ratio of pyroxene to plagioclase in this unit is approximately 85:15 %. The pyroxenite reef is in sharp contact with an overlying 20 cm anorthosite seam (Fig. 4.1.1F). The anorthosite is mottled in texture and, within fractures, pyroxene and sulphides tend to be concentrated as 1 mm fine grains. At the bottom contact, between the underlying pyroxenite and the overlying anorthosite, is a 3 cm-wide sulphide-rich zone (predominantly chalcopyrite and pentlandite) (Fig 4.1.1F). The anorthosite seam is, in turn, overlain by a 48 cm thick pyroxenite (Fig. 4.1.1D). Orthopyroxene within this unit occurs as 4 - 7 mm subhedral to euhedral cumulus grains amongst interstitial plagioclase (in 85:15 % ratio, respectively). Sulphides, which are abundant, occur as 2 mm disseminated grains. In total, the pyroxenite present in the Merensky Reef measures 11.08 metres thick.

The pyroxenite reef is overlain by a 23 cm norite (Fig. 4.1.2) unit, which represents the start to the hangingwall. The norite also appears as spotted in texture, with pyroxene occurring as ± 0.4 cm subhedral grains. Here, the ratio of pyroxene to plagioclase is approximately 70:30 %. Minor 1 mm specks of sulphides are also visible. The norite gradually changes into a 15 cm thick leuconorite, which in turn is overlain by spotted anorthosite (Fig. 4.1.1E). The spotted anorthosite is approximately 74 cm in length and comprises ± 0.4 cm subhedral grains of

pyroxene with plagioclase (in a 10:90 % ratio, respectively). Chloritisation is present and is associated with fractures. In some areas, zones of 'whiter' plagioclase which comprise finer (± 0.2 cm) grains of pyroxene occur. In these zones, pyroxene grain boundaries appear to be better defined and fine fractures are common. The spotted anorthosite gradually changes into the overlying mottled mottled anorthosite (Fig. 4.1.1B) which occupies the top 1.32 metres of the hangingwall. Dark grey to black irregular grains of interstitial pyroxene occur with milky-white plagioclase in a 10:90 % ratio, respectively. Minor chloritisation of this unit is observed, imparting a slight green colour to the core, which is commonly associated with minor fractures in the rock.

4.1.1. Comparisons between boreholes ELF-395 and -393

When comparing boreholes ELF-395 and ELF-393 (Fig. 4.1.4), the lithological units correlate relatively well with only a few exceptions. First and foremost, both cores are stratigraphically displaced (most likely as a result of a dip in stratigraphy between both drillcore locations). Lithologically, the most notable difference between these units is the presence of a 3 mm chromitite stringer in ELF-395 (at the contact between the reef and footwall rocks) and the absence of chromitite in ELF-393. Instead, ELF-393 comprised leuconorite and norite units at the same lithological location. The pyroxenitic reef in both cores is relatively equal in length, however, it is more difficult to constrain the location of a pegmatitic pyroxenite in ELF-395. Furthermore, ELF-395 contains a 20 cm anorthositic seam (near the top of the pyroxenite reef) which is absent in ELF-393. With regard to the hangingwall sequences both drill cores correlate relatively well.

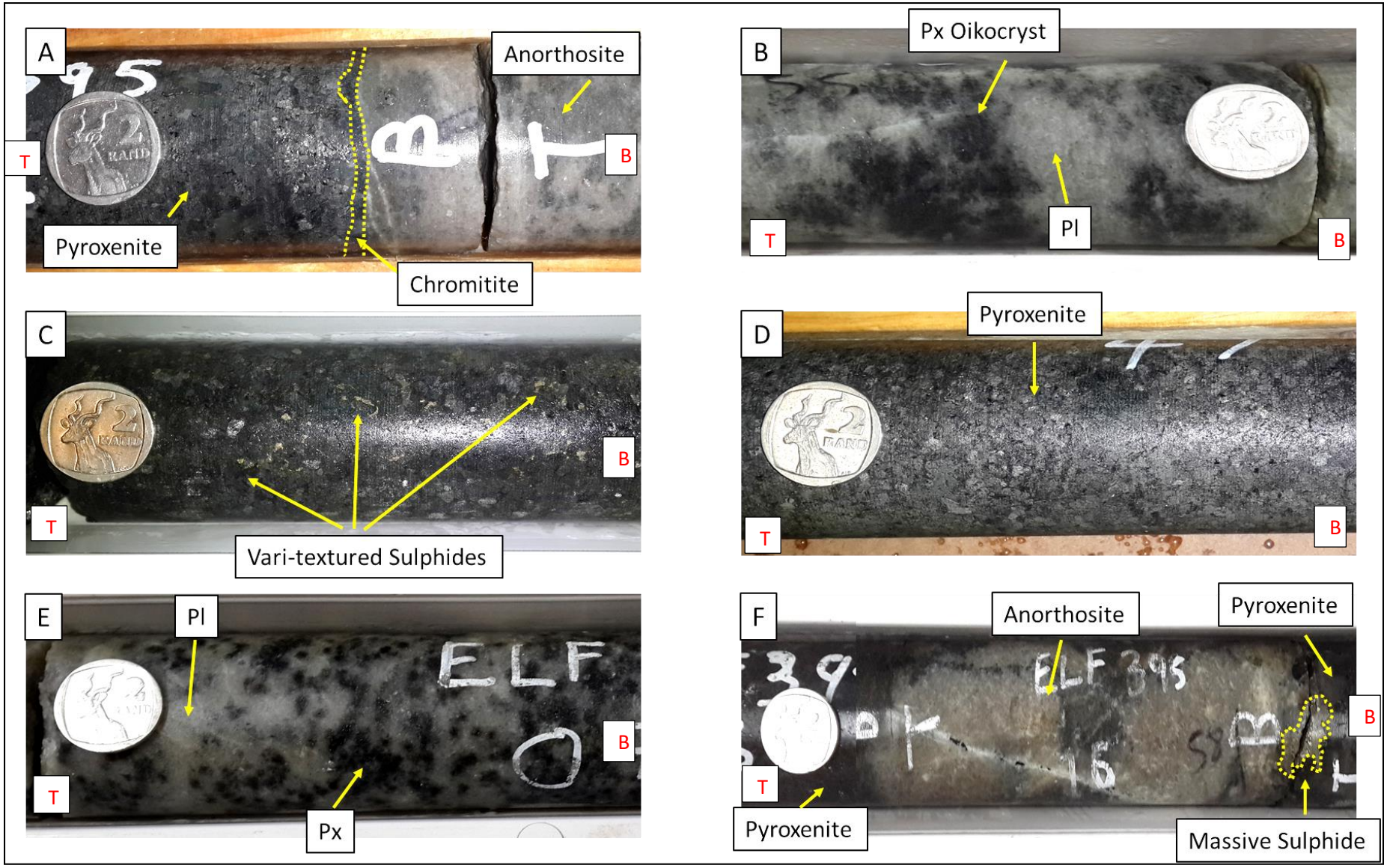

Figure 4.1.1. Notable macroscopic features from borehole ELF-395. **A)** 3 mm chromitite seam bounded by overlying pyroxenitic reef and underlying anorthositic footwall units. **B)** Mottled anorthosite from the hangingwall, **C)** Vari-textured sulphides are common in the pyroxenite reef unit. **D)** The reef pyroxenite. **E)** Spotted anorthosite from the hangingwall. **F)** The 20 cm anorthosite seam above the underlying pyroxenitic reef unit (note the 2 - 3 cm massive sulphide grains at the contact). Note T (i.e., top) and B (i.e., bottom) indicate stratigraphic up positions.

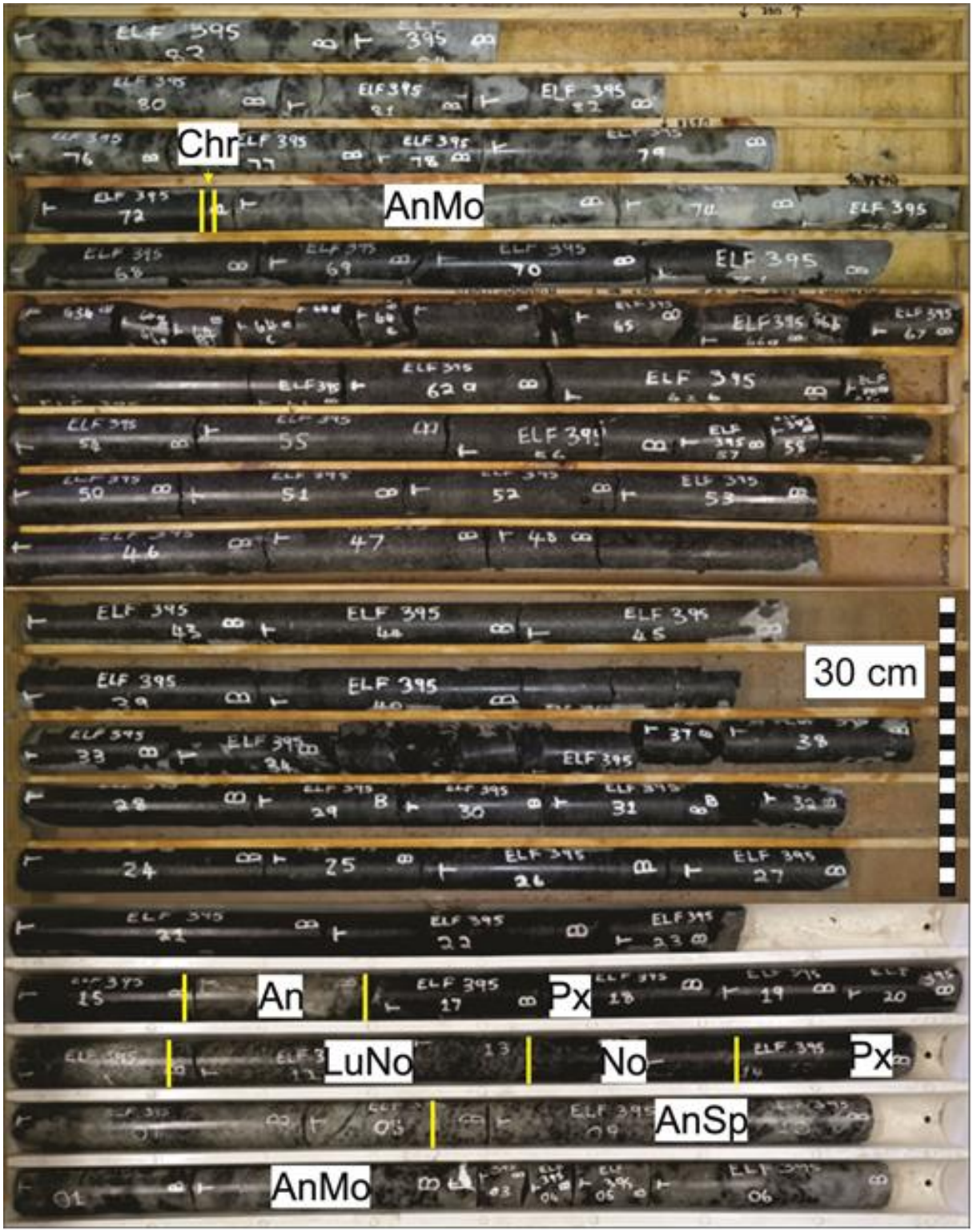

Figure 4.1.2. Borehole ELF-395, representing wide-reef Merensky, from the Eland Platinum mines, Western Bushveld. The bottom left corner represents the start of hangingwall while the top right corner marks the end of the footwall. Note scale in the figure.

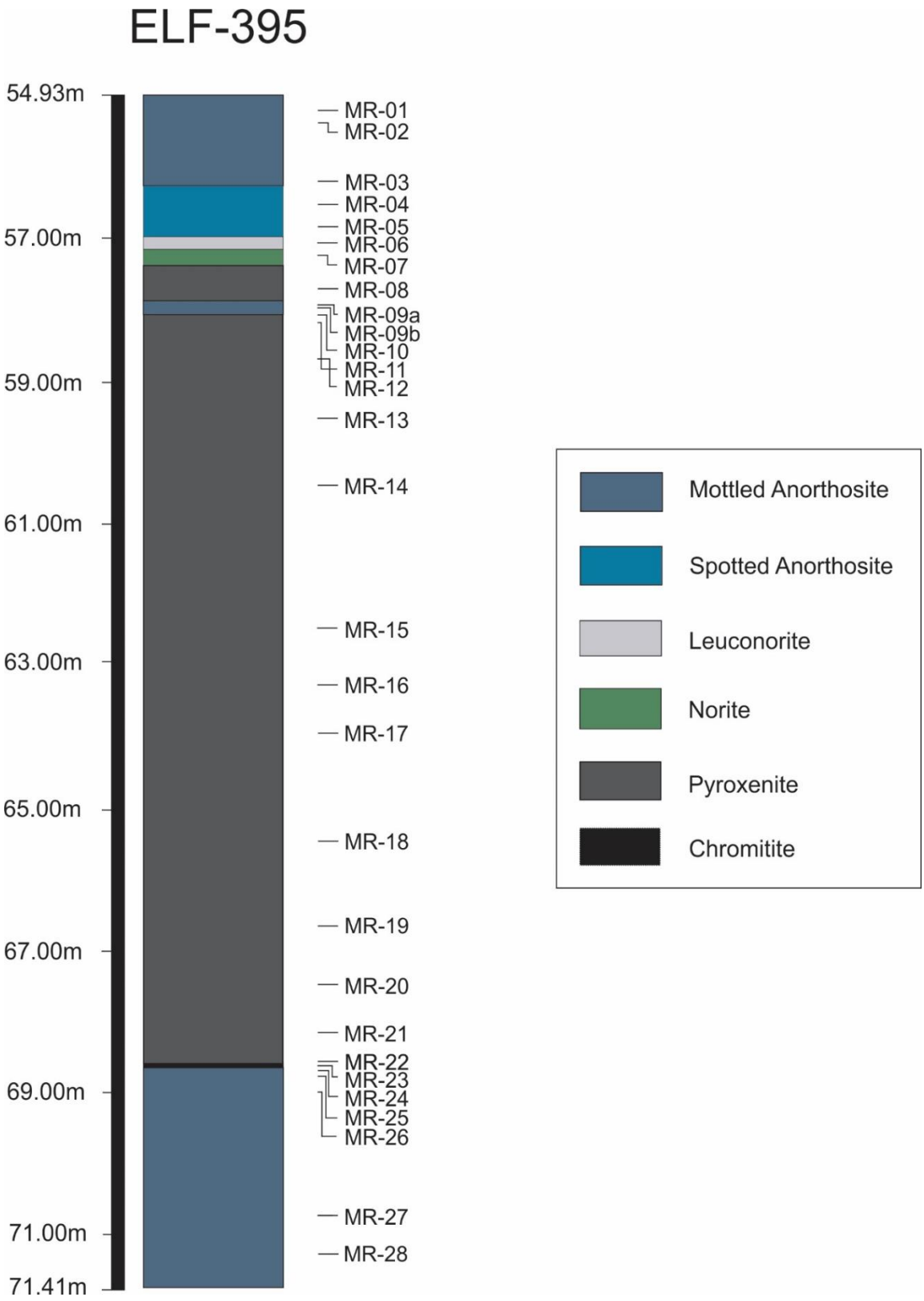

Figure 4.1.3. Core log of borehole ELF-395 representing the wide-reef Merensky facies. Note sample locations are also shown.

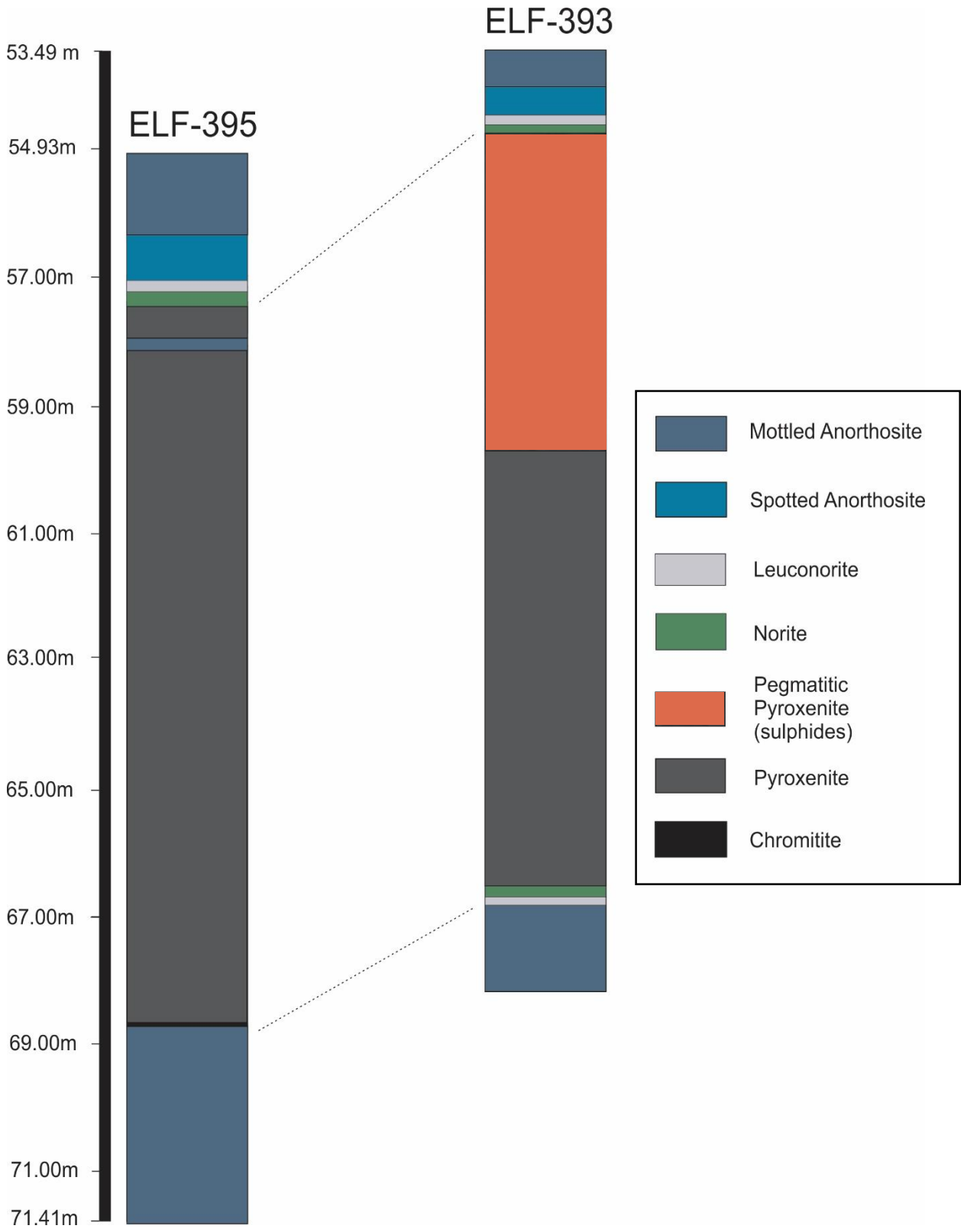

Figure 4.1.4. A comparison of core logs from borehole ELF-395 and ELF-393. Major differences include the presence of a chromitite stringer in ELF-395, as well as a 20 cm anorthositic seam within the pyroxenitic reef. Furthermore, the noritic and leuconoritic units (above the footwall) which are present in ELF-393 are absent in ELF-395.

4.2. Petrography

This chapter comprises the petrographic analysis of borehole ELF-395. Both normal (i.e., covered) and polished thin sections were analysed (see Chapter 3.2.1). Modal abundances for the 28 thin section samples of borehole ELF-395 (as calculated by a James Swift Point Counter) are presented below in figure 4.2.1. The lithological suites in this study have been defined based on correct technical mineralogical criteria and on common usage (for ease of comparison with previous workers). For example, anorthosites (which should contain > 90% plagioclase) include a modal range between > 80% and 90% plagioclase while pyroxenites (which should contain < 10% plagioclase) include a modal range between > 10 and 20% plagioclase. The data collected are presented in the form of Merensky rock units (e.g., Merensky Reef pyroxenite) so as to constrain trends in mineralogy with respect to stratigraphic height.

4.2.1. Merensky Reef Hangingwall Anorthosite

The modal proportions of minerals in this rock is recorded in figure 4.2.1 (from samples MR-01 to MR-05). Plagioclase is the most abundant mineral in this rock and typically occurs as cumulus, 0.3 to 3.0 mm grains. The grains are typically subhedral to euhedral in shape (Fig. 4.2.2A). These grains exhibit both Carlsbad and Albite polysynthetic twinning and are relatively free of inclusions. Significant sericitization of plagioclase is observed in this rock and sulphides and oxides show a close association to the replacement texture. Furthermore, plagioclase often exhibits zoning, and grain boundaries show triple point junctions (Fig. 4.2.2A).

Orthopyroxene occurs as intercumulus, subhedral, 2.5 mm-wide grains. Inclusions of 0.2 to 0.5 mm subhedral plagioclase laths and clinopyroxene are common (Fig. 4.2.2B). Orthopyroxene typically shows exsolution lamellae. Clinopyroxene, which is more abundant in the hangingwall anorthosite than orthopyroxene, occurs as intercumulus, 0.5 to 2.5 mm anhedral to subhedral grains.

Oxides show a low abundance in the hangingwall anorthosite (between 0.4 and 1.2 modal %). Oxides identified include ilmenite, rutile and chromite and all occur as 0.1 to 0.2 mm anhedral

to subhedral grains. Typically, these oxides occur between silicate grain boundaries (e.g., adjacent to plagioclase) and show a strong spatial association with biotite (Fig. 4.2.2C & D) and sericite. Commonly, ilmenite hosts rutile lamellae (Fig. 4.2.2E).

Base metal sulphides (BMS) comprise pentlandite, pyrrhotite, pyrite and chalcopyrite and occur as anhedral 0.1 to 0.3 mm aggregates (Fig. 4.2.2F). Typically, BMS show a strong association with biotite, chlorite, sericite and serpentine.

Other minerals identified in the hangingwall anorthosite, include accessory serpentine, chlorite and biotite. Chlorite and biotite often occur together as 0.2 to 0.8 mm anhedral aggregates in the interstitial groundmass.

4.2.2. Merensky Reef Hangingwall Leuconorite

The modal composition of this rock is recorded in figure 4.2.1 (from sample MR-06). Plagioclase, which is the most abundant mineral in the rock, occurs as cumulus, anhedral to subhedral equant grains. Grain size varies between approximately 0.5 and 2.5 mm. The plagioclase is largely inclusion-free and is often altered to sericite (Fig. 4.2.3A). Triple point junctions are apparent and grains show slight zoning.

Orthopyroxene, which occurs as a subhedral intercumulus phase, varies in grain size between 0.4 and 1.5 mm. Ophitic textures are common where larger (approximately 3.0 to 4.0 mm) oikocrysts occur, which enclose subhedral 0.3 to 0.5 mm plagioclase chadacrysts (Fig. 4.2.3B). Clinopyroxene, also occurring as an intercumulus phase, is subhedral to euhedral in shape. Grain size varies between 0.5 and 3.2 mm and subhedral 0.2 to 1.0 mm plagioclase inclusions are common (Fig. 4.2.3D).

Oxides are slightly more abundant within the leuconorite hangingwall compared to the overlying anorthositic unit. Minerals identified include rutile, ilmenite and chromite which occur as 0.05 to 0.2 mm anhedral to subhedral grains adjacent to the surrounding silicates. Commonly, ilmenite hosts rutile lamellae (like the anorthosite HW).

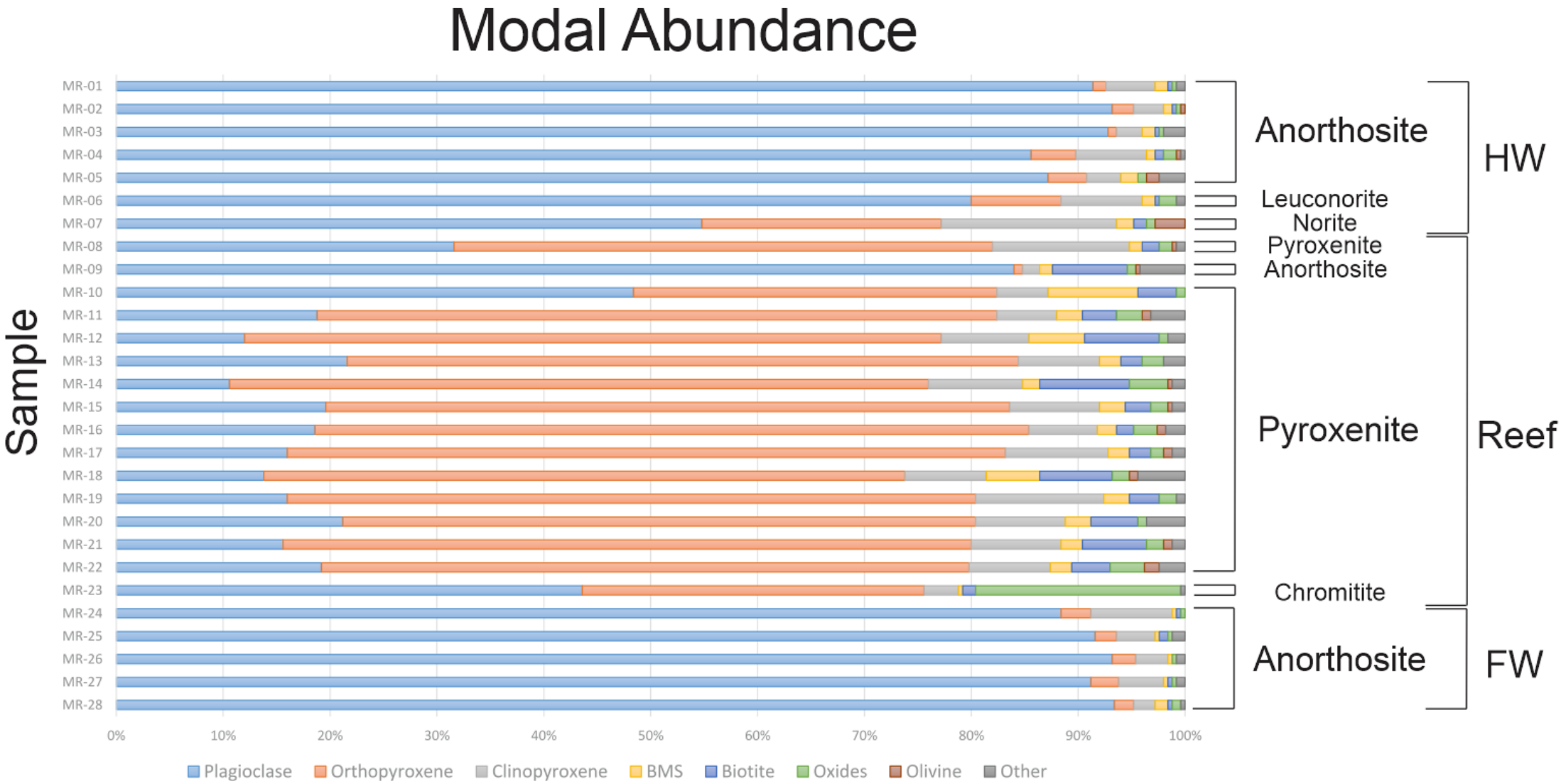

Figure 4.2.1. Modal abundance estimates of various minerals from different rock units in the Merensky Reef. Note: sericite modal abundances have been included with plagioclase. Also note that sample MR-23 is not entirely a chromitite in itself as the thin section encompasses both the pyroxenite unit above, and the anorthosite unit below the chromitite stringer.

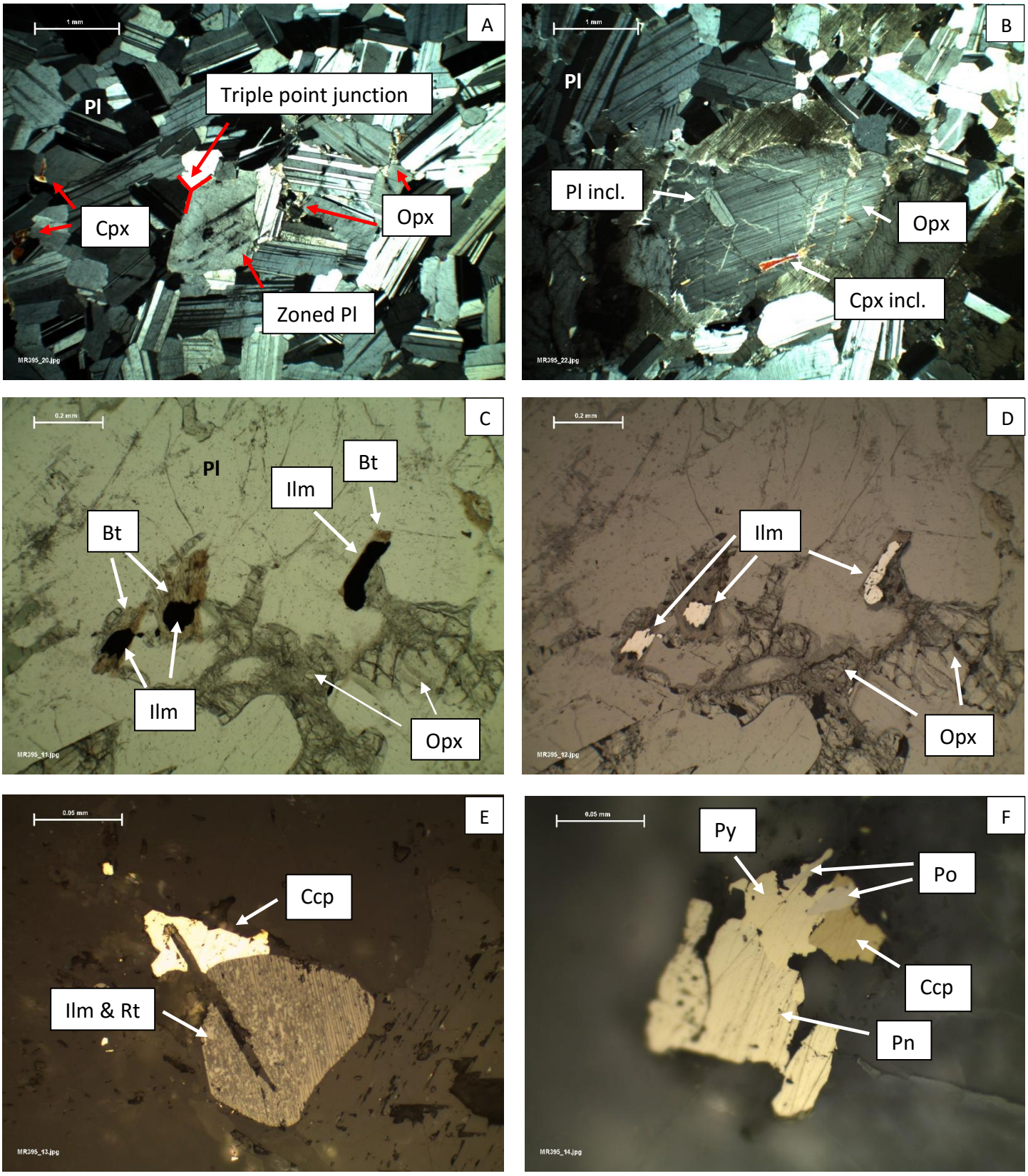

Figure 4.2.2. Photomicrographs taken from the MR HW anorthosite. **A)** XPL image of characteristic anorthositic texture (note the triple point junctions at grain boundaries). **B)** XPL image of Opx oikocryst with a Pl chadacryst and Cpx inclusion (i.e., ophitic texture). **C)** & **D)** PPL and RL photomicrographs (respectively) showing the close association of Ilm and Bt. This association was also observed with other oxides, as well as BMS. **E)** RL image of rutile lamellae in ilmenite. **F)** RL image showing a BMS aggregate comprising pyrrhotite, pentlandite, chalcopyrite and pyrite.

Base metal sulphides occur as anhedral to subhedral aggregates comprising chalcopyrite, pentlandite, pyrite and pyrrhotite (Fig. 4.2.3C). Typically grain size varies between 0.05 and 0.3 mm in size.

Biotite and chlorite occur as accessory phases within the leuconorite hangingwall. These minerals show a strong association to oxides and BMS. Both biotite and chlorite occur as anhedral to subhedral grains and grain size varies between 0.1 and 0.5 mm and 0.2 and 0.3 mm, respectively.

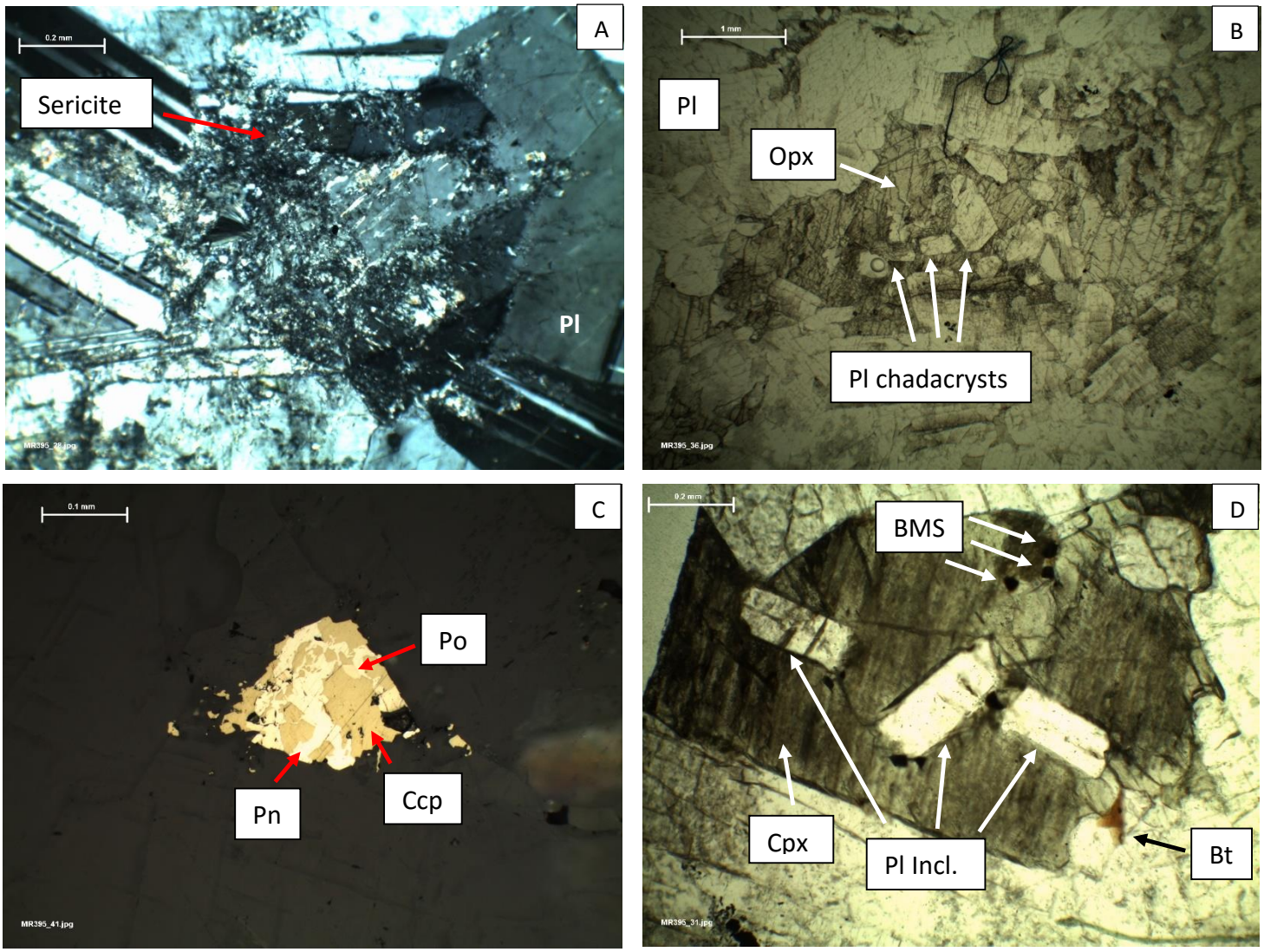

Figure 4.2.3. Photomicrographs taken from the MR HW leuconorite (sample MR-06). **A)** XPL image of sericitic alteration of plagioclase. **B)** PPL image of Opx oikocryst with Pl chadacrysts (i.e., ophitic texture). **C)** RL photomicrograph of BMS aggregate comprising pentlandite, chalcopyrite and pyrrhotite. **D)** PPL image of Pl inclusions in Cpx. Also shown are grains of biotite and BMS.

4.2.3. Merensky Reef Hangingwall Norite

A noticeable change in the modal abundance (Fig. 4.2.1) of all major minerals occurs at the base of norite (sample MR-07). Furthermore, a significant increase in grain size is recorded in most minerals. Plagioclase occurs as an interstitial phase which varies in size between 0.5 and 2.5 mm. Grain shape varies between anhedral to subhedral and grains are relatively inclusion free. Triple point junctions were identified in the rock and plagioclase shows minor zoning.

Orthopyroxene occurs as subhedral, 0.6 to 3.0 mm cumulus grains which contains inclusions of 0.1 - 0.3 mm anhedral to subhedral exsolved clinopyroxene, trapped plagioclase and biotite. Clinopyroxene is present as 0.5 to 2.0 mm, cumulus anhedral grains. Larger (~ 15.0 mm) anhedral to subhedral oikocrysts also occur which contain subhedral 0.5 to 1.5 mm plagioclase chadacrysts and anhedral, 0.5 to 1.0 mm partially resorbed orthopyroxene (Fig. 4.2.4A & B).

Oxides identified include rutile, ilmenite (Fig. 4.2.4F) and chromite. Typically, these oxides are present as < 0.1 mm inclusions within pyroxene (Fig. 4.2.4E) or as larger 0.1 to 0.3 mm anhedral grains which show a strong association with biotite.

Base metal sulphides comprising pyrite, pentlandite, pyrrhotite and chalcopyrite occur as 0.2 – 0.6 mm anhedral to subhedral aggregates (Fig. 4.2.4D). Furthermore, sulphides were identified as < 0.1 mm inclusions within pyroxene (Fig. 4.2.4E).

Accessory minerals identified include chlorite, biotite, hornblende and quartz. Biotite, which is the most abundant mineral of the above mentioned, occurs as subhedral 0.2 mm grains and is found in close proximity to oxides and sulphides (Fig. 4.2.4C).

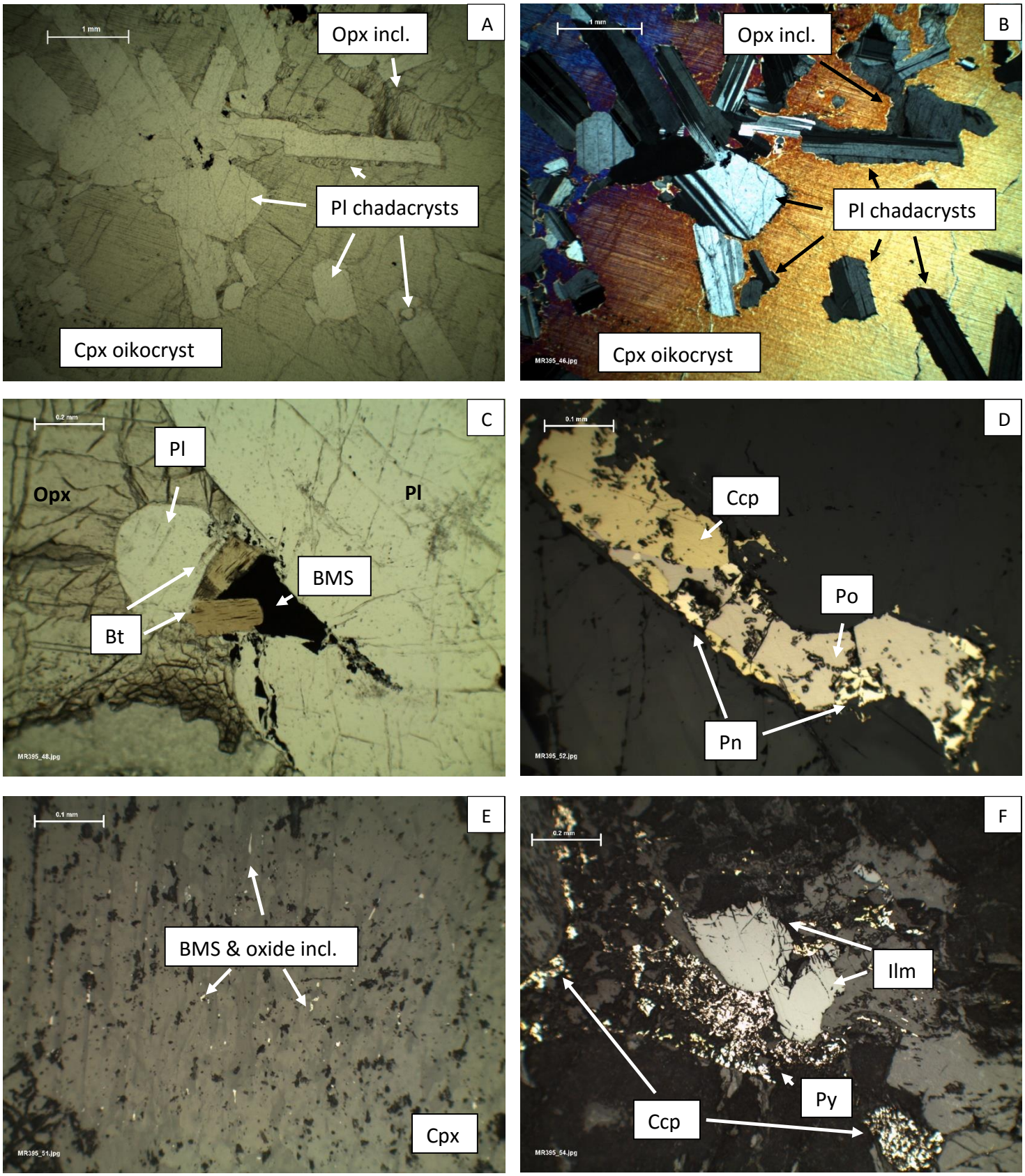

Figure 4.2.4. Photomicrographs taken from the MR HW norite. **A)** & **B)** PPL and XPL photomicrographs (respectively) showing a Cpx oikocryst with subhedral plagioclase chadacrysts and anhedral Opx inclusions. **C)** PPL image showing BMS and biotite association. **D)** RL photomicrograph showing a BMS aggregate comprising pyrrhotite, pentlandite and chalcopyrite. **E)** RL image showing abundant (< 0.1 mm) BMS and oxide inclusions within Cpx. **F)** RL image showing ilmenite and adjacent chalcopyrite and pyrite.

4.2.4. Merensky Reef Anorthosite

This unit (sample MR-09) occurs within the reef and is separated by overlying and underlying pyroxenite. The modal composition for this unit is recorded in figure 4.2.1. Plagioclase occurs as 0.3 to 7.0 mm, anhedral cumulus grains. Like the previous units, plagioclase is often sericitized and shows minor zoning and triple point junctions (Fig. 4.2.5B). Furthermore, plagioclase shows undulose extinction and grains exhibit evidence of deformation (Fig. 4.2.5A).

Orthopyroxene is mostly absent in this unit but, where present, occurs as intercumulus, 0.5 – 0.7 mm anhedral grains. Clinopyroxene generally occurs as intercumulus, 0.2 – 0.4 mm subhedral grains. Larger (> 3 mm) oikocrysts containing subhedral 0.1 – 1 mm plagioclase inclusions were also identified.

Oxides, comprising ilmenite, rutile and chromite, are present as 0.1 – 0.2 mm anhedral to subhedral aggregates (Fig. 4.2.5C). These oxides are also found as inclusions within plagioclase and pyroxenes.

BMS, comprising pyrite, chalcopyrite, pentlandite, pyrrhotite and sphalerite, occur as 0.05 mm inclusions within plagioclase and pyroxene, as well as separate 1.0 – 1.2 mm aggregates. Sphalerite was identified adjacent to chalcopyrite and as inclusions within chalcopyrite (Fig. 4.2.5D).

Biotite is relatively abundant in this unit (Fig. 4.2.1) and occurs as 0.3 – 0.4 mm anhedral grains, as well as larger (± 2.5 mm) subhedral to euhedral grains (Fig. 4.2.5E), which are associated with BMS. Furthermore, biotite is often replaced by chlorite (Fig. 4.2.5F).

Other accessory minerals identified in this unit included minor hornblende.

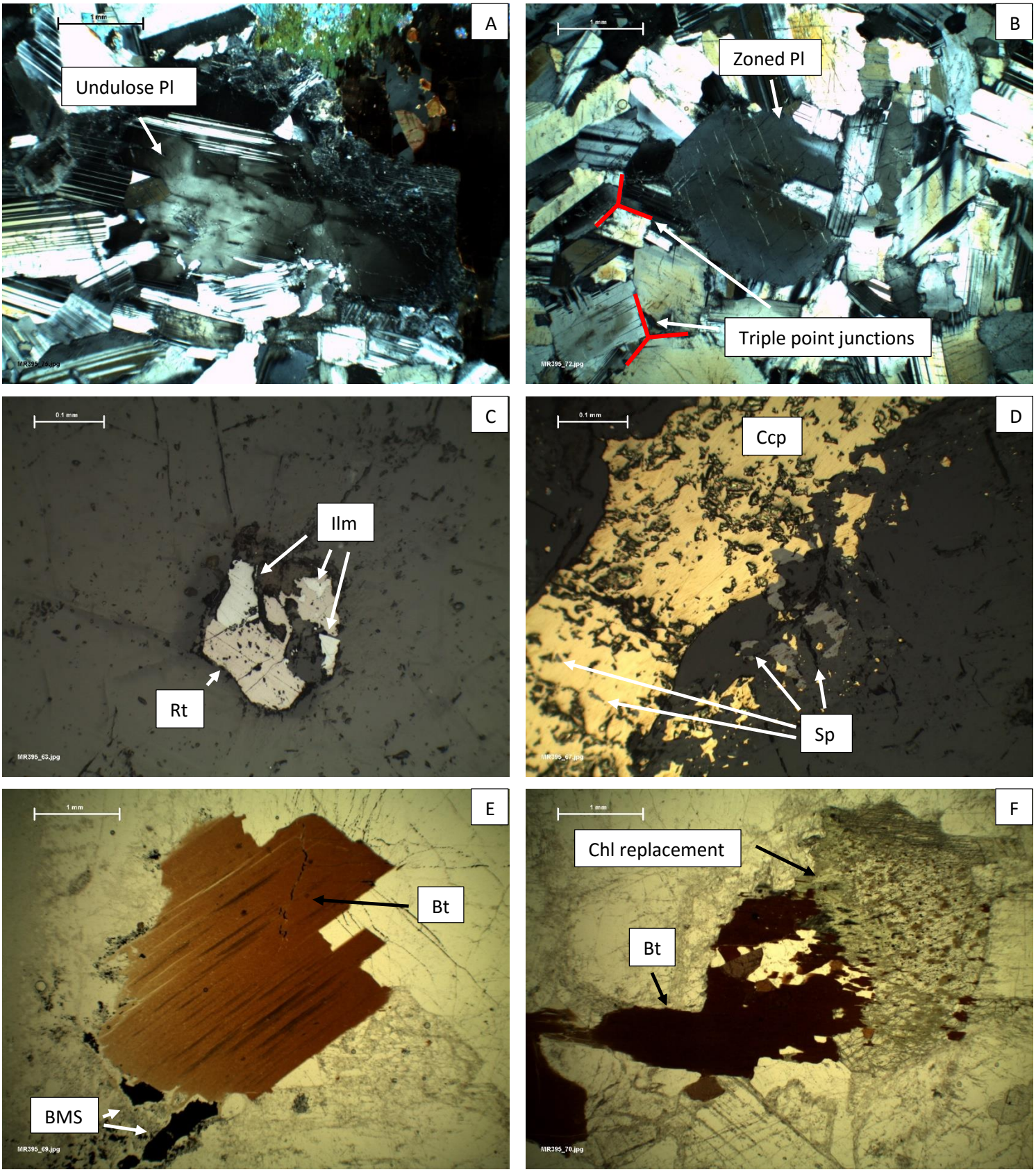

Figure 4.2.5. Photomicrographs taken from the MR anorthosite. **A)** XPL image of Pl showing undulose extinction and deformation. **B)** XPL photomicrograph showing triple point junctions at grain boundaries and zoned Pl. **C)** RL image showing an oxide aggregate comprising Rt and Ilm. **D)** RL photomicrograph showing sphalerite occurring adjacent to Ccp and as inclusions within the sulphide. **E)** PPL image showing large (> 3.0 mm) Bt and adjacent BMS. **F)** PPL image showing chlorite replacing Bt.

4.2.5. Merensky Reef Pyroxenite

The modal abundances for this unit are recorded in samples MR-08 and MR-10 to MR-22 (Fig. 4.2.1). Plagioclase, which occurs as an interstitial phase and is anhedral to subhedral in shape, shows a variable grain size throughout this unit (between 0.5 to 8.0 mm). Generally, plagioclase is inclusion-free (although inclusions of BMS and oxides were recorded) and typically shows deformation features in the form of undulose extinction, deformation twins and pinched and bent twin lamellae. Furthermore, in contrast to the HW units, no significant zoning as well as sericitization was observed in this unit.

Orthopyroxene is the most abundant mineral within this unit. Generally, orthopyroxene occurs as cumulus, subhedral to euhedral, 1.5 to 8.0 mm wide grains (Fig. 4.2.6C) which show a progressive grain size increase with stratigraphic depth. Orthopyroxene often shows deformation features within the pyroxenitic reef, including kink bands (Fig. 4.2.6F) and indented contacts at grain boundaries. Inclusions of anhedral to subhedral, 0.2 to 0.4 mm exsolved clinopyroxene, resorbed plagioclase, biotite, oxides and sulphides are common (Fig. 4.2.6G). Clinopyroxene occurs as cumulus, subhedral 0.5 to 2.0 mm grains which contain inclusions of sulphides, oxides, plagioclase and biotite. Larger, 7.0 mm to 15.0 mm clinopyroxene oikocrysts also occur within the unit and, in addition to the inclusions mentioned above, also contains inclusions of resorbed, rounded orthopyroxene (Fig. 4.2.6E & I). Furthermore, clinopyroxene may be found on the rims of orthopyroxene grains.

Oxides identified in this unit comprise ilmenite, rutile and chromite. Typically, these minerals occur as anhedral to subhedral aggregates which range in size from 0.1 to 3.5 mm and show a spatial association with biotite (Fig. 4.2.6J). Furthermore, oxides also occur as inclusions in both pyroxene types, as well as plagioclase (as mentioned above). Ilmenite often shows exsolution lamellae of rutile.

Base metal sulphides comprise chalcopyrite, pyrrhotite, pyrite and pentlandite (in order of decreasing abundance) which occur as anhedral to subhedral 0.2 to 5.0 mm aggregates (Fig. 4.2.6H). Typically, these BMS occur on silicate grain margins and show a strong spatial association with biotite (Fig. 4.2.6B).

Accessory minerals in this unit comprise biotite, chlorite, olivine, serpentine, hornblende, muscovite (Fig. 4.2.6D), sphalerite and quartz. Biotite, which is more abundant in this unit compared to the overlying HW units, is present as anhedral to subhedral 0.5 to 4.0 mm grains. Chlorite, which often replaces biotite (Fig. 4.2.6A), occurs as subhedral 1.0 to 3.5 mm grains. Serpentine, a hydrous alteration product of olivine, occurs as veinlets which traverse across the rock.

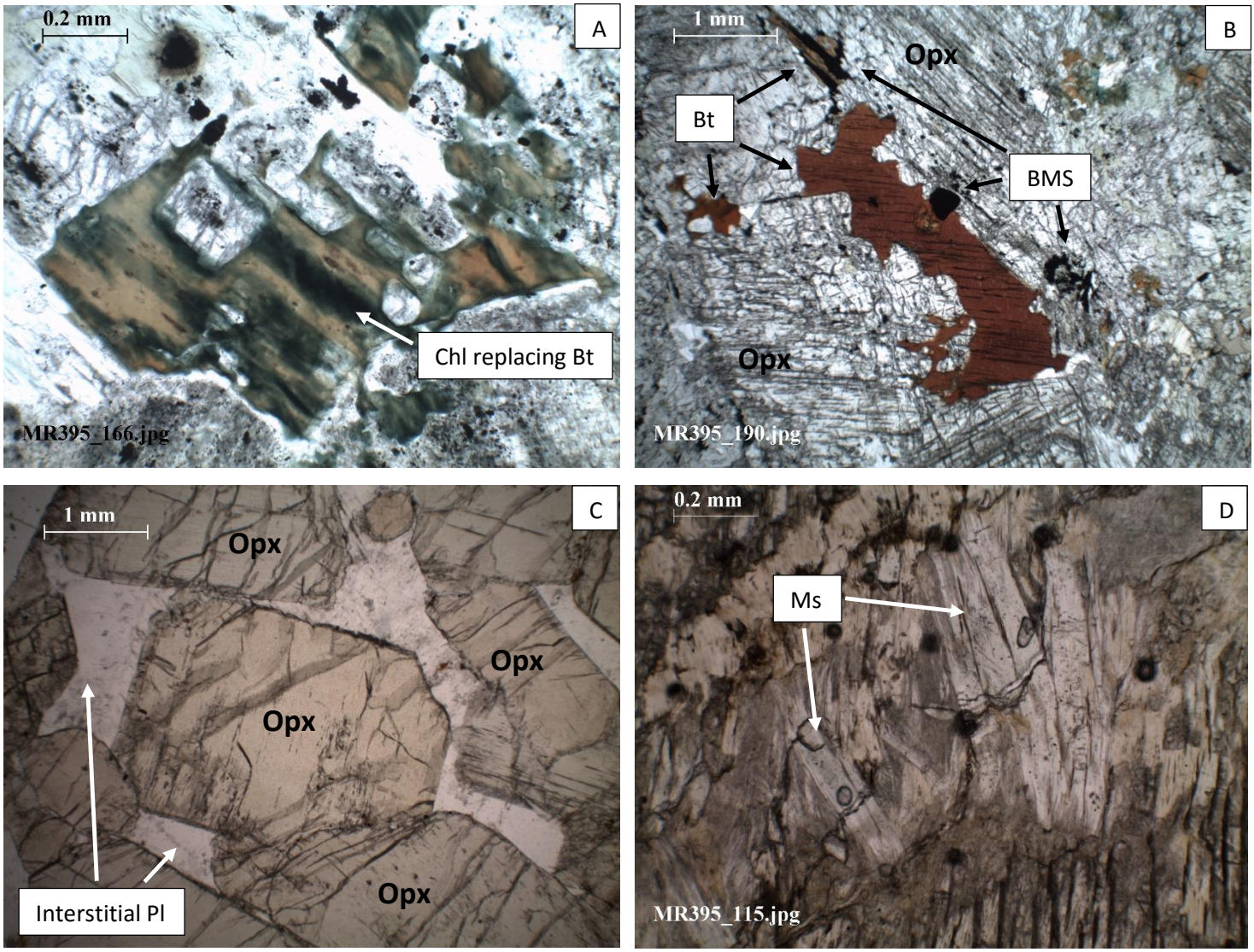

Figure 4.2.6. Photomicrographs taken from the MR pyroxenite. **A)** PPL image of chlorite replacing biotite. **B)** PPL photomicrograph showing large (1 – 3 mm) biotite and adjacent BMS. **C)** PPL image of subhedral to euhedral Opx and interstitial plagioclase. **D)** PPL photomicrograph of lath-shaped muscovite.

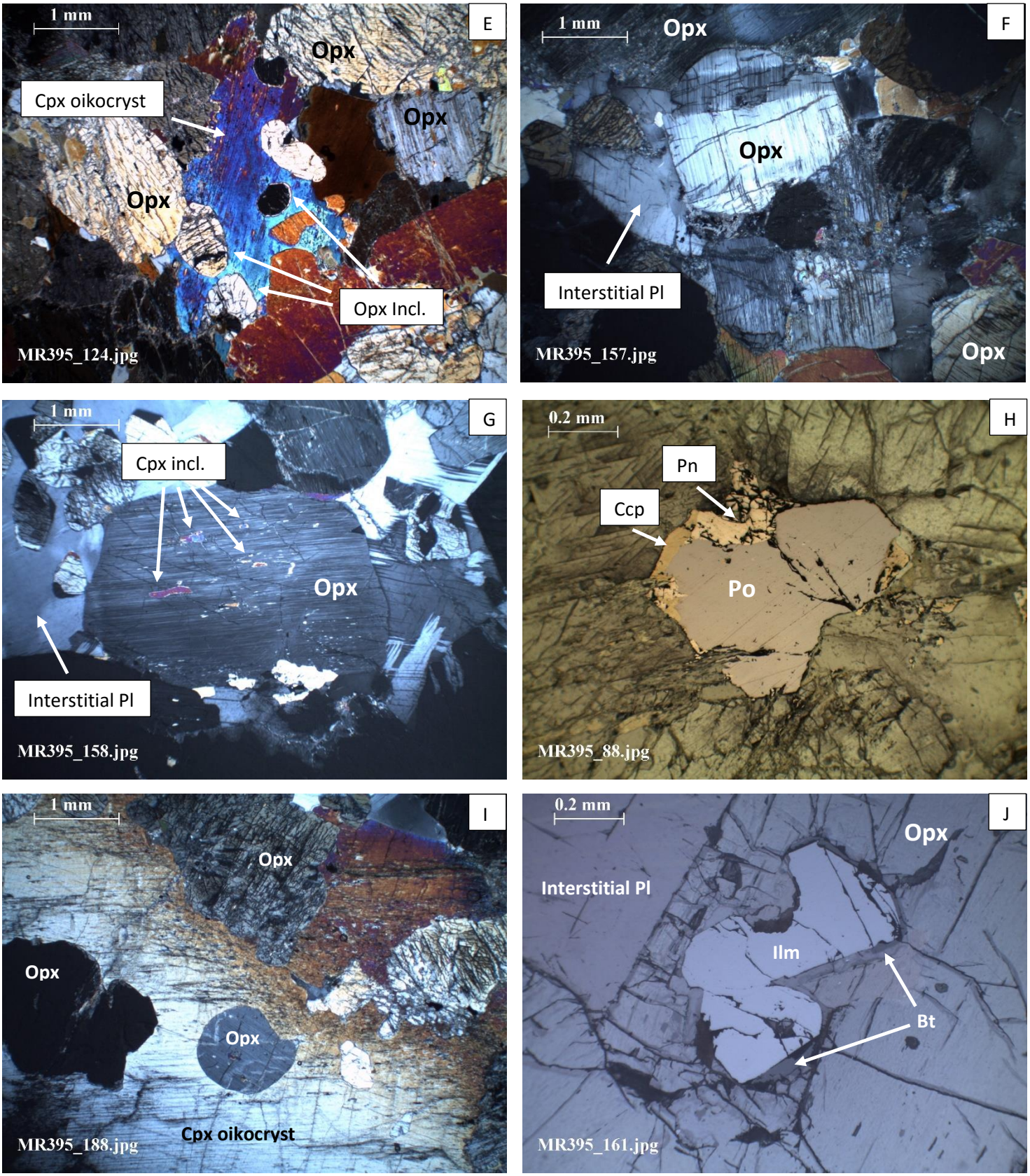

Figure .6. (*cont.*) Photomicrographs taken from the MR pyroxenite. **E)** XPL image of a Cpx oikocrysts containing inclusions of Opx. **F)** XPL photomicrograph of Opx showing deformation, i.e., kink band (a common feature in the MR pyroxenite). **G)** XPL image of Opx showing exsolution lamellae and Cpx inclusions. **H)** RL image of a BMS aggregate comprising pyrrhotite, pentlandite and chalcopyrite. **I)** XPL image of a Cpx oikocryst with resorbed Opx chadacrysts. **J)** RL photomicrograph showing oxide (i.e., ilmenite) and biotite spatial association.

4.2.6. Merensky Reef Chromitite

Note that sample MR-23, which comprises the chromitite stringer to the MR, also contains overlying pyroxenite and underlying anorthosite units. Thus, the modal abundance for sample MR-23 (Fig. 4.2.1) is not strictly limited to just the chromitite stringer. However, the petrographic analysis that follows is an investigation of the chromitite stringer exclusively.

Plagioclase occurs as large intercumulus oikocrysts which range in size between 2.5 and 6.0 mm. Plagioclase is subhedral to euhedral in shape and commonly show undulose extinction and pericline twinning (as well as pinched twins). Minor sericitization of plagioclase is observed within the seam.

Orthopyroxene is present as intercumulus, subhedral 2.0 to 8.0 mm oikocrysts (Fig. 4.2.7B) which comprise 0.1 to 0.4 mm inclusions of subhedral clinopyroxene and plagioclase. Furthermore, orthopyroxene shows evidence of deformation i.e., kink bands (Fig. 4.2.7C). Clinopyroxene occurs as intercumulus, subhedral 0.8 to 2.0 mm grains (Fig. 4.2.7B). Both pyroxene groups combined make up approximately 35 % of the modal abundance in the chromitite stringer.

Oxides present in this unit comprise chromite, ilmenite and rutile. Chromite ranges from 0.5 to 2.5 mm in size and grains are cubic to amoeboidal in shape (Fig. 4.2.7A). The chromite grains occur as a ~ 3 mm stringer which defines the layering in the rock. These chromite grains contain inclusions of orthopyroxene and plagioclase (Fig. 4.2.7A) which are subhedral in shape and range between 0.2 and 0.4 mm in size. Typically, chromite shows evidence of annealing in which smaller individual grains join to become larger (Fig. 4.2.7F) as well as apparent reaction rims with surrounding orthopyroxene (typically grains which are inclusion-free) (Fig. 4.2.7D).

BMS comprise chalcopyrite, pyrite, pyrrhotite and pentlandite which are present in small abundances (< 1 %) and occur as interstitial, 0.1 to 0.3 mm anhedral aggregates. Other accessory minerals identified include biotite, serpentine and olivine. Biotite is present as anhedral 0.2 to 0.6 mm grains. Serpentine is present as veinlets which traverse through the unit (Fig. 4.2.7E).

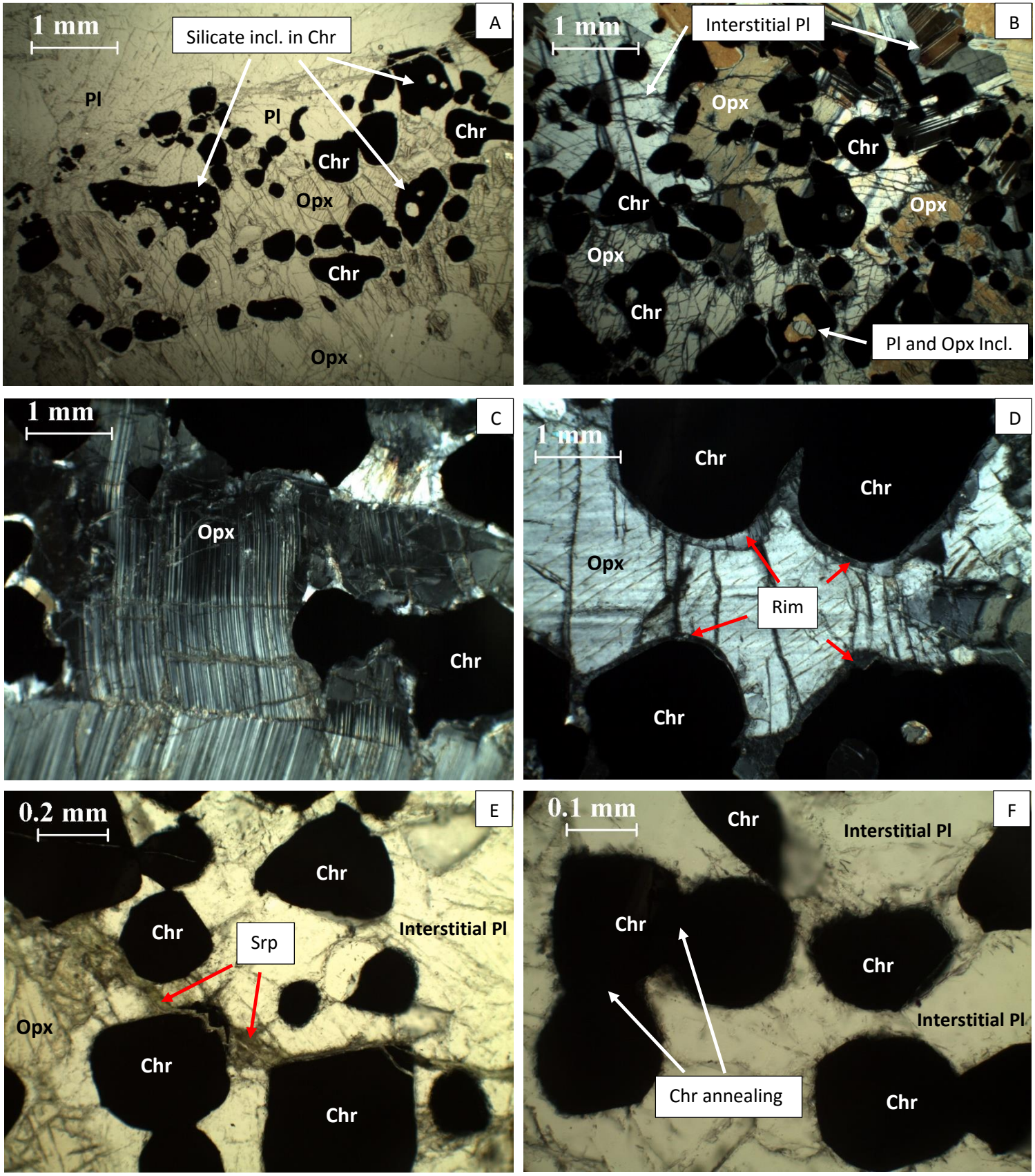

Figure 4.2.7. Photomicrographs taken from the MR chromitite. **A)** PPL image of Pl and Opx inclusions within Chr and typical amoeboidal shapes. **B)** XPL photomicrograph showing cumulus Chr and intercumulus Pl and Opx. **C)** XPL image showing deformation in Opx. **D)** XPL photomicrograph showing apparent reactions rims between Chr and Opx. **E)** PPL image showing serpentine veins cutting through chromites and silicates. **F)** PPL image showing annealing between chromite grains.

4.2.7. Merensky Reef Footwall Anorthosite

The modal proportions of this rock are recorded in figure 4.2.1 (from samples MR-24 to MR-28). Plagioclase, which is the most abundant mineral in this rock, occurs as cumulus, 0.5 to 6.0 mm wide grains. The grains are subhedral to euhedral in shape. Sericitic alteration of plagioclase is a common feature of this rock and shows a strong spatial association to BMS and oxides. Plagioclase shows both undulose extinction as well as albite and polysynthetic twins. Generally, plagioclase is free of inclusions, however, inclusions of orthopyroxene were observed in larger plagioclase grains (Fig. 4.2.8C). Furthermore, minor zoning in plagioclase is common and triple point junctions (Fig. 4.2.8C) are discernible at plagioclase grain boundaries.

Orthopyroxene occurs as intercumulus, anhedral to subhedral 0.2 to 1.5 mm grains. Inclusions of 0.2 to 0.3 mm subhedral plagioclase are common (Fig. 4.2.8D). Clinopyroxene is present as 0.1 to 2.0 mm anhedral to subhedral grains which, like orthopyroxene, are intercumulus (Fig. 4.2.8E). Inclusions of subhedral ± 0.2 mm plagioclase grains within clinopyroxene were observed.

Oxides identified in this unit comprise ilmenite, rutile and chromite. The oxides typically occur as aggregates which are subhedral in shape and range between 0.2 and 0.4 mm in size. Commonly, ilmenite hosts exsolution lamellae of rutile (Fig. 4.2.8A).

Base metal sulphides, which comprise pentlandite, pyrrhotite, pyrite and chalcopyrite, occur as anhedral to subhedral 0.1 to 0.3 mm aggregates (Fig. 4.2.8B).

Other minerals identified in this unit include minor biotite, chlorite and K-feldspar. Biotite is present as 0.1 - 0.2 mm subhedral grains which are found in close proximity to BMS (Fig. 4.2.8F).

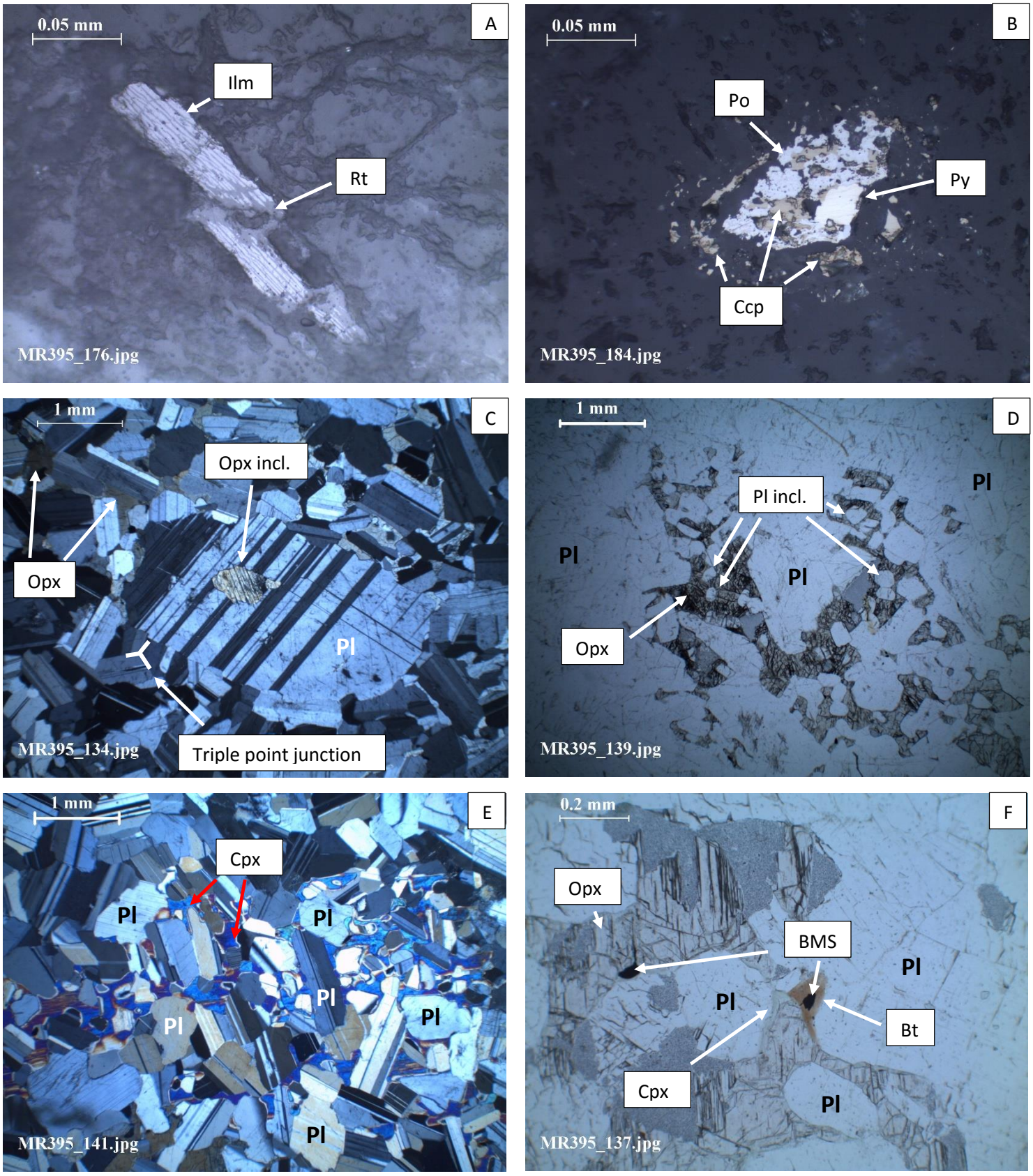

Figure 4.2.8. Photomicrographs taken from the MR FW anorthosite. **A)** RL image of Rt exsolution lamellae in Ilm. **B)** RL photomicrograph showing a BMS aggregate comprising pyrrhotite, pyrite and chalcopyrite. **C)** XPL image of an Opx inclusion within cumulus Pl. Also note the presence of triple point junctions and intercumulus Opx. **D)** PPL image showing Pl inclusions within intercumulus Opx. **E)** XPL photomicrograph showing cumulus Pl and intercumulus Cpx. **F)** PPL image showing the distinctive spatial association of BMS and Bt.

4.2.8. Comparisons between boreholes ELF-395 and -393

Some notable similarities between boreholes ELF-395 and -393 were identified during the petrographic investigation. Despite differences in lithology between the two cores, modal abundances for equivalent units were well correlated. In addition to this, significant increases in cumulus mineral grain sizes, towards the reef (from the HW and FW rocks), were recorded in both boreholes. In both ELF-393 and -395, plagioclase occurred as a cumulus phase within the HW and FW units and as an interstitial phase within the reef units. Furthermore, the presence of zoning, triple point junctions and sericitization of plagioclase which were identified in the plagioclase-rich lithologies of this study, were also identified in borehole ELF-393.

In both ELF-393 and -395, ortho- and clinopyroxene occur as intercumulus minerals within the HW and FW units and as cumulus phases within the reef units. Ophitic textures of orthopyroxene oikocrysts and plagioclase chadacrysts were observed in both ELF-393 and -395, as well as inclusions of exsolved clinopyroxene, biotite, BMS and oxides. Large (up to 15.0 mm) clinopyroxene oikocrysts containing inclusions of rounded orthopyroxene and plagioclase chadacrysts were also identified in both boreholes ELF-393 and -395. Furthermore, in both drillcores (particularly within the pyroxenitic reef) orthopyroxene showed exsolution lamellae of clinopyroxene, and clinopyroxene was often found on the rims of orthopyroxene. Additionally, evidence of deformation in orthopyroxene was recorded within the reef units of both ELF-393 and -395.

The presence and abundance of oxides were fairly similar in both boreholes (with the exception of the chromitite stringer in ELF-395). Furthermore, in both boreholes, oxides typically occurred as anhedral to subhedral aggregates which ranged in size between 0.1 and 3.5 mm and comprised predominantly chromite, ilmenite and rutile. Typically, ilmenite showed rutile exsolution lamellae (i.e., Ti-exsolution). Furthermore, oxides showed a strong spatial association to surrounding biotite and sericite. In borehole ELF-395, chromite comprised inclusions of silicates, however, chromite in ELF-393 was largely inclusion free. Moreover, chromite showed evidence of annealing in ELF-395 and not in ELF-393.

Base metal sulphides showed significant similarities in boreholes ELF-393 and -395. Typically, BMS comprised disseminated chalcopyrite, pyrrhotite, pentlandite and pyrite (in order of decreasing abundance) which occurred as anhedral irregular blebs/aggregates on silicate grain boundaries and as inclusions within orthopyroxene, clinopyroxene and plagioclase. Generally the BMS ranged between 1 and 5 % in modal abundance and showed an enrichment in the reef (i.e., pyroxenite unit) relative to the hangingwall and footwall rocks. Furthermore, in both boreholes, BMS commonly showed a strong spatial association to surrounding biotite, sericite, chlorite and serpentine.

In both boreholes ELF-393 and -395 pervasive hydrous alteration and the presence of hydrous minerals were identified. Alteration features included the sericitization of plagioclase and serpentinization of olivine, while hydrous minerals identified comprised biotite, chlorite, muscovite and hornblende. Typically these minerals occur in low abundances but appear to control the spatial distribution of BMS and oxides as mentioned above. Other accessory minerals identified in both cores included minor olivine, K-feldspar and quartz.

4.3. Mineral Chemistry

Electron probe micro-analysis (EPMA) was conducted at Rhodes University using a Jeol JXA 8230. The analytical conditions for the mineral analysis are explained in Chapter 3.2.2. Quantitative point analyses were determined for plagioclases, pyroxenes (both groups), oxides, base metal sulphides, biotites and platinum-group minerals. Back-scattered electron images were produced to highlight characteristic mineral assemblages. Furthermore, elemental maps were created to show mineral associations, particularly for sulphides and oxides.

4.3.1. Plagioclase

Table 4.3.1 lists representative plagioclase compositions from all lithological units of the MR in borehole ELF-395 (refer to Appendix 1 for the complete compositional plagioclase datasheet). Plagioclase compositions (both cores and inclusions) for all major lithological units of borehole ELF-395 are shown in figure 4.3.1. Within the hangingwall units (comprising anorthosite, leuconorite and norite) plagioclase is present as a cumulus phase. This is also true for the anorthositic reef unit and anorthositic footwall. Interstitial plagioclase was observed in the pyroxenite and chromitite reef units.

Minor variation in An content, CaO, K_2O and Na_2O was recorded in plagioclase cores and inclusions for the anorthositic HW (from a total of 26 analyses). Specifically, cores (15 analyses) ranged from An_{72} to An_{77}, 14.2 to 15.2 wt. %, 0.12 to 0.25 wt. % and 2.34 to 2.91 wt. %, respectively. Inclusions (13 analyses) showed similar compositions to cores which ranged from An_{75} to An_{77}, 14.7 to 15.8 wt. %, 0.15 to 0.22 wt. % and 2.44 to 2.65 wt. %, respectively. As seen in figure 4.3.1, plagioclase cores and inclusions for the anorthositic HW both plot within the bytownite field (i.e., between 70 and 90 % An).

The leuconoritic HW (from a total of 19 analyses) showed less compositional variation (with regards to An content, CaO, K_2O and Na_2O in plagioclase) compared with the overlying anorthositic HW. Cores (6 analyses) ranged from An_{75} to An_{77}, 14.8 to 15.3 wt. %, 0.17 to 0.21 wt. % and 2.45 to 2.60 wt. %, respectively. Inclusions (13 analyses) showed similar compositions to cores and ranged from An_{75} to An_{77}, 14.7 to 15.8 wt. %, 0.15 to 0.22 wt. % and 2.44 to 2.65 wt. %, respectively.

Table 4.3.1. Representative plagioclase compositions from various units of borehole ELF-395. Data are presented in wt. % and plagioclases were normalised to 8 oxygens.

Sample Name	MR02_fsp_5	MR06_fsp_incl15	MR07_fsp24	MR09_fsp_incl52	MR16_fsp98	MR21_fsp128	MR23_fsp158	MR24_fsp180
Unit	Anorthosite HW	Leuconorite HW	Norite HW	Anorthosite Reef	Pyroxenite Reef	Pyroxenite Reef	Chromitite Reef	Anorthosite FW
SiO_2 (wt. %)	51.30	50.72	50.73	51.51	53.38	55.45	50.69	51.79
TiO_2 (wt. %)	0.14	0.00	0.00	0.09	0.23	0.12	0.00	0.02
Al_2O_3 (wt. %)	30.25	30.89	30.36	30.49	29.18	27.81	30.98	30.25
FeO (wt. %)	0.32	0.32	0.28	0.35	0.06	0.15	0.56	0.22
MnO (wt. %)	0.07	0.00	0.00	0.00	0.00	0.00	0.08	0.01
MgO (wt. %)	0.02	0.01	0.02	0.04	0.02	0.01	0.01	0.03
CaO (wt. %)	14.58	15.23	14.85	14.70	13.31	11.51	15.28	14.62
Na_2O (wt. %)	2.91	2.48	2.70	2.79	3.60	4.72	2.56	2.89
K_2O (wt. %)	0.21	0.17	0.21	0.21	0.28	0.30	0.16	0.21
BaO (wt. %)	0.00	0.18	0.01	0.01	0.00	0.06	0.00	0.04
SrO (wt. %)	0.00	0.00	0.00	0.00	0.00	0.00	0.00	0.00
Total (wt. %)	**99.80**	**99.99**	**99.17**	**100.18**	**100.06**	**100.13**	**100.32**	**100.06**
Si	2.34	2.32	2.33	2.34	2.42	2.50	2.31	2.36
Al	1.63	1.66	1.64	1.63	1.56	1.48	1.66	1.62
Ti	0.00	0.00	0.00	0.00	0.01	0.00	0.00	0.00
Fe	0.01	0.01	0.01	0.01	0.00	0.01	0.02	0.01
Mn	0.00	0.00	0.00	0.00	0.00	0.00	0.00	0.00
Mg	0.00	0.00	0.00	0.00	0.00	0.00	0.00	0.00
Zn	0.00	0.00	0.00	0.00	0.00	0.00	0.00	0.00
Ca	0.71	0.75	0.73	0.72	0.65	0.56	0.75	0.71
Na	0.26	0.22	0.24	0.25	0.32	0.41	0.23	0.25
K	0.01	0.01	0.01	0.01	0.02	0.02	0.01	0.01
Ba	0.00	0.00	0.00	0.00	0.00	0.00	0.00	0.00
Total Cations	**4.97**	**4.97**	**4.97**	**4.97**	**4.96**	**4.97**	**4.98**	**4.97**
An Content	72.56	76.47	74.30	73.48	66.03	56.40	75.99	72.78
Ab Content	26.20	22.49	24.43	25.25	32.33	41.82	23.05	25.98
Or Content	1.24	1.04	1.27	1.27	1.64	1.77	0.96	1.24

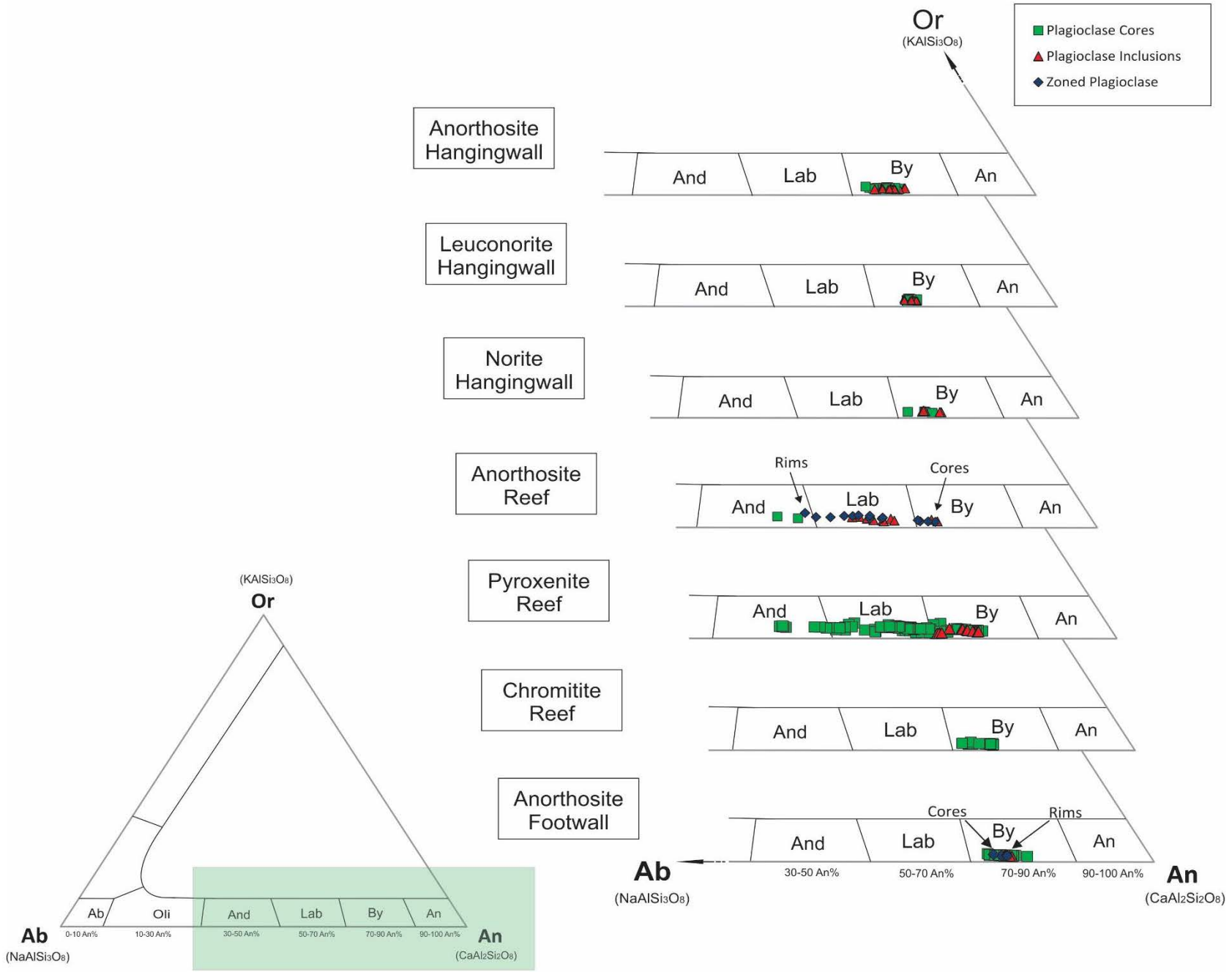

Figure 4.3.1. Plagioclase ternary plot for all units of the Merensky Reef. Both plagioclase cores and inclusions are included (as well as zoned grains which exhibit both normal and reverse zoning). Plagioclase showed varied compositions and ranged from andesine (30 to 50 % An) to anorthite (90 to 100 % An).

Like the anorthositic HW, plagioclase cores and inclusions within the leuconorite HW unit plot within the bytownite field (Fig. 4.3.1).

The norite HW unit (from a total of 19 analyses) exhibited similar An content, CaO, K_2O and Na_2O to the overlying units previously mentioned. However, small variations were recorded between plagioclase cores and inclusions. Cores (4 analyses) ranged from An_{72} to An_{76}, 14.2 to 15.0 wt. %, 0.18 to 0.24 wt. % and 2.42 to 2.73 wt. %, respectively. Inclusions showed marginally higher An content, CaO and Na_2O, while K_2O was slightly lower, compared to plagioclase cores, ranging from $An_{74.0}$ to $An_{77.1}$, 14.7 to 15.5 wt. %, 2.55 to 2.99 wt. % and 0.16 to 0.21 wt. %, respectively. Plagioclase cores and inclusions for this unit, like the overlying anorthosite and leuconorite units, plot within the bytownite field (Fig. 4.3.1).

The anorthositic reef unit (from a total of 26 analyses) showed a high degree of variability in An content, CaO, K_2O and Na_2O compared to the hangingwall units. Plagioclase cores (16 analyses) ranged from An_{47} to An_{73}, 9.59 to 14.6 wt. %, 0.20 to 0.52 wt. % and 2.82 to 5.72 wt. %, respectively, while inclusions (10 analyses) ranged from An_{60} to An_{74}, 11.8 to 14.7 wt. %, 0.21 to 0.38 wt. % and 2.79 to 4.27 wt. %, respectively. Unlike the hangingwall units, plagioclase cores and inclusions in the anorthositic reef plot not only in the bytownite field, but also extend into the labradorite and andesine fields (Fig. 4.3.1). Furthermore, variation between plagioclase cores and rims identified higher An content and CaO values, and lower Na_2O values in cores (e.g., $An_{70\text{-}73}$ versus $An_{62\text{-}64}$, 14.0 – 14.6 wt. % versus 12.5 – 13.0 wt. % and 2.82 – 3.12 wt. % versus 3.80 – 4.00 wt. %, respectively). These observations are consistent with normal zoning (Fig. 4.3.6A).

The underlying pyroxenite reef (from a total of 114 analyses), like the anorthositic reef unit, shows high variability in An content, CaO, K_2O and Na_2O. Cores (98 analyses) ranged from $An_{45\text{-}78}$, 9.12 to 15.5 wt. %, 0.06 to 0.44 wt. % and 2.31 to 6.13 wt. %, respectively, while inclusions (16 analyses) ranged from $An_{71\text{-}78}$, 14.1 to 15.3 wt. %, 0.06 to 0.23 wt. % and 2.38 to 3.19 wt. %, respectively. Plagioclase cores plot within the andesine, labradorite and bytownite fields while inclusions plot only within the bytownite field (Fig. 4.3.1). A BSE image of euhedral plagioclase from this unit is shown in figure 4.3.6E.

The chromitite unit showed only slight variability in An content, CaO, K_2O and Na_2O. Only plagioclase cores (17 analyses) were analysed in this unit and ranged from An_{71-77}, 14.5 to 15.6 wt. %, 0.14 to 0.24 wt. % and 2.49 to 3.08 wt. %, respectively. Like the hangingwall units, plagioclase from the chromitite unit plots within the bytownite field (Fig. 4.3.1).

The anorthositic footwall unit (from a total of 32 analyses) showed similar An content, CaO, K_2O and Na_2O values to the anorthositic HW (although the An content is marginally higher). Cores (31 analyses) ranged from An_{72} to An_{79}, 14.6 to 15.7 wt. %, 0.14 to 0.24 wt. % and 2.19 to 2.94 wt. %, respectively, while inclusions (2 analyses) ranged from An_{76} to An_{77}, 15.1 to 15.4 wt. %, 0.14 to 0.16 wt. % and 2.49 to 2.50 wt. %, respectively. Plagioclase cores and inclusions in the anorthositic footwall plot within the bytownite field and showed, although only marginally, the highest An content in the MR (Fig. 4.3.1). Furthermore, variation between plagioclase cores and rims identified lower An content and CaO values, and higher Na_2O values (e.g., An_{74-75} versus An_{75-76}, 14.7 – 15.1 wt. % versus 15.0 – 15.2 wt. % and 2.69 – 2.79 wt. % versus 2.51 – 2.63 wt. %, respectively). These observations are consistent with reverse zoning.

4.3.2. Pyroxenes

Table 4.3.2 lists representative pyroxene compositions from all lithological units of the MR in borehole ELF-395 (refer to Appendix 2 for the complete compositional clinopyroxene datasheet and Appendix 3 for the complete compositional orthopyroxene datasheet). Orthopyroxene and clinopyroxene compositions (for cores, rims and inclusions) from all major lithological units of borehole ELF-395 are shown in figure 4.3.2. Within the hangingwall units both pyroxene groups are present as intercumulus phases. This is also true for the anorthositic reef unit and anorthositic footwall. Cumulus pyroxene was recorded in the pyroxenite and chromitite reef units.

Analysis of both orthopyroxene and clinopyroxene from the anorthositic hangingwall (from a total of 21 analyses) was conducted on cores and inclusions. Minor variation in CaO, MgO, FeO and Mg # (Mg# = molar Mg / molar ($Mg+Fe^{2+}$)) was recorded in orthopyroxene cores (2 analyses) which ranged from 1.12 to 2.24 wt. %, 24.5 to 25.0 wt. %, 16.3 to 17.0 wt. % and 72 to 73, respectively. Clinopyroxene cores (17 analyses) showed significantly more variation and

ranged from 19.4 to 23.2 wt. %, 11.2 to 16.0 wt. %, 5.64 to 13.35 wt. % and 76 to 82, respectively, while clinopyroxene inclusions (2 analyses) ranged from 22.71 to 22.73 wt. %, 14.95 to 15.05 wt. %, 5.54 to 5.98 wt. % and 81 to 82, respectively. As seen in figure 4.3.2, orthopyroxene cores plot within the enstatite field while clinopyroxene cores and inclusions plot mostly within the diopside field but also extend into the augite field.

Analysis of pyroxene from the leuconorite hangingwall unit (from a total of 13 analyses) was conducted on clinopyroxene cores only. Clinopyroxene cores ranged in CaO, MgO, FeO and Mg # between 21.8 to 23.2 wt. %, 14.3 to 14.7 wt. %, 6.31 to 7.39 wt. % and 77 to 81, respectively. Compositions plot within the diopside field (Fig. 4.3.2).

Orthopyroxene cores and inclusions and clinopyroxene cores, inclusions and rims were analysed in the norite hangingwall unit (from a total of 20 analyses). With regard to CaO, MgO, FeO and Mg #, orthopyroxene cores ranged from 1.00 to 1.51 wt. %, 24.2 to 25.0 wt. %, 17.3 to 18.1 wt. % and 71 to 72, respectively, while inclusions showed slightly more variation and ranged from 0.49 to 1.54 wt. %, 24.8 to 26.0 wt. %, 16.1 to 17.7 wt. % and 71 to 74, respectively. Clinopyroxene cores ranged in CaO, MgO, FeO and Mg # between 20.0 to 23.1 wt. %, 11.2 to 16.0 wt. %, 6.17 to 13.35 wt. % and 77 to 81, respectively, while inclusions showed less variation and ranged from 22.5 to 23.0 wt. %, 14.5 to 14.7 wt. %, 6.18 to 6.65 wt. % and 79 to 81, respectively. Furthermore, clinopyroxene rims ranged in CaO, MgO, FeO and Mg # between 22.4 to 23.6 wt. %, 14.9 to 15.0 wt. %, 6.50 to 6.65 wt. % and 80 to 81, respectively. Orthopyroxene cores and inclusions plot well within the enstatite field while clinopyroxene cores, inclusions and rims plot mostly within the diopside field but, like the anorthositic hangingwall, also extend into the augite field (Fig. 4.3.2).

The anorthositic reef unit showed only slight variability in CaO, MgO, FeO and Mg #, in which clinopyroxene cores (7 analyses) ranged from 21.9 to 23.3 wt. %, 15.4 to 15.8 wt. %, 4.21 to 6.20 wt. % and 82 to 85, respectively. Clinopyroxene cores plot within the diopside field as seen in figure 4.3.2.

Analysis of both orthopyroxene and clinopyroxene from the pyroxenite reef unit (from a total of 190 analyses) was conducted on cores, inclusions and rims. With regard to CaO, MgO, FeO and Mg #, orthopyroxene cores (116 analyses) exhibited a high degree of variability and ranged from 0.54 to 8.58 wt. %, 23.1 to 29.3 wt. %, 9.64 to 15.0 wt. % and 76 to 83, respectively. Like orthopyroxene cores, clinopyroxene cores (41 analyses) showed significant variability in CaO, MgO, FeO and Mg # and ranged from 12.5 to 23.5 wt. %, 11.2 to 21.0 wt. %, 4.60 to 13.4 wt. % and 78 to 88, respectively, while inclusions (26 analyses) showed moderate variation and ranged from 20.7 to 24.4 wt. %, 15.1 to 16.7 wt. %, 2.57 to 6.18 wt. % and 82 to 88, respectively. Clinopyroxene rims (7 analyses) showed only slight variation in CaO, MgO, FeO and Mg # and ranged from 21.8 to 23.7 wt. %, 15.9 to 16.6 wt. %, 3.71 to 5.27 wt. % and 84 to 86, respectively. BSE images of clinopyroxene rims are shown in figures 4.3.6C and D. Mostly, orthopyroxene cores plot within the diopside field, but also extend into the pigeonite field, while clinopyroxene cores, inclusions and rims mostly plot within the diopside field (with some scatter into the augite field) (Fig. 4.3.2).

Ortho- and clinopyroxene cores, analysed in the chromitite reef unit (from a total of 14 analyses), showed moderate to high variation in CaO, MgO, FeO and Mg #, respectively. Orthopyroxene cores (6 analyses) ranged from 0.72 to 3.58 wt. %, 26.6 to 28.2 wt. %, 12.1 to 14.2 wt. % and 78 to 80, respectively, while clinopyroxene cores (8 analyses) ranged from 21.0 to 23.6 wt. %, 11.2 to 15.7 wt. %, 5.00 to 13.4 wt. % and 72 to 84, respectively. Orthopyroxene and clinopyroxene cores in the chromitite reef, like the pyroxenite reef, plot within the enstatite (extending into the pigeonite field) and diopside (extending into the augite field) fields (Fig. 4.3.2).

Analysis of pyroxene from the anorthositic footwall unit (from a total of 10 analyses) was conducted on clinopyroxene cores and inclusions only. Clinopyroxene cores ranged in CaO, MgO, FeO and Mg # between 19.7 to 23.4 wt. %, 14.5 to 15.5 wt. %, 6.9 to 10.0 wt. % and 74 to 78, respectively, while inclusions ranged from 22.5 to 22.7 wt. %, 15.1 to 15.6 wt. %, 6.60 to 7.56 wt. % and 77 to 80, respectively. Like the anorthositic HW, clinopyroxene cores and inclusions mostly plot within the diopside field but also extend into the augite field (Fig. 4.3.2).

Table 4.3.2. Representative pyroxene compositions from various units of borehole ELF-395. Data are presented in wt. % and pyroxenes were normalised to 6 oxygens.

Sample Name	MR02_cpx5	MR06_cpx4	MR07_opx12	MR09_cpx53	MR13_cpx_rim	MR16_opx82	MR23_opx141	MR24_cpx_incl65
Unit	Anorthosite HW	Leuconorite HW	Norite HW	Anorthosite Reef	Pyroxenite Reef	Pyroxenite Reef	Chromitite Reef	Anorthosite FW
SiO_2 (wt. %)	52.96	52.72	54.02	53.47	53.72	55.63	55.42	53.52
TiO_2 (wt. %)	0.26	0.44	0.14	0.59	0.29	0.13	0.18	0.55
Al_2O_3 (wt. %)	1.13	1.65	1.23	1.69	2.05	1.29	1.26	1.31
Cr_2O_3 (wt. %)	0.15	0.45	0.34	0.50	1.01	0.50	0.57	0.00
FeO (wt. %)	7.43	7.39	18.06	5.45	5.27	11.51	13.16	6.78
MnO (wt. %)	0.21	0.13	0.27	0.13	0.21	0.34	0.35	0.38
MgO (wt. %)	14.16	14.67	24.53	15.49	15.99	27.93	27.69	15.15
CaO (wt. %)	23.08	22.34	1.44	22.97	21.99	2.71	1.81	22.67
Na_2O (wt. %)	0.24	0.25	0.03	0.35	0.34	0.05	0.02	0.21
Total (wt. %)	**99.62**	**100.01**	**100.07**	**100.63**	**100.87**	**100.07**	**100.44**	**100.57**
Si	1.97	1.95	1.97	1.96	1.95	1.98	1.97	1.97
Ti	0.01	0.01	0.00	0.02	0.01	0.00	0.00	0.02
Al	0.05	0.07	0.05	0.07	0.09	0.05	0.05	0.06
Cr	0.00	0.01	0.01	0.01	0.03	0.01	0.02	0.00
Fe	0.24	0.23	0.55	0.17	0.16	0.34	0.39	0.21
Mn	0.01	0.00	0.01	0.00	0.01	0.01	0.01	0.01
Mg	0.79	0.81	1.34	0.84	0.87	1.48	1.47	0.83
Ca	0.92	0.89	0.06	0.90	0.86	0.10	0.07	0.89
Na	0.02	0.02	0.00	0.03	0.02	0.00	0.00	0.02
Total Cations	**4.00**	**4.00**	**3.99**	**4.00**	**3.99**	**3.99**	**3.99**	**4.00**
Mineral Type	*Cpx*	*Cpx*	*Opx*	*Cpx*	*Cpx*	*Opx*	*Opx*	*Cpx*
Mg# (Fe_{tot})	76	78	71	84	84	81	79	80
En Content	40.18	41.90	68.41	44.09	45.85	76.46	75.72	42.72
Wo Content	47.09	45.87	2.89	47.00	45.32	5.33	3.55	45.95
Fs Content	12.72	12.24	28.69	8.91	8.83	18.21	20.74	11.33

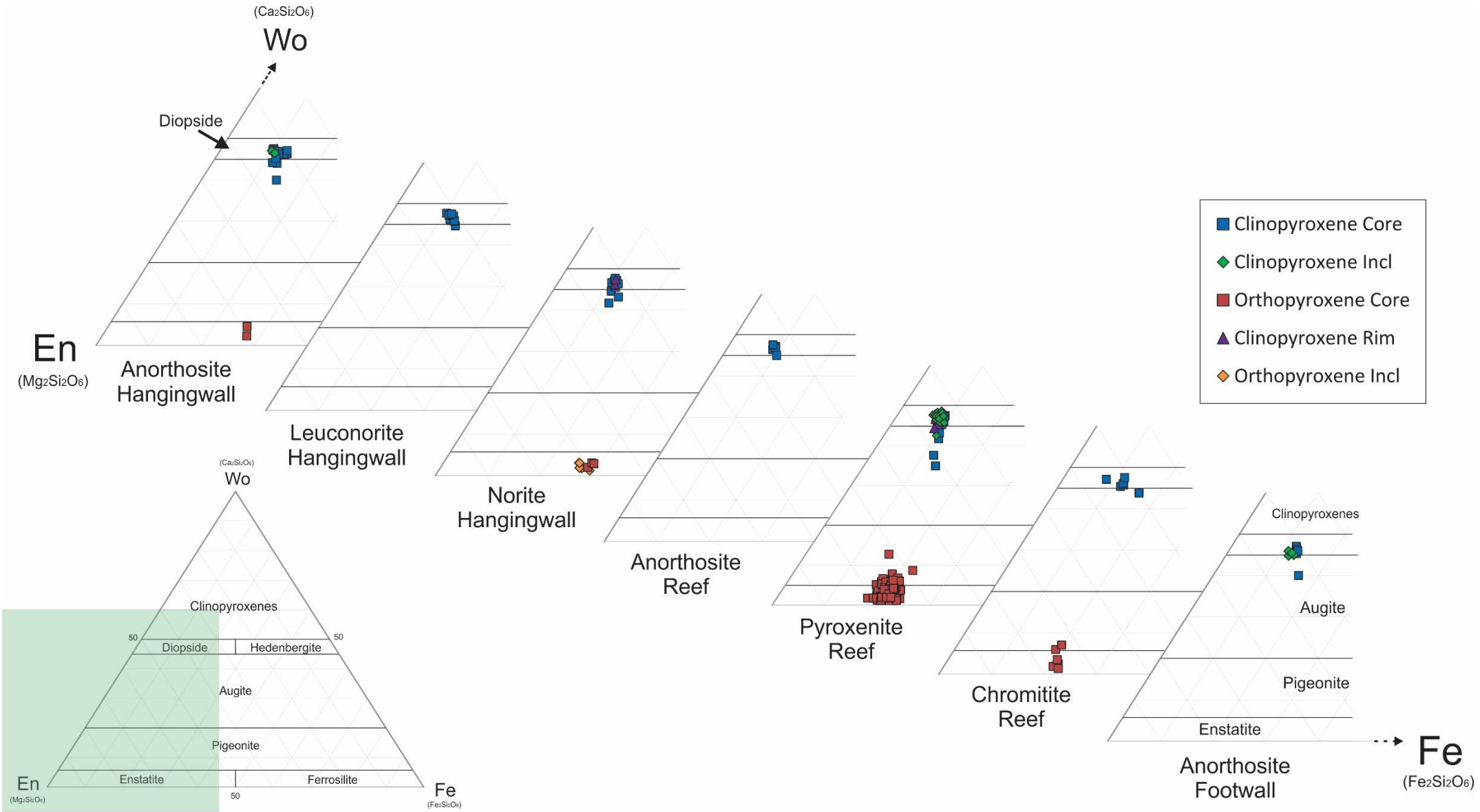

Figure 4.3.2. Pyroxene ternary plot for all units of the Merensky Reef from borehole ELF-395. Both orthopyroxene and clinopyroxene cores, inclusions and rims have been included. Generally points plot within the enstatite and diopside fields for all units.

4.3.3. Base Metal Sulphides

BMS have an average modal abundance of approximately 2 % throughout borehole ELF-395 and, as mentioned in Chapter 4.2, occur as disseminated aggregates of pyrite, chalcopyrite, pyrrhotite and pentlandite which show a strong spatial association with biotite and sericite. Table 4.3.3 lists representative BMS compositions from various units of borehole ELF-395. Refer to Appendix 3 for the complete compositional dataset.

Mineral analysis of pyrite (from 13 analyses) showed small variation in S and Fe ranging from 54.1 to 55.3 wt. % (avg. 54.7 wt. %) and 42.8 to 46.7 wt. % (avg. 44.7 wt. %), respectively. Pyrrhotite (from 4 analyses) showed compositional S and Fe ranges from 40.1 to 40.4 wt. % (avg. 40.3 wt. %) and 57.5 to 60.3 wt. % (avg. 58.5 wt. %), respectively.

Pentlandite (from 10 analyses) ranged in S, Fe and Ni from 33.1 to 34.3 wt. % (avg. 33.8 wt. %), 25.2 to 32.0 wt. % (avg. 29.1 wt. %) and 35.1 to 40.5 wt. % (avg. 36.8 wt. %), respectively.

Mineral analysis of chalcopyrite identified compositional ranges in S, Cu and Fe (from 10 analyses) as follows: 35.2 to 35.8 wt. % (avg. 35.5 wt. %), 32.3 to 34.4 wt. % (avg. 33.4 wt. %) and 30.0 to 32.1 wt. % (avg. 30.9 wt. %), respectively.

An elemental map (as shown in figure 4.3.3) highlights the association of BMS as aggregates. The map was produced with the following elements in mind: S, Fe, Ni and Cu. Pyrite (high S – moderate Fe) and pyrrhotite (high Fe – moderate S) make up the core of the aggregate. Pentlandite (Ni-rich) and chalcopyrite (Cu-rich) occurred on the margins of the pyrite and pyrrhotite core.

BSE images of BMS aggregates are shown in figures 4.3.6F and H. Figure 4.3.6H shows the same grain aggregate as the elemental map in figure 4.3.3.

Table 4.3.3. Representative base metal sulphide compositions from various units of borehole ELF-395. Data are presented in wt. % and mineral identification is given.

Sample Name	MR07_BMS49	MR13_BMS123	MR06_BMS40	MR13_BMS130	MR19_BMS134	MR21_BMS148	MR13_BMS128	MR19_BMS135
Unit	Norite HW	Pyroxenite Reef	Leuconorite HW	Pyroxenite Reef	Pyroxenite Reef	Pyroxenite Reef	Pyroxenite Reef	Pyroxenite Reef
S (wt. %)	54.33	33.31	40.44	35.27	54.86	33.65	40.05	35.64
Fe (wt. %)	44.99	31.74	57.87	30.79	46.16	26.09	60.33	30.78
Cu (wt. %)	0.00	0.00	0.07	33.69	0.00	0.00	0.00	34.01
Ni (wt. %)	0.78	35.48	0.78	0.00	0.13	39.89	0.39	0.05
Zn (wt. %)	0.02	0.00	0.00	0.39	0.00	0.04	0.02	0.00
Pb (wt. %)	0.17	0.00	0.24	0.08	0.16	0.33	0.05	0.05
Total (wt. %)	**100.28**	**100.52**	**99.39**	**100.22**	**101.31**	**100.01**	**100.84**	**100.53**
Identified Mineral	*Pyrite*	*Pentlandite*	*Pyrrhotite*	*Chalcopyrite*	*Pyrite*	*Pentlandite*	*Pyrrhotite*	*Chalcopyrite*

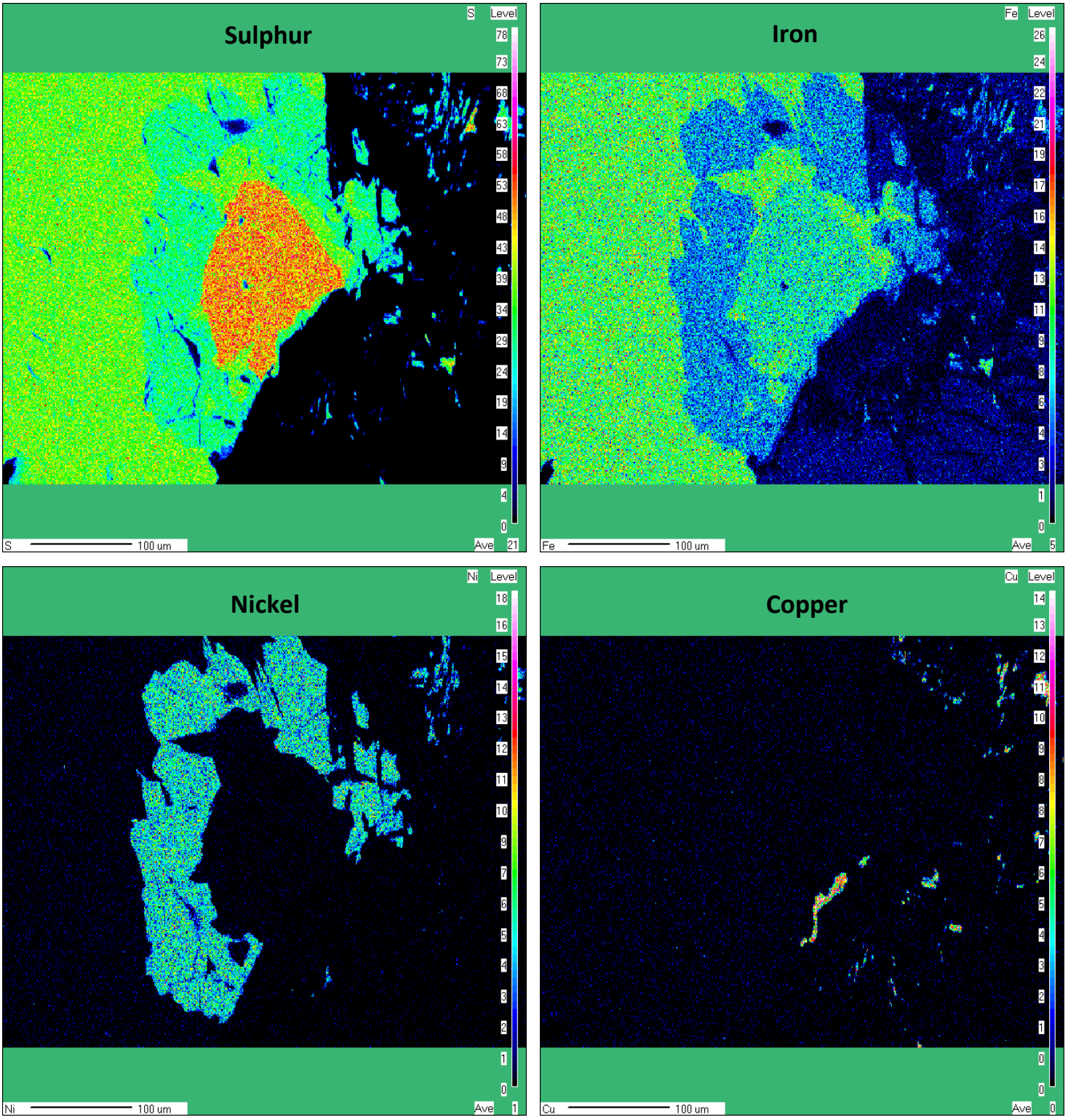

Figure 4.3.3. An elemental map illustrating the association of BMS. The core of the above aggregate is dominated by pyrite (high S – moderate Fe) and surrounded by pyrrhotite (moderate S – high Fe) and pentlandite (Ni-rich). Chalcopyrite (Cu-rich) occurs as a thin 'sliver' on the aggregate margins. The map was produced from the pyroxenite reef unit (sample MR-19).

4.3.4. Oxides

Oxides identified during mineral analysis included chromite, rutile and ilmenite. Representative compositions of the above mentioned minerals are shown in Table 4.3.4. For the complete oxide compositional datasheet, see Appendix 4. Excluding the chromitite unit, oxides occur in relatively low modal abundances (~ 2 %) throughout ELF-395. From a total of 46 analyses, chromite showed significant variation in MgO, FeO, Al_2O_3, Cr_2O_3 and TiO_2 ranging from 0.21 to 7.00 wt. % (avg. 2.93 wt. %), 32.0 to 55.7 wt. % (avg. 44.4 wt. %), 3.18 to 13.5 wt. % (avg. 7.47 wt. %), 35.3 to 46.9 wt. % (avg. 42.8 wt. %) and 0.18 to 2.27 wt. % (avg. 1.01 wt. %), respectively. Interestingly, sample MR-23 (i.e., the chromitite unit) and MR-10 (correlating to the upper PGE (+ Cu and Ni) peak) show higher Cr_2O_3 and MgO values (Fig. 4.3.4) compared to the remainder of the samples (all from the pyroxenite unit). A BSE image of chromite grains from the chromitite stringer (and various points of analysis) is shown in figure 4.3.6B.

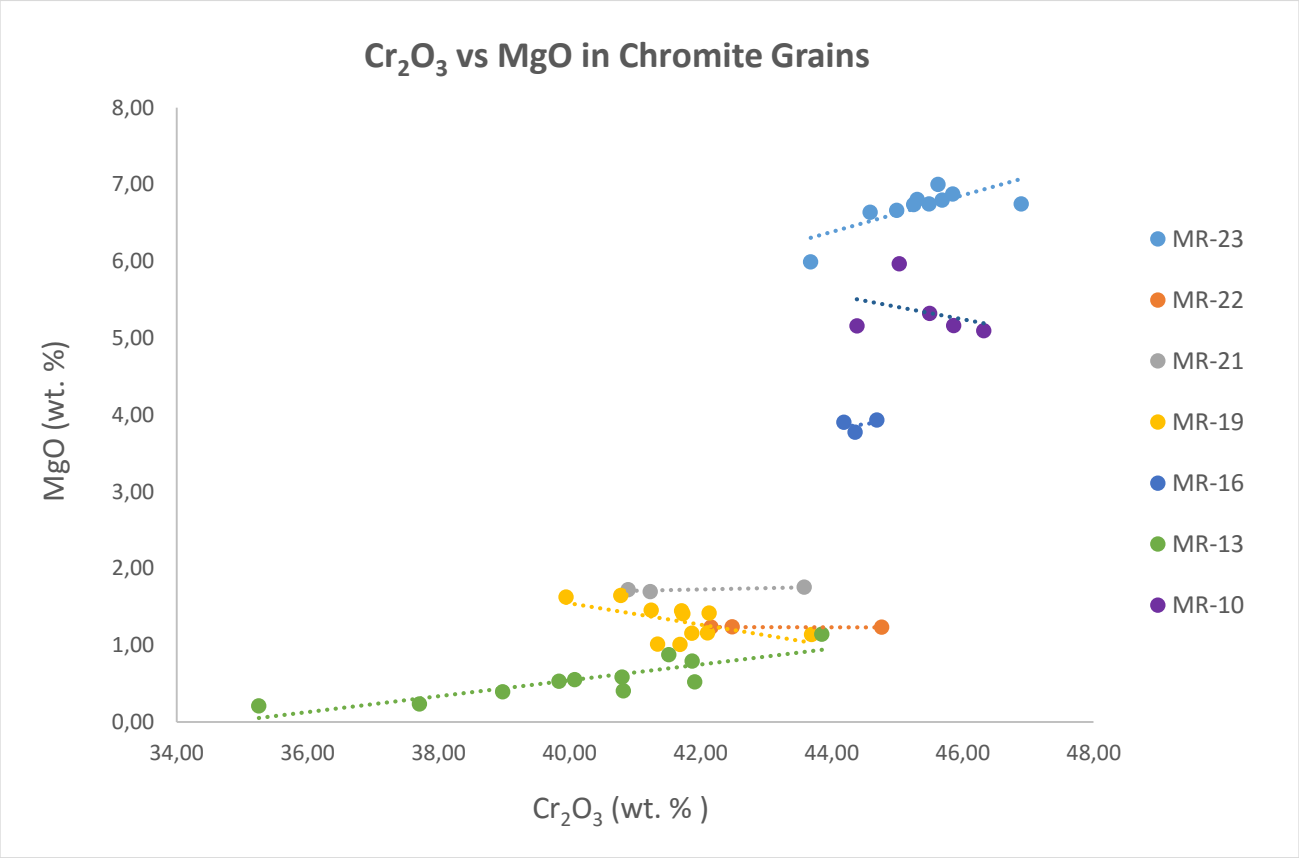

Figure 4.3.4. Cr_2O_3 versus MgO in chromite grains from borehole ELF-395. Samples MR-10 and MR-23 (correlating to the upper and lower PGE peaks) showed higher enrichment in Cr_2O_3 and MgO compared to the remainder of the samples from the pyroxenite unit.

Table 4.3.4. Representative oxide compositions from various units of borehole ELF-395. Data are presented in wt. % and mineral identification is given. Rutiles were normalised to 2 oxygens, ilmenites to 3 oxygens and chromites to 4 oxygens.

Sample Name	MR02_Rut/Ilm 5	MR02_Rut/Ilm 6	MR02_Rut/Ilm4	MR07_ox14	MR10_ox31	MR13_ox47	MR19_ox71	MR23_chr37
Unit	Anorthosite HW	Anorthosite HW	Anorthosite HW	Norite HW	Pyroxenite Reef	Pyroxenite Reef	Pyroxenite Reef	Chromitite Reef
TiO_2 (wt. %)	94.94	89.78	52.25	52.04	1.55	0.89	0.50	1.06
Cr_2O_3 ((wt. %)	0.08	0.11	0.01	0.15	45.86	40.80	41.73	45.69
Al_2O_3 (wt. %)	0.08	0.47	0.05	0.04	9.58	5.45	4.62	12.91
ZnO (wt. %)	0.02	0.03	0.03	0.00	0.10	0.30	0.00	0.11
FeO ((wt. %)	2.01	1.39	41.18	40.05	36.94	50.52	50.51	32.74
MnO (wt. %)	0.15	0.05	5.23	6.20	0.39	0.79	0.66	0.46
MgO (wt. %)	0.00	0.01	0.00	0.05	5.16	0.58	1.41	6.80
CaO (wt. %)	0.58	2.97	0.28	0.06	0.00	0.02	0.01	0.00
SiO_2 (wt. %)	0.03	2.84	0.02	0.04	0.03	0.03	0.01	0.01
V_2O_3 (wt. %)	1.45	1.17	0.41	0.29	0.39	0.55	0.57	0.36
Total (wt. %)	**99.34**	**98.80**	**99.46**	**98.91**	**100.01**	**99.93**	**100.01**	**100.13**
Si	0.00	0.04	0.00	0.00	0.00	0.00	0.00	0.00
Al	0.00	0.01	0.00	0.00	0.40	0.25	0.21	0.52
Ti	0.97	0.91	0.99	1.00	0.04	0.03	0.01	0.03
Fe	0.02	0.02	0.87	0.85	1.09	1.62	1.62	0.93
Mn	0.00	0.00	0.11	0.13	0.01	0.03	0.02	0.01
Mg	0.00	0.00	0.00	0.00	0.27	0.03	0.08	0.35
Zn	0.00	0.00	0.00	0.00	0.00	0.01	0.00	0.00
Ca	0.01	0.04	0.01	0.00	0.00	0.00	0.00	0.00
Cr	0.00	0.00	0.00	0.00	1.28	1.24	1.27	1.23
V	0.01	0.01	0.01	0.00	0.01	0.01	0.01	0.01
Total Cations	**1.01**	**1.03**	**1.99**	**1.99**	**3.11**	**3.21**	**3.23**	**3.08**
Identified Mineral	*Rutile*	*Rutile*	*Ilmenite*	*Ilmenite*	*Chromite*	*Chromite*	*Chromite*	*Chromite*

Ilmenite mineral analysis, from 3 analyses, showed minor variation in FeO, TiO_2, MnO, MgO, V_2O_3 and Cr_2O_3 compositions ranging from 40.1 to 44.6 wt. % (avg. 41.9 wt. %), 47.4 to 52.3 wt. % (avg. 50.6 wt. %), 5.23 to 6.20 wt. % (avg. 5.58 wt. %), 0.00 to 0.05 wt. % (avg. 0.03 wt. %), 0.29 to 0.63 wt. % (avg. 0.44 wt. %) and 0.01 to 0.68 wt. % (avg. 0.23 wt. %), respectively.

Mineral analysis of rutile grains (from 2 analyses) showed minor variation in FeO, V_2O_3, Cr_2O_3 and TiO_2 compositions ranging from 1.39 to 2.01 wt. % (avg. 1.70 wt. %), 1.17 to 1.45 wt. % (avg. 1.31 wt. %), 0.08 to 0.11 wt. % (avg. 0.09 wt. %) and 89.8 to 94.9 wt. % (avg. 92.4 wt. %), respectively.

Ti-exsolution of rutile from ilmenite, as observed during the petrographic analysis, was mapped for Fe and Ti (Fig. 4.3.5). Rutile can be identified by higher Ti concentrations (in pink) than ilmenite (green), while ilmenite is more enriched in iron (also green) than rutile (dark blue). A BSE image of the same grain, from the anorthositic footwall, is shown in figure 4.3.6G.

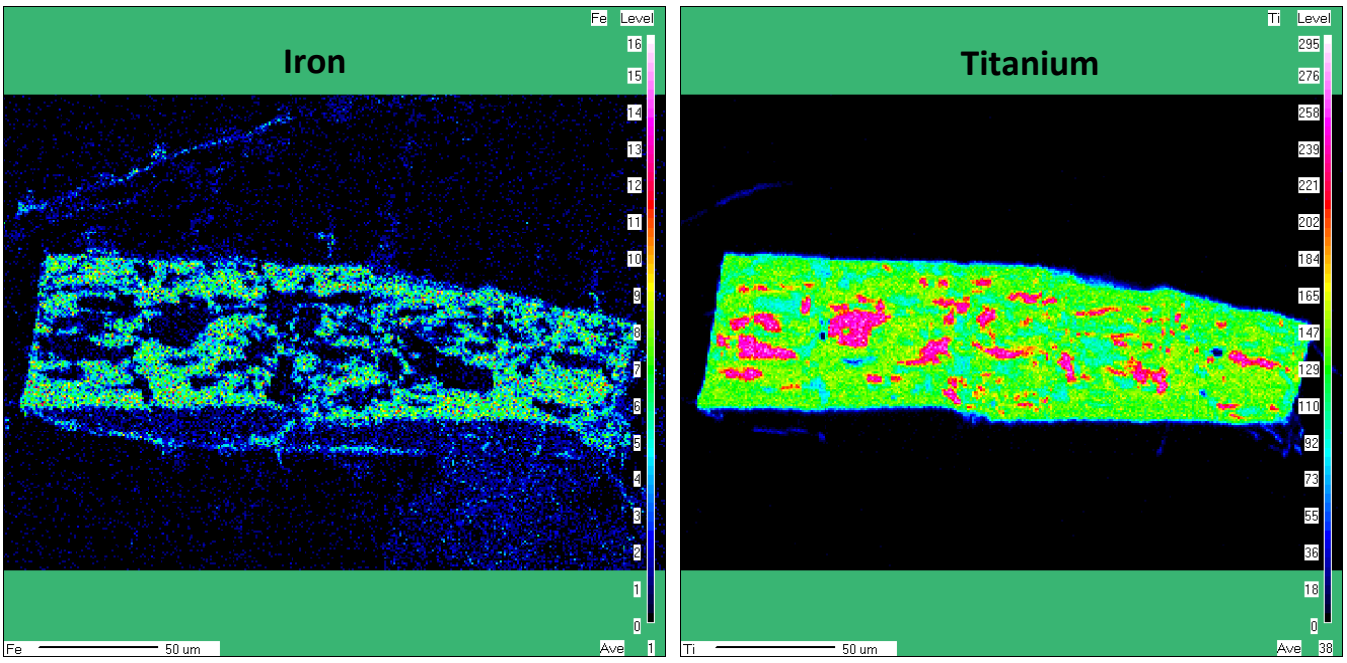

Figure 4.3.5. An elemental map illustrating Ti-exsolution of rutile (high Ti) in ilmenite (low to moderate Ti). The map was produced from anorthosite footwall unit (sample MR-24).

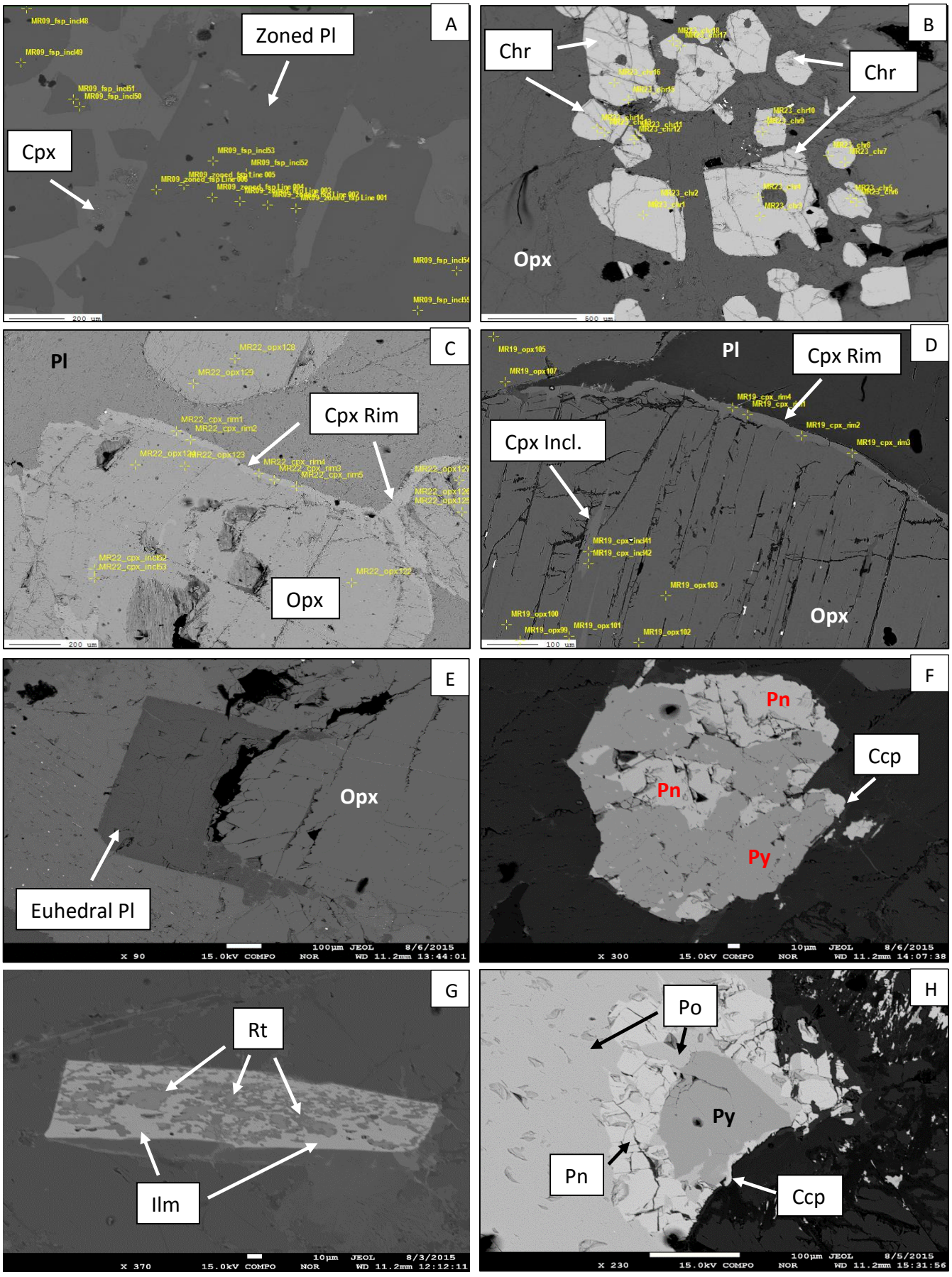

Figure 4.3.6. BSE images showing characteristic features and minerals from borehole ELF-395. **A)** Zoned plagioclase with analytical points shown (sample MR-09). **B)** Chromite grains from the chromitite stringer (sample MR-23). **C & D)** Cpx rims on adjacent Opx and surrounding interstitial Pl (from sample MR-22 and -19, respectively). **E)** Euhedral Pl and adjacent Opx (sample MR-16). **F**) BMS aggregate showing pyrite, pentlandite and chalcopyrite association. **G)** Ti-exsolution of Rt from Ilm (sample MR-24). **H)** BMS association in aggregate. Shown are pyrite (core), pyrrhotite, pentlandite and chalcopyrite (margins) (sample MR-19).

4.3.5. Biotite

Representative biotite compositions are shown in Table 4.3.5. For the complete biotite compositional datasheet see Appendix 5. Biotite is found in all units of borehole ELF-395 and occurs as an accessory mineral (averaging 2.5 % modal abundance). From 50 analyses, biotite ranged in SiO_2, TiO_2, Al_2O_3, FeO, MgO and K_2O compositions from 36.8 – 44.2 wt. % (avg. 39.3 wt. %), 0.54 – 5.73 wt. % (avg. 3.90 wt. %), 10.0 – 14.0 wt. % (avg. 13.2 wt. %), 7.10 – 12.5 wt. % (avg. 9.02 wt. %), 15.0 – 20.9 wt. % (avg. 18.4 wt. %) and 6.34 – 10.4 wt. % (avg. 9.23 wt. %), respectively. Furthermore, F and Cl ranged between 0.00 – 0.62 wt. % (avg. 0.34 wt. %) and 0.23 – 0.49 wt. % (avg. 0.33 wt. %), respectively.

Table 4.3.5. Representative biotite compositions from various units of borehole ELF-395. Data are presented in wt. % and was normalized to 11 oxygens.

Sample Name	MR09_bt23	MR09_bt28	MR19_bt49	MR19_bt51
Unit	Anorthosite Reef	Anorthosite Reef	Pyroxenite Reef	Pyroxenite Reef
SiO_2 (wt. %)	38.52	38.34	39.98	40.00
TiO_2 (wt. %)	5.73	5.16	3.76	3.82
Al_2O_3 (wt. %)	12.70	13.23	13.60	13.40
FeO (wt. %)	10.99	9.80	7.97	7.89
MnO (wt. %)	0.04	0.01	0.04	0.03
MgO (wt. %)	16.00	17.11	19.78	19.58
CaO (wt. %)	0.00	0.02	0.03	0.00
Na_2O (wt. %)	0.09	0.10	0.21	0.19
K_2O (wt. %)	10.24	10.28	9.62	9.89
F (wt. %)	0.36	0.44	0.36	0.52
Cl (wt. %)	0.33	0.31	0.34	0.31
Cr_2O_3 (wt. %)	0.48	0.50	0.92	0.98
H_2O (wt. %)	3.79	3.77	3.92	3.84
Subtotal (wt. %)	99.28	99.07	100.50	100.46
O=F, Cl (wt. %)	0.23	0.26	0.23	0.29
Total (wt. %)	**99.05**	**98.81**	**100.27**	**100.17**
Si	2.82	2.80	2.84	2.84
Al	1.10	1.14	1.14	1.12
Ti	0.32	0.28	0.20	0.20
Fe	0.67	0.60	0.47	0.47
Mn	0.00	0.00	0.00	0.00
Mg	1.75	1.86	2.09	2.07
Ca	0.00	0.00	0.00	0.00
Na	0.01	0.01	0.03	0.03
K	0.96	0.96	0.87	0.89
F	0.08	0.10	0.08	0.12
Cl	0.04	0.04	0.04	0.04
Cr	0.03	0.03	0.05	0.06
Total Cations	**7.78**	**7.82**	**7.82**	**7.83**

4.3.6. Platinum-Group Minerals

PGM were analysed to identify partitioning behaviour between PGE and surrounding silicates, suphides and oxides, as well as to determine which PGM are present in the Merensky Reef. Sample MR-23 was investigated (i.e., the chromitite unit) as it is the most PGE enriched sample from borehole ELF-395 and thus had the greatest chance of hosting PGE phases. Quantitative data by point analyses showed poor totals (none within the range of 98.5 to 101.5 wt. %) and thus this data cannot be relied upon too heavily but they do provide some indication of the general type of PGM present and their partitioning behaviour. These poor totals most likely reflect the types of standards used and erroneous overlap corrections during analysis, as well as the small size of PGM (typically between 1 and 10 microns) and poor surfaces (e.g., rough/irregular surfaces and the presence of cracks).

Borehole ELF-395 showed the presence of Pt-Pd bearing (Fig. 4.3.7), Cu-Rh-Pt bearing (i.e., ferhodsite) and Pt-Pd (+Bi, Te) (i.e., merenskyite) PGM species. These were identified near adjacent chromite grains or on the margins of BMS species. Analysis of borehole ELF-393 showed similar PGM species to ELF-393 (e.g., merenskyite) as well as Pt (+Bi, Te) (i.e., moncheite) species (see Table 4.3.6).

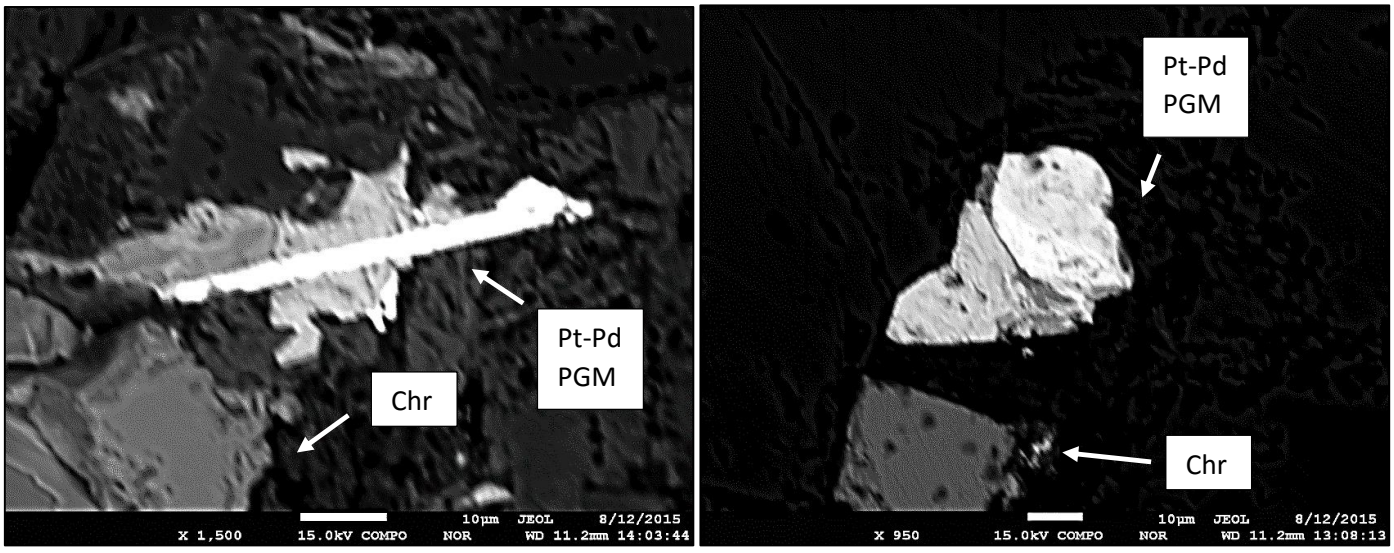

Figure 4.3.7. BSE images showing Pt-Pd bearing PGM and adjacent chromite grains. Both PGM were found in the chromitite unit (sample MR-23).

Table 4.3.6. Platinum-group mineral compositions from the norite hangingwall and footwall units of borehole ELF-393. Data are presented in wt. %.

Sample Name	4C_PGM_1	4C_PGM_2	4C_PGM_3	19_PGM1
Unit	Norite HW	Norite HW	Norite HW	Norite FW
Pt (wt. %)	27.38	32.24	40.77	0.00
Pd (wt. %)	4.03	0.88	0.33	39.69
Re (wt. %)	0.00	0.00	0.00	0.00
Ru (wt. %)	0.00	0.00	0.00	0.00
Rh (wt. %)	0.00	0.14	0.15	0.00
Os (wt. %)	2.26	2.48	3.32	2.71
Ir (wt. %)	0.00	0.00	0.00	0.00
Au (wt. %)	0.00	0.00	0.00	0.15
Te (wt. %)	35.28	43.36	19.80	33.43
As (wt. %)	0.00	0.00	14.70	0.05
S (wt. %)	0.25	0.16	1.57	0.06
Bi ((wt. %)	16.70	8.87	8.39	26.74
Fe (wt. %)	2.05	1.65	2.17	1.77
Cu (wt. %)	0.18	0.00	0.15	0.38
Ni (wt. %)	0.44	0.08	0.26	0.00
Total (wt. %)	**88.57**	**89.85**	**91.58**	**104.98**
Identified PGM	*Moncheite*	*Moncheite*	*Moncheite*	*Merenskyite*

4.3.7. Comparisons between boreholes ELF-395 and -393

Some similarities may be drawn between boreholes ELF-395 and -393 with regard to their mineral chemistry. For example, general trends of decreasing An content and CaO, as well as increasing K_2O and Na_2O, in plagioclase compositions from hangingwall or footwall units towards the reef units were observed in both boreholes. Similarly, in both boreholes ELF-395 and -393, reverse zoning of plagioclase grains was observed in the anorthositic footwall unit while normal zoning was observed in the anorthositic reef and leuconoritic unit, respectively. Furthermore, units between both boreholes correlated relatively well to one another. For example, similar CaO and K_2O values were recorded for plagioclase cores and inclusions in the leuconoritic unit of ELF-395 and -393. However, An content in cores and inclusions was marginally higher in ELF-395 versus -393, while Na_2O was lower in -395 compared to -393. Plagioclase core and inclusion compositions between both boreholes were most differentiated in the norite units, in which marginally higher K_2O and Na_2O, and lower An content and CaO, were recorded in borehole ELF-393 compared to -395. However, plagioclase core

compositions (An content, CaO, Na_2O and K_2O) for ELF-393 were well within the ranges recorded in -395. Like the anorthositic hangingwall unit, similar CaO and K_2O values in plagioclase cores were observed in the anorthositic footwall unit, while An content was higher in ELF-395 (i.e., plagioclases plotted in both bytownite and labradorite fields of ELF-393 but only in the bytownite field of -395) and Na_2O was only marginally higher in ELF-393.

Ortho- and clinopyroxene grains were relatively similar and comparable in boreholes ELF-395 and -393. For example, in both boreholes, orthopyroxenes plotted within the field of enstatite while clinopyroxenes plotted within the diopside field. Scatter in compositions, into the pigeonite and augite fields, was also recorded in both boreholes. However, when comparing the norite units from both boreholes, a number of differences in orthopyroxene and clinopyroxene compositions were observed. For example, orthopyroxene cores and inclusions in the norite hangingwall units show similar CaO ranges. However, FeO was shown to be marginally higher in ELF-395 while MgO in orthopyroxene inclusions was marginally higher in ELF-393. Clinopyroxene cores and inclusions showed relatively good correlations between both boreholes in the norite hangingwall unit. Orthopyroxene cores, within the pyroxenitic reef units of both boreholes, showed similar ranges for CaO and MgO, but FeO showed enrichment in ELF-393 while clinopyroxene inclusions and rims showed a higher enrichment in FeO and depletion in MgO for ELF-393.

Compositional differences in oxides were recorded between both boreholes. For example, larger compositional ranges for MgO were recorded in chromite grains of ELF-395 (i.e., 0.21 – 7.00 wt. %) compared to -393 (i.e., 0.74 – 4.21 wt. %) while TiO_2 was marginally lower in ELF-395 versus -393. Ilmenite showed the greatest variation between both boreholes, in which higher average FeO and MnO, and lower average MgO and Cr_2O_3, was recorded in grains from ELF-395 versus -393. Rutile grains recorded marginally higher FeO and V_2O_3 in ELF-395 compared to -393, while slightly lower TiO_2 was recorded in ELF-395 (avg. 92.4 wt. %) versus -393 (avg. 94.7 wt. %).

Base metal sulphides, which occur as grain aggregates, showed similar compositions in both boreholes. For example, compositional ranges for pentlandite, pyrrhotite and chalcopyrite were

similar in both ELF-395 and -393. However, pyrite showed marginally higher S in ELF-395 compared to -393 while Fe was proportionally lower in -395 versus -393.

Biotite showed similar compositional ranges for SiO_2, Al_2O_3, FeO, MgO, K_2O, Cl and F in boreholes ELF-395 and -393. However, biotite showed a greater enrichment in TiO_2 in ELF-395 (avg. 3.90 wt. %) versus ELF-393 (avg. 0.38 wt. %).

4.4. Whole-rock Major Element Geochemistry

Whole-rock major element oxide data are presented in Table 4.4.1 and Appendix 6. Variations in major element oxide concentrations plotted against stratigraphic depth are shown in figure 4.4.1. The data has been interpreted from the top to the bottom of the sequence, i.e., down the stratigraphy. SiO_2 shows slight variability (about 47 - 48 wt. %) in the anorthositic hangingwall before gradually increasing, to about 51 wt. %, within the pyroxenitic reef unit which underlies the hangingwall. A sharp decrease to about 46 wt. % is recorded at the bottom contact of the anorthositic seam and the following pyroxenitic reef. Thereafter, concentrations are relatively constant (between 51 and 55 wt. %) before decreasing gradually towards the underlying chromitite stringer (~ 48 - 49 wt. %) and maintaining constant concentrations (about 48 - 50 wt. %) through the remainder of the anorthositic footwall unit. Fe_2O_3, MgO and MnO show relatively similar trends. Low levels of concentration (with some variability) for Fe_2O_3, MgO and MnO occur in the anorthositic hangingwall (0 - 3 wt. %, 0 - 2 wt. % and 0.02 - 0.05 wt. %, respectively). A gradual increase in Fe_2O_3, MgO and MnO concentration (approximately 10 wt. %, 17 wt. % and 0.18 wt. %, respectively) is recorded in the pyroxenitic reef. Significant drops in concentration levels for Fe_2O_3, MgO and MnO occur in the underlying anorthositic seam (about 2 wt. %, 1 wt. % and 0.05 wt. %, respectively) before a sharp increase in the following pyroxenitic unit (~ 14 wt. %, 22 wt. % and 0.22 wt. %, respectively). Thereafter, concentrations of Fe_2O_3, MgO and MnO are relatively constant through the pyroxenitic reef before a sharp decrease is recorded in the anorthositic footwall (~ 1.2 wt. %, 0.4 wt. % and 0.02 wt. %, respectively).

Na_2O, Al_2O_3 and CaO show trends opposite to that of SiO_2, Fe_2O_3, MgO and MnO. High concentration levels (with some variability) are recorded in the anorthositic hangingwall for Na_2O, Al_2O_3 and CaO (~ 2.1 - 2.5 wt. %, 29 - 32 wt. % and 13.8 - 15 wt. %, respectively). A decrease in Na_2O, Al_2O_3 and CaO (about 1 wt. %, 13 wt. % and 7 wt. %, respectively) occurs in the following pyroxenite unit before a significant increase in the underlying anorthositic seam (3.6 wt. %, 25 wt. % and 12 wt. %, respectively). Concentration levels in Na_2O, Al_2O_3 and CaO then drop to 0.6 wt. %, 5.5 wt. % and 4.3 wt. %, respectively, and remain relatively constant throughout the pyroxenite reef. An increase in concentrations of Na_2O, Al_2O_3 and CaO is recorded from the underlying chromitite stringer (about 1 wt. %, 12 wt. % and 6.5 wt. %, respectively) to the anorthositic footwall, where concentrations remain relatively constant (~ 2.5 wt. %, 31 wt. % and 15 wt. %, respectively).

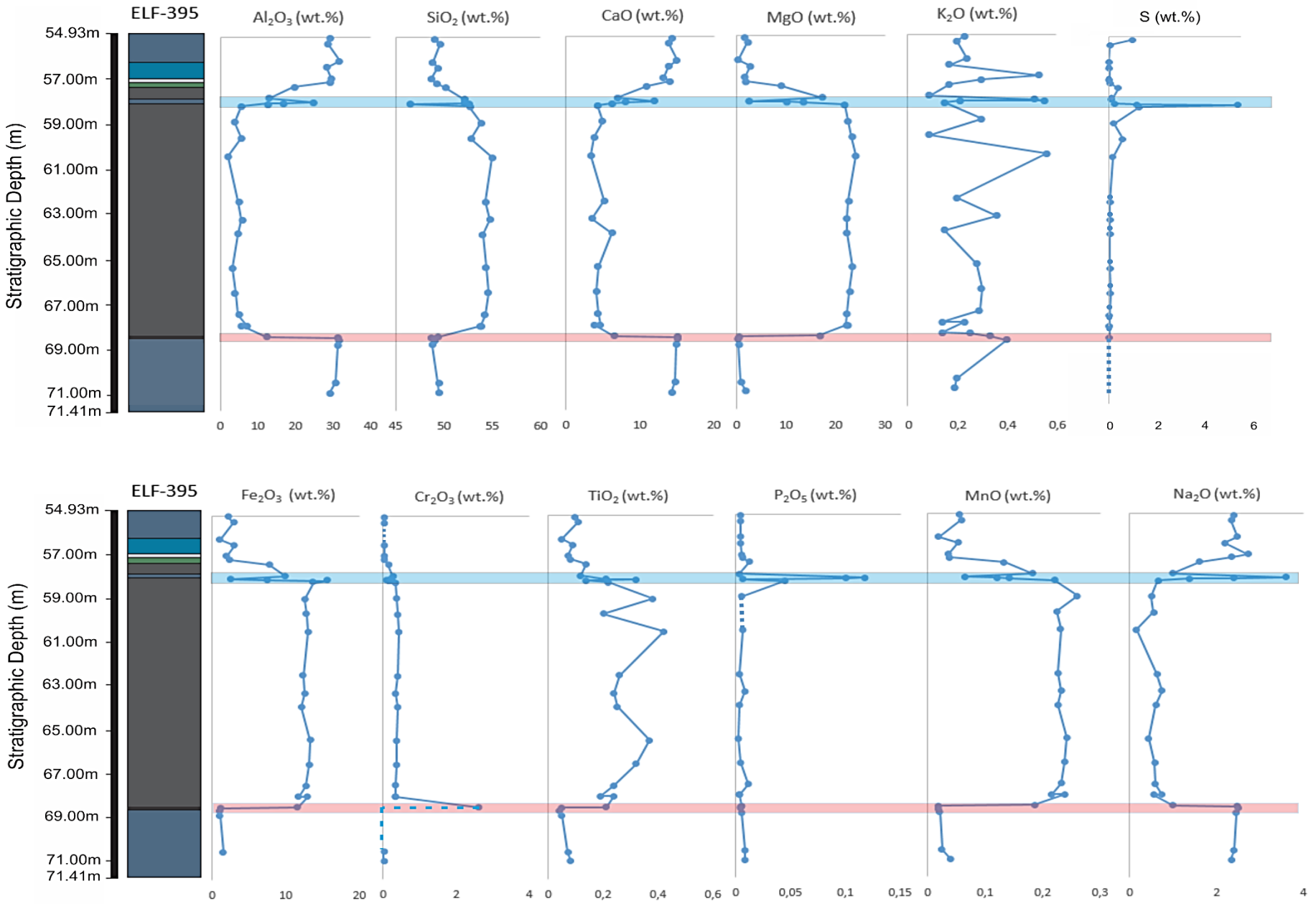

Figure 4.4.1. Whole-rock major element oxide concentration variations in borehole ELF-395. The blue highlighted area correlates to the anorthositic seam within the reef and the red highlighted area correlates to the chromitite stringer separating the footwall from the reef.

S concentration levels are relatively constant and low throughout all units (about 0 - 1 wt. %) with the exception of a high concentration spike (5.22 wt. %) occurring at the contact between the anorthositic seam and the underlying pyroxenite reef. Here, cm-scale sulphides were observed macroscopically (see Fig 4.1.2F). This particular peak is also associated with enrichments in Cu and Ni (see Chapter 4.5) suggesting the presence of Cu-rich (i.e., chalcopyrite) and Ni-rich (i.e., pentlandite) sulphide species. Like S, Cr_2O_3 shows relatively low concentrations (0 - 0.03 wt. %) in all lithologies except in the pyroxenite reef (~ 0.1 - 0.45 wt. %) and the chromitite stinger (2.61 wt. %). Likewise, P_2O_5 maintains low levels of concentration in borehole ELF-395 (about 0.001 - 0.01 wt. %) with the exception of the anorthosite seam (0.12 wt. %).

K_2O and TiO_2 concentration levels are both significantly variable throughout borehole ELF-395. TiO_2 and K_2O concentrations in the footwall and hangingwall units range from 0.05 - 0.14 wt. % and 0.19 - 0.53 wt. %, respectively. However, TiO_2 and K_2O concentrations in the pyroxenitic reef range from 0.19 - 0.42 wt. % (noticeably higher) and 0.09 - 0.56 wt. % (on average lower, but also more variable), respectively. At the chromitite stringer, TiO_2 follows the trends of Fe_2O_3, MgO, MnO and SiO_2 (i.e., depletion) whereas K_2O is more similar to CaO, Al_2O_3 and Na_2O, i.e., slight enrichment compared to most of the overlying pyroxenite.

Whole-rock major element oxide binary plots are provided in figure 4.4.2. Both CaO and Na_2O show very strong positive correlations when plotted against Al_2O_3 (Fig. 4.4.2A and B). As expected, anorthosites plot in high CaO and high Na_2O fields versus high Al_2O_3 fields, respectively, whereas pyroxenites show the exact opposite trend. MgO concentrations show a very strong negative correlation with Al_2O_3 (Fig. 4.4.2C) and as such, pyroxenites are found in high MgO – low Al_2O_3 fields whereas anorthosites are found in low MgO – high Al_2O_3 fields. A moderately strong negative correlation is observed when SiO_2 is plotted against Al_2O_3 concentrations (Fig. 4.4.2F). Pyroxenites and anorthosite plot as two separate clusters, with the former being found in high SiO_2 – low Al_2O_3 fields whereas anorthosites plot in fields of low SiO_2 – high Al_2O_3.

Table 4.4.1. Whole-rock major element oxide compositions for borehole ELF-395. All data is presented in wt. % and where no value is given represents data below the detection limit. * The sample length corresponds to the core length that was sampled. ** S is included in the table below although it was analysed separately using a HH-XRF machine (see Chapter 4.2.4). Abbreviations follow those defined in Table 3.1.1.

Sample	MR-01	MR-02	MR-03	MR-04	MR-05	MR-06	MR-07	MR-08	MR-09a	MR-09b	MR-10	MR-11	MR-12	MR-13	MR-14
Lithology	AnMo	AnMo	AnSp	AnSp	AnSp	LuNo	No	Px	An	An	Px	Px	Px	Px	Px
Stratigraphic Depth (m)	55.07	55.31	56.09	56.38	56.89	57.05	57.27	57.80	57.97	58.01	58.04	58.13	58.88	59.60	60.43
*Sample Length (cm)	2.00	2.00	2.00	2.00	2.00	2.00	2.00	2.00	2.00	2.00	2.00	2.00	2.00	2.00	2.00
Al_2O_3 (wt. %)	29.20	28.64	31.73	28.31	29.47	29.12	19.58	12.91	24.89	16.95	12.64	5.46	3.94	5.63	2.17
BaO (wt. %)	0.01	0.01	0.01	0.01	0.02	0.01	0.01	0.01	0.03	0.03	0.01	0.01	0.02	0.01	0.01
CaO (wt. %)	14.30	13.82	14.97	13.90	13.22	14.04	10.95	6.99	11.97	8.00	6.18	4.31	4.99	3.77	3.36
Cr_2O_3 (wt. %)	0.02	0.02	<LOD	0.02	0.02	0.02	0.13	0.25	0.07	0.13	0.21	0.33	0.37	0.39	0.44
Fe_2O_3 (wt. %)	2.19	2.87	1.08	2.97	1.99	2.40	7.77	9.95	2.44	7.46	15.63	13.71	12.54	12.79	13.01
K_2O (wt. %)	0.23	0.20	0.24	0.17	0.53	0.30	0.17	0.09	0.51	0.55	0.21	0.15	0.30	0.09	0.56
LOI (wt. %)	0.62	0.29	0.34	0.17	1.75	0.35	0.20	-0.16	1.26	1.19	2.07	0.43	0.69	0.38	1.24
MgO (wt. %)	1.56	2.21	0.24	2.81	1.57	1.95	9.07	17.16	2.54	10.11	13.45	21.75	22.46	23.21	23.98
MnO (wt. %)	0.06	0.06	0.02	0.05	0.04	0.04	0.13	0.18	0.06	0.12	0.14	0.22	0.26	0.23	0.23
Na_2O (wt. %)	2.37	2.32	2.48	2.17	2.72	2.34	1.62	0.98	3.60	2.38	1.37	0.64	0.49	0.55	0.16
P_2O_5 (wt. %)	0.00	0.00	0.00	0.00	0.01	0.01	0.01	0.00	0.12	0.10	0.01	0.04	0.01	<LOD	0.01
**S (wt. %)	0.97	0.04	0.00	0.03	0.03	0.05	0.37	0.11	0.22	1.13	5.22	1.23	0.20	0.55	0.15
SiO_2 (wt. %)	49.07	49.57	48.87	49.32	48.66	49.22	50.11	52.05	52.06	52.53	46.40	52.60	53.85	52.75	54.91
TiO_2 (wt. %)	0.10	0.11	0.05	0.09	0.07	0.08	0.14	0.12	0.21	0.32	0.14	0.22	0.38	0.20	0.42
Total (wt. %)	99.72	100.10	100.04	99.99	100.05	99.88	99.90	100.54	99.76	99.87	98.47	99.87	100.29	99.99	100.50

Table 4.4.1: (*cont.)*

Sample	MR-15	MR-16	MR-17	MR-18	MR-19	MR-20	MR-21	MR-22	MR-23	MR-24	MR-25	MR-26	MR-27	MR-28
Lithology	Px	Px	Px	Px	Px	Px	Px	Px	Chr	AnMo	AnMo	AnMo	AnMo	AnMo
Stratigraphic Depth (m)	62.48	63.30	63.95	65.50	66.63	67.63	68.14	68.61	68.64	68.68	68.79	69.00	70.73	71.17
***Sample Length (cm)**	2.00	2.00	2.00	2.00	2.00	2.00	2.00	2.00	2.00	2.00	2.00	2.00	2.00	2.00
Al_2O_3 (wt. %)	4.82	5.71	4.65	3.34	4.08	4.83	6.99	5.49	12.27	31.27	31.71	31.33	30.73	29.3
BaO (wt. %)	0.01	0.01	0.01	0.01	0.01	0.01	0.01	0.01	0.01	0.01	0.01	0.01	0.01	0.01
CaO (wt. %)	5.20	3.46	6.19	4.33	4.11	4.39	4.70	3.85	6.48	15.12	15.03	14.96	14.78	14.36
Cr_2O_3 (wt. %)	0.41	0.33	0.41	0.38	0.36	0.35	0.34	0.33	2.61	<LOD	<LOD	<LOD	0.01	0.01
Fe_2O_3 (wt. %)	12.32	12.58	12.12	13.32	13.10	12.70	11.77	12.92	11.56	1.21	1.07	1.07	1.50	2.26
K_2O (wt. %)	0.20	0.36	0.15	0.28	0.30	0.29	0.14	0.23	0.14	0.25	0.33	0.40	0.20	0.19
LOI (wt. %)	-0.20	-0.10	-0.08	-0.08	-0.21	0.25	0.05	0.25	0.05	0.38	0.41	0.51	0.24	0.13
MgO (wt. %)	22.57	22.17	22.25	23.32	22.81	22.26	22.16	22.34	16.69	0.42	0.23	0.36	0.86	1.85
MnO (wt. %)	0.23	0.23	0.23	0.24	0.24	0.23	0.22	0.24	0.19	0.02	0.02	0.02	0.03	0.04
Na_2O (wt. %)	0.62	0.75	0.59	0.43	0.56	0.58	0.73	0.54	0.99	2.47	2.50	2.45	2.41	2.33
P_2O_5 (wt. %)	0.00	0.01	0.00	0.00	0.00	0.01	0.00	0.00	0.01	0.00	0.00	0.01	0.01	0.01
****S (wt. %)**	0.05	0.05	0.03	0.05	0.07	0.03	0.02	0.03	0.02	<LOD	<LOD	<LOD	<LOD	<LOD
SiO_2 (wt. %)	54.31	54.77	54.02	54.33	54.57	54.22	53.78	53.90	49.34	48.74	49.02	48.77	49.36	49.44
TiO_2 (wt. %)	0.26	0.24	0.25	0.37	0.32	0.24	0.19	0.24	0.21	0.05	0.04	0.05	0.07	0.08
Total (wt. %)	100.76	100.54	100.78	100.27	100.24	100.36	101.07	100.33	100.55	99.95	100.37	99.95	100.19	100.01

MgO, when plotted against Fe_2O_3 (Fig. 4.4.2D), shows a very strong positive correlation. Pyroxenites plot in areas of both high MgO and high Fe_2O_3 whereas anorthosites show the exact opposite trend. Chromitite and norites (as well as leuconorites) plot somewhere between these two extremes. Fe_2O_3 versus SiO_2 concentrations (Fig. 4.4.2E) show a moderately strong positive correlation. Pyroxenites plot in high Fe_2O_3 – high SiO_2 fields whereas anorthosites plot in low Fe_2O_3 – moderate SiO_2 fields.

Cr_2O_3 versus Fe_2O_3 concentrations (Fig. 4.4.2G) shows no significant correlation and most lithologies plot in the low Cr_2O_3 field and spread across variable Fe_2O_3 concentrations. Chromitite, as expected, is the exception to this, i.e., high Cr_2O_3. MgO, when plotted against CaO (Fig. 4.4.2H), shows a very strong negative correlation. Pyroxenites plot in high MgO – low CaO fields whereas anorthosites plot in low MgO – high CaO fields. TiO_2 versus MnO concentrations (Fig. 4.4.2I) show a strong positive correlation. Pyroxenites plot in the high MnO field of the graph and have variable TiO_2 concentrations whereas anorthosites comprise low MnO concentrations and generally low TiO_2 concentrations.

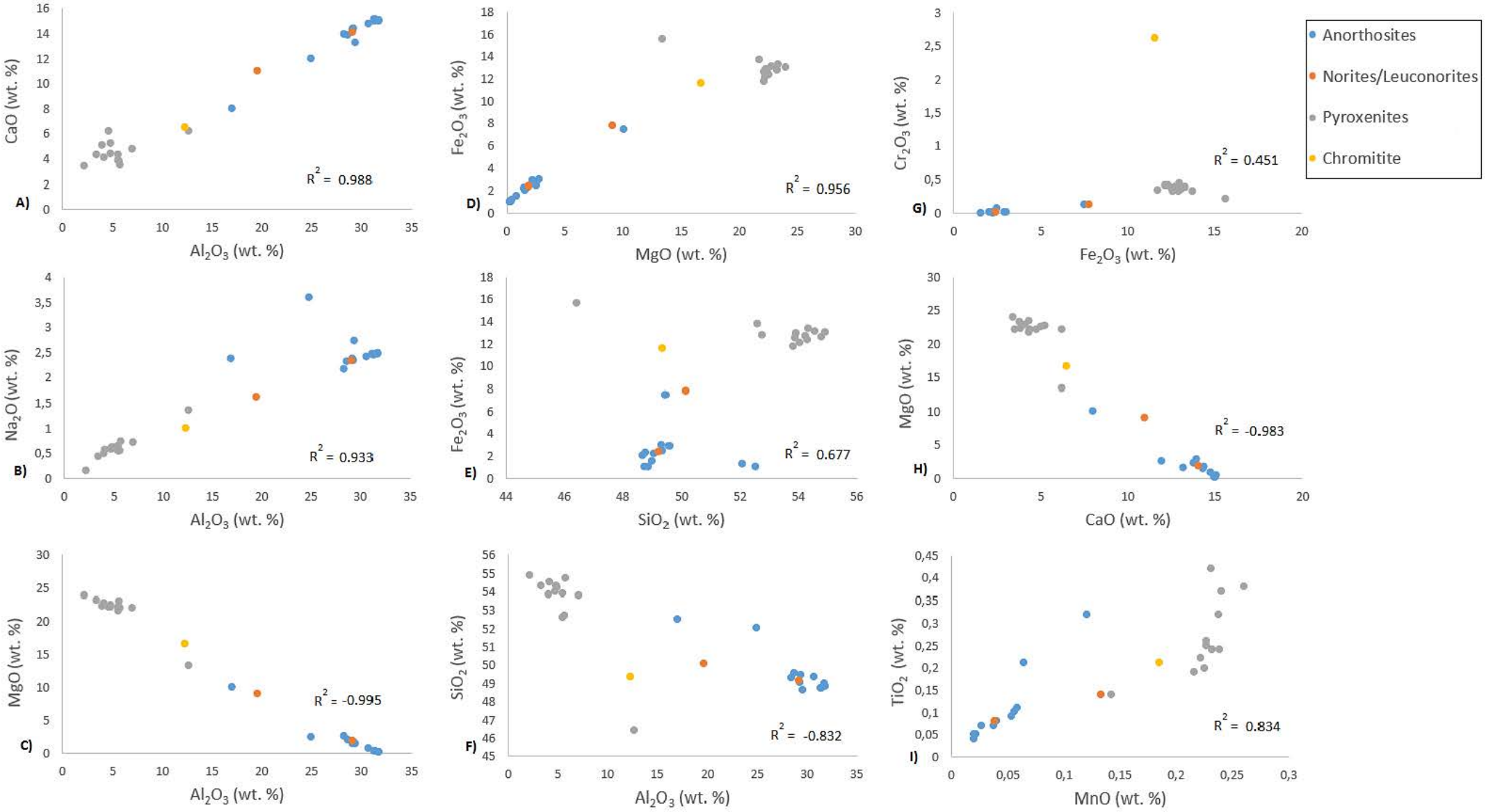

Figure 4.4.2. Whole-rock major element oxide binary plots for Al_2O_3, SiO_2, MgO, MnO, CaO, Na_2O, Fe_2O_3, Cr_2O_3 and TiO_2 for borehole ELF-395. The correlation coefficient (R^2) is given for each diagram.

4.5. Whole-rock Trace Element Geochemistry

Trace element concentrations, analysed by ICP-MS, for boreholes ELF-395 and ELF-393, are presented in Appendices 7 and 8, respectively. Trace elements analysed for borehole ELF-393 were included in this chapter so a comparison between boreholes ELF-393 and ELF-395 can be made. The data has been interpreted from the top to the bottom of the sequence, i.e., down the stratigraphy. Stratigraphic concentration profiles for Cu, Ni, Cr, Co, Sr and Zr, in boreholes ELF-395 and ELF-393, are shown in figures 4.5.1 and 4.5.2.

In borehole ELF-395, Cu (Fig. 4.5.1) shows low levels of enrichment in the anorthosite hangingwall (< 100 ppm) which gradually increases towards the norite, pyroxenite and anorthosite seam units. An upper peak (2098 ppm) is recorded in the pyroxenitic reef (underlying the anorthositic seam). Enrichment in Cu is observed underlying the upper peak, with concentrations ranging between 1530 and 753 ppm. Thereafter, Cu concentrations drop to < 100 ppm for the remainder of the reef and into the underlying chromitite (41 ppm) and anorthositic footwall units (6 to 13 ppm). The overall enrichment pattern of Ni (Fig. 4.5.1) is noticeably similar to Cu, with low levels of enrichment recorded in the anorthositic hangingwall (between 25 and 156 ppm) and gradual increases in the underlying norite, pyroxenite and anorthosite seam units. The upper peak, which coincides with the pyroxenitic reef underlying the anorthositic seam, has a recorded value of > 4100 ppm (i.e., above the upper detection limit). Enrichment in Ni is observed underlying the upper peak, with concentrations ranging between 3841 and 1870 ppm, before dropping throughout the remainder of the pyroxenite unit (between 542 and 602 ppm). Moderate levels of Ni enrichment were recorded in the chromitite stringer while the anorthosite footwall is depleted (507 ppm and 9 to 41 ppm, respectively).

Cr (Fig. 4.5.1) shows depleted concentrations in both the anorthositic HW and FW units, in which concentrations typically range between 11 and 178 ppm. An increase in Cr concentrations is recorded in the leuconorite unit (116 ppm) through to the norite unit (888 ppm). The anorthositic seam is markedly more enriched in Cr than anorthositic HW and FW units (between 468 and 951 ppm). High levels of enrichment are recorded in the pyroxenitic reef where Cr concentrations range between 1501 and 3221 ppm. The chromitite stringer, at the base of the reef, has a Cr concentration of > 4500 ppm (i.e., above the upper detection limit).

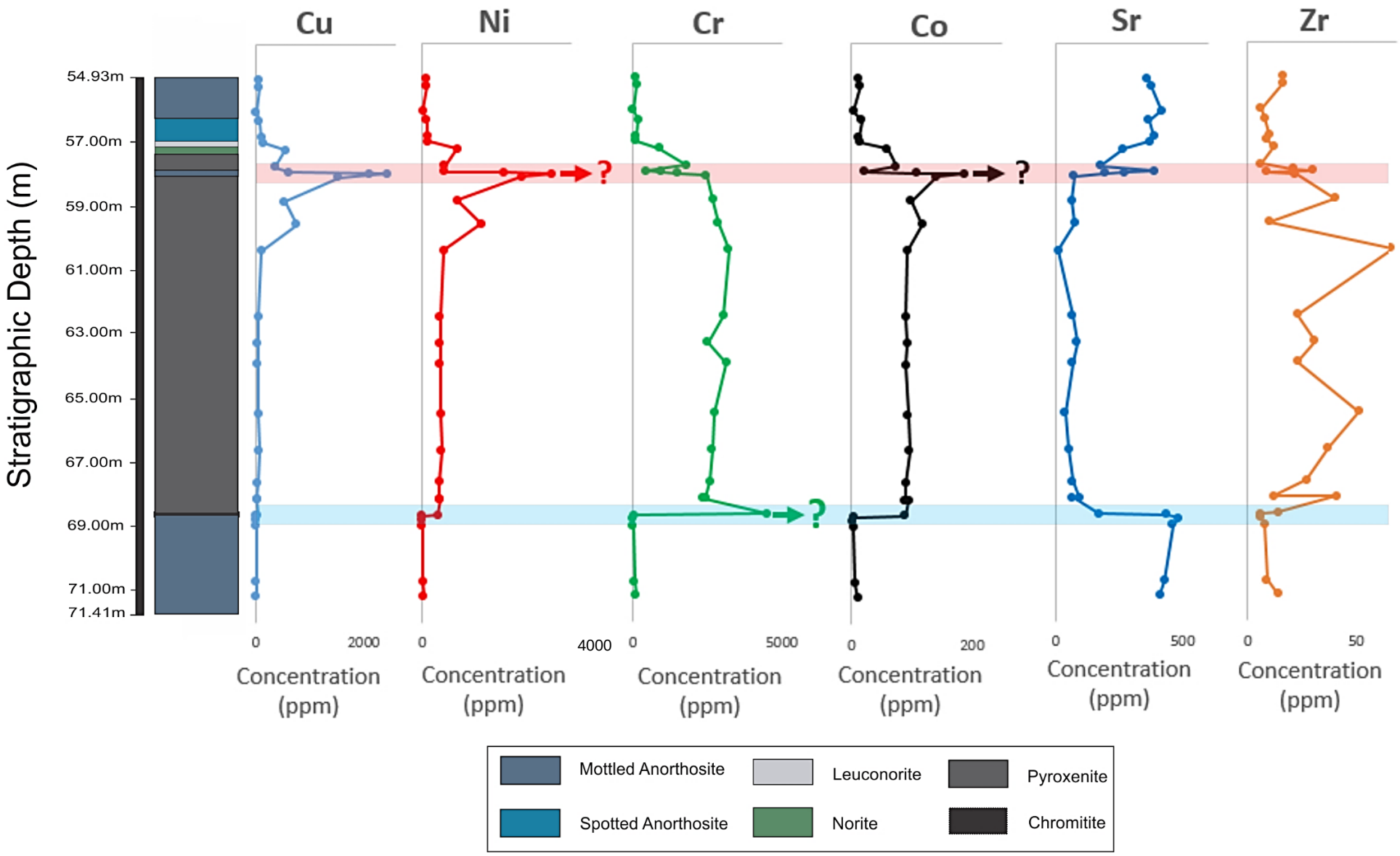

Figure 4.5.1. Whole-rock trace element (Cu, Ni, Cr, Co, Sr and Zr) stratigraphic concentration profiles for borehole ELF-395. The red highlighted area correlates to the anorthositic seam within the reef (and underlying pyroxenite unit) and the blue highlighted area correlates to the chromitite stringer at the base of the reef. Question marks denote upper detection limits for the respective elements.

Co shows a similar pattern of enrichment to Cu and to Ni (Fig. 4.5.1). Low levels of enrichment in Co are recorded in the anorthositic hangingwall (3 to 17 ppm) and footwall (3 to 11 ppm) units. Co concentrations increase towards the norite unit (59 ppm) and peak in the pyroxenitic reef underlying the anorthositic seam (> 187 ppm; i.e., above the upper detection limit). Concentrations show high levels of enrichment underlying the above mentioned peak (100 to 141 ppm) before gradually decreasing and remaining relatively uniform for the remainder of the reef (~ 90 ppm). The chromitite stringer shows a similar concentration in Co to the overlying pyroxenite unit (89 ppm).

Sr (Fig. 4.5.1) has an enrichment pattern unlike the previously mentioned elements. Instead, Sr shows preferential enrichment within plagioclase-rich rocks. Thus, high levels of Sr enrichment are recorded in the anorthositic HW, FW and seam units with concentrations ranging between 361 to 418 ppm, 411 to 484 ppm and 273 to 391 ppm, respectively. The leuconorite and norite units also record high to moderately high Sr concentration levels of 371 ppm and 268 ppm, respectively. Low to moderate Sr concentrations are recorded in the pyroxenite reef where Sr ranges in concentration between 38 and 193 ppm. The chromitite stringer has a Sr concentration value of 172 ppm.

Zirconium has a highly variable pattern of enrichment in ELF-395 (Fig. 4.5.1). The anorthositic HW and FW units are relatively alike and Zr concentrations range between < 6 and 16 ppm and 6 and 14 ppm, respectively. The leuconorite unit has a marginally lower Zr concentration (9 ppm) than the underlying norite unit (12 ppm). Furthermore, the anorthosite seam shows higher Zr concentrations than its anorthositic counterparts with concentrations ranging between 21 and 30 ppm. The pyroxenitic reef records the highest Zr concentrations on average, although these are quite variable, where concentrations range between 9 and 67 ppm. Zr appears to significantly decrease towards the underlying chromitite stringer (with a recorded Zr value of only 14 ppm).

Borehole ELF-393 shows some notable similarities to ELF-395 with regard to trace element stratigraphic profiles. However, in ELF-393, although Cu doesn't achieve a maximum peak of 2098 ppm, Cu shows significantly more enrichment in all other units compared to ELF-395 (Fig. 4.5.2). Cu concentrations in the anorthositic HW range between 76 - 139 ppm while the

anorthositic FW ranges between 25 - 296 ppm. Leuconorite and norite units show moderate to high Cu enrichments in the hangingwall (328 to 359 ppm and 985 to 1503 ppm, respectively) while the footwall units are far more depleted (40 ppm and 49 ppm, respectively). An upper Cu peak of 1508 ppm is recorded at the start of the pegmatitic pyroxenite reef and, thereafter, concentrations range between 36 and 1487 ppm, with noticeable enrichment underlying the upper Cu peak (similar to ELF-395). In the underlying pyroxenite unit, Cu concentrations range between 41 and 85 ppm.

Ni (Fig. 4.5.2) shows a similar pattern of enrichment to Cu, in which the anorthositic HW and FW units record low Ni concentrations (112 - 164 ppm and 30 - 205 ppm, respectively). Leuconorite and norite units show moderate to high Ni enrichment, however, the HW units have a higher nickel concentration compared to the FW units (601 - 621 ppm and 2280 - 2945 ppm versus 544 ppm and 602 ppm, respectively). The pegmatitic pyroxenite is the most enriched unit in ELF-393, where Ni concentrations range between 497 and 3497 ppm. The underlying pyroxenite unit shows a flat Ni profile which is the result of little variability in concentrations (between 393 and 516 ppm).

Chromium (Fig. 4.5.2) shows a concentration profile in ELF-393 that is unlike the profile recorded in ELF-395. This is superficially consistent with the absence of a chromitite stringer at the base of the reef in ELF-393. In the anorthositic HW and FW units, Cr ranges in concentration between 123 and 155 ppm and 42 and 102 ppm, respectively. Unlike Cu and Ni, the leuconorite unit is more enriched in Cr in the FW (2054 ppm) compared to the HW (between 527 and 947 ppm) while the opposite is true for the norite unit (2149 ppm and between 1851 and 2301 ppm, respectively). No distinct upper or lower Cr peak was observed in ELF-393. The pegmatitic pyroxenite unit recorded Cr concentrations in the range of 2259 and 2822 ppm whereas the underlying pyroxenite unit ranged between 1563 and 2367 ppm.

With the exception of the upper peak, Co has a concentration profile rather similar to Cr (Fig. 4.5.2). Low Co concentrations are recorded in the anorthositic HW and FW units with concentrations ranging between 9 - 15 ppm and 5 - 11 ppm, respectively. Like Cr, and opposite to that of Cu and Ni, the footwall leuconorite is more enriched in Co compared to the hanging-

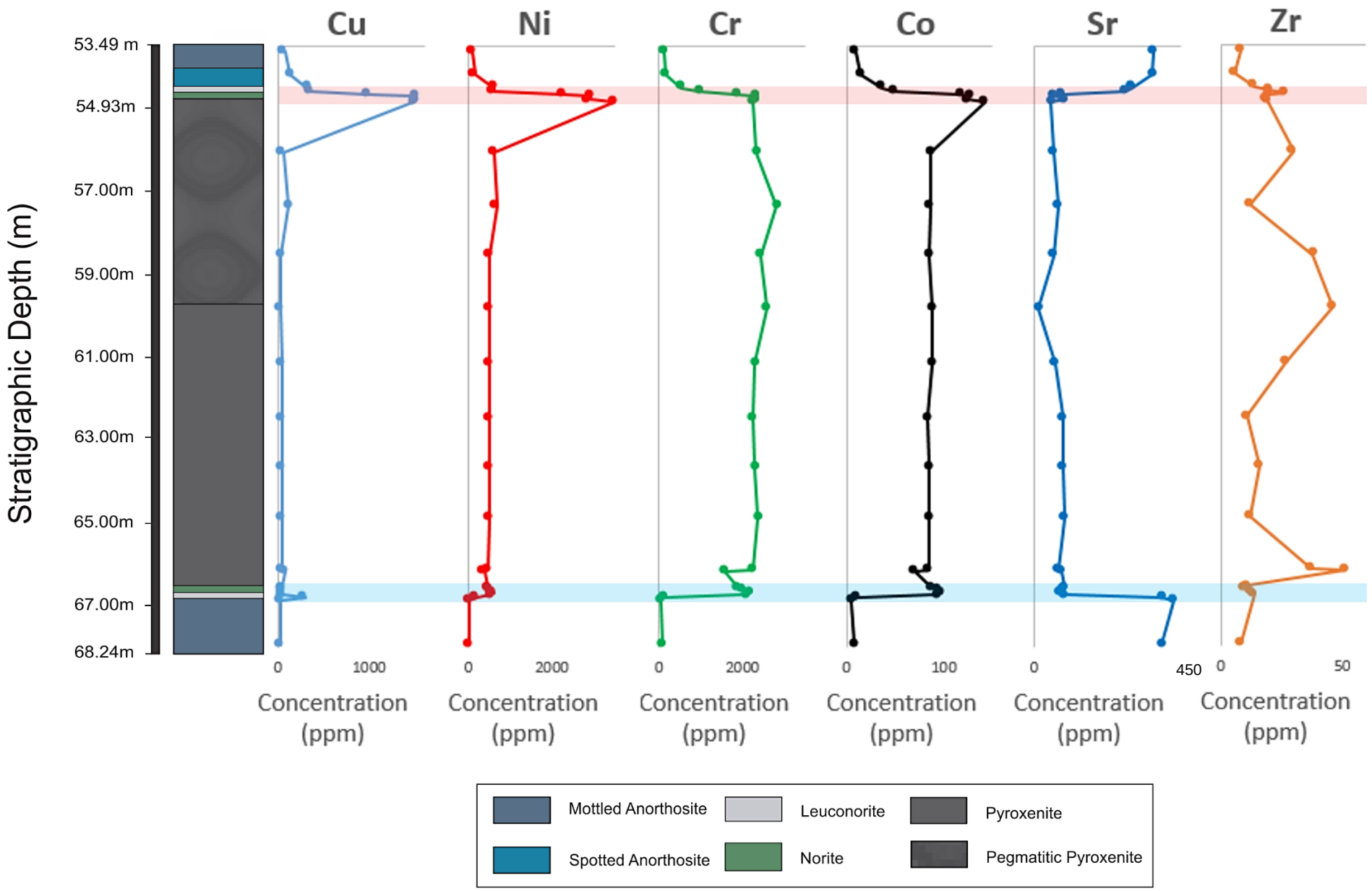

Figure 4.5.2. Whole-rock trace element (Cu, Ni, Cr, Co, Sr and Zr) stratigraphic concentration profiles for borehole ELF-393. The red highlighted area correlates to the hangingwall norite unit and the blue highlighted area correlates to the footwall norite unit at the base of the reef.

wall (92 ppm versus 36 to 48 ppm) while the reverse is true for the norite unit (97 ppm versus 117 to 127 ppm). Co concentrations range between 85 and 142 ppm in the pegmatitic pyroxenite and 70 and 93 ppm in the underlying pyroxenite.

Sr (Fig. 4.5.2) shows high levels of enrichment in the anorthositic HW and FW units (364 to 368 ppm and 391 to 428 ppm, respectively). Furthermore, the leuconorite HW is more enriched in Sr than the FW unit (between 280 and 301 ppm versus 95 ppm, respectively). This is also true for the norite HW versus FW units (between 83 and 608 ppm versus 77 ppm, respectively). The pegmatitic pyroxenite shows Sr concentrations ranging between 13 and 93 ppm. The lowest Sr concentration marks the change from the pegmatitic pyroxenite to the underlying pyroxenite which ranges in concentration from 68 to 95 ppm. The absence of an anorthositic seam within the reef in borehole ELF-393 reflects the lack of a correlating Sr peak. The opposite is true for borehole ELF-395 and this marks the largest difference in Sr between the two boreholes.

Like ELF-395, Zr has a highly variable pattern of enrichment in ELF-393 (Fig. 4.5.2).. Zr shows more enrichment in the leuconorite HW unit compared to the FW unit (between 14 and 20 ppm versus 14 ppm, respectively). Likewise, the norite HW unit shows higher enrichment in Zr compared to the FW unit (between 20 and 26 ppm versus 12 ppm, respectively). The reef units show the highest degree of Zr concentration variability. The pegmatitic unit varies in concentration between 12 and 46 ppm while the underlying pyroxenite unit varies between 10 and 51 ppm.

Whole-rock trace elements versus MgO binary plots for ELF-395 are displayed in figure 4.5.3. Cu, Ni and Cr all show weak positive correlations (R^2 <0.4) with MgO. Anorthosites and leuconorites (i.e., plagioclase-rich rocks) plot in the low Cu, Ni and Cr versus low MgO fields (near the origin). Norite and chromitite lithologies plot in moderate MgO fields (approximately between 8 and 17 wt. %) versus low Cu, Ni and Cr fields (with the obvious exception of chromitite, which plots in the high Cr field). Pyroxenites mostly plot within high MgO (~ 22 to 24 wt. %) fields and show quite variable Cu and Ni concentration fields (between 20 and

2100 ppm and 540 and > 4100 ppm, respectively). Pyroxenites show relatively little Cr scatter ranging between 2300 and > 4500 ppm (excluding two outliers).

Incompatible elements such as Nb and Zr (Fig. 4.5.3) show a similar pattern when plotted against MgO. Both elements show moderately strong ($0.4 \geq R^2 < 0.7$) positive correlations with MgO. Anorthosites and leuconorites plot in low Nb – low MgO and low Zr – low MgO fields, respectively. Pyroxenites plot in high MgO fields and show variable Nb and Zr concentrations. Norite and chromitite lithologies plot as intermediates between these two lithological limits (both units showing relatively low concentrations of Nb and Zr).

Sr when plotted against MgO shows a very strong ($R^2>0.9$) negative correlation (Fig. 4.5.3). Anorthosites and leuconorites plot the in high Sr – low MgO fields while pyroxenites plot in low Sr – high MgO fields. Norite and chromitite both plot in moderate Sr – moderate MgO fields.

Binary plots for Ti versus MgO (Fig. 4.5.3) show a strong ($R^2=0.825$) positive correlation. Anorthosites plot in the low Ti – low MgO field (mostly between 240 and 600 ppm Ti). Norite plots in the moderate Ti – low to moderate MgO fields while chromitite plots in the moderate Ti – moderate MgO field. Pyroxenites plot in the high MgO field and show a variable Ti concentration field (ranging between approximately 1100 to 2700 ppm).

Other incompatible elements like Nd and Ce when plotted against MgO (Fig. 4.5.3) show weak ($R^2<0.4$) positive correlations. Both elements show a similar pattern, in which anorthosites and leuconorite plot in respective low Nd and Ce versus low MgO fields. The exception to this are two anorthosite outliers which belong to the anorthositic reef seam (being more enriched in Nd and Ce). Pyroxenites cluster in the low to moderate Nd (and Ce) – high MgO field. Norite and chromite occur as intermediates between the two extremes.

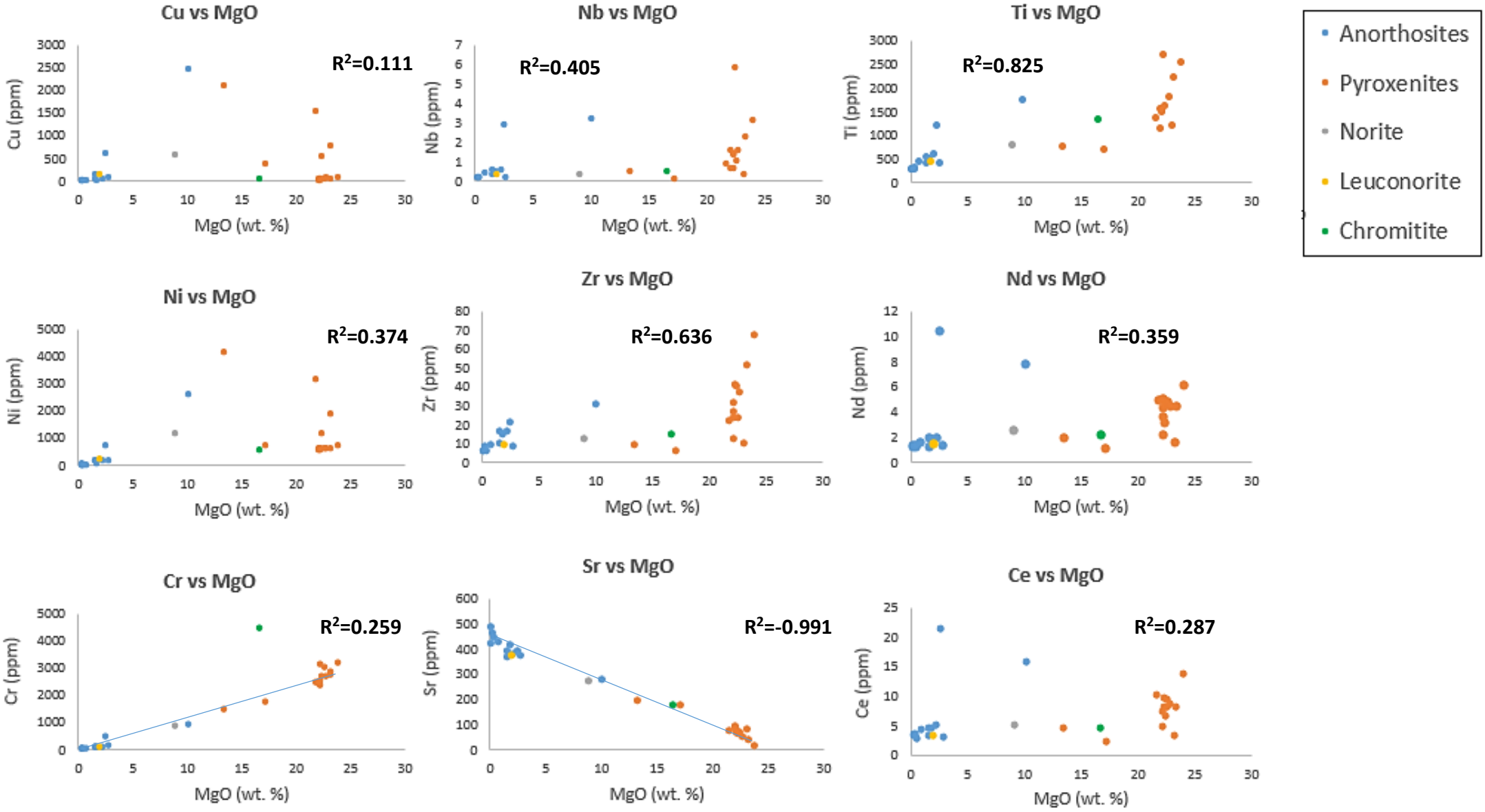

Figure 4.5.3. Whole-rock trace elements vs MgO binary plots for borehole ELF-395. The correlation coefficient (R^2) is given for each diagram.

Trace element binary plots for boreholes ELF-395 and ELF-393 are provided in figures 4.5.4 and 4.5.5, respectively. In borehole ELF-395, Cr shows weak positive correlations to Cu and Ni (R^2=0.037 and 0.294, respectively). Anorthosites and leuconorites plot in low Cr – low Cu and – low Ni fields. Outliers, belonging to the anorthositic seam, plot in higher Cr – higher Cu and Ni fields. Norites plots in low to moderate Cr – low to moderate Cu and Ni fields, respectively. Pyroxenites show some scatter but, typically, plot in high Cr – moderate Cu and Ni fields. Exceptions to this are samples belonging to, and spatially associated with, the upper peak (e.g., MR-10 and -11). Chromitite plots in the high Cr – low Cu and Ni fields, respectively. Cu versus Ni (Fig. 4.5.4) shows a strong positive correlation (R^2>0.9). Anorthosites plot near the origin of the diagram in fields of low Cu – low Ni. Outliers of anorthosite, correlating to the anorthosite seam, show higher concentrations of Cu and Ni.

When plotted against high field strength elements (HFSE) (Fig. 4.5.4) such as Zr, Ni and Cu show almost no correlation (R^2<0.1). Anorthosites, as well as leuconorite, norite and chromitite units generally plot in the low Ni/low Cu – low Zr fields. Pyroxenites show significant scatter, ranging from the high Ni and high Cu – low Zr fields to the low Ni and low Cu – high Zr fields, respectively.

When plotted against one another (e.g., niobium versus zirconium and hafnium versus thorium) (Fig. 4.5.4) the HFSE show strong (e.g., Nb versus Zr; R^2=0.732) to very strong (e.g., Hf versus Th; R^2=0.930) positive correlations. Similarly, incompatible rare earth elements (REE) when plotted against one another (e.g., Ce versus Nd and Ce versus Sm) show strong positive correlations (R^2>0.9) (Fig. 4.5.4).

Trace element binary plots from borehole ELF-393 (Fig. 4.5.5) show some similarities to ELF-395 (particularly with regard to correlation coefficients). Cr shows weak positive correlations to Cu and Ni (i.e., R^2<0.4). Anorthosites plot in the low Cu and low Ni versus low Cr fields. Leuconorites show more enrichment in Cr compared to the anorthosites (although Cu and Ni concentrations are similar). An exception to this is an outlier that plots in significantly higher Cr concentrations (sample ELF-393-20). Norites show high Cu and high Ni versus high Cr concentrations. Pyroxenite units plot in the low Cu/low Ni – high Cr fields while pegmatitic

pyroxenite units plot in the higher Cr concentration fields. Pegmatitic pyroxenite outliers (samples ELF-393-5 and -14) correlate to the upper Ni and Cu peaks within borehole ELF-393 and thus plot in the higher Cu and Ni concentrations fields.

Cu (Fig. 4.5.5) shows a strong positive correlation with Ni (R^2>0.9). Anorthosites, leuconorites and pyroxenites plot in the low Cu – low Ni fields. Norites plot in the high Cu - high Ni fields while pegmatitic pyroxenites show some scatter and plot in the low Cu – low Ni fields. Outliers (associated with the upper Cu and Ni peaks) show significantly more Cu and Ni enrichment.

Ni and Cu (Fig. 4.5.5) show weak correlations with HFSE ($R^2 \leq 0.1$). Anorthosites and leuconorites plot near the origin. Pyroxenites show some scatter and range from the low Cu/low Ni – low Zr fields to the low Cu/low Ni – high Zr fields, respectively. Likewise, norites range from the low Cu/low Ni – low Zr fields to the high Cu/high Ni – low Zr fields. Pegmatitic pyroxenites show the highest degree of scatter but typically plot in the low Cu/low Ni fields with variable Zr concentration ranges. Outliers, corresponding to the upper Cu and Ni peaks, show significantly more Cu and Ni enrichment.

When plotted against one another (e.g., Nb versus Zr and Th versus Hf) (Fig. 4.5.5), the HFSE show strong ($R^2 \geq 0.8$) positive correlations. Similarly, incompatible REE when plotted against one another (e.g., Ce versus Nd and Ce versus Sm) show strong positive correlations (R^2>0.9) (Fig. 4.5.5).

Chondrite-normalised rare earth element plots for boreholes ELF-395 and -393 are provided in figures 4.5.7 and 4.5.8, respectively. Eu-anomalies plotted against stratigraphic depth for boreholes ELF-395 and -393 are shown in figure 4.5.6. Borehole ELF-395 (Fig. 4.5.7) shows the typical fractionation of light rare earth elements (LREE) compared to heavy rare earth elements (HREE). This general enrichment of LREE relative to HREE can be expressed by $(La/Lu)_N$ ratios which range between 9.56 - 36.23, 2.19 - 19.03, 2.12 - 9.80 and 3.28 for the anorthosite, norite/leuconorite, pyroxenite and chromitite units, respectively.

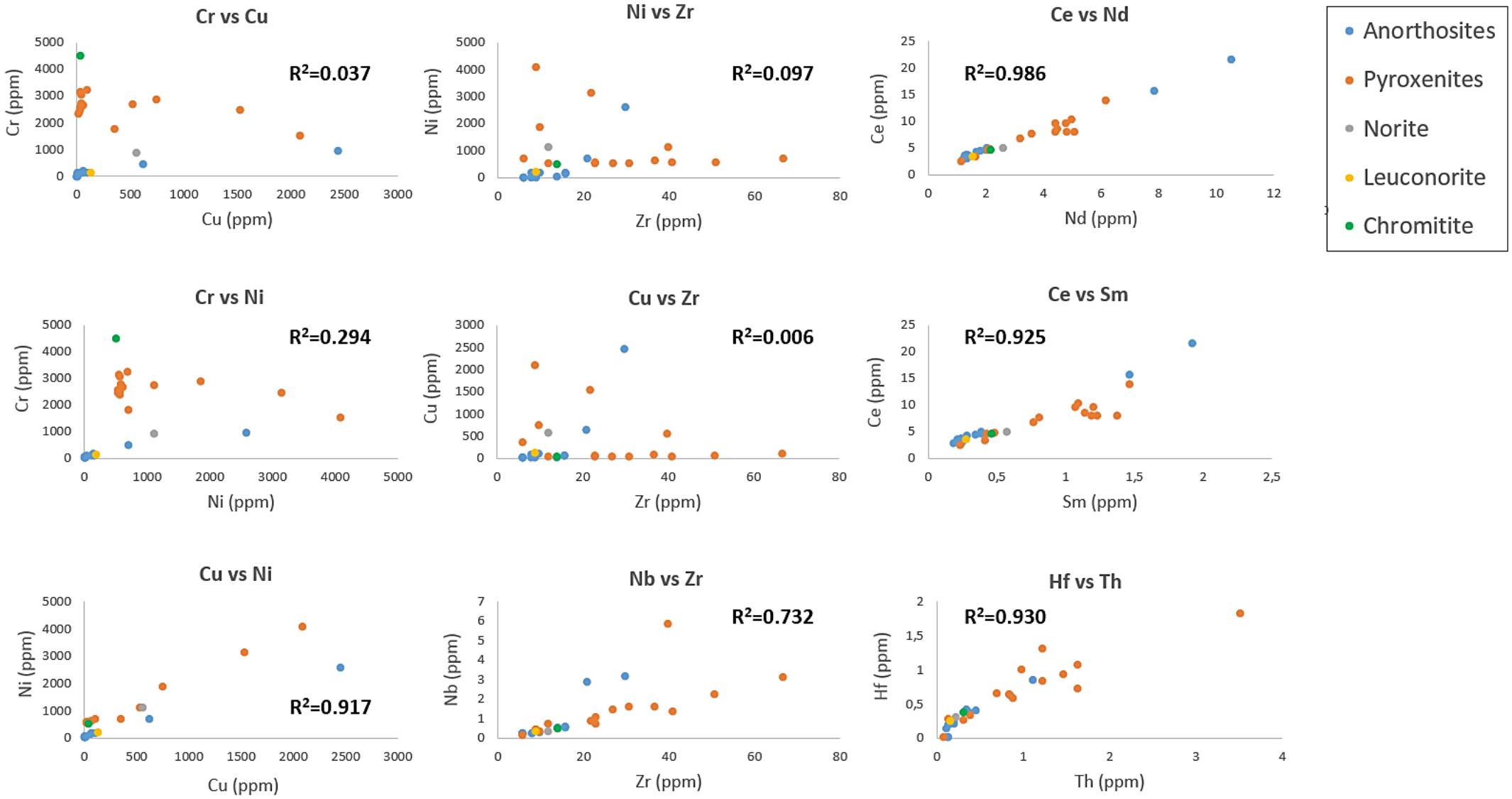

Figure 4.5.4. Whole-rock trace element binary plots for borehole ELF-395. The correlation coefficient (R^2) is given for each diagram.

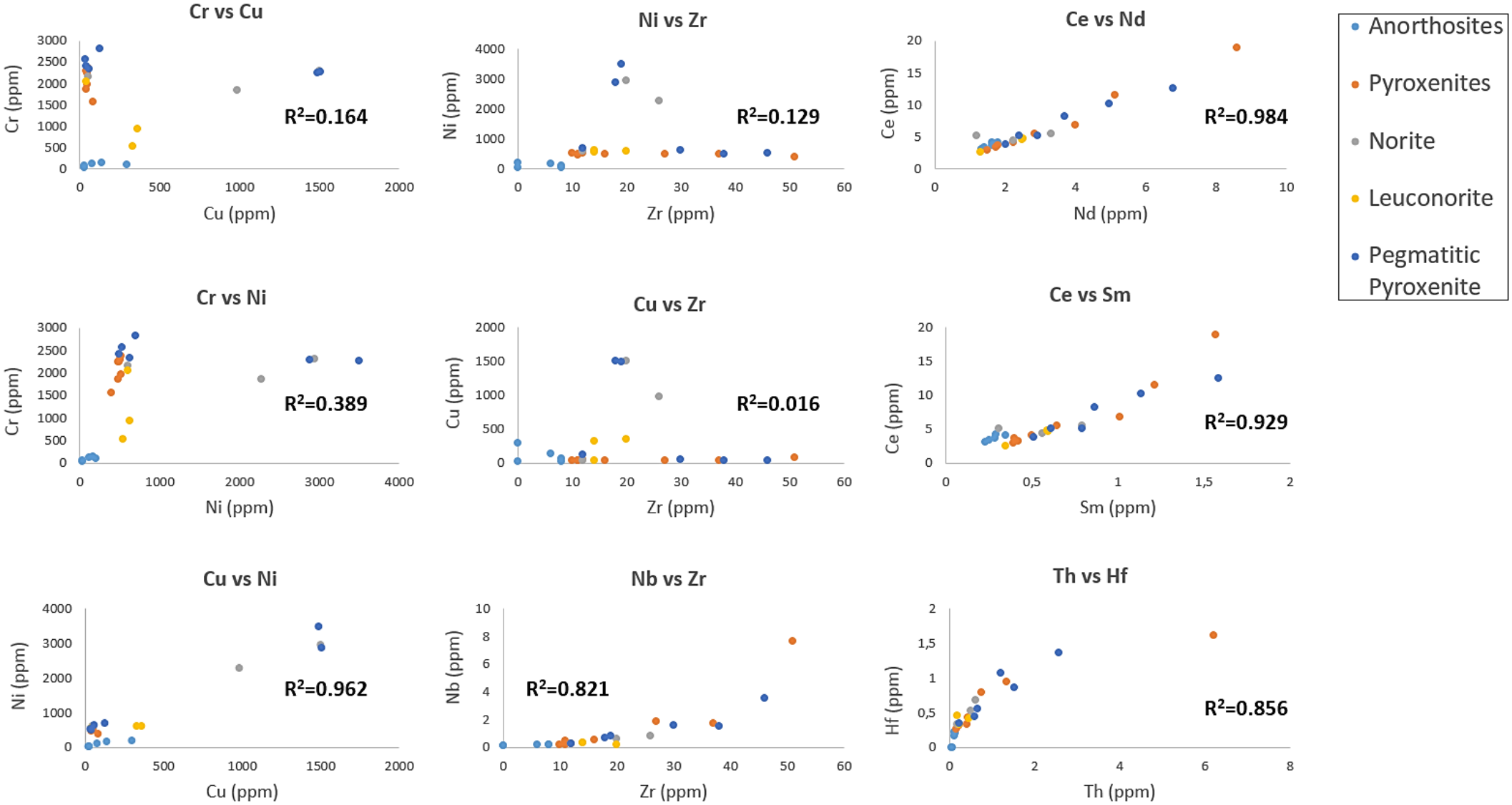

Figure 4.5.5. Whole-rock trace element binary plots for borehole ELF-393. The correlation coefficient (R^2) is given for each diagram.

LREE ratios indicate moderate enrichment of the LREE in all units (although the anorthositic units record the highest values), e.g., $(La/Sm)_N$ values between 3.87 - 6.21, 2.82 - 4.36, 1.65 - 3.49 and 3.11 for the anorthosite, norite/leuconorite, pyroxenite and chromitite units, respectively. $(Gd/Yb)_N$ ratios (i.e., HREE ratios) for the anorthosite, norite/leuconorite, pyroxenite and chromitite units range between 1.44 - 3.31, 0.63 - 3.22, 0.76 - 2.14 and 0.89, respectively. Sample MR-09A (i.e., anorthosite), seen in the norite/leuconorite plot, shows a negative slope from Gd to Lu which explains the maximum $(La/Lu)_N$ and $(Gd/Yb)_N$ values observed for the norite/leuconorite unit (i.e., 19.03 and 3.22, respectively). Positive Eu-anomalies, of various magnitudes, were identified in all units with the exception of the pyroxenite unit, anorthositic reef and the chromitite unit (i.e., below 1) (Fig. 4.5.6). Samples MR-08 and MR-10 are the only pyroxenite samples which showed positive Eu-anomalies (1.66 and 1.64, respectively). A maximum positive Eu-anomaly of 3.41 was recorded in the anorthosite hangingwall (sample MR-03).

Borehole ELF-393 (Fig. 4.5.8) shows close similarities to borehole ELF-395. However, the absence of chromitite and the presence of pegmatitic pyroxenite in ELF-393 (unlike in ELF-395) means that these two units cannot be fully compared across drillcores. Furthermore, differences between the two boreholes are demonstrated by the superior enrichment of REE in the norite/leuconorite units of ELF-395 versus ELF-393 (i.e., between 1 and 100 times C1-chondrite versus between 1 and 10 times C1-chondrite, respectively).

Like ELF-395, ELF-393 shows the fractionation of LREE over HREE. $(La/Lu)_N$ ratios range between 11.59 - 21.00, 1.60 - 4.08, 1.70 - 3.20 and 1.87 - 4.09 for the anorthosite, norite/leuconorite, pegmatitic pyroxenite and pyroxenite units, respectively. LREE ratios such as $(La/Sm)_N$ range between 4.03 - 5.32, 1.95 - 2.54, 1.78 - 3.15 and 1.97 - 3.26 for the anorthosite, norite/leuconorite, pegmatitic pyroxenite and pyroxenite units, respectively and suggest a moderate enrichment of the LREE in all units.

$(Gd/Yb)_N$ ratios (i.e., HREE ratios) for the anorthosite, norite/leuconorite, pyroxenite and chromitite units range between 1.49 - 2.44, 0.68 - 1.32, 0.76 - 1.14 and 0.64 - 1.42, respectively.

$(Gd/Yb)_N$ ratios show discrepancies within the norite/leuconorite unit in which samples ELF-393-03 and -04A are higher (1.32 and 1.11, respectively) compared to samples ELF-393-4B, -4C, -19 and -20 (0.82, 0.75, 0.68 and 0.71, respectively). Positive Eu-anomalies were recorded in the anorthositic and leuconoritic hangingwall and footwall units (Fig. 4.5.6). However, the noritic hangingwall unit recorded negative Eu-anomalies while the footwall unit showed no Eu-anomaly (sample ELF-393-19) to a marginally positive Eu anomaly (samples ELF-393-20). The pegmatitic pyroxenite and pyroxenite reef units showed negative Eu-anomalies (with the exception of samples ELF-393-18 and -17, which show no Eu-anomaly). The footwall anorthosite unit recorded a noticeably more positive Eu-anomaly than the hangingwall unit (with a maximum of 4.8).

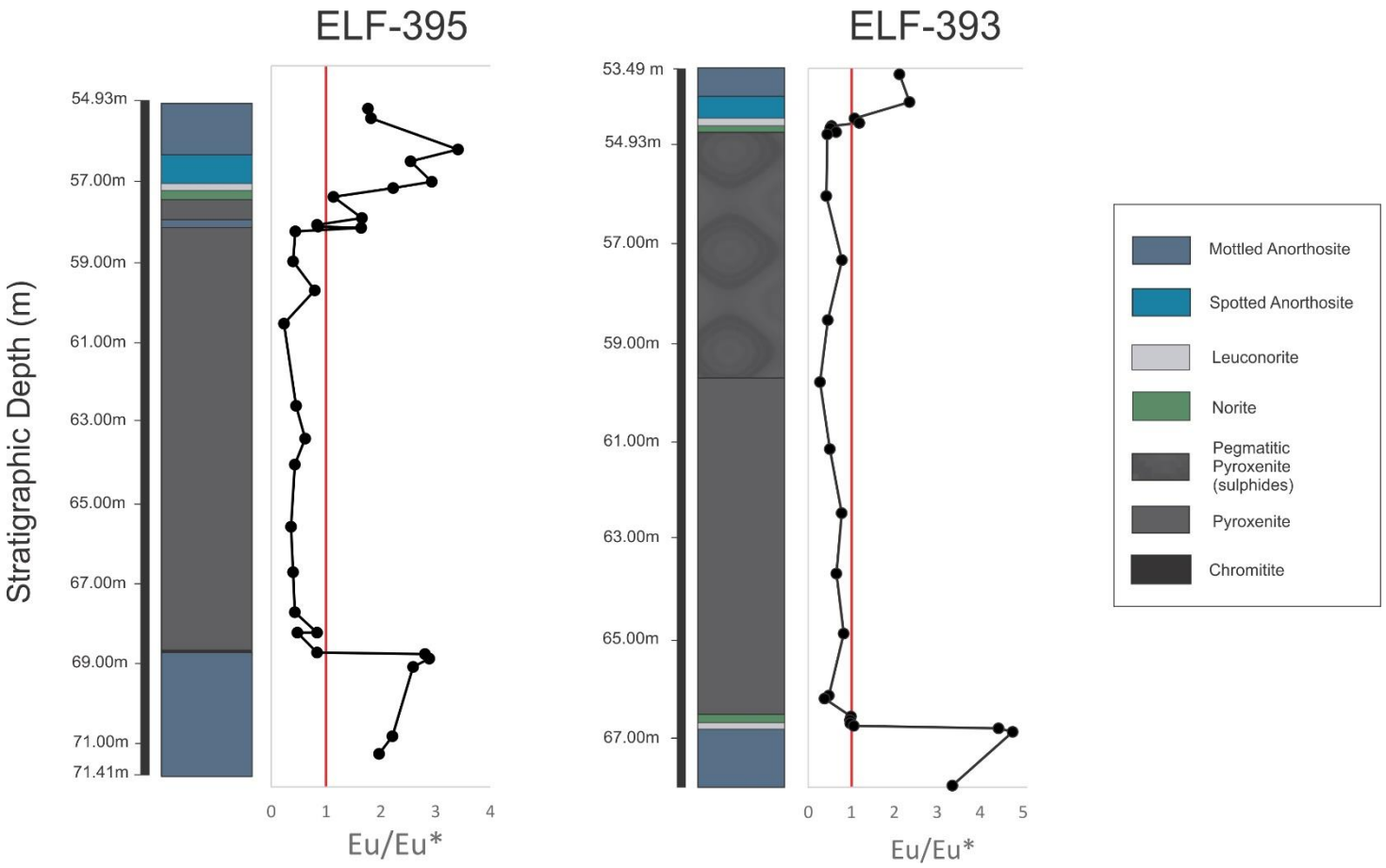

Figure 4.5.6. Whole-rock normalised Eu-anomalies for boreholes ELF-395 and -393. Points left of the red line (i.e., below 1) represent negative anomalies while points right of the red line (i.e., above 1) represent positive anomalies. Eu normalised to C1-Chondrite after Anders and Grevesse (1989).

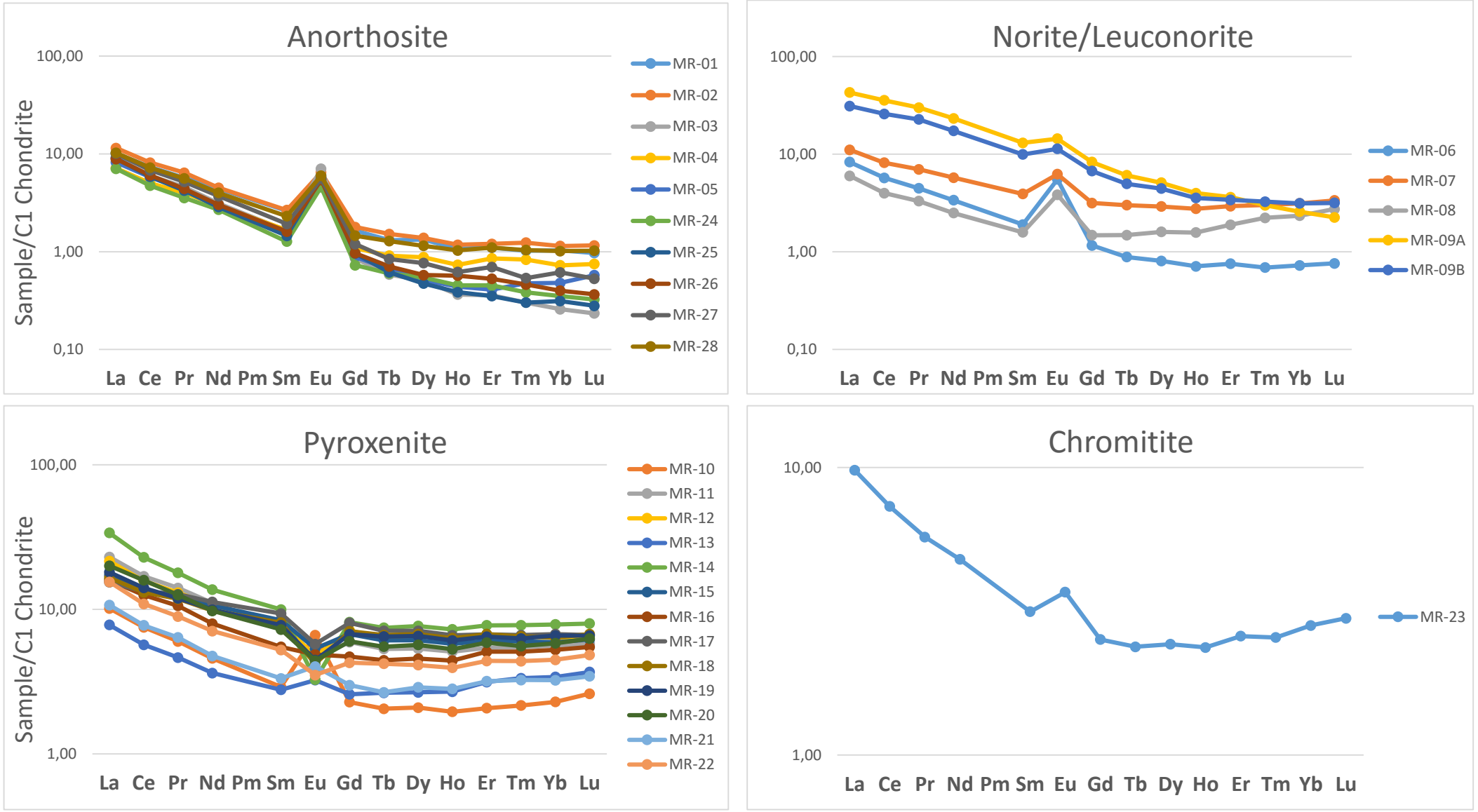

Figure 4.5.7. Whole-rock REE plots for the anorthosite, leuconorite/norite, pyroxenite and chromitite units of borehole ELF-395. Note samples MR-09A and MR-09B (i.e., anorthosites) have been included in the norite/leuconorite plot because of similarities in enrichment and pattern. Plots are normalised to C1-Chondrite after Anders and Grevesse (1989).

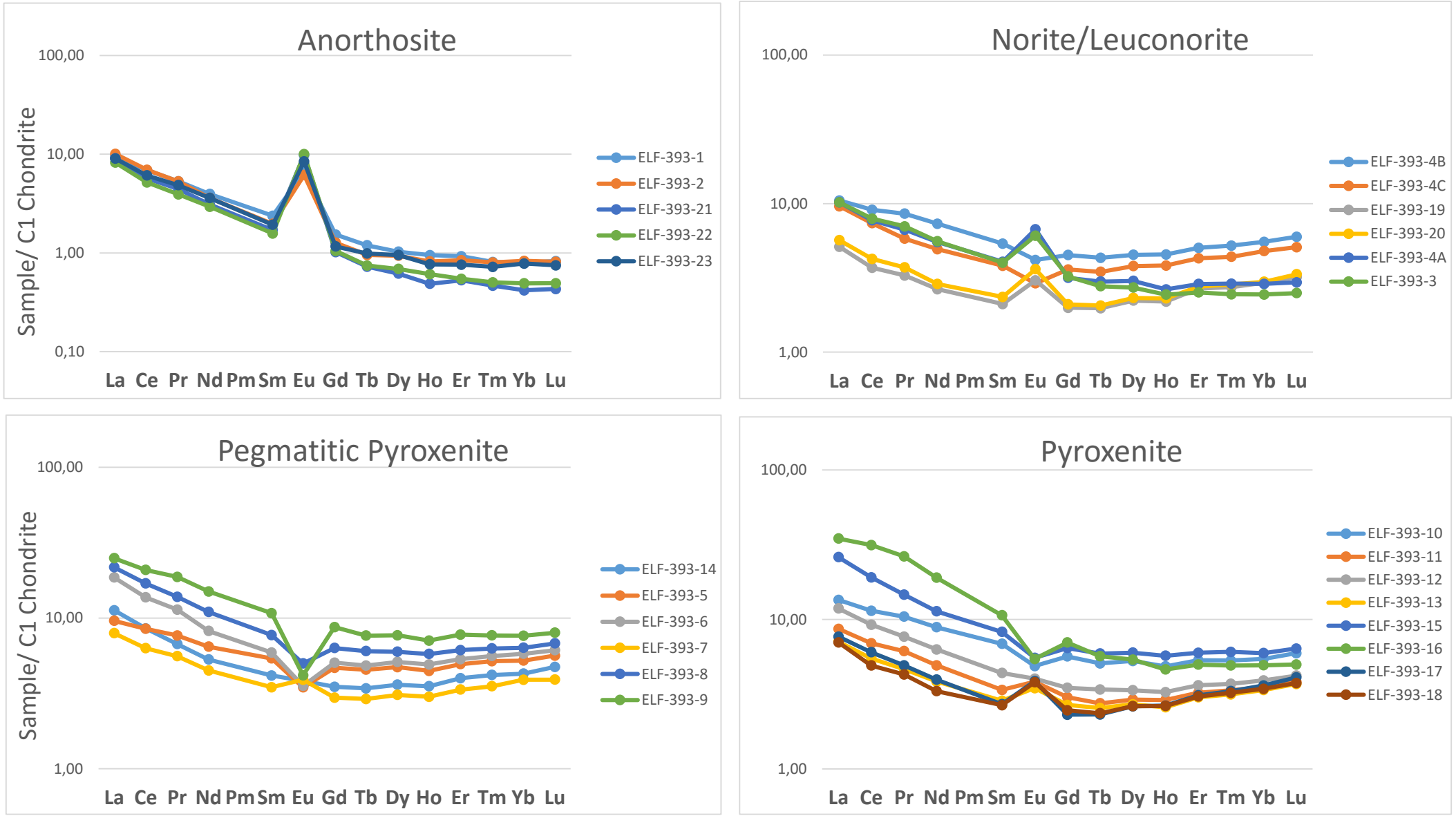

Figure 4.5.8. Whole-rock REE plots for the anorthosite, leuconorite/norite, pegmatitic pyroxenite and pyroxenite units of borehole ELF-393. Plots are normalised to C1-Chondrite after Anders and Grevesse (1989).

4.6. Whole-rock Platinum-group Element Geochemistry

Whole-rock PGE and Au abundance data, analysed by fire assay, are presented in Table 4.6.1 and in Appendix 9. For the sampling strategy see Chapter 3.2.3. As mentioned in Chapter 1.1.2, PGE are generally subdivided into 2 major groups on the basis of their refractory and geochemical properties: Pd-group PGE (i.e., PPGE; Pd, Pt and Rh) and Ir-group PGE (i.e., IPGE; Ru, Os and Ir) (Barnes *et al*., 1985). The data has been interpreted from the top to the bottom of the sequence, i.e., down the stratigraphy.

In the wide-reef Merensky (i.e., borehole ELF-395) all PGE show two significant peaks within the sampled 16.48 metre stratigraphic succession (Fig. 4.6.1). The first PGE peak in the stratigraphic succession (i.e., the peak that occurs at a lesser stratigraphic depth) is recorded at the base of the anorthositic seam, and in contact with the underlying pyroxenitic unit within the reef (58.04 - 58.13 metres). An enrichment of PGE occurs underlying this peak for approximately 2 metres until a depth of 60.43 metres (still within the pyroxenitic reef). Thereafter, concentrations of PGE remain relatively low through the pyroxenite until the sharp transition into chromitite (68.64 metres) where a high concentration spike in PGE is observed. Thereafter, PGE concentration levels remain low throughout the underlying footwall rocks. The superior PGE enrichment of the stratigraphically lower peak compared to the upper peak is known as a bottom-loaded PGE mineralisation style (Viljoen, 1999).

Concentration profiles for Pt, Pd, Rh, Ru, Ir, Os and Au are shown in figure 4.6.2. Os and Ir are the least enriched of all the PGE. Concentrations in the stratigraphically higher peak recorded maximum values of 168 ppb and 69 ppb, respectively, while the lower peak recorded concentrations of 461 ppb and 435 ppb, respectively. Rh and Ru show maximum PGE concentrations of 160 ppb and 527 ppb in the upper peak and 1292 ppb and 3803 ppb in the lower peak, respectively. Pd, in the upper peak, has a concentration maximum of 3340 ppb while in the lower peak it reaches 2083 ppb. This indicates that the PGE mineralisation style of Pd is bottom-loaded, unlike all other PGE which show a top-loaded mineralisation style. Pt is the most enriched PGE in the stratigraphic succession and reaches concentrations of 2885 ppb in the upper peak and 10616 ppb in the lower peak.

Table 4.6.1. Whole-rock PGE (+Au) abundances for borehole ELF-395 (representing the Merensky wide-reef facies). All data is presented in ppb and where no value is given represents data below the detection limit. * The sample length corresponds to the core length that was sampled. Abbreviations follow those defined in Table 3.1.1.

Sample	Lithology	Stratigraphic Depth (m)	*Sample Length (cm)	Ru (ppb)	Rh (ppb)	Pd (ppb)	Os (ppb)	Ir (ppb)	Pt (ppb)	Au (ppb)
MR-01	AnMo	55.07	2.00	2.18	1.77	4.27	2.21	0.61	21.99	12.78
MR-02	AnMo	55.31	2.00	0.39	0.40	5.18	0.09	0.19	4.33	19.00
MR-03	AnSp	56.09	2.00	2.13	1.34	2.00	0.82	0.37	28.74	4.19
MR-04	AnSp	56.38	2.00	1.21	0.53	5.69	0.25	0.21	10.13	9.50
MR-05	AnSp	56.89	2.00	2.60	2.10	6.19	1.04	0.58	39.31	4.12
MR-06	LuNo	57.05	2.00	0.62	0.36	5.80	0.17	0.17	9.70	18.40
MR-07	No	57.27	2.00	6.62	2.38	29.45	0.98	1.49	65.59	96.90
MR-08	Px	57.80	2.00	34.41	19.86	109.07	5.31	5.45	161.58	39.95
MR-09a	An	57.97	2.00	27.68	9.23	276.28	6.60	4.19	343.29	173.03
MR-09b	An	58.01	2.00	129.16	43.98	1158.56	34.89	19.20	2809.13	221.52
MR-10	Px	58.04	2.00	422.01	146.88	3339.70	168.12	65.25	2297.29	92.75
MR-11	Px	58.13	2.00	526.66	159.62	1690.11	87.77	69.47	2885.38	289.45
MR-12	Px	58.88	2.00	143.72	41.79	411.27	22.79	20.25	494.97	179.98
MR-13	Px	59.60	2.00	60.22	40.26	468.69	9.05	10.45	587.57	290.87
MR-14	Px	60.43	2.00	4.02	4.30	33.04	0.82	0.99	138.11	29.84
MR-15	Px	62.48	2.00	1.98	0.91	11.47	0.58	0.35	26.79	4.50
MR-16	Px	63.30	2.00	2.21	0.96	2.40	0.35	0.34	9.69	2.44
MR-17	Px	63.95	2.00	2.47	1.07	2.53	0.33	0.42	8.74	3.45
MR-18	Px	65.50	2.00	7.11	0.98	2.79	0.97	0.59	10.08	1.95
MR-19	Px	66.63	2.00	7.84	4.32	3.90	7.07	1.40	28.68	1.99
MR-20	Px	67.63	2.00	13.74	2.17	3.68	1.51	1.21	20.56	5.69
MR-21	Px	68.14	2.00	13.07	1.64	15.66	1.62	1.01	19.77	3.91
MR-22	Px	68.61	2.00	21.02	5.25	55.05	3.23	2.36	64.64	6.21
MR-23	Chr	68.64	2.00	3803.03	1291.91	2082.71	460.71	434.93	10615.92	14.61
MR-24	AnMo	68.68	2.00	2.85	0.12	3.36	0.32	0.34	1.13	0.86
MR-25	AnMo	68.79	2.00	1.85	0.19	0.51	0.14	0.19	1.07	1.04
MR-26	AnMo	69.00	2.00	1.65	1.47	0.40	0.35	0.40	6.26	<LOD
MR-27	AnMo	70.73	2.00	0.81	0.46	0.72	0.23	0.28	1.91	1.49
MR-28	AnMo	71.17	2.00	2.01	0.17	1.26	0.14	0.22	0.96	<LOD

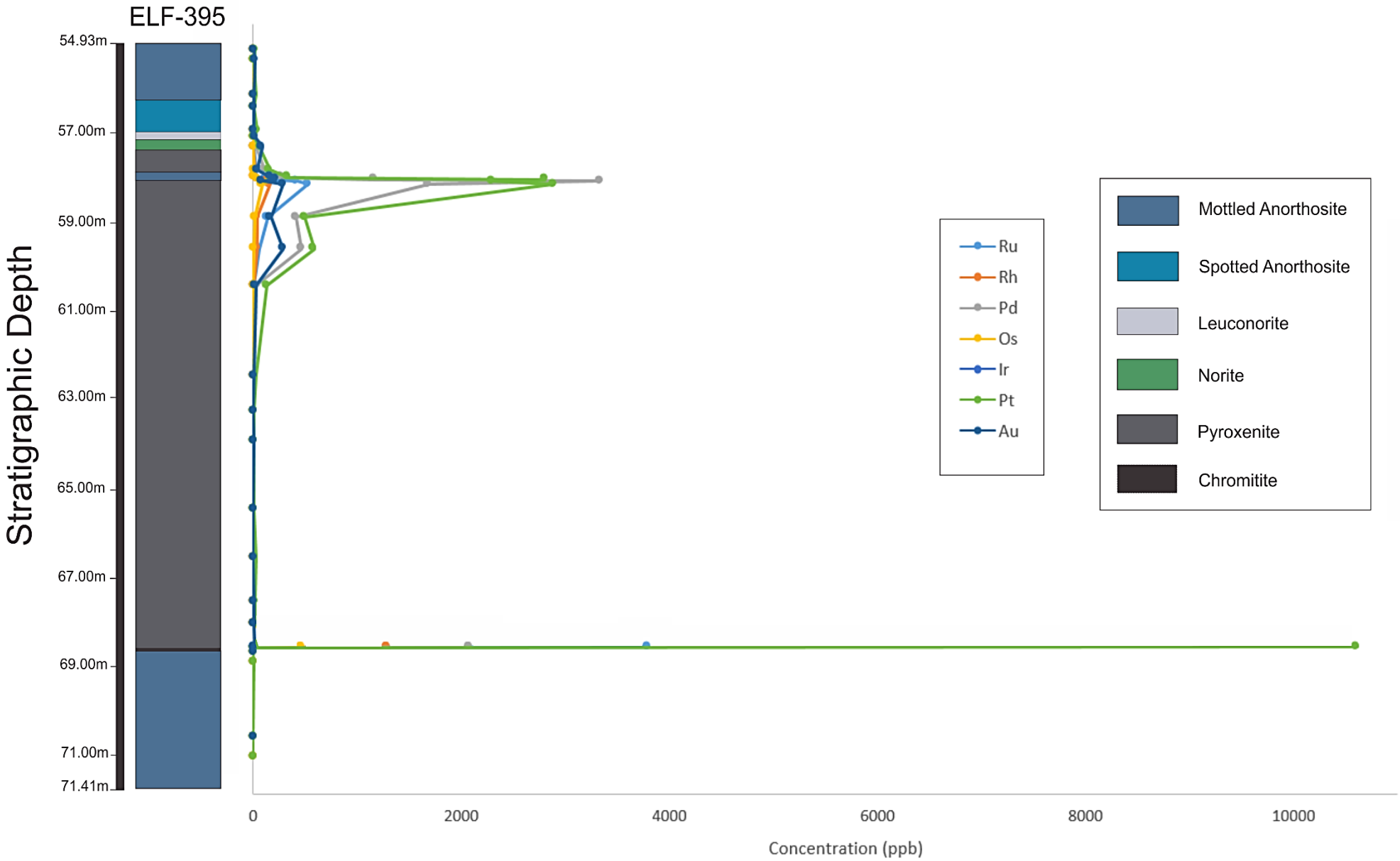

Figure 4.6.1. Concentration profile for all PGE (+Au) within borehole ELF-395. Units for all PGE are given in ppb. Note the two concentration peaks within the pyroxenitic reef (at the base of the anorthosite seam) and in the chromitite stringer (overlying the footwall rocks).

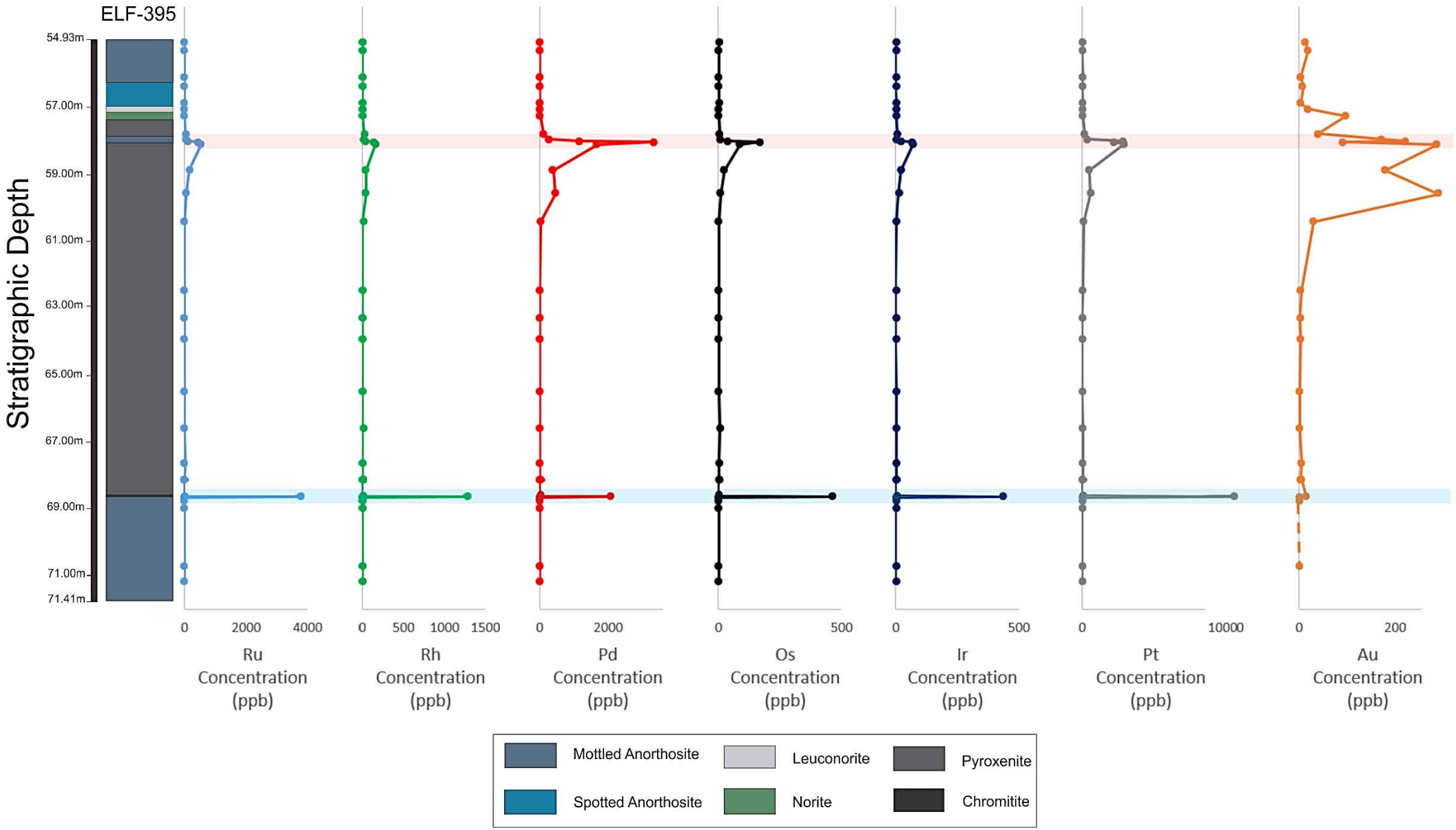

Figure 4.6.2. Whole-rock PGE (+Au) stratigraphic concentration profiles for borehole ELF-395 (representing Merensky wide-reef facies). Note the red highlighted area corresponds to the base of the anorthositic seam in the pyroxenitic reef, while the blue highlighted area corresponds to the chromitite stringer at the base of the reef.

Au is far more variable than the PGE in borehole ELF-395. For example, like Pd, Au has a top-loaded mineralisation style, however, further enrichments and depletions are observed adjacent to the stratigraphically higher peak. The maximum concentration recorded in the upper peak is 289 ppb while the lower peak recorded a concentration of 15 ppb.

Total PGE concentrations versus stratigraphic depth are shown in figure 4.6.3. Total PGE concentrations remain low in the anorthositic hangingwall (~ 408 ppb) and footwall (4.8 - 11 ppb) rocks to the Merensky Reef. Leuconorite and norite units record total PGE concentrations of 35 ppb and 203 ppb, respectively. These units represent the start to the first stratigraphic peak (i.e., maximum concentration of 6532 ppb) which occurs at the base of the anorthositic seam and in contact with the underlying pyroxenite unit (as mentioned above). Total PGE concentration levels remain markedly high, for approximately two metres, following the stratigraphically higher peak with recorded values of 1467 ppb total PGE. The pyroxenite unit shows total average PGE enrichment levels of 71 ppb. The largest concentration of total PGE is recorded within the chromitite unit which shows levels of enrichment up to a maximum of 18704 ppb total PGE.

Cu/Pd, Pt/Pd, Pd/Ir and Pt+Pd/IPGE ratios for borehole ELF-395 are shown in figure 4.6.4. In figure 4.6.4, high Cu/Pd ratios are recorded in the Merensky Reef hangingwall units, in which the hangingwall anorthosite typically ranges between 7757 to 17552 while the leuconorite and norite units record Cu/Pd values of 23508 and 18890, respectively. At the first appearance of pyroxenite in the reef, Cu/Pd values decrease to, and range between, 628 and 4386. Cu/Pd ratios increase midway through the reef recording values between 16442 and 18202 before dropping in the chromitite unit (~ 19). A sharp increase in Cu/Pd ratios follows in the underlying anorthositic footwall (10577 to 18469).

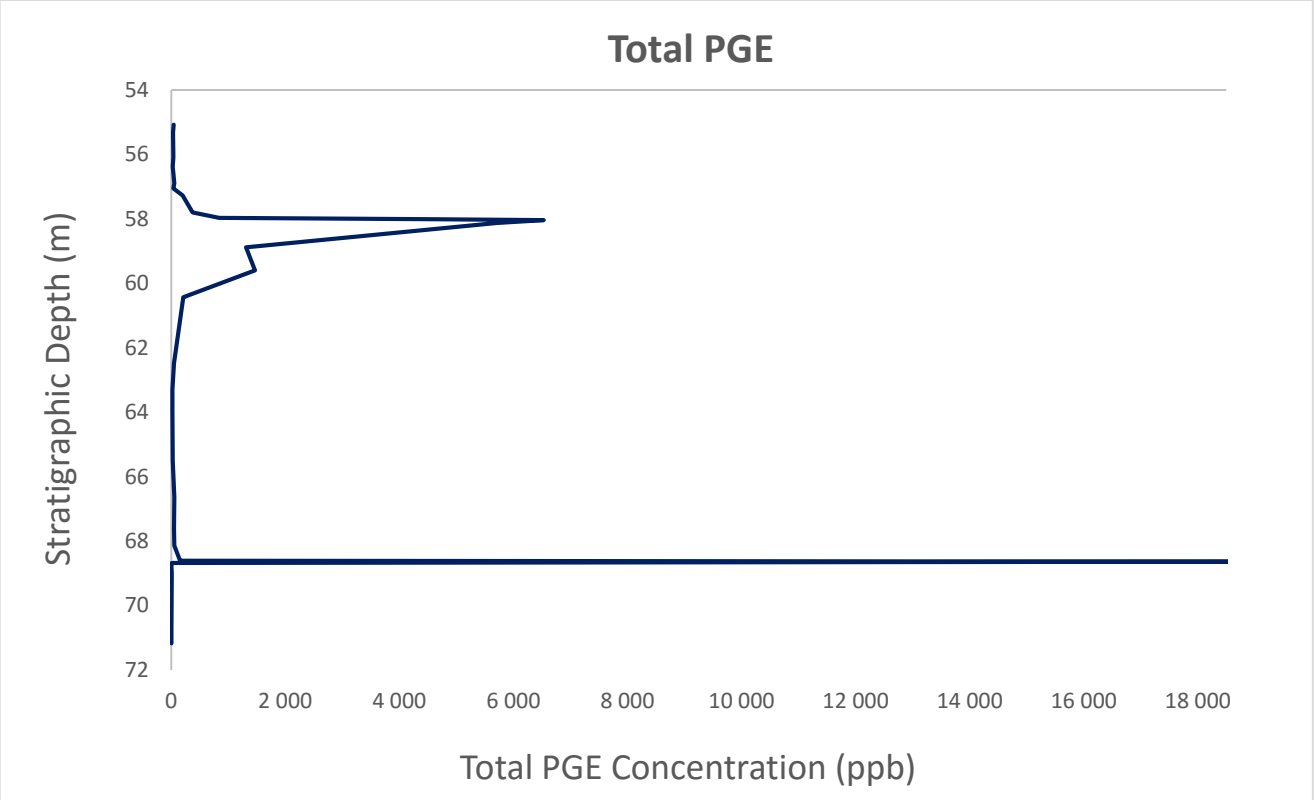

Figure 4.6.3. Total PGE concentrations versus stratigraphic depth in borehole ELF-395. Note the two peaks pertaining to the pyroxenitic unit at the base of the anorthosite seam (58.04 metres; 6532 ppb) and the chromitite stringer at the base of the pyroxenitic reef (68.64 metres; 18704 ppb). Underlying the upper peak, a sustained enrichment in PGE (for about 2 metres) is observable. Units are given in ppb.

Pd/Ir ratios (Fig. 4.6.4) show high variability in the anorthositic hangingwall unit (5.4 to 28) compared to the anorthositic footwall unit (1.0 to 9.9). Within the reef, Pd/Ir ratios show a progressive decrease with depth and values range between 2.8 to 66. The chromitite unit in borehole ELF-395, which correlates with the occurrence of the stratigraphically lower PGE peak, has a recorded Pd/Ir value of 4.8.

Pt+Pd/IPGE ratios (Fig. 4.6.4), like Pd/Ir, show high variability in the anorthositic hangingwall unit (ranging between 5.2 and 14.0) compared to the anorthositic footwall unit (ranging between 0.73 and 2.8). Pt+Pd/IPGE ratios in the pyroxenitic reef can be subdivided into two major sections: 1) the stratigraphically higher half of the reef shows an enrichment in Pt+Pd/IPGE (with a maximum value of 29.4) and 2) the stratigraphically lower half of the reef

is relatively uniform where values range between 1.5 and 4.5. Underlying the reef, the chromitite unit shows a low recorded Pt+Pd/IPGE value of 2.7.

Whole-rock PGE (+Au, Cu and Ni) binary plots for borehole ELF-395 are provided in figure 4.6.5. Correlation coefficients for all PGE (+Au, Cu, Ni, Cr and S) are shown in Table 4.6.2. Os, Ir, Ru, Rh and Pt all correlate well with one another (e.g. R^2>0.960). This is particularly interesting given that Os, Ir and Ru are part of the IPGE and Rh and Pt are part of the PPGE. Pd shows only a moderately strong correlation with Pt (R^2=0.700) and Os (R^2=0.741) and even poorer correlations against Ir, Ru and Rh (R^2=0.560 - 0.600). However, Pd is well correlated with S (R^2=0.820) and Ni (R^2=0.812) and moderately to well correlated with Cu (R^2=0.729). Au shows extremely poor correlations with all IPGE (+Rh) (R^2<0.100), a very poor correlation with Pt (R^2=0.208), a poor correlation with Pd (R^2=0.435) and strong correlations with Cu and Ni (R^2 values of 0.740 and 0.719, respectively). S is well correlated with Pd, as mentioned above, and with Ni (R^2=0.820) and shows a strong correlation with Cu (R^2=0.739). Cu and Ni, as expected, show very strong correlations with each other (R^2=0.917). Cr is only moderately correlated with all IPGE (as well as Rh and Pt) with R^2 values ≥ 0.400. However, Pd shows an even poorer correlation with Cr (R^2=0.275). These whole-rock correlation coefficients are very similar to the whole-rock PGE correlation coefficients reported by Barnes and Maier (2002a), which include similar IPGE-Rh-Pt and S-Pd behaviour.

Figure 4.6.6 illustrates logarithmic-scale plots of PGE concentrations in borehole ELF-395 to highlight the behaviour of PGE and Au in the MR (specifically in the upper and low PGE peaks). The upper and lower PGE peaks, as illustrated on the diagrams, correlate with increases in both IPGE and PPGE. Furthermore, depletions in all PGE are also observed in figure 4.6.6, particularly underlying the lower peak, and as a series of depletions (troughs) and enrichments (peaks) overlying the upper peak. The same observations were made in borehole ELF-393, which suggest this may be a common feature in Merensky Reef, although this is yet to be validated in other reef facies (such as thin reef facies).

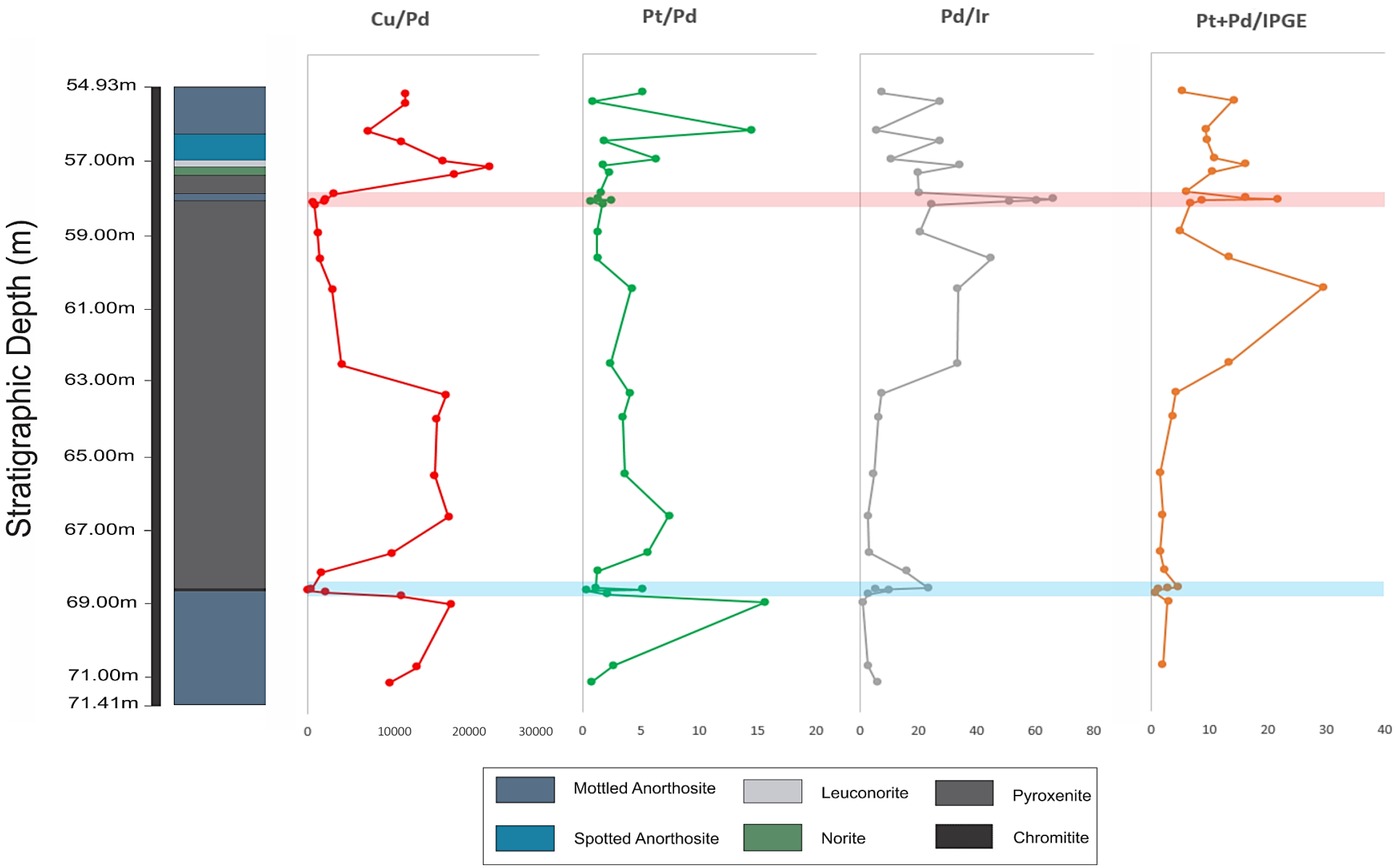

Figure 4.6.4. Concentration ratio profiles for PGE (+Cu) for borehole ELF-395. Note the two peaks pertaining to the pyroxenitic unit at the base of an anorthositic seam (red highlighted area) and the chromitite stringer at the base of the pyroxenitic reef (blue highlighted area). Units are given in ppb.

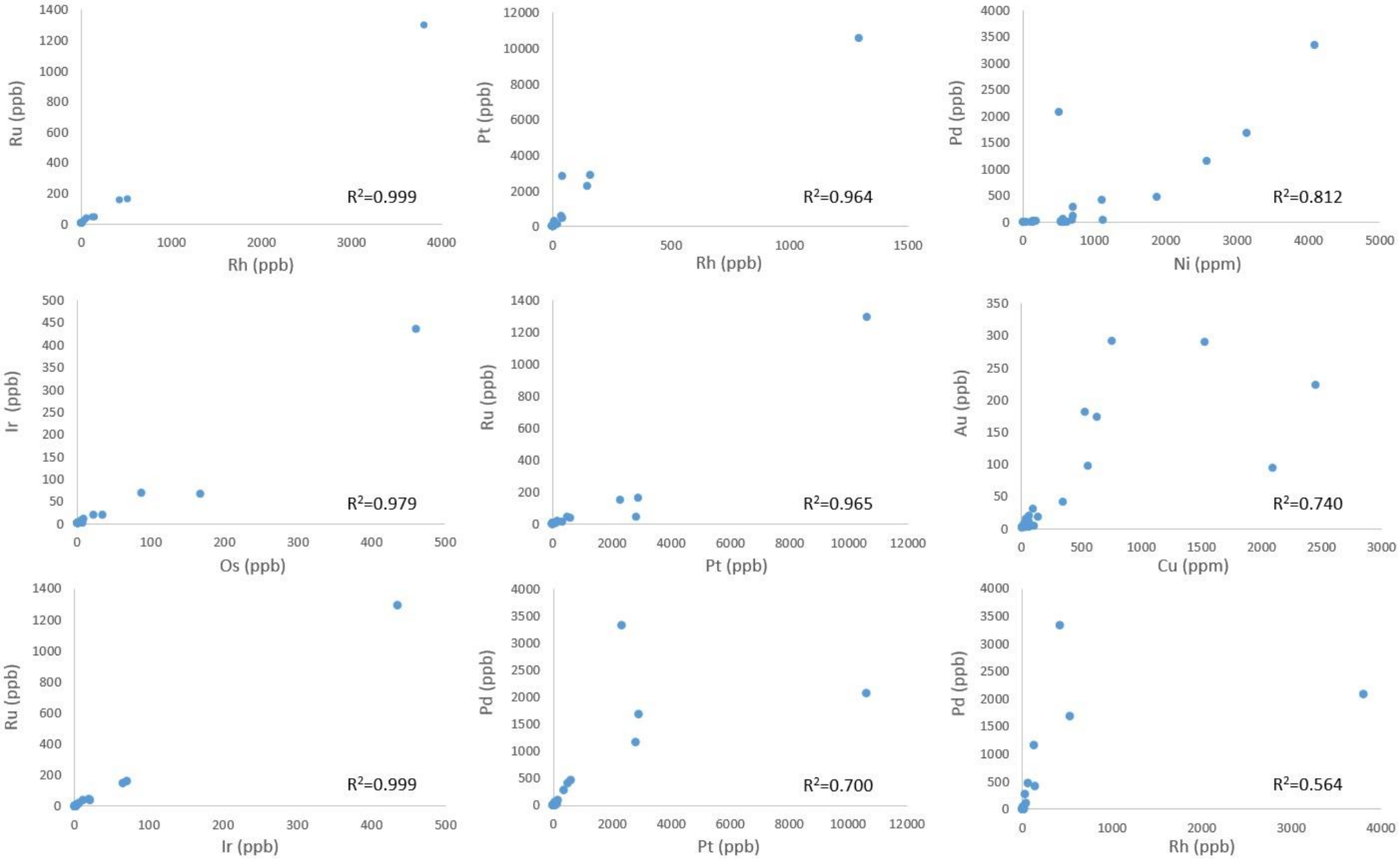

Figure 4.6.5. Whole-rock PGE (+Au, Cu and Ni) binary plots for borehole ELF-395. The correlation coefficient (R^2) for each diagram is given.

Table 4.6.2. Correlation coefficients for whole-rock PGE (+Au, Cu, Ni, Cr and S) from borehole ELF-395. Units represented in R^2 values.

	Os	*Ir*	*Ru*	*Rh*	*Pt*	*Pd*	*Au*	*Cu*	*Ni*	*S*	*Cr*
Os	1										
Ir	0.979	1									
Ru	0.970	0.999	1								
Rh	0.970	0.999	1.000	1							
Pt	0.969	0.972	0.965	0.964	1						
Pd	0.741	0.601	0.566	0.564	0.700	1					
Au	0.092	0.053	0.028	0.027	0.208	0.435	1				
Cu	0.213	0.079	0.043	0.041	0.288	0.729	0.740	1			
Ni	0.294	0.145	0.104	0.102	0.311	0.812	0.719	0.917	1		
S	0.299	0.104	0.063	0.064	0.207	0.820	0.333	0.739	0.820	1	
Cr	0.432	0.450	0.448	0.448	0.433	0.275	0.167	0.037	0.294	0.006	1

As previously mentioned, it has been shown that Rh and Pt behave surprisingly similarly to the IPGE (Ir, Os and Ru). However, Pd tends to behave in an opposite manner to the IPGE (+Rh and Pt). This is particularly true in the overlying rocks to upper PGE peak in which various depletions and peaks record this trend (Fig. 4.6.6). Like Pd, Au behaves variably and doesn't track any of the PGE where all PGE peak together. However, Au does show interesting enrichment associations with certain PGE (for example Au-Pd, Au-Pt-Pd-Os, Au-Pt-It-Ru-Rh, Au-Ru and Au-Ir-Ru-Rh-Pd peaks).

Although Rh and Pt behave more similarly to the IPGE than to Pd throughout most of the rock, classical PPGE peaks (Pd, Rh and Pt) also occur in which the PPGE are enriched and the IPGE are depleted. However, no instances of IPGE peaks were found to occur in borehole ELF-395, which were identified in borehole ELF-393.

Primitive mantle normalized PGE (+Au, Cu and Ni) plots are shown in figure 4.6.7. Primitive mantle normalization values (Table 4.6.3) are after Barnes and Maier (1999). All elements are presented in order of increasing chalcophile character (Wilson and Chunnett, 2006).

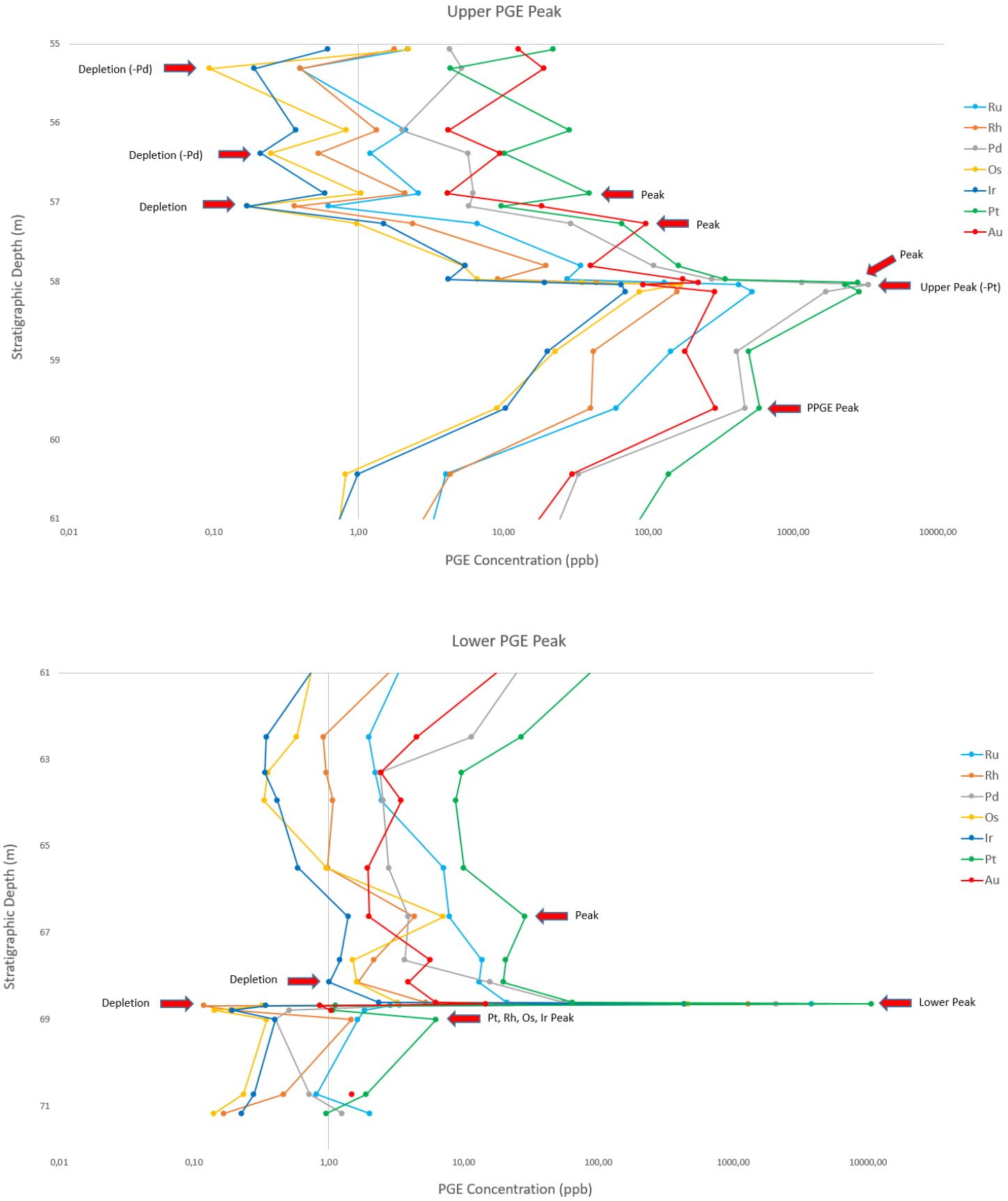

Figure 4.6.6. Upper and lower PGE peaks observed in the pyroxenite reef and in the chromitite stringer for borehole ELF-395. Note areas of enrichment (peaks) and depletions, as well as the occurrences of PPGE and IPGE peaks. It is also important to note the variability observed in Au. Units are given in ppb.

Table 4.6.3. Primitive mantle normalisation values for PGE, Au, Ni and Cu (after Barnes and Maier, 1999). *Ni and Cu have concentration units in ppm.

Element	Concentration (ppb)
*Ni	2000
Os	3.4
Ir	3.4
Ru	5
Rh	0.95
Pt	7
Pd	3.97
Au	0.99
*Cu	28

A primitive mantle normalized plot for the anorthosite unit (Fig. 4.6.7) (comprising both hangingwall and footwall units) shows the least amount of PGE (+Au, Ni and Cu) enrichment, relative to the primitive mantle, compared to the other lithologies in the Merensky reef. Ni occurs at approximately 0.1 times the primitive mantle before a sharp increase to Os (at 1 times the primitive mantle). Ir shows a slights depletion, ranging between 0.1 and 1 times the primitive mantle. Further rises are reported in Ru and Rh, through to Pt (at approximately 10 times the primitive mantle), which creates a relatively steep pattern. Pd shows a strong depletion relative to Pt and ranges between 1 and 10 times the primitive mantle. Au shows the highest levels of enrichment compared to the PGE, occurring between 10 and 100 times the primitive mantle, before decreasing to Cu at 1 to 10 times the primitive mantle. All samples show similar patterns of enrichment, however, the anorthosite samples show a progressive enrichment in PGE (+Au, Cu and Ni) with increasing stratigraphic depth, i.e., MR-01 is the least enriched whereas MR-28 is the most enriched.

Both leuconorite and norite units have been included in a primitive mantle normalized plot (Fig. 4.6.7), which correlate to samples MR-06 and MR-07, respectively. MR-08 (pyroxenite) and MR-09a (anorthosite) have been included in this plot on the basis of their similar patterns to MR-06 and MR-07. Overall, this plot is more enriched in PGE (+Au, Cu and Ni) than the anorthosites. Ni occurs at 1 times the primitive mantle (with the exception of MR-06). Os is enriched relative to Ni in MR-09a and MR-08, while the opposite is true for MR-06 and MR-07. Steep positive profiles are seen from Ir through to Ru, Rh and Pt. Pt shows enrichment levels between 10 and 100 times the primitive mantle (with the exception of MR-06 - at about

1 times the primitive mantle). Pd shows similar enrichment levels to Pt (producing a flat trend) before a steep increase to Au (as in the anorthosite) with enrichment levels at about 100 times the primitive mantle (with the exception of MR-06; at about 10 times the primitive mantle). Cu occurs at between 10 and 100 times the primitive mantle for samples MR-07, -08 and -09a and at about 10 times the primitive mantle for sample MR-06.

Pyroxenitic rocks of the reef are shown in figure 4.6.7. Sample MR-09b (i.e., anorthosite) is included in the plot because of similarities in pattern to the pyroxenite. This most likely reflects the high PGE concentrations seen in MR-09b which forms part of the upper PGE peak (correlating to MR-10; as illustrated by its high PGE enrichment levels in the plot). Ni occurs approximately between 1 and 10 times the primitive mantle and a sharp increase is seen towards Os (between 10 and 100 times the primitive mantle). A slight depletion is seen in Ir (with enrichment levels only just less than Os). Steep enrichment patterns are observed from Ru to Pt (at approximately 1000 times the primitive mantle) before levelling out to Pd (also about 1000 times the primitive mantle). MR-10 shows more of an enrichment in Pd compared to the other samples (at over 1000 times the primitive mantle) which reflects the highest Pd concentrations recorded in any of the samples of this study (i.e. the upper peak). Unlike the anorthositic and noritic/leuconoritic units, Au is not as enriched and shows a generally flat trend from Pd. Cu shows a depletion relative to Au and occurs between 10 and 1000 times the primitive mantle. The primitive mantle normalized PGE (+Au, Cu and Ni) plot produced for the pyroxenites shows a good comparison to the primitive mantle normalized PGE (+Au, Cu and Ni) plot produced for the silicates of the MR by Barnes and Maier (2002a), both in pattern and in similar levels of enrichment.

A primitive mantle normalized PGE (+Au, Cu and Ni) plot for the chromitite unit of borehole ELF-395 is shown in figure 4.6.7. Ni occurs between 0.1 and 1 times the primitive mantle which is its lowest level of enrichment compared to the other normalized plots. A sharp increase occurs between Ni and Os (about 100 times the primitive mantle). Ir shows similar levels of enrichment to Os (giving a flat profile between the two elements). Gradual increases are observed from Ir through to Pt (at over 1000 times the primitive mantle) before a sharp decrease from Pt, through to Pd, Au and Cu (just over 1 times the primitive mantle). Like the pyroxenite, the chromitite PGE (+Au, Cu and Ni) mantle normalized plot shows good comparisons to the

chromitite plot produced by Barnes and Maier (2002a) in terms of pattern and levels of PGE enrichment. Barnes and Maier (2002b) note that chromitites in the CZ should show strongly arched patterns due to enrichment in PGE over Cu and Ni.

4.6.1. Comparisons between boreholes ELF-395 and -393

Borehole ELF-395, when compared to borehole ELF-393, shows a number of differences in terms of whole-rock PGE geochemistry. For example, although borehole ELF-393 had two major peaks of PGE enrichment like borehole ELF-395, borehole ELF-393 showed a top-loaded PGE mineralisation style. Viljoen (1999) and Cawthorn (2012) suggest that this is more typical of wider-reef facies of the Merensky. Furthermore, unlike borehole ELF-395, the two prominent PGE peaks identified in borehole ELF-393 were constrained to the presence of norite in both hangingwall and footwall units (on the margins of the reef). Both boreholes ELF-393 and ELF-395 show a sustained enrichment in PGE underlying the upper peaks. However, the above mentioned enrichment in PGE was shown to coincide with the presence of a pegmatoidal pyroxenite in borehole ELF-393. No pegmatoid was identified in borehole ELF-395. Furthermore, borehole ELF-395 comprises a chromitite stringer at the base of the reef whereas borehole ELF-393 contained no chromitite stringer. Major differences in PGE concentrations can be distinguished between boreholes ELF-393 and -395. For example, in the upper peak and lower peak, total PGE concentrations for borehole ELF-393 reached 1987 ppb and 494 ppb, respectively. This is considerably less when compared to borehole ELF-395: 6532 ppb in the upper peak and 18704 ppb in the lower peak.

Other key dissimilarities between boreholes ELF-393 and -395 include PGE correlations and behaviour. In borehole ELF-393, it was shown that Rh behaved similarly to the IPGE while Pt followed Pd. However, in borehole ELF-395, both Rh and Pt correlate well to the IPGE and Pd behaves in an opposite manner. In ELF-393, Au showed no preferred correlation to neither IPGE nor PPGE.

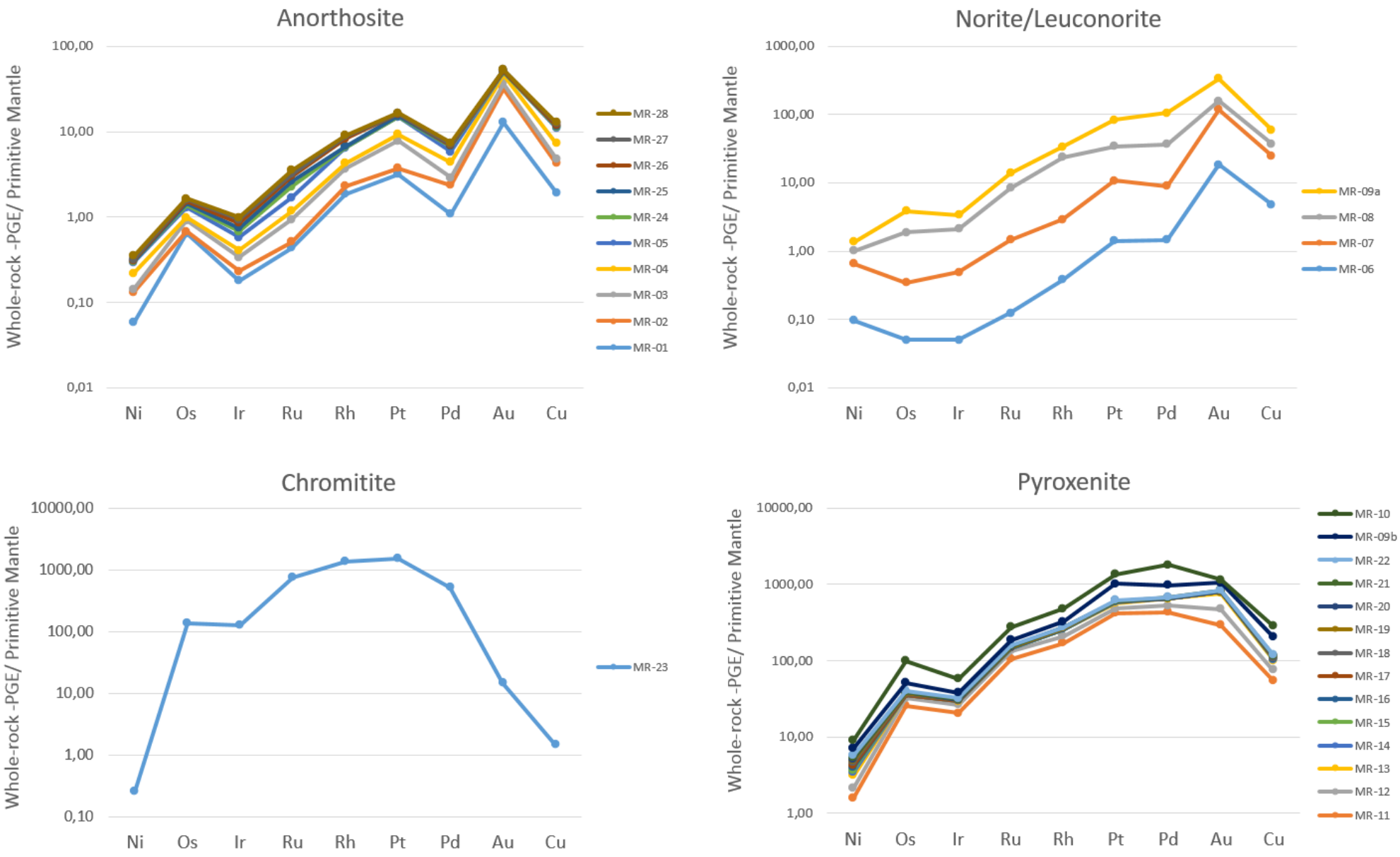

Figure 4.6.7. Primitive mantle normalized PGE (+Au) plots for the anorthosite FW and HW units, leuconorite and norite units, pyroxenitic reef and the chromitite stringer for borehole ELF-395. Primitive mantle values after Barnes and Maier (1999).

Logarithmic plots of PGE concentrations in borehole ELF-393 identified the presence of peaks in which all PGE show enrichment. Overlying and underlying the upper and lower PGE peaks, zones of depletion were identified in which all PGE show a depletion. Furthermore, borehole ELF-393 also showed separate IPGE and PPGE peak enrichment. Borehole ELF-395 shows similar PGE peaks and zones of depletion (overlying the upper peak and underlying the lower peak), as well as PPGE peaks. However, no IPGE peaks were identified in borehole ELF-395.

Other differences highlighted between boreholes ELF-393 and -395 are evident in primitive mantle normalised plots. For example, norite/leuconorite primitive mantle normalised plots from borehole ELF-393 showed a higher degree of enrichment than that of borehole ELF-395. This reflects the presence of high PGE concentrations within this unit (resulting in the upper PGE peak). Furthermore, within the pyroxenite units, borehole ELF-395 is far more enriched in PGE and shows a steeper profile when compared to borehole ELF-393. Comparing the anorthosite units in both boreholes shows that ELF-395 has a steeper profile, as well as negative Pd and Ir anomalies which were not observed in borehole ELF-393.

Chapter 5. Discussion

5.1. Petrographic Features of the Merensky Reef

Petrographically, the Merensky Reef can be subdivided into three main zones based on similar mineral characteristics and textures. For example, the main textural difference between the hangingwall and footwall units and the reef is the appearance of cumulus plagioclase and intercumulus clino- and orthopyroxene versus cumulus clino- and orthopyroxene and interstitial plagioclase, respectively. Where plagioclase is present as a cumulus phase, extensive zoning and evidence of triple point junctions is found (this includes within the anorthosite reef unit). This suggests that both the HW and FW units (as well as the anorthosite reef unit) underwent recrystallization some time after their emplacement. Plagioclase exhibited no zoning, nor did pyroxene exhibit triple point junctions in the pyroxenite reef unit, suggesting that this unit did not experience recystallization after emplacement.

Other characteristic differences between the anorthositic HW and FW units and the reef include significant changes in modal abundances (see Fig. 4.2.1) and variations in overall mineral size. For instance, ortho- and clinopyroxene increase in grain size and in modal abundance from both the HW and FW units towards the reef, with the former being the most abundant mineral in the reef. Other minerals which share this change include BMS, oxides and micas. Furthermore, orthopyroxene grain shape varies from mostly subhedral in the hangingwall and footwall units to mostly euhedral in the reef units. These observations are comparable to those made by Vermaak and Hendriks (1976).

Ophitic textures are common throughout the hangingwall, reef and footwall units of the Merensky, although particularly prominent in the hangingwall norite and reef pyroxenite units. Both ortho- and clinopyroxene oikocrysts were identified in this study, although the former is more locally constrained to just the reef pyroxenite unit. In addition to inclusions of subhedral plagioclase in orthopyroxene, anhedral, rounded resorbed orthopyroxene was identified in clinopyroxene oikocrysts (Fig. 4.2.6I). The existence of enclosed plagioclase chadacrysts in orthopyroxene and clinopyroxene oikocrysts indicates that plagioclase crystallized prior to the crystallization of orthpyroxene or clinopyroxene, while same concept is true for orthpyroxene inclusions in clinopyroxene oikocrysts. Observations of ophitic textures in the Merensky Reef

are consistent with those of previous authors (Cameron, 1982; Eales *et al*., 1991). Eales *et al*. (1991) attributed the formation of these ophitic textures to a process of magma-mixing in which the texture may develop through the mixing of evolved, plagioclase-bearing residual magma and primitive magma (with orthopyroxene on the liquidus). The fact that plagioclase crystallized prior to the crystallization of orthopyroxene suggests that the Merensky Reef experienced more than one crystallization event. One possible explanation for this is the introduction of a new influx of magma and the subsequent mixing between this new magma and the resident, more evolved magma (reflected in the ophitic textures in the reef).

The early crystallization of plagioclase within orthopyroxene can be depicted on an An-Fo-SiO_2 ternary phase diagram. Two possible models are presented to explain the paragenetic sequence presented above. In the first model (Fig. 5.1.1A), plagioclase crystallizes first at some point within the red triangle and moves away from the An apex until it encounters the plagioclase-orthopyroxene cotectic (i.e., c-d join). At this point, orthopyroxene begins crystallizing in the system, growing around existing plagioclase laths. New plagioclase crystallizing will form at the exposed ends of existing laths or as new grains. However, radiogenic isotopic evidence presented by Prevec *et al*. (2005) suggest that plagioclase is in isotopic disequilibrium with orthopyroxene in the Merensky Reef (see subsection 5.4). To account for the observed paragenetic sequence of early plagioclase, followed by orthopyroxene, a more complex model is presented. In the second model (Fig. 5.1.1B), magma mixing occurs between one magma, which is crystallizing plagioclase (see point 1), and a second magma, which is crystallizing orthopyroxene (see point 2). Through the mixing of magma 1 and magma 2, orthopyroxene will crystallize around existing plagioclase (Eales *et al*., 1991). Essentially, the first model only requires one parent magma whereas the second model requires multiple magmas with different saturated phases.

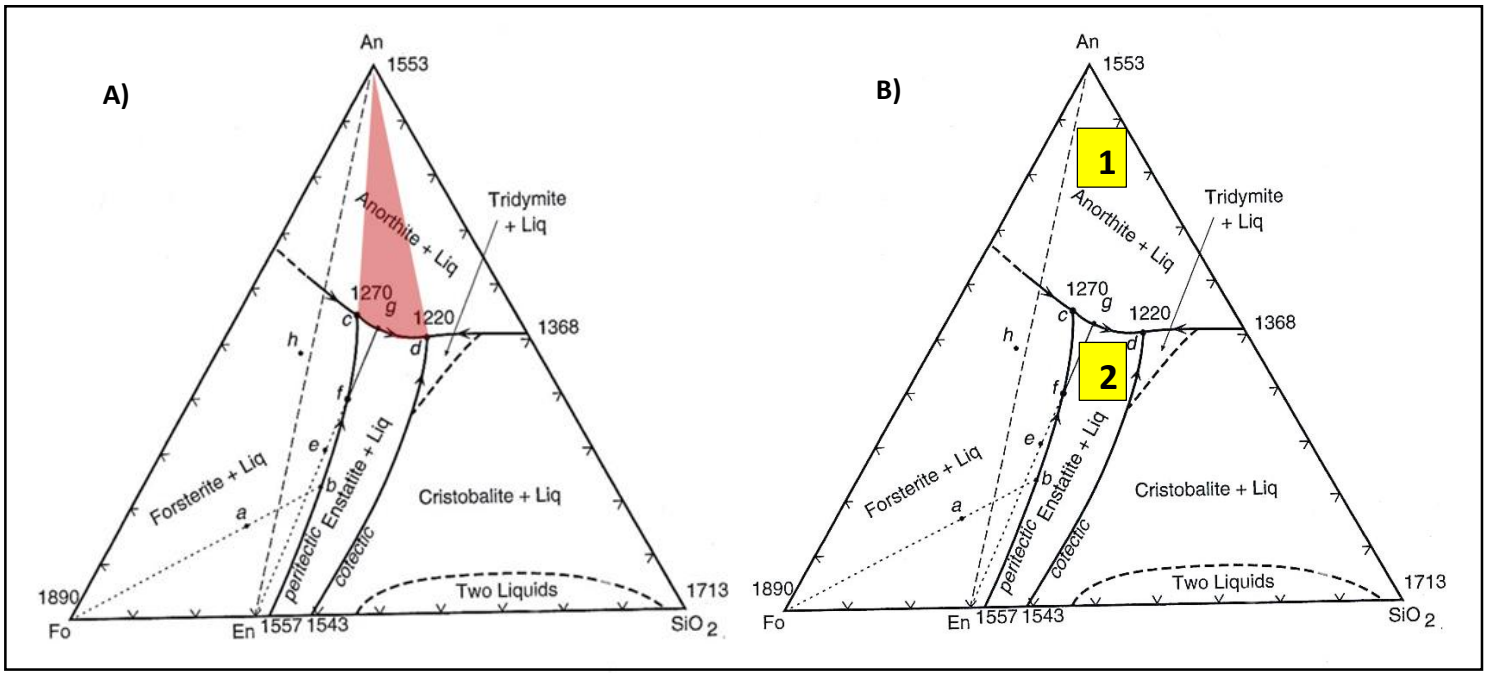

Figure 5.1.1. Isobaric diagrams for an An-Fo-Si system at 0.1 MPa. Illustrated are the cotectic and peritectic curves in the system. To account for the presence or plagioclase inclusions in orthopyroxene, two models are presented: the first model (A) involves plagioclase crystallizing first, followed by plagioclase and orthopyroxene at the cotectic (c-d join). The second model (B) involves the mixing of one magma (which is crystallizing plagioclase – point 1) with another magma (crystallizing orthopyroxene – point 2). Images after Anderson (1915).

Cumulus orthopyroxene grains and oikocrysts show clinopyroxene exsolution lamellae in all units of the Merensky Reef, however, significant exsolution of clinopyroxene in orthopyroxene hosts were observed in the pyroxenite unit. This is also evident in figure 4.3.2 which showed a scatter of points from the enstatite and diopside fields to the pigeonite and augite fields. Thus, the points in the pigeonite and augite fields most likely represent exsolution lamellae compositions. In addition to exsolution lamellae, clinopyroxene was also observed as rims on orthopyroxene. If these clinopyroxene rims are the product of crystallization of trapped interstitial liquid, one would expect these rims to be more evolved than clinopyroxene which evolved from the host (Raines, 2014). However, Mg # are similar for both exsolved clinopyroxene and clinopyroxene rims. It is possible that these clinopyroxene rims are thus a reaction between early orthopyroxene and liquid or they represent the sub-solidus migration of exsolved clinopyroxene in the host orthopyroxene to grain boundaries (Raines, 2014).

Olivine is present in only small modal proportions in borehole ELF-395, occuring sporadically within the pyroxenite unit. Mitchell and Scoon (2007) who investigated wide-reef Merensky facies from Winnaarshoek in the eastern Bushveld Complex inferred that a general absence of olivine may reflect somewhat more passive crystallization conditions in which the facies formed at lower temperatures. They further suggested that not only does this explain a general absence in olivine, it also explains the lower grade in the mineralized reef zone and the poorly developed, relatively thin chromitite stringers. These observations are consistent with those made for borehole ELF-395. To explain the more passive conditions at Winnaarshoek, Mitchell and Scoon (2007) suggested that the rocks at Winnaarshoek formed more distal to a major feeder zone within the Bushveld magma chamber. They also report on the presence of fewer regional potholes between the Merensky Reef and UG2 chromitite layer.

Base metal sulphides (BMS) identified in this study comprised pyrrhotite, pentlandite, chalcopyrite, pyrite and minor sphalerite. Typically, BMS occur as irregular blebs or aggregates which vary in size between < 1mm and 5 mm and in modal abundance between 1 and 5 % (showing a particular concentration in the pyroxenite reef unit). Wilson and Chunnett (2006) suggested that the distribution of sulphide in the Merensky Reef was influenced by the distribution and amount of trapped interstitial silicate liquid, i.e., as plagioclase. Interstitial plagioclase occurs commonly as large oikocrysts encompassing inclusions of orthopyroxene. Sulphides tend to be concentrated in the spaces where interstitial plagioclase did not crystallize (Wilson and Chunnett, 2006). BMS show a strong association to hydrous minerals and alteration assemblages in the Merensky Reef, in which BMS, typically, are found in close proximity to biotite, chlorite and hornblende grains, as well as adjacent to sericite and serpentine. Vermaak and Hendriks (1976) noted that BMS showed evidence of interaction and replacement with silicates which may form biotite and hornblende as an alteration and reaction product.

Oxides identified in borehole ELF-395 include chromite, rutile and ilmenite which, like the BMS, form as aggregates ranging between 0.1 and 3.0 mm in size. Oxides show particular abundance in the pyroxenite reef unit and are closely associated to hydrous silicates and alteration features in the reef (similar to BMS). Commonly, ilmenite hosts rutile lamellae. This most likely reflects the exsolution of titanium from ilmenite. Cumulus chromite exists within

the chromitite stringer at the base of the pyroxenite reef unit, in which individual chromite grains range between 0.5 and 2.5 mm in size and are cubic to amoeboidal in shape. Inclusions of both plagioclase and orthopyroxene were identified in chromite grains which indicates that the crystallization of plagioclase and orthopyroxene preceded the crystallization of chromite. Annealling of chromite grains is a common feature in the chromitite stringer in which small grains amalgamate to minimize surface energy. Furthermore, chromite shows apparent reaction rims (Fig. 4.2.7F) with surrounding orthopyroxene, typically those which are inclusion free. Admittedly, no mineral chemistry was conducted on these rims, but these rims most likely represent some other Fe-spinel (possibly formed through a reaction of orthopyroxene with chromite).

5.2. Evidence for Hydrous Fluids in the Merensky Reef

Evidence of late hydrous fluids is presented in the form of abundant hydrous minerals and alteration features which occur throughout the Merensky Reef. Where present, primary igneous textures are not as well preserved as in areas where these minerals and features are absent. The most common hydrous mineral in the Merensky Reef is biotite which occurs in all units of the Merensky Reef (albeit in varying abundances). Typically, biotite shows a progressive increase in grain size and abundance from both the footwall and hangingwall units towards the reef (reaching sizes up to 5 mm). Furthemore, biotite shows a close spatial association to chlorite and is often replaced by the latter. Other hydrous minerals identified in the Merensky Reef include muscovite and hornblende. In addition to the presence of hydrous minerals, alteration of primary igneous minerals is abundant. For example, sericitization of plagioclase is a common alteration feature in the Merensky Reef (although typically constrained to the plagioclase-rich lithologies in the hangingwall and footwall units), as is serpentinisation of olivine (which is constrained to the pyroxenite reef unit). These observations coincide well with those made by Vermaak and Hendriks (1976). The pervasive hydrous alteration features and minerals presented here suggest the presence of late deuteric alteration (Ballhaus and Stumpfl, 1986; Prevec *et al.,* 2005). Processes of subsolidus alteration by an intercumulus fluid (see subsection 5.6) may have been intitiated by the compaction of the cumulus pile (Boudreau and Muerer, 1999). Evidence of a such a compaction is presented in subsection 5.3. The implications of hydrous fluids in remobilizing PGE are discussed in subsection 5.8.3

5.3. Evidence for Strain/Deformation in the Reef

Evidence for high temperature strain/deformation in the Merensky Reef is observed, petrographically, in plagioclase and orthopyroxene of the reef anorthosite, pyroxenite and chromitite units. Deformation twins (e.g., spindle-shaped twins), undulose extinction and pinched and bent twin lamellae were identified in plagioclase, while orthopyroxene showed kink bands and indented contacts between grain boundaries, suggesting that plagioclase and orthopyroxene experienced dislocation creep (Barnes and Maier, 2002a). Schoenberg *et al*. (1999) interpreted the rounded orthopyroxene grains, enclosed in clinopyroxene oikocrysts (as observed in this study), to be a strain effect formed by postcumulus mineral reaction and deformation. Deformation features were not observed in any other minerals which suggest that deformation occurred after the crystallization of plagioclase and orthopyroxene but before the formation of other silicates. These observations coincide well with other literature (Schoenberg *et al*., 1999; Barnes and Maier, 2002a; Godel *et al*., 2006). Barnes and Maier (2002a) intepreted the deformation to be a product of gravititional compaction of a crystal mush pile comprising an orthopyroxene and plagioclase framework.

5.4. Mineral Disequilibrium in the Merensky Reef

In recent years, it has been shown that mineral disequilibrium occurs in the Bushveld Complex (Mathez and Waight, 2003; Prevec *et al*., 2005). Using Pb-isotopes, Mathez and Waight (2003) showed that mineral disequilibrium exists between plagioclase and sulphide in the Merensky and Bastard Reef units. Similarly, Prevec *et al*. (2005) found, using Sm-Nd isotopes, that mineral disequilibrium occurred between coexisting orthopyroxene and plagioclase in the Merensky Reef. Prevec *et al*. (2005) showed that plagioclase was isotopically depleted (i.e., less crustally contaminated) relative to orthopyroxene.

A dissertation by Raines (2014) also reported on the occurrence of mineral disequilibrium between orthopyroxene and plagioclase in the Merensky Reef, from Winnaarshoek in the eastern Bushveld Complex. In addition to Sm-Nd isotopes, Raines (2014) also reported textural and mineral compositional evidence for mineral disequilibrium. Notable textural and compositional similarites between Raines (2014) and this study are drawn here. As reported by Raines (2014), textural evidence for mineral disequilibirum includes, but is not limited to, the

presence of resorbed plagioclase grains within orthopyroxene or relict plagioclase, clinopyroxene exsolution lamellae in orthopyroxene and resorbed orthopyroxene in clinopyroxene. In addition to this, further evidence of mineral disequilibrium includes discontinuous rims of clinopyroxene surrounding orthopyroxene and orthopyroxene and plagioclase and clinopyroxene inclusions in either orthopyroxene or clinopyroxene oikocrysts. Such observations were documented during the petrographic analysis of this study (see Chapter 4.2). It is also possible that the rims surrounding chromite and adjacent orthopyroxene, as mentioned in subsection 5.1, may represent a disequilibrium reaction between chromite and orthopyroxene, although there is no compositional evidence to support this.

Resorbed grains of plagioclase within orthopyroxene and resorbed orthopyroxene in clinopyroxene are well documented in the Bushveld Complex (Eales *et al*., 1990; Eales *et al*., 1991; Cawthorn and Barry, 1992; Eales and Cawthorn, 1996). This suggests plagioclase and subsequently orthopyroxene existed at an early stage within a melt, before their resorption and enclosure within orthopyroxene and clinopyroxene (*in situ*), respectively, prior to intercumulus plagioclase crystallization (Eales *et al*., 1991). As already mentioned, Eales *et al*. (1991) suggested that such textures may arise from the mixing of evolved, residual liquids (bearing plagioclase on the liquidus) and more primitive liquids.

Compositional evidence for mineral disequilibrium in this study comprises large ranges in plagioclase, orthopyroxene and clinopyroxene compositions relative to the various units in borehole ELF-395. For example, the average An content of inclusions (comprising some chadacrysts) is higher than that of both interstitial and cumlus plagioclase in the hangingwall, footwall and reef units. A similar observation to this was made by Raines (2014). Furthermore, clinopyroxene inclusions, rims and exsolution lamellae have, on average, higher Mg numbers than that of cumlus and intercumulus clinopyroxene. The implication of this is that intercumulus/cumulus textures of clinopyroxene are more evolved than other texures of clinopyroxene (i.e., inclusions, exsolution lamellae and rims) (Raines, 2014). Admittedly, no comparison between the above mentioned textures and clinopyroxene as oikocrysts could be made in this study. However, Raines (2014) found that oikocrystic texures of clinopyroxene comprised, on average, lower Mg numbers than that of other textures of clinopyroxenes and

were in fact more similar to orthopyroxene Mg numbers (which is consistent with equilibrium crystallization).

Evidence of mineral disequilibirum in the reef has certain implications for the reef's petrogenesis. For instance, Prevec *et al*. (2005) suggested that mineral disequilibrium between plagioclase and pyroxene may be interpretated by either primary igneous processes or by secondary (i.e., late magmatic/hydrothermal) processes. Although a hydrothermal process could induce isotopic disequlibrium, Prevec *et al*. (2005) rejected such a process on the grounds of the supporting textural evidence. Furthermore, Prevec *et al*. (2005) suggested that petrological evidence for a primary magmatic model is misleading in that mineral assemblages may represent a mixture of multiple magmas and such mineral assemblages have experienced late magmatic recrystallization. The implications of this is that it is difficult to relate observed mineral assemblages to proposed source magma compositions and such mineral assemblages most likely represent the mixtures of crystals from multiple source liquids (Prevec *et al*., 2005). Prevec *et al*. (2005) thus envisaged a model in which a new pulse of magma, which is pre-contaminated, is introduced over a pre-existing anorthositic sub-Merensky footwall. Subsequent density-driven mixing of orthopyroxene with earlier formed, less contaminated plagioclase would explain the observed isotopic disequilibrium in the Reef and is supported by textural evidence.

5.5. Evolution of the Merensky Reef

Compositional variation in plagioclase and ortho- and clinopyroxene between units provides information on the evolution the Merensky Reef. Using ranges and averages in core compositions of plagioclase (Table 5.5.1), as well as figure 4.3.1, various trends are identifiable in borehole ELF-395. Essentially, from both the HW and FW units to the Reef units (specifically the anorthosite reef unit) trends of decreasing CaO, FeO and An content, and increasing Na_2O and K_2O, are observed. MgO remains relatively uniform. Trends of decreasing An content and CaO towards the reef units suggest that plagioclase evolves in composition towards these units, while increases in Na_2O reflect the degree of fractional crystallization in plagioclase (Frost and Frost, 2013). Moreover, decreases in FeO towards the reef imply a progressive melt evolution in the rocks (Frost and Frost, 2013). In summary, the reef units

(specifically the anorthosite and pyroxenite units) appear to be the most evolved units in the Merensky Reef while the hangingwall and footwall units appear to be the most primitive. Furthermore, the hangingwall and footwall anorthosite are largely comparable with similar An content, K_2O, Na_2O, MgO and CaO averages. Only average FeO varies between the two units (0.34 versus 0.48 wt. %, respectively).

Within the pyroxenite reef, core compositions of interstitial plagioclase show significant variation with regard to An content (An_{50-76}). Furthermore, trends of decreasing An content within the pyroxenitic unit are recorded with increasing stratigraphic depth (before increasing in the last half-metre towards the chromitite stringer). This suggests that, within the pyroxenitic unit, plagioclase becomes more evolved with stratigraphic depth. One way of interpreting such a trend is that interstitial liquid present within the pyroxenite unit crystallized trapped plagioclase (which is more evolved than plagioclase in norites, leuconorites and anorthosites). In order to explain evolving compositions with height in the pyroxenite unit, the base of the pyroxenite unit would have had to be more pyroxene-rich (i.e., less plagioclase to buffer crystallizing plagioclase) than the upper pyroxenite. Thus, An content could increase with decreasing percentages of interstitial liquid. However, as shown in Fig. 4.2.1, modal abundances for orthopyroxene and clinopyroxene within the pyroxenite unit remain relatively uniform. This would suggest more homogeneous plagioclase compositions, but such observations were not evident in this study. Another possible explanation for evolving plagioclase compositions with depth in the pyroxenite unit, which seems more likely in this case, is linked to an upwards percolation process, in which trapped, plagioclase-rich liquid rises through the cumulus pile after compaction (as has been discussed in subsections 5.2 and 5.3). As the plagioclase-rich liquid percolates up through the cumulus pile, it equilibrates with Ca in pyroxene, becoming progressively depleted in Ca (cf. Table 5.5.1) as pyroxenes become enriched in Ca (cf. Table 5.5.2). Crystallization of plagioclase from the trapped, intercumulus fluid would thus result in evolved compositions near the base of the pyroxenite unit towards more primitive compositions at the top of the pyroxenite unit.

Table 5.5.1. Minimum, maximum and average plagioclase core compositions for the various units of the Merensky Reef. All data is presented in wt. % (excluding An content).

		Anorthosite FW	*Chromitite*	*Pyroxenite Reef*	*Anorthosite Reef*	*Norite HW*	*Leuconorite HW*	*Anorthosite HW*
n		*31*	*17*	*98*	*16*	*4*	*6*	*15*
CaO	*Min*	14.55	14.48	9.12	9.59	14.23	14.78	14.17
	Max	15.67	15.61	15.47	14.60	14.97	15.31	15.24
	Avg	**15.04**	**15.02**	**12.94**	**12.21**	**14.72**	**15.05**	**14.80**
MgO	*Min*	0.01	0.00	0.00	0.02	0.01	0.01	0.00
	Max	0.06	0.05	0.07	0.07	0.02	0.03	0.04
	Avg	**0.03**	**0.02**	**0.02**	**0.03**	**0.02**	**0.02**	**0.02**
FeO	*Min*	0.22	0.20	0.00	0.14	0.21	0.17	0.21
	Max	0.70	0.56	0.35	0.39	0.35	0.57	0.45
	Avg	**0.48**	**0.36**	**0.20**	**0.27**	**0.28**	**0.34**	**0.34**
Na_2O	*Min*	2.19	2.49	2.31	2.82	2.55	2.45	2.34
	Max	2.94	3.08	6.13	5.72	2.99	2.60	2.91
	Avg	**2.63**	**2.70**	**3.81**	**4.13**	**2.73**	**2.53**	**2.66**
K_2O	*Min*	0.14	0.14	0.06	0.20	0.16	0.17	0.12
	Max	0.24	0.24	0.44	0.52	0.21	0.21	0.25
	Avg	**0.18**	**0.18**	**0.23**	**0.34**	**0.19**	**0.19**	**0.18**
% An	*Min*	72.40	71.30	44.60	47.00	71.60	75.20	71.80
	Max	79.10	76.50	78.00	73.20	75.70	76.70	77.40
	Avg	**75.20**	**74.70**	**64.40**	**60.80**	**74.00**	**75.80**	**74.60**

As previously mentioned, plagioclase zoning was identified in the Merensky Reef. Plagioclase compositional zoning is a common feature in the Bushveld Complex, specifically in the anorthosites and norites of the UG2 – Merensky Reef interval, and is typically reversely zoned (Maier, 1995). In this study, the anorthosite footwall unit exhibited reversely zoned plagioclase while the anorthosite reef unit showed normal zoned plagioclase. Characterising reverse zoning are increases in An content, CaO, MgO and FeO, and decreases in Na_2O, from core to rim while the opposite is true for normal zoning. The implication of this is that the footwall unit underwent reheating (forming calcic-rich rims) and re-equilibration with a hotter, more primitive magma while the anorthosite reef unit cooled relatively slowly and interstitial plagioclase present in the unit equilibrated with a trapped, more evolved liquid (Prevec *et al*., 2005; Seabrook *et al*., 2005). Reheating of the footwall anorthosite could be explained by possible magma mixing in a chamber, a quick release of volatiles in water-saturated magma or by the rapid movement of magma in a chamber or through a conduit (Vernon, 2004). In the case of magma mixing, a thermal exchange and a chemical interaction is induced between the primitive magma and the resident, more evolved magma (containing already-crystallized plagioclase) (Shcherbakov *et al*., 2011).

In addition to a compositional analysis of plagioclase, pyroxene compositions may elucidate key parameters in the formation of the Merenksy Reef. Ranges and average core compositions for clinopyroxene from the various units of the Merensky Reef are provided in Table 5.5.2. General trends of increasing CaO and Mg # and decreasing FeO are observed in clinopyroxene core compositions from both hangingwall and footwall units towards the reef units (particularly the pyroxenite reef unit). This trend is also recorded in average clinopyroxene inclusion compositions, as well as in average orthopyroxene core compositions (albeit the average Mg # is marginally lower in the pyroxenite unit; ~ 80).

Table 5.5.2. Minimum, maximum and average clinopyroxene core compositions for the various units of the Merensky Reef. All data is presented in wt. % (excluding Mg numbers).

		Anorthosite FW	***Chromitite***	***Pyroxenite Reef***	***Anorthosite Reef***	***Norite HW***	***Leuconorite HW***	***Anorthosite HW***
n		*10*	*6*	*55*	*7*	*8*	*13*	*17*
CaO	*Min*	19.69	21.05	16.98	21.86	20.05	21.80	19.42
	Max	23.43	23.60	24.35	23.29	23.10	23.23	23.16
	Avg	**22.36**	**22.50**	**22.69**	**22.81**	**21.89**	**22.75**	**22.21**
FeO	*Min*	6.60	6.72	2.57	4.21	6.17	6.10	5.64
	Max	9.98	9.62	8.21	6.20	13.35	7.75	13.35
	Avg	**7.73**	**7.55**	**4.91**	**5.33**	**8.07**	**6.83**	**7.42**
Mg#	*Min*	73.5	72.0	79.7	81.8	77.3	75.9	76.1
	Max	79.9	78.9	87.6	84.6	81.3	80.5	81.5
	Avg	**77.1**	**77.3**	**84.5**	**83.4**	**79.9**	**78.1**	**78.8**

Based on the above mentioned trends, and the use of figure 4.3.2, the hangingwall and footwall units appear to be the most differentiated and evolved units (i.e., the most FeO-enriched and containing the lowest Mg #) while the pyroxenite and anorthosite reef units appear to be the most primitive units (i.e., the least FeO-enriched and containing the highest Mg #). As observed with plagioclase compositions, the hangingwall and footwall anorthosite units comprise similar CaO, FeO and Mg #. The similarity between the hangingwall and footwall units, with regards to plagioclase and pyroxene compositions, may suggest a sill-type injection of magma, representing the reef, into a formerly continuous homogeneous unit (Mitchell and Scoon, 2007; Kruger, 2010).

Within the pyroxenite reef unit, both orthopyroxene and clinopyroxene core compositions showed little variation with regards to average Mg # (between 78 and 82 and 82 and 85, respectively). Furthermore, no trends of increasing or decreasing Mg numbers with increasing stratigraphic height were identified in either cumulus clino- or orthopyroxene core compositions. These observations are consistent with those of Mitchell and Scoon (2007) and Raines (2014). Prevec *et al*. (2005) suggested that subsolidus slow cooling could account for the overall consistency in orthopyroxene compositions, in which only the movement of Mg^{2+} and Fe^{2+} are required in order to reach homogenization.

5.6. Evidence for Trapped Liquid in the Merensky Reef Pyroxenite

As shown in figure 4.5.1, Zr showed a particularly high enrichment within the pyroxenitic reef unit. Wilson and Chunnett (2006) argued that highly-incompatible to incompatible (e.g., REE) trace elements monitor the behaviour of trapped liquid within the cumulus pile. Essentially, trace minerals rich in incompatible elements are crystallized from these residual melts and thus record these incompatible element enrichments (Mathez, 1995; Wilson and Chunnett, 2006). Synonymous enrichments in HREE, e.g., Er, Tb and Tm (Fig. 5.6.1), show similar enrichment patterns and thus most likely point to a trapped liquid control. It has been suggested that the rocks in the UCZ contain a liquid component between 3 and 40% (Barnes and Maier, 1999; Barnes and Maier, 2002b).

Maier *et al*. (2013) suggested that the enrichment of incompatible trace elements within pyroxenitic rocks reflect the trapping of residual liquid during injections of slurries into semi-consolidated footwall rocks. The observed enrichments in incompatible elements within the pyroxenitic reef unit, and corresponding trapped liquid signatures, correlate with increases in size of negative Eu-anomalies (Fig. 4.5.6). Essentially, with increasing amounts of trapped liquid, the Eu-anomalies become increasingly negative; an observation also shared by Wilson and Chunnett (2006). This suggests that the trapped liquid itself had a negative Eu-anomaly (Wilson and Chunnett, 2006). However, two exceptions to this were found in samples MR-08 and MR-10 (within the pyroxenite unit). In both samples, positive Eu-anomalies and corresponding depletions in incompatible trace elements were observed. One possible explanation for this may be due to the proximity that samples MR-08 and -10 share with the anorthositic reef seam. Positive Eu-anomalies are consistent with the presence of cumulus

plagioclase, in which plagioclase preferentially concentrates Eu (as Eu^{2+} which substitutes for Ca^{2+}) over other REE; thus imparting a positive Eu-anomaly signature (Weill and Drake, 1973). However, the anorthositic reef unit itself contains a negative Eu-anomaly. To explain the above mentioned observation requires an intricate process in which the anorthositic seam represents the injection of plagioclase-rich liquid into adjacent pyroxenites. The liquid begins to crystallize plagioclase primocrysts which have positive Eu-anomalies. As further liquid is injected through the fracture, the fracture finally solidifies (but without any fractionation of plagioclase). Thus, late plagioclase will be compositionally similar to the parent liquid while early plagioclase (now present in the adjacent pyroxenites; MR-08 and MR-10) are more evolved. In summary, the pyroxenites immediately adjacent to the anorthosite reef reflect physical separation of plagioclase crystals from the parent liquid (accounting for the positive Eu-anomalies).

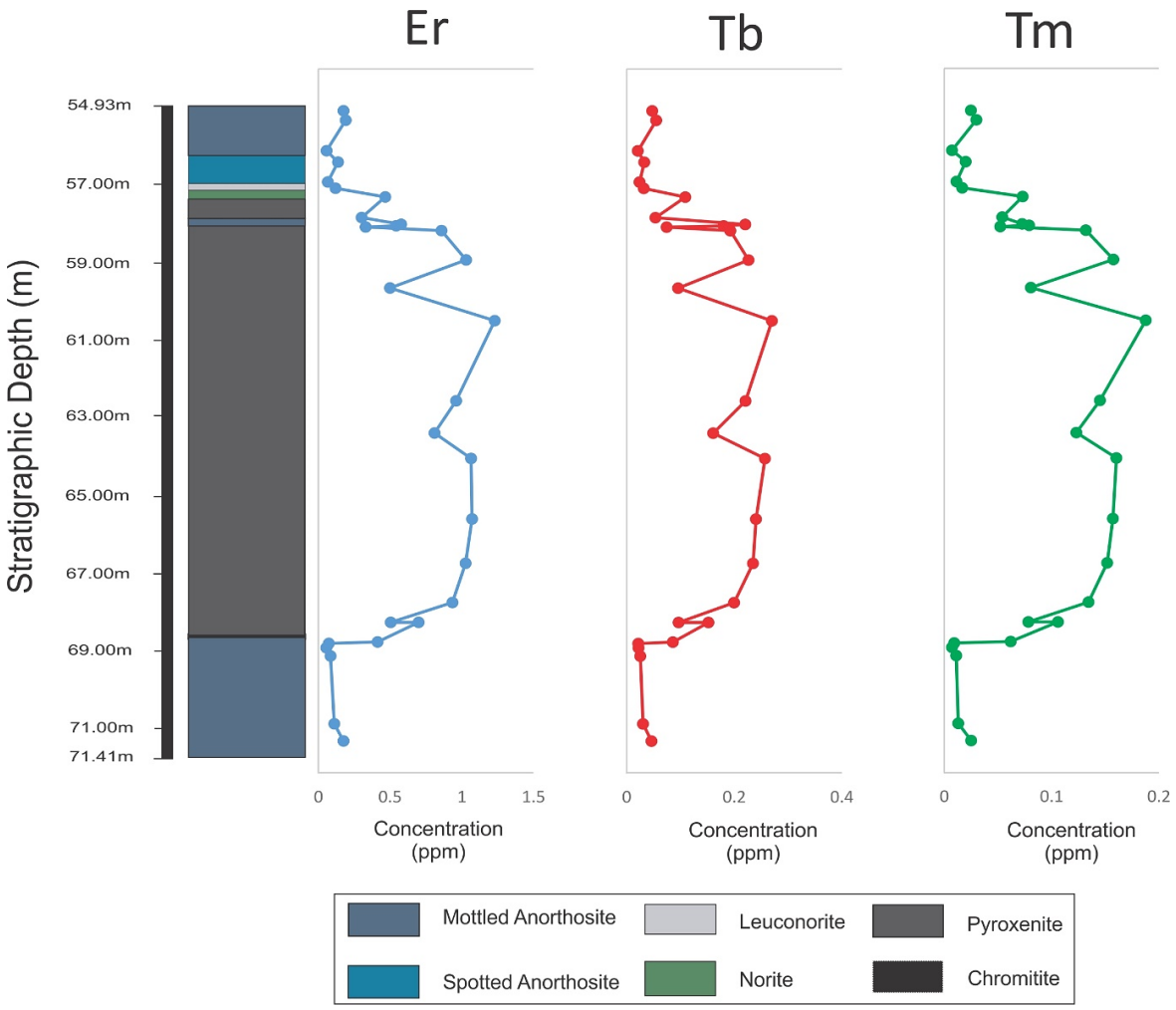

Figure 5.6.1. Whole-rock incompatible trace element (Er, Tb and Tm) stratigraphic concentration profiles for borehole ELF-395. Note the enrichment of these HREE within the pyroxenitic reef unit.

Sample MR-14, which showed the greatest enrichment in incompatible elements (e.g., Zr, Tb, Tm and Er) as well as the most negative Eu-anomaly can thus be interpreted as having the highest residual trapped liquid component. REE patterns (Fig. 4.5.7) for the pyroxenite unit showed that sample MR-14 also contains the steepest profile (e.g., $[La/Lu]_N$=4.24). Wilson and Chunnett (2006) indicated that steeper REE patterns for pyroxenites are related to increasing amounts of trapped liquid. However, anorthosites and other plagioclase-enriched rocks (e.g., leuconorites and norites) which show steeper REE patterns ($[La/Lu]_N$=9.56 - 39.23, 10.91 and 3.30, respectively; Fig. 4.5.7) reflect an increase in the amount of cumulus plagioclase present and the preferential incorporation of La (a LREE) into plagioclase (Wilson and Chunnett, 2006).

Furthermore, Wilson and Chunnett (2006) interpreted the varying amounts of trapped liquid in the Merensky Reef to be a result of variable rates of cooling and crystallization. They further suggested that higher temperature magma (as evident by higher Mg #; see subsection 5.5) were most effective in trapping interstitial liquid. This conclusion would seem to be particularly applicable to the pyroxenite unit of this study.

5.7. Mineralogical Controls on Whole-Rock Geochemistry

Whole-rock major oxide element profiles (Fig. 4.4.1) are consistent with control by the dominant rock-forming minerals identified during the macroscopic and petrographic investigation of borehole ELF-395. Al_2O_3, CaO and Na_2O patterns of enrichment coincide with the presence of plagioclase-rich lithologies, in which plagioclase is present as a cumulus phase (i.e., enrichment in the HW, FW and the anorthositic seam). The pyroxenite unit shows low concentrations of Al_2O_3, CaO and Na_2O (i.e., plagioclase present as an interstitial phase and in low abundances). Binary plots (Fig. 4.4.2) of CaO vs Al_2O_3 and Na_2O vs Al_2O_3 show that anorthosites, leuconorites and norites plot in fields of high Al_2O_3 versus high CaO (and high Na_2O) while pyroxenites show the opposite trend (plotting relatively close to the origin). Strong positive correlations (R^2>0.9) in the above mentioned major element oxides are observed. Sr has an enrichment profile identical to that of Al_2O_3, CaO and Na_2O. The enrichment of Sr in plagioclase-rich lithologies (also seen in borehole ELF-393; Fig. 4.5.2) reflects the partitioning of Sr into plagioclase during fractional crystallization (Drake and Weill, 1975).

MgO, MnO, Fe_2O_3 and SiO_2 patterns of enrichment (Fig. 4.4.1) coincide with the presence of pyroxene-rich lithologies (i.e., pyroxenite unit) in which pyroxene (both ortho- and clinopyroxene) are present as a cumulus phase. Decreasing MgO and FeO upwards the stratigraphy in the HW indicate a progressive melt evolution. Binary plots (Fig. 4.4.2) of Al_2O_3 versus SiO_2 or MgO, as well as CaO versus MgO, show strong negative correlations (R^2>-0.8). Pyroxenites plot in the top-left section of diagram (i.e., high SiO_2 or MgO versus low Al_2O_3 or CaO) while anorthosites, leuconorite and norite show the opposite trend.

Although apatite was not observed during the petrographic analysis of this study, relatively high P_2O_5 values (of up to 0.12 wt. %) were recorded, specifically in the anorthositic reef unit (Fig. 4.4.1), suggesting that this phase may be present, albeit in low abundances, within the unit and thus requires further investigation.

S patterns of enrichment (Fig. 4.4.1) remain relatively low throughout the Merensky Reef but peaks (5.21 wt. %) at the contact between the anorthosite reef and the underlying pyroxenite unit. This peak in S coincides with peaks observed in PGE and base metals (Cu, Ni and Co; Fig. 4.5.1) suggesting the presence of sulphides (particularly chalcopyrite and pentlandite). This may reflect a PGE control by sulphide liquid (see subsection 5.8.1). Base metals (e.g. Cu, Ni and Co) in borehole ELF-393 (Fig. 4.5.2) similarly are enriched together in an upper peak and it is expected these peaks would also coincide with a peak in S. The homogenous concentrations recorded in Cu and Ni within the pyroxenite unit suggests S-saturation (see Fig. 4.5.1).

Concentrations of Cr_2O_3 remain relatively low in the borehole ELF-395 with the exception of a peak in chromitite unit (2.61 wt. %). The pyroxenite unit shows relative enrichment in Cr (Fig. 4.5.1), and is particularly homogenous, compared to the HW and FW. This suggests that Cr is controlled by pyroxene, and is particularly evident in Fig. 4.4.2G. In borehole ELF-393 (Fig. 4.5.2), no spike in Cr was observed (indicating the absence of a chromitite stringer), however, like EFL-395, Cr showed relative enrichment in the pyroxenite and pegmatite lithologies. TiO_2 patterns of enrichment (Fig. 4.4.1) show high variability in borehole ELF-395, however, TiO_2 is particularly enriched in the pyroxenite unit. This most likely reflects the presence of Ti-bearing phases such as ilmenite and rutile (as described in Chapter 4.2).

Arndt *et al*. (2005) suggested that relatively high SiO_2 contents (Fig. 4.4.1) and the enrichment of incompatible trace elements (Fig. 4.5.1 and Fig. 5.6.1) constitute geochemical evidence that rocks of the BC result from crustal contamination (Irvine, 1977, 1980; Eales and Cawthorn, 1996). They further suggested that the relatively high SiO_2 contents would have led to crystallization of abundant orthopyroxene (which is reflected by high SiO_2 in the pyroxenite unit).

Wilson and Chunnett (2006) characterized chondrite normalized REE patterns (Fig. 4.5.7) by their shape and Eu anomalies. In this study, 3 patterns can be identified based on Eu anomalies: 1) strong positive Eu anomalies; 2) strong negative Eu anomalies; 3) weak negative (or no) Eu anomalies. Further subdivisions of REE patterns can be ascribed to their shape e.g., LREE enriched patterns, HREE depleted patterns, U-shaped patterns and flat patterns (Wilson and Chunnett, 2006). The patterns observed in anorthosite, norite/leuconorite and pyroxenite in borehole ELF-395 closely resemble those in ELF-393.

In borehole ELF-395, LREE are more enriched than HREE (as expressed by $(La/Lu)_N$ ratios > 1). Kottke-Levin *et al.* (2009) suggested that the fractionation of LREE relative to HREE is a typical feature in the rocks of the BC and that such fractionation trends are expected from mafic melts derived from the mantle. Where HREE patterns are flat or U-shaped (i.e., $(Gd/Yb)_N \sim 1$), Wilson and Chunnett (2006) suggested this indicates a control by orthopyroxene. They argue that cumulus orthopyroxene crystallizes from an evolved liquid, thus producing HREE enrichment (Wilson and Chunnett, 2006). Such patterns are observed predominantly within the pyroxenite unit and in the chromitite unit of this study (Fig. 4.5.7).

The variability in Eu anomalies may be attributed to a control by plagioclase (as mentioned in subsection 5.6). Where Eu anomalies are strongly negative, one would expect crystallization of plagioclase from intercumulus liquids within the cumulus pile (Wilson and Chunnett, 2006). Such negative Eu anomalies are observed within the pyroxenite unit (Fig. 4.5.7) with the exception of sample MR-08 and MR-10 (as discussed in subsection 5.6). To account for positive Eu anomalies, as seen in anorthosite, norite/leuconorite and in the chromitite units (Fig. 4.5.7), Wilson and Chunnett (2006) suggested that such trends occur where plagioclase forms as chadacrysts (i.e. cumulate phases). This is in agreement with the petrographic analysis

of this study (see Chapter 4.2). The fact that the chromitite shows a positive Eu anomaly is unusual given that chromite is the only cumulus mineral present in the seam, however, this most likely reflects the inclusion of cumulus plagioclase from the underlying footwall anorthosite into the whole-rock signature of sample MR-23 (see Chapter 4.2).

Thus, the whole-rock geochemistry in the Merensky Reef (particularly in the silicate layers; anorthosite, leuconorite, norite and pyroxenite) is controlled by the mutual influence of co-precipitating minerals competing for major elements (e.g., Mg, Al, Cr or Fe) (Kottke-Levin *et al.,* 2009). The variation observed in REE patterns suggest the presence of different magmas. Wilson and Chunnett (2006) argued that fractionated by-products of varying combinations of MZ and CZ parental magmas are required to explain the observed REE patterns in the Merensky Reef.

5.8. PGE Mineralisation and Distributions in the Merensky Reef

In light of the results of this study, a number of parameters need to be met when considering any model for the formation of the reef: 1) the enrichment of IPGE, Rh and Pt relative to Pd, S, Cu, Ni and Au in the chromitite stringer and vice versa in the upper (chromitite-absent) peak; 2) the subdivision of the pyroxenitic reef by differing geochemical characteristics; 3) the association of PGE and PGM with BMS; 4) depletions in PGE recorded above and below the lower peak; 5) separation of IPGE and PPGE peaks.

Three possible processes are considered in explaining the observed PGE mineralisation of the Merensky Reef. It is suggested that these processes are not neccesarily mutally exclusive and that ultimately the formation of the Merensky Reef could be the result of any one, or the combination of any or all, of these processes. The three possible processes are: 1) the collection of PGE by an immiscible sulphide liquid; 2) the collection and redistribution of PGE from a late magmatic/hydrothermal fluid rising from the underlying cumulate pile; 3) the crystallization of PGE as PGM direcly from the magma. The implications of each of the models, respective to the results of this study, will be considered in proposing a model for the formation of the Merensky reef.

5.8.1. Collection of PGE by an Immiscible Sulphide Liquid

The dominant and arguably most popular model for the mineralisation of PGE is the collection of PGE by an immiscible sulphide liquid (Campbell *et al*., 1983; Naldrett, 1999; Barnes and Maier, 2002a). Such an orthomagmatic model is particularly favoured because of the evident association of PGM to BMS in the Merensky Reef (Kinloch, 1982; Barnes and Maier, 2002b). Godel *et al*. (2010) showed, with the use of high-resolution X-ray computed tomography, that 95-97% of PGM in the Merensky Reef chromitites are closely associated with BMS (at the borders between sulphides, chromites and silicates). In the sulphide collection model (refer to Fig. 2.2.1), magma mixing between resident, evolved magma and a new injection of primitive magma may produce sulphide saturation in the mixed magma and an immiscible sulphide liquid (Campbell *et al*., 1983). The PGE (as well as Au, Ni and Cu), which have high partition coefficients into sulphide liquid (Table 5.8.1), are collected by this immiscible sulphide liquid and subsequently settle (along with other cumulus phases) onto the cumulate pile to form the reef (Campbell *et al*., 1983; Naldrett, 1999).

The process has also been envisaged through the contamination of a newly injected magma with country rock (Irvine, 1980; Kruger and Schoenberg, 1998; Cawthorn, 2002). In fact, Cawthorn (2002) argued that the mixing of magmas alone will not produce sulphide saturation (and with it sulphide immiscibility). Instead he suggests crustal contamination as a source for sulphide oversaturation and immiscibility. Some authors suggest that such contamination processes may occur within staging chambers beneath the main Bushveld chamber and that the sourced magma carries entrained droplets of sulphides (rich in PGE) and already-crystallized chromite microphenocryts (Lee and Butcher, 1990; Eales, 2000; Arndt *et al*., 2005; Eales and Costin, 2012). It has been suggested that the sulphide collection model could be repeated at the start of each cyclic unit within the Lower and Critical Zone (Barnes and Maier, 2002b). The collection process of PGE by immiscible sulphide liquid may be enhanced through the amount of time that the sulphide droplets interact with the silicate magma, the mass of silicate magma available to the immiscible sulphide liquid (to equilibrate with) and the turbulence within the system (Naldrett, 1997; 1999).

Barnes and Maier (2002b) suggested that in some cases, sulphide liquid may have percolated downwards through the cumulate pile (displacing interstitial silicate liquid) and enriching the

underlying mafic rocks in PGE. This could explain the enrichment in PGE observed in the rocks immediately underlying the upper peak (see figures 4.6.1 and 4.6.2). However, one would expect the rocks immediately underlying the lower peak to also show this enrichment in PGE, which is not evident in this study. It is possible that this could be specific to Merensky facies type, as Cawthorn (2010) reported PGE mineralisation into the footwall rocks beneath the chromitite stringer in the thin-reef Merensky facies. Similarly, Lomberg and Rupprecht (2010) reported sulphide mineralisation (rich in PGE) in the footwall rocks, but argued that the extent of transgression is controlled by the host rock and suggested that anorthosite typically hosts greater mineralisation than do other lithologies (such as norites). However, observations from this study indicate that the anorthosite footwall is depleted in PGE (see figures 4.61, 4.6.2; 4.6.3 and 4.6.7).

Based on covariance analysis, Lee (1983) subdivided metals from the Merensky Reef into two groups: 1) Ni, Cu, Au and Pd and 2) Ir, Rh, Pt and Cr. He suggested that Pt, Ir and Rh were controlled by PGM or spinel (see PGM model below – subsection 5.8.2) and Pd and Au were controlled by sulphides (Barnes and Maier, 2002b). These groupings and assumptions are significant for observations made in this study. For example, Pd did not correlate well with any of the other PGE (Table 4.6.2) and unlike the other PGE, which were enriched in the chromitite (i.e., lower peak), Pd was enriched at the top of the pyroxenite (Fig. 4.6.2). This is particularly visible in the primitive mantle-normalized diagram for the pyroxenite unit, in which MR-10 is more Pd-enriched relative to any other sample. Furthermore, Pd shows good correlations with base metals (Cu and Ni), as well as S (Table 4.6.2), all showing enrichment at the same stratigraphic position (Fig. 4.5.1 and Fig. 4.4.1, respectively). Macroscopic (Fig. 4.1.2F) and petrographic examination identified the presence of large BMS (predominantly chalcopyrite and pentlandite) which coincided with the upper Pd peak. It can therefore be assumed, as suggested by Lee (1983), that Pd is controlled almost exclusively by sulphide in the upper PGE peak. This most likely reflects the high sulphide/silicate partition coefficient ($D_{sulph/sil}$) of Pd into sulphide liquid (see Table 5.8.1) (Maier and Barnes, 1999).

Like Pd, Au showed particular enrichment in the upper PGE peak (i.e., top-loaded mineralisation style) and is suggested to be controlled almost exclusively by sulphide in the upper peak (Fig. 4.6.2). However, Au is quite variable throughout the rest of the sampled

sequence of rocks and shows no preferred correlation to either the IPGE nor PPGE (Table 4.6.2). This observation was also identified in borehole ELF-393 (Largatzis, 2014) and is illustrated by the low correlation coefficient (R^2=0.208) of Au versus Pt (i.e., PPGE) seen in figure 5.8.1. The variability in the distribution of Au indicates that Au is not entirely controlled by the same geochemical processes that control the PGE in the rest of the sampled sequence.

Contrasting characteristics in PGE geochemistry within the upper and lower pyroxenitic reef unit (see figure 4.6.4) suggest that the PGE mineralisation was controlled by different geochemical processes in each of these sections (Wilson and Chunnett, 2006). Pt/Pd and Cu/Pd ratios are useful geochemical tools for inferring primary magmatic processes (e.g., fractional segregation of sulphides from a magma and scavenging by sulphide liquids) (Maier *et al*., 1998; Barnes and Maier, 2002b; Wilson and Chunnett, 2006). Naldrett (2004) suggested that areas with low Pt/Pd (i.e., troughs) possibly reflect low Pt incompatibility compared to Pd, such that Pd became preferentially concentrated within partial melt while increases in Cu/Pd may indicate the scavenging of Pd by such sulphide melts. Pt/Pd ratios in the RLS are higher than in most mafic volcanic rocks (about 1.7 versus 1) (Barnes and Maier, 2002b). Barnes and Maier (2002b) attributed this to the higher enrichments in Pt in the sills compared to basalts. Furthermore, Barnes and Maier (2002b) suggested that the high Pt/Pd ratios of the RLS are similar to Pt/Pd ratios recorded in komatiites and thus they have inferred that komatiitic magmas may be relevant to Bushveld petrogensis.

In this study, the pyroxenite unit can be subdivided into the upper pyroxenite and lower pyroxenite unit on the basis of varying PGE geochemistry. The lower pyroxenite unit is characterized by depletions in PGE tenor and total PGE (figures 4.6.2 and 4.6.3, respectively), as well as high Cu/Pd (with values ranging between 16000 and 19000) and Pt/Pd ratios (Fig. 4.6.4), suggesting that sulphide underwent fractional segregation, while scavenging by sulphide liquids occurred in the lower pyroxenite unit (Naldrett and Wilson, 1990; Wilson and Chunnett, 2006). This may be related to the high sulphide/silicate partition coefficients for PGE (being greater than that of base metals) between the silicate magma and the sulphide liquid (Table 5.8.1). In contrast, the upper pyroxenite unit is associated with enrichments in PGE tenor and total PGE, as well as low Pt/Pd and Cu/Pd ratios. Wilson and Chunnett (2006)

suggested this may indicate a dynamic system in which PGE-undepleted magma and S are introduced to the system during simultaneous sulphide precipitation

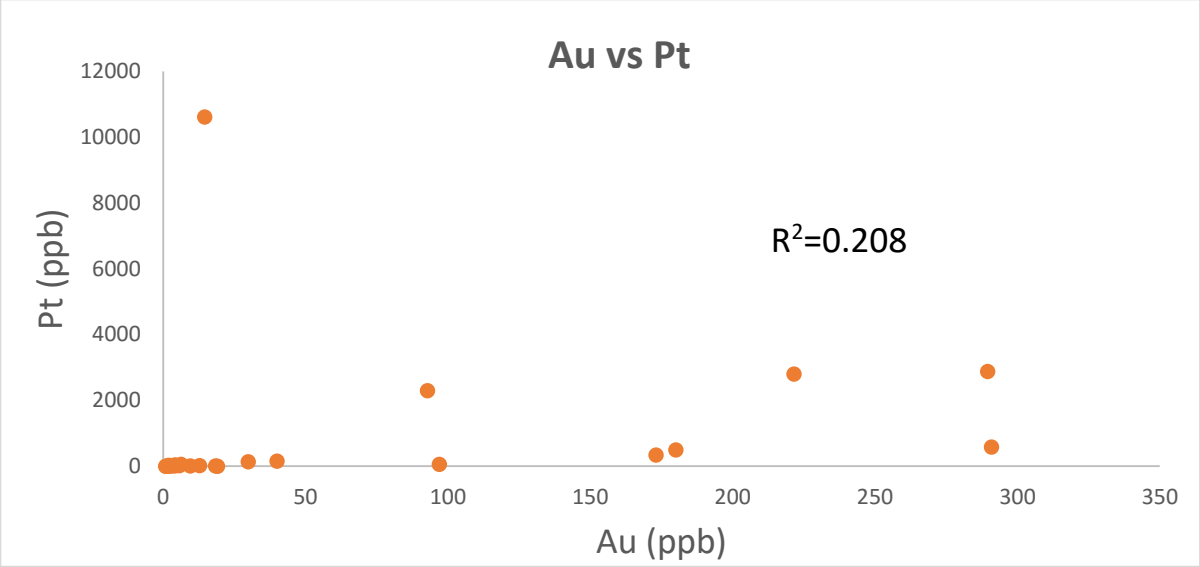

Figure 5.8.1. Whole-rock geochemical variation diagram for Au and Pt. Note the low correlation coefficient. Units are given in ppb.

Primitive-mantle normalized diagrams for PGE and Au (Fig. 4.6.7), from all lithologies of the MR, show the characteristic arch-shaped pattern which has been reported for the MR (Barnes and Maier, 2002a; Naldrett, 2004; Wilson and Chunnett, 2006). The plots are similar to those produced by Barnes and Maier (2002a) from their study of the MR at Impala Platinum Mine. The variations in pattern indicate that not all platinum-group elements and gold are controlled exclusively by the lithology (Wilson and Chunnett, 2006).

Logarithmic plots of PGE concentrations (Fig. 4.6.6) in borehole ELF-395 identified the presence of peaks in which all PGE show enrichment. Essentially, these peaks correlate to the upper and lower PGE peaks discussed above. Similar observations were identified in borehole ELF-393 and were inferred to be sulphide peaks in which sulphide liquid acted as the primary control on PGE partitioning (Largatzis, 2014). However, the enrichment in PGE at the base of the Merensky pyroxenite coincides with the presence of chromitite and suggest chromite is the primary control of PGE in this horizon. Alternatively, the co-precipitation of chromite and PGM could explain the enrichment of PGE in this unit (see subsection 5.8.2).

Table 5.8.1. Partition coefficients for PGE and chalcophile metals. Table after Barnes and Maier (1999) and (2002b) and references therein.

Os	Ir	Ru	Rh	Pt	Pd	Au	Ni	Cu	References
Alloy-Sulphide Liquid									
50-130	50-120	>30	30-110	90-300	0.9-2.0		1.3		Fleet and Stone (1991)
	135-324		1-6.5	0.04-0.15			0.1	0.06-0.16	Li *et al*. (1996)
Alloy-Silicate Liquid									
10^6-10^7	10^{12}			10^{15}	10^7	10^7			Borisov and Palme (1997)
Sulphide Liquid-Silicate Liquid									
>31000	>50000	>12000	>140000	>18000	>92000		810-1300		Sattari *et al*. (2002)
700-5300	1500-4700	1200-4100		1100-6900	1200-6300	30-3000			Fleet *et al*. (1999)
	14000				23000	15000-18000	575-836	1383	Peach *et al*. (1990)
Monosulphide Solid Solution - Sulphide Liquid Sulphur Saturated									
4.3	3.6	4.2	3.03	0.2	0.2	0.09	0.84	0.27	Fleet *et al*. (1993)
Monosulphide Solid Solution - Sulphide Liquid Sulphur Undersaturated									
	0.08-1.4		0.4-0.8	0.01-0.05	0.01-0.07		0.18-0.36	0.17-0.2	Barnes *et al*. (1997)
Monosulphide Solid Solution - Sulphide Liquid Sulphur Oversaturated									
	5-17		3.9-11	0.14-0.24	0.13-0.24		0.7-1.2	0.22-0.27	Barnes *et al*. (1997)

Depletions (or troughs) in PGE were identified in both boreholes in which all PGE are depleted relative the underlying or overlying rocks. In borehole ELF-393, these depletions were located immediately overlying and underlying the upper and lower PGE peaks, respectively (Largatzis, 2014). It was inferred that such depletion haloes may have formed through an Ostwald-ripening type of mechanism, in which PGE within these zones were absorbed into the larger upper and lower PGE peaks, respectively, by post-crystallizational modification. It was therefore suggested that these depletions formed through a secondary process which overprinted the primary distribution of PGE in these zones (Largatzis, 2014). In borehole ELF-395, such depletions were identified underlying and overlying the lower peak but no evidence of a distinct depletion trough was found immediately overlying or underlying the upper peak, although depletions were found higher up in the stratigraphic sequence.

Furthermore, borehole ELF-393 displayed the presence of separate IPGE (Or, Ir and Ru) and PPGE peaks (Rh, Pt, Pd). To the author's knowledge, such a distinct separation of peaks has not been documented in the literature on the Merensky Reef. In this study, one example of a PPGE peak was identified (underlying the upper peak) but no evidence of an IPGE peak was recognised. The separation of IPGE peaks and PPGE peaks suggest a different partitioning behaviour for the IPGE and PPGE in borehole ELF-395. One model that may be appropriate in explaining this phenomenon is a sulphide fractionation model presented by Maier and Barnes (1999).

The sulphide fractionation model assumes that sulphide cumulates, and not sulphide liquid, are responsible for the preferential enrichment, as seen in the Critical Zone, of Os, Ir, Ru and Rh over Pt and Pd (Barnes and Maier, 2002b). Previous work by Naldrett *et al*. (1982) and Naldrett (2004) have shown that base metal sulphide liquids fractionate and PGE and chalcophiles partition between an early monosulphide solid solution (Mss) and the residual Cu-rich fractionated liquid (i.e., the intermediate solid solution; Iss) (Dare *et al*., 2011). In an Fe-S-Ni system, pyrrhotite (Fe-rich) is the first phase crystallized from the Mss at about 1160 °C (Naldrett, 2004). Further cooling will promote the crystallization of pentlandite (Ni-rich) at about 865 °C (Naldrett, 2004). With progressive time and decreasing temperature, the residual liquid becomes increasingly Cu-rich and chalcopyrite subsequently crystallizes from the Iss (Naldrett, 2004).

Experimental work by Fleet *et al.* (1993) showed that under S-saturated conditions, the IPGE (Os, Ir and Ru) and Rh are compatible in the Mss (D values range between 3.03 to 4.3) while the PPGE (Pt and Pd) are incompatible in the Mss (D values equal to 0.2) (see Table 5.8.1). The IPGE and Ru will therefore strongly partition into the Mss (by a factor of >50) while Pt and Pd (and Au) partition into the Iss and later precipitate as PGM (Patten *et al*., 2013). Barnes and Maier (2002b) suggested that the removal of some of the fractionated sulphide liquid is necessary, after the formation of the Mss, to explain for the whole-rock enrichment of Os, Ir, Ru and Rh. They proposed that the sulphide liquid was expelled by liquefaction of the cumulate pile via a seismic event (e.g., injection of new magma) or by cementation (e.g., through the growth of oikocrysts) and compaction of the cumulate pile (see subsection 5.3).

5.8.2. Crystallization of PGE as PGM

Experimental work by Brenan and Andrews (2001) showed that commonly observed inclusions of laurite and Ru-Os-Ir alloys within chromian spinels may be interpreted as a primary magmatic texture. This is because laurite and Ru-Os-Ir alloys are stable at chromian-spinel-based liquidus temperatures (Brenan and Andrews, 2001). They further argued that the crystallization of laurite and Ru-Os-Ir alloys in the presence of immiscible sulphide liquid is unlikely because of the low intrinsic abundances of PGE in igneous rocks and the high solubility of Ru in molten sulphide. It is important to note that in this study, S concentrations were extremely low within the chromitite unit (0.02 wt. %), and assuming that S was not lost, this suggest that PGE are not controlled by the presence of sulphide in the chromitite stringer. However, the chromitite units of the Merensky Reef have been shown to comprise BMS and thus in order to explain the enrichment of Os, Ir, Ru, Rh and Pt in the chromitite unit of this study, it is suggested that the BMS would have to be introduced after the crystallization of PGM (Barnes and Maier, 2002b).

Hiemstra (1979) proposed a model for the formation of PGE mineralized reefs in which PGM crystallize directly from a silicate magma (as laurite, Os-Ir alloys and Pt alloys). Vermaak and Hendriks (1976) suggested sulphide to be the principal host of PGM in the Merensky Reef (although chromite also has potential to be a host). Braggite, laurite, cooperite and sperrylite are considered to be the most common precious metal-bearing minerals in the Merenksy Reef

(Vermaak and Hendriks, 1976). In this study, ferhodsite (Cu-Rh-Pt bearing), merenskyite (Pt-Pd-Bi-Te bearing) and moncheite (Pt-Bi-Te bearing) were identified adjacent to chromite and BMS grain boundaries (see Chapter 4.3.6).

One flaw in the model presented by Hiemstra (1979) is that it predicts that the magma must become saturated in PGM. However, PGE are only present in ppb concentrations within the magma (Mathez, 1999; Barnes and Maier, 2002a). Thus, to overcome this limitation, Tredoux *et al*. (1995) presented a model (Fig. 2.1.5) in which PGE amalgamate together as aggregates, or rather as clusters, which preconcentrate the PGE. The IPGE, which are heavier than the PPGE, are more likely to form clusters (Tredoux *et al*., 1995). In a S-poor environment, these clusters eventually merge to form PGE alloys which may act as nucleation sites for early-formed oxides and silicates (Tredoux *et al*., 1995). However, Godel *et al*. (2010) argued that for such a model, one would expect most of the PGM to be enclosed in chromite and/or silicates. Based on their observations from 3-D X-ray computed tomography, they found that most of the PGM were located at the border between sulphides, chromites and silicates.

The model presented by Tredoux *et al*. (1995) predicts the enrichment of Os, Ir, Ru (and possibly Rh). However, in this study, synonomous enrichments in Os, Ir, Ru, Rh, and Pt were recorded in the chromitite unit (as shown in the primitive mantle nomalized plot; figure 4.6.7). This indicates that some phase is controlling Os, Ir, Ru, Rh and Pt more than Pd. The enrichment of these elements within the chromitite unit is further demonstrated by the bottom-loaded PGE mineralisation style, for the respective elements, observed in this study (see figures 4.6.1 and 4.6.2). These observations would suggest that chromite is the PGE controlling phase in this unit (an assumption shared by Barnes and Maier, 2002a). In a similar study (Largatzis, 2014) in which no chromitite was present at a lower peak, this preferential enrichment was also absent, and the concentraion of PGE within this zone instead suggested a sulphide control. Assuming that Os, Ir, Ru, Rh and Pt share similar behaviour, the preferred enrichment of Os, Ir, Ru, Rh and Pt relative to Pd in chromitite stringer (and in the lower pyroxenite unit) may be expressed by low Pd/Ir ratios (Fig. 4.6.4). Furthermore, the low Pt + Pd/IPGE value associated with the chromitite stringer (Fig. 4.6.4) could reflect fractional crystallization in which the IPGE tend to partition into chromitite more readily than Pt and Pd (Brügmann *et al*., 1987; Von Gruenewaldt *et al*., 1989). However, Cr showed only moderately strong correlations with the

IPGE (+ Rh and Pt) and the IPGE (+ Rh and Pt) showed stronger correlations with each other (see Table 4.6.2). This observation was similarly recorded by Barnes and Maier (2002a).

Thus, to account for the enrichment of Os, Ir, Ru, Rh and Pt in the chromitites, Barnes and Maier (2002a) appealed to a model after Capobianco *et al*. (1994) in which Ru and Rh partition into chromite during oxide precipitation but Pd does not. The precipitation of chromite in turn promotes the crystallization of Os, Ir and Pt clusters. Barnes and Maier (2002a) suggested that the partitioning of Ru and Rh into chromite destabilizes these clusters and this results in the precipitation of both PGM (enriched in Os, Ir, Ru, Rh and Pt but not Pd) and chromite (see figure 5.8.2). Furthermore, the argument presented by Godel *et al*. (2010) above, could be circumvented in that PGM would precipitate in the spaces between co-precipitating chromite and silicate grain boundaries. This model is considered to only be applicable to borehole ELF-395 which comprises a chromitite unit. In borehole ELF-393, no chromitite unit was identified and thus some other model is required (Largatzis, 2014). Instead, as mentioned above, this most likely represents the collection of PGE by an immiscible sulphide liquid (Campbell *et al*., 1983)

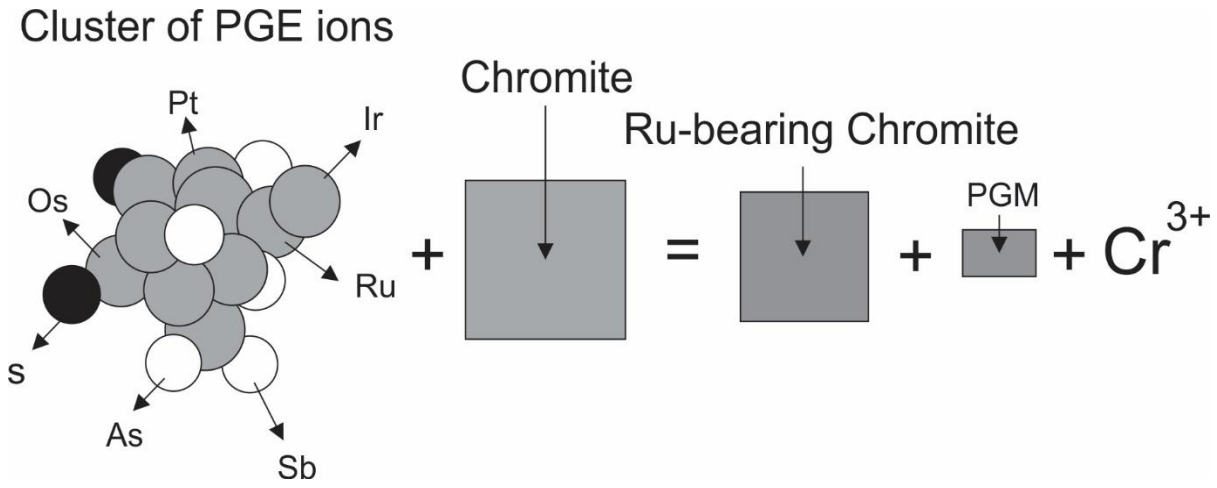

Figure 5.8.2. The cluster model. PGE ions and chalcophile elements cluster together in a silicate melt. Ru (+Rh) may partition into chromite if the magma becomes saturated in chromite. Subsequently, the cluster may be destabilized resulting in both chromite and PGM precipitating. Image modified and adapted from Barnes and Maier (2002b).

5.8.3. Collection and Redistribution of PGE by Late Magmatic/Hydrothermal Fluids

The role of late hydrous fluids in remobilising PGE has become an increasingly popular model to explain the PGE distributions in mineralized reefs (Nicholson and Mathez, 1991; Boudreau and Meurer, 1999; Boudreau, 2008). In this model (refer to Fig. 2.2.1), the upward migration of Cl-rich intercumulus fluids (driven by compaction) dissolves local sulphides; releasing base metals and PGE, which can then partition into the fluid. This fluid then rises up through the cumulate pile until it encounters a layer in which the intercumulus fluid is water-undersaturated. Here, the fluid is dissolved into the intercumulus silicate liquid and the base metals, S and PGM, which the fluid was carrying, are then reprecipitated as BMS to form a reef.

Petrographic evidence for the collection and redistribution of PGE by late hydrous fluids, in this study, is presented in subsection 5.1.2. Ballhaus and Stumpfl (1986) suggested that hydrous silicates and associated alterations in the Merensky Reef developed in proximity to BMS from volatile-enriched, highly fractionated intercumulus melts. This would explain the commonly observed association seen between BMS and hydrous silicates/alterations in this study. However, as mentioned in subsection 5.1, this association could also be explained by the interaction and replacement of silicates by BMS, in which biotite and hornblende are formed as an alteration and reaction product (Vermaak and Hendriks, 1976). It is further possible that both processes could occur; i.e., two hydrous assemblages, in which the first higher temperature assemblage (e.g., through the replacement of silicates by BMS) is overprinted by a later, lower temperature assemblage (e.g., from a fractionated intercumulus melt).

The presence of a pegmatoid in the Merensky Reef has been suggested as evidence for the above presented model (Nicholson and Mathez, 1991; Boudreau, 2008). This coarse grained texture has been used as pervasive evidence for a high fluid content in the magma from which it crystallized (Nicholson and Mathez, 1991; Boudreau, 2008). In this study, although the reef was shown to be coarse-grained, no such pegmatoid was identified. This most likely reflects the wide-reef Merensky facies from which borehole ELF-395 was drilled. Viljoen (1999) noted that in such wide-reef facies, the pegmatoidal unit was less pronounced and completely absent in some cases (see Fig. 2.3.1). This is particularly interesting as borehole ELF-393, which also represents the wide-reef facies, did contain a pegmatoidal pyroxenite which overlied the

pyroxenite unit (Largatzis, 2014). Barnes *et al*. (2002b) argued that pegmatoids may form if the rock is held close to the solidus temperature for longer than normal. Cawthorn and Boerst (2006), in their analysis of the pegmatoid, found no geochemical evidence for the addition of greater concentrations of fluids (as well as incompatible elements) in the pegmatoid compared with overlying pyroxenite. Instead, they attributed the formation of the pegmatitic pyroxenite to the addition of superheated magma which allowed for a period of non-accumulation of grains and increased interaction at the crystal-liquid interface (thus allowing for grain enlargement).

Other evidence cited in literature which supports this model includes the presence of Cl-rich apatites in the reef (Boudreau *et al*., 1986) as well as the REE enrichment observed in pyroxene (Mathez, 1995). Furthermore, experimental studies have shown that in the presence of Cl and S, at temperatures of 1000 °C, Pt and Pd are mobile (Fleet and Wu, 1993). Cawthorn (1996) suggested that the REE enrichment in pyroxene can be explained by the growth of pyroxene from highly evolved liquids as a result of *in situ* fractionation. This view is also supported by Wilson and Chunnett (2006) in their study of the Merensky Reef and also seems applicable to the results of this study (see subsection 5.7).

One major flaw with a late magmatic/hydrothermal fluid model, as discussed by Godel *et al*. (2007), is that it has difficulty in accounting for the stratigraphically higher chromitite layer in the Merensky Reef. While it may be possible to argue that this model is responsible for the formation of the first, stratigraphically lower chromitite layer, Godel *et al*. (2007) suggested that after the formation of the first chromitite layer, the fluid would then have been depleted in S and metals by the time it reached the second chromitite layer (particularly in the wide-reef facies). While no upper chromitite layer was identified in this study, an upper PGE peak does still exist and thus, in considering its formation is a result of late magmatic fluids, the rationale of this argument may still be applied here.

One way to assess the magnitude of fluid migration in the Merensky Reef is to model the dispersion of mobile elements such as Rb and Cs (Wilson and Chunnett, 2006). If weak correlations are observed when such mobile elements are plotted against incompatible (immobile) elements then one may assume that the reef has been affected extensively by the

migration of fluids (Wilson and Chunnett, 2006). In this study, Rb and Cs show strong to moderately strong correlations (Table 5.8.2) with incompatable elements (Zr, Hf, Nb and Th), respectively. This suggest that extensive fluid migration did not occur in the Merenksy Reef, but, as suggested by Wilson and Chunnett (2006), this does not exclude the possibility of limited-scale redistribution by late hydrous fluids in the Merensky Reef (e.g., deuteric alteration).

Table 5.8.2. Correlation coefficients for mobile elements (Rb and Cs) versus incompatible elements (Zr, Hf, Nb and Th) from borehole ELF-395. Units represented in R^2 values.

	Rb	***Cs***	***Zr***	***Hf***	***Nb***	***Th***
Rb	1					
Cs	0.892	1				
Zr	0.746	0.469	1			
Hf	0.748	0.471	0.991	1		
Nb	0.642	0.459	0.732	0.752	1	
Th	0.792	0.531	0.924	0.930	0.721	1

5.9. A Petrogenetic Model for the Merensky Reef

The observations and interpretations made in section 5.8 suggest that a combination of processes are required to account for the distribution of PGE and ultimately for the formation of the Merensky Reef. In summary, the enrichment of Os, Ir, Ru, Rh and Pt in the lower PGE peak, which coincides with the presence of the chromitite unit, can be accounted for by a model involving the crystallization of PGM, and the co-precipitation of chromite (Capobianco *et al*., 1994; Tredoux *et al*., 1995; Barnes and Maier, 2002a). However, observations made in the upper peak (e.g., enrichment in Cu, Ni, Pd, Au and S) best fit a model involving the collection of PGE by an immiscible sulphide liquid (Campbell *et al*., 1983; Naldrett, 1999). Furthermore, contrasting characteristics in PGE geochemistry within the upper and lower pyroxenitic reef unit suggest variations in geochemical processes, in which the PGE distribution in the lower pyroxenite may be attributed to sulphide fractional segregation and sulphide scavenging (Naldrett and Wilson, 1990), while the upper pyroxenite may have formed through a more

dynamically controlled emplacement of PGE-undepleted magma and S during simultaneous sulphide precipitation (Naldrett, 2004; Wilson and Chunnett, 2006). Furthermore, the fractionation of sulphide liquids (Naldrett *et al*., 1982; Naldrett, 2004; Dare *et al*., 2011) has important implications for the observed PGE distributions in the pyroxenite unit (i.e., separation of IPGE and PPGE peaks). Depletions in PGE occurring above and below the lower PGE peak, are attributed to an Ostwald-ripening type of mechanism (see subsection 5.8.1). It is suggested that extensive remobilisation of PGE by late hydrous fluids is not apparent in this study of the Merensky Reef, however, this does not rule out limited-scale redistribution of PGE as evident by late stage hydrous alteration (Wilson and Chunnett, 2006).

Thus, the results of this study favour a model (Fig. 5.9.1) for the Merensky Reef as follows: A lateral injection of pre-contaminated (SiO_2-rich) magma (Fig. 5.9.1A) over pre-existing proto-anorthosite, representing the footwall to the Merensky Reef, introduced already-crystallized orthopyroxene to the magma chamber (Prevec *et al*., 2005; Maier *et al*., 2013). The introduction of this hotter, more primitive magma resulted in the reheating of the anorthositic floor, causing extensive recrystallization. Magma-mixing between the resident (plagioclase-bearing), more evolved magma and the hotter, more primitive magma promoted oxide crystallization which in turn promoted the crystallization of Os, Ir and Pt clusters (Irvine, 1975; 1977; Capobianco *et al*., 1994; Tredoux *et al*., 1995). Ru and Rh, present within the silicate magma, partitioned into chromite (however, Pd did not), which in turn destabilized the clusters and resulted in the co-precipitation of chromite and PGE clusters, as PGM (Capobianco *et al*., 1994; Tredoux *et al*., 1995; Barnes and Maier, 2002a). This resulted in the observed enrichment of Os, Ir, Ru, Rh and Pt in the chromitite stringer. Magma mixing also resulted in the formation of ophitic textures comprising orthopyroxene oikocrysts and inclusions of earlier-crystallized plagioclase chadacrysts (Eales *et al*., 1991). This accounted for mineral disequilibrium between feldspar and orthopyroxene (Prevec *et al*., 2005). Furthermore, reheating and re-equilibration of the footwall unit, during magma mixing, promoted reverse zoning in already-crystallized plagioclase (Vernon, 2004; Shcherbakov *et al*., 2011).

Subsequent pulses of the same magma (Fig. 5.9.1B) brought in further amounts of already-crystallized orthopyroxene, as well as promoted the crystallization of plagioclase from the contaminated magma, thus creating a crystal mush pile (Prevec *et al*., 2005). It is suggested

that the later pulses of magma assimilated with the roof of the chamber and wall rocks (e.g., through conduits). The crustal contamination of this magma, coupled with magma-mixing, resulted in the saturation of sulphide and the formation of an immiscible sulphide liquid (Irvine, 1980; Campbell *et al.*, 1983; Naldrett and Wilson, 1990; Kruger and Schoenberg, 1998; Naldrett, 1999; Cawthorn, 2002). However, the sulphide fractionally segregated and PGE was effectively scavenged (more so than the base metals) from the silicate magma (Campbell *et al.*, 1983; Naldrett and Wilson, 1990; Naldrett, 1999). Thereafter, sulphides were deposited in the interstitial spaces of the cumulus pile along with co-precipitating silicates (such as orthopyroxene and minor plagioclase) which accounted for the formation of the lower cumulus pile (i.e., lower pyroxenite unit). The silicate magma at this stage was depleted in PGE and fractional segregation of sulphide ceased (Naldrett and Wilson, 1990).

A fresh influx of PGE undepleted magma (Fig. 5.9.1B) was introduced at the top of the lower cumulus pile (i.e., at the top of the lower pyroxenite). Inputs of S, from increasing amounts of crustal contamination, induced sulphide saturation and sulphide immiscibility, thus forming the upper PGE peak (enriched in Cu, Ni, Pd and Au relative to the IPGE, Rh and Pt) (Fig. 5.9.1B) (Campbell *et al*., 1983; Lee, 1983; Naldrett and Wilson, 1990; Naldrett, 1999; Maier and Barnes, 1999; Wilson and Chunnett, 2006). The collection process of PGE by immiscible sulphide liquid may have been enhanced through the amount of time that the immiscible sulphide liquid spent within the silicate magma (Naldrett, 1997; 1999). Thereafter, the sulphides percolated downwards (Fig. 5.9.1C) through the cumulus pile, displacing the interstitial liquid and enriching the underlying mafic rocks in sulphide and PGE, which accounted for the enrichment underlying the upper peak (Barnes and Maier, 2002b). Finally, plagioclase-rich liquid was injected into the pyroxenite unit (Fig. 5.9.1C) and crystallized to form the anorthositic seam unit. The anorthosite unit cooled relatively slowly and interstitial plagioclase present within the unit equilibrated with trapped, more evolved liquid which resulted in normal zoning of plagioclase (Prevec *et al*., 2005).

During the cooling of the sulphide liquid, a process of sulphide fractionation occurred in which an early monosulphide solution (Mss) and a residual fractionated liquid (intermediate solid solution; Iss) formed (Naldrett *et al*., 1982; Naldrett, 2004; Dare *et al*., 2011). Saturated conditions thereafter resulted in the IPGE partitioning into the Mss whereas the PPGE

partitioned into the Iss, and later precipitated as PGM (Fleet *et al*., 1993; Maier and Barnes, 1999; Patten *et al*., 2013).

REE-enriched orthopyroxene, and later clinopyroxene, crystallized from the fractionated trapped liquid within the intercumulus pile, imparting the incompatible element signatures seen within the pyroxenite unit (Cawthorn, 1996; Wilson and Chunnett, 2006). During gravitational compaction of the crystal mush pile, plagioclase and orthopyroxene were deformed and the fractionated intercumulus fluid rose through the cumulus pile (Fig. 5.9.1. B), further crystallizing plagioclase and orthopyroxene as oikocrysts which cemented the pile (Barnes and Maier, 2002a). Furthermore, this upwards percolating intercumulus fluid would have removed some of the fractionated sulphide liquid in the cumulus pile and thus accounted for the enrichment of IPGE versus PPGE and the separation of IPGE and PPGE peaks (Barnes and Maier, 2002b; Largatzis, 2014). Any residual trapped liquid left within the intercumulus pile eventually escaped into the overlying magma (Barnes and Maier, 2002a). It is suggested that such migrating hydrous fluids would have only resulted in limited-scale remobilization of PGE, but caused extensive deuteric alteration within the reef (Prevec *et al*., 2005; Wilson and Chunnett, 2006).

Lastly, through an Ostwald-ripening type of process, PGE underlying and overlying the lower PGE peak, were absorbed into this peak, creating depletion haloes in these zones (Largatzis, 2014). This would have overprinted the primary distribution of PGE in these zones (Largatzis, 2014).

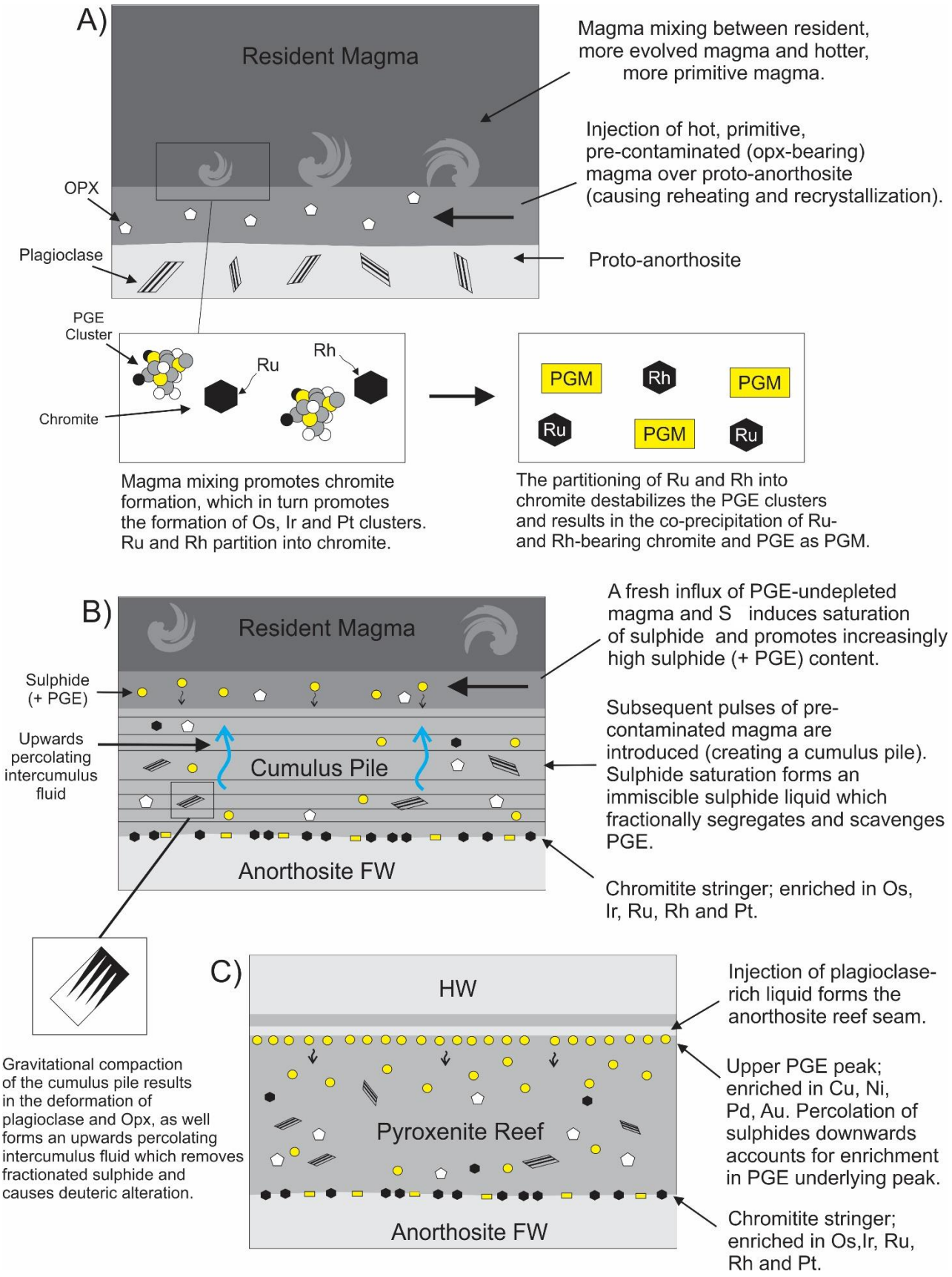

Figure 5.9.1. A petrogenetic model for the Merensky Reef. The model suggest that multiple geochemical processes are required to account for the PGE distributions in the Merensky Reef. Parts of this image are modified and adapted after Barnes and Maier (2002b) and Naldrett *et al*. (2009).

Chapter 6. Summary and Conclusion

The distribution of platinum-group elements (PGE) in ultramafic to mafic layered complexes may provide important information on the petrogenesis of metalliferous PGE-bearing reefs. In spite of the vast existing literature and economic importance of such deposits, the controls in the formation of such reefs still remain controversial. In this study, PGE distributions were used to identify petrogenetic controls and processes responsible for the formation of the Merensky Reef in the Bushveld Complex. Evidence from this study suggest that the petrogenesis of the Merensky Reef is the result of more than one geochemical process.

1) Wide-reef Merensky was obtained from Eland Platinum Mines in the western Bushveld. The drillcore, i.e., ELF-395, measured 16.48 metres in length and was sampled 5 metres into the bottom section of the hangingwall unit and 3 metres into the top section of the footwall unit. From the bottom of the sampled drillcore to the top of the drillcore the sequence was as follows: footwall anorthosite, a 3 mm thick chromitite stringer, an overlying 11.08 metre thick pyroxenite unit, a 23 cm norite unit, a 15 cm thick leuconorite unit and a 2.06 metre thick anorthosite unit. Furthermore, bounded by pyroxenite, and occurring half a metre from the top of the unit, a 20 cm thick anorthositic seam was identified. No evidence of an upper chromitite stringer nor a pegmatoidal pyroxenite unit was recognized in borehole ELF-395.

2) Petrographic analysis of borehole ELF-395 identified the presence of cumulus plagioclase and intercumulus ortho- and clinopyroxene in the footwall anorthosite, reef anorthosite and hangingwall norite, leuconorite and anorthosite units while cumulus ortho- and clinopyroxene and interstitial plagioclase was identified in the pyroxenite reef unit. Zoning of plagioclase and the presence of triple point junctions (consistent with reheating and recrystallization, respectively) were observed in all plagioclase-rich lithologies (e.g., anorthosites, leuconorites and norites). Furthermore, plagioclase and orthopyroxene exhibited evidence of deformation in the pyroxenite unit (e.g., deformation twinning). It was suggested that deformation could have occurred through the compaction of the cumulus pile (Barnes and Maier, 2002a). Oikocrysts of orthopyroxene and clinopyroxene comprising inclusions of resorbed plagioclase chadacrysts and resorbed anhedral orthopyroxene (hosted in clinopyroxene) were common. The formation of these ophitic

textures were attributed to a process involving magma mixing (Eales *et al*., 1991). Inclusions of plagioclase within orthopyroxene, and orthopyroxene in clinopyroxene, indicated a paragenetic sequence as follows: plagioclase, followed by orthopyroxene and then clinopyroxene. Moreover, textural and compositional evidence suggested that plagioclase and orthopyroxene were in mineral disequilibrium with one another (Prevec *et al*., 2005). Base metal sulphides occurred as disseminated aggregates and were particularly abundant in the pyroxenite unit, as were oxides. Furthermore, BMS and oxides showed a strong spatial association to hydrous minerals and alteration. Chromite present in the chromitite stringer exhibited grain annealing and showed apparent reaction rims with surrounding orthopyroxene (possibly representing a disequilibrium feature). Olivine was relatively absent in borehole ELF-395. The presence of hydrous minerals and alteration features in the Merensky Reef were suggested to have formed by late deuteric alteration.

3) Mineral chemistry of plagioclase cores recorded ranges for An content in the Merensky Reef as follows: An_{72-79} in the anorthositic footwall, An_{71-77} in the chromitite stringer, An_{45-78} in the pyroxenite reef unit, An_{47-73} in the anorthosite reef unit, An_{72-76} in the norite hangingwall, An_{75-77} in the leuconorite hangingwall and An_{72-77} in the anorthosite hangingwall. In addition to decreasing An contents from both the hangingwall and footwall units towards the reef (specifically the anorthosite reef unit), trends of decreasing CaO and FeO, and increasing Na_2O and K_2O, were also recorded. The data suggest that the reef units (specifically the anorthosite reef unit) are more evolved than the footwall and hangingwall units. Reverse zoning of plagioclase was identified in the anorthosite footwall unit while normal zoning was identified in the anorthosite reef unit. The implication of this is that the footwall unit underwent reheating and re-equilibration with a hotter, more primitive magma while the anorthosite reef unit cooled relatively slowly and interstitial plagioclase present within the unit equilibrated with a trapped, more evolved liquid (Prevec *et al*., 2005; Seabrook *et al*., 2005). Pyroxene compositions were less variable compared to plagioclase compositions. Mg # in clinopyroxene cores ranged as follows: 74 - 78 in the anorthositic footwall, 72 - 84 in the chromitite stringer, 78 - 88 in the pyroxenite reef unit, 82 - 85 in the anorthosite reef unit, 77 - 81 in the norite hangingwall, 77 – 81 in the leuconorite hangingwall and 76 – 82 in the anorthosite hangingwall. Furthermore, in addition to increasing Mg # towards the reef units (particularly the pyroxenite unit) from both the HW and FW units, trends of increasing CaO and decreasing FeO were also recorded. Based on

these trends and variation in pyroxene compositions, the hangingwall and footwall units appear to be more evolved than the reef units (particularly the pyroxenite unit).

4) Whole-rock major, minor and trace element geochemistry provided further information on the petrogenesis of the Merensky Reef. The pyroxenite reef shows enrichment in incompatible elements (e.g., Zr) and negative Eu-anomalies which indicate a trapped liquid control (Wilson and Chunnett, 2006; Maier *et al*., 2013). Furthermore, variation in REE patterns suggest that the Merensky Reef is the result of multiple magmas. The whole-rock major element geochemistry in the Merensky Reef (particularly in the silicate layers) was attributed to a control by the mutual influence of co-precipitating minerals competing for major elements (Kottke-Levin *et al.*, 2009). Cu, Ni and Co showed a maximum enrichment peak at the contact between the anorthosite seam and the underlying pyroxenite reef. These peaks coincided with a S peak and suggested a primary control by sulphide. Cu, Ni, Co and S concentrations remained relatively enriched in the underlying two metres below the peak. Cr showed depletions in the HW and FW units, relative enrichment in the pyroxenite unit and a maximum concentration peak within the chromitite stringer.

5) Whole-rock PGE geochemistry identified two main PGE peaks: 1) a stratigraphically higher peak (i.e., upper PGE peak) which coincided with peaks in Cu, Ni, Co and S and 2) a stratigraphically lower peak (i.e., lower PGE peak) which coincided with the chromitite stringer. The upper PGE peak showed enrichment in Pd and Au relative to all other PGE while the lower PGE peak showed enrichment in Os, Ir, Ru, Rh and Pt relative to Pd (+ Au). The formation of the lower peak was consistent with a model involving the co-precipitation of chromite and PGE clusters (Capobianco *et al*., 1994; Tredoux *et al*., 1995; Barnes and Maier, 2002a) while the upper peak was attributed to a model involving the collection of PGE by an immiscible sulphide liquid (Campbell *et al*., 1983; Naldrett, 1999). Total PGE contents recorded up to ~ 6 ppm in the upper peak while the lower peak had a total PGE concentration of ~ 18.7 ppm. Furthermore, PGE were shown to remain relatively enriched underlying the upper PGE peak (as reported in Cu, Ni, Co and S concentrations). No enrichment in PGE was reported in the underlying rocks below the lower PGE peak. High Cu/Pd and Pt/Pd ratios within the lower pyroxenite unit indicated a process of sulphide fractional segregation and scavenging while the inverse (as recorded in the upper pyroxenite) was attributed to a more dynamic system in which both S and PGE undepleted magma were entering the zone at the same time as sulphide precipitation (Wilson and

Chunnett, 2006). Logarithmic plots of PGE distributions in the Merensky Reef showed a separation of peaks, in which distinct PPGE peaks were observed (while IPGE was depleted). Although no IPGE peaks were recorded, they were identified in a similar study (Largatzis, 2014) and thus suggested different partitioning behaviours for the PPGE versus the IPGE. The separation of the PPGE from the IPGE peaks was interpreted to reflect a sulphide fractionation model in which IPGE partition into the Mss and PPGE partition into the Iss (Naldrett *et al*., 1982; Fleet *et al*., 1993; Maier and Barnes, 1999; Naldrett, 2004; Dare *et al*., 2011; Patten *et al*., 2013). It was suggested that later upwards percolating intercumulus fluids may be able to remove some of the fractionated sulphide liquid (thus accounting for the separation of PPGE peaks from IPGE peaks) (Barnes and Maier, 2002b). Furthermore, zones of depletion were identified, in which all PGE are depleted. These zones were observed immediately above and below the lower PGE peak, as well as above the upper PGE peak. Similar observations were recorded in Largatzis (2014) and were interpreted to represent an Ostwald ripening-type mechanism in which PGE surrounding the main PGE peaks were absorbed into it.

The proposed model for the formation of the Merensky Reef suggested that a combination of geochemical processes and multiple replenishments of magma are required to account for its formation, including the collection of PGE by an immiscible sulphide liquid (Campbell *et al*., 1983; Naldrett, 1999) and the crystallization of PGE as PGM (Capobianco *et al*., 1994; Tredoux *et al*., 1995; Barnes and Maier, 2002a). Extensive redistribution of PGE by late magmatic/hydrothermal fluids was not evident from the results of this study, but this does not rule out limited-scale redistribution of PGE (Wilson and Chunnett, 2006) as suggested by pervasive deuteric alteration. It is suggested that PGE distributions provide a useful tool in investigating the petrogenesis of metalliferous (PGE-bearing) reefs and that the findings of this study may be applied to other-PGE mineralized reefs.

References

Anders, E., & Grevesse, N., 1989. Abundances of the elements: Meteoritic and solar. *Geochimica et Cosmochimica acta*, 53(1), 197-214.

Anderson, O., 1915. The system anorthite-forsterite-silica. *American Journal of Science, 4th Series*, 39, 407-454.

Arndt, N., Jenner, G., Ohnenstetter, M., Deloule, E., & Wilson, A. H., 2005. Trace elements in the Merensky Reef and adjacent norites Bushveld complex South Africa. *Mineralium Deposita*, 40(5), 550-575.

Ballhaus, C. G., & Stumpfl, E. F., 1986. Sulfide and platinum mineralization in the Merensky Reef: evidence from hydrous silicates and fluid inclusions. *Contributions to Mineralogy and Petrology*, 94(2), 193-204.

Ballhaus, C. G., & Sylvester, P., 2000. Noble metal enrichment processes in the Merensky Reef, Bushveld Complex. *Journal of Petrology*, 41(4), 545-561.

Barnes, S.-J. & Maier, W. D., 1999. The fractionation of Ni, Cu and the noble metals in silicate and sulfide liquids. In: Keays, R. R. (ed.) *Dynamic Processes in Magmatic Ore Deposits and their Application in Mineral Exploration. Geological Association of Canada, Short Course Notes* 13, 69–106.

Barnes, S.-J., & Maier, W.D., 2002a. Platinum-group elements and microstructures of normal Merensky Reef from Impala platinum mines, Bushveld Complex. *Journal of Petrology*, 43(1), 103-128.

Barnes, S.-J., & Maier, W.D., 2002b. Platinum-group element distributions in the Rustenburg layered suite of the Bushveld Complex, South Africa. *The Geology, geochemistry, mineralogy and mineral beneficiation of platinum-group elements*, 54, 431-458.

Barnes, S.-J., Makovicky, E., Makovicky, M., Rose-Hansen, J., & Karup-Moller, S., 1997. Partition coefficients for Ni, Cu, Pd, Pt, Rh, and Ir between monosulfide solid solution and sulfide liquid and the formation of compositionally zoned Ni-Cu sulfide bodies by fractional crystallization of sulfide liquid. *Canadian Journal of Earth Sciences*, 34(4), 366-374.

Barnes, S.-J., Naldrett, A. J., & Gorton, M. P., 1985. The origin of the fractionation of platinum-group elements in terrestrial magmas. *Chemical Geology*, 53(3), 303-323.

Bell, T., 2015. Platinum Group Metals (PGMs) - What are PGMs?. [ONLINE]. Available at: http://metals.about.com/od/properties/a/Platinum-Group-Metals-Pgms.htm. [Accessed 19 March 15].

Borisov, A., & Palme, H., 1997. Experimental determination of the solubility of platinum in silicate melts. *Geochimica et Cosmochimica Acta*, 61(20), 4349-4357.

Boudreau, A. E., 2008. Modeling the Merensky Reef, Bushveld Complex, Republic of South Africa. *Contributions to Mineralogy and Petrology*, 156(4), 431-437.

Boudreau, A. E., & Meurer, W. P., 1999. Chromatographic separation of the platinum-group elements, gold, base metals and sulfur during degassing of a compacting and solidifying igneous crystal pile. *Contributions to Mineralogy and Petrology*, 134(2-3), 174-185.

Boudreau, A. E., Mathez, E. A., & McCallum, I. S., 1986. Halogen geochemistry of the Stillwater and Bushveld Complexes: evidence for transport of the platinum-group elements by Cl-rich fluids. *Journal of Petrology*, 27(4), 967-986.

Brenan, J. M., & Andrews, D., 2001. High-temperature stability of laurite and Ru–Os–Ir alloy and their role in PGE fractionation in mafic magmas. *The Canadian Mineralogist*, 39(2), 341-360.

Brügmann, G. E., Arndt, N. T., Hofmann, A. W., & Tobschall, H. J., 1987. Noble metal abundances in komatiite suites from Alexo, Ontario and Gorgona Island, Colombia. *Geochimica et Cosmochimica Acta*, 51(8), 2159-2169.

Cameron, E. N., 1982. Upper Critical Zone, Eastern Bushveld Complex. *Economic Geology*, 77(6), 1307-1327.

Cameron, E.N., 1980. Evolution of the lower critical zone, central sector, eastern Bushveld Complex. *Economic Geology*, 75, 845-875.

Campbell, I.H., Naldrett, A.J. & Barnes, S.J., 1983. A model for the origin of the platinum-rich sulfide deposits in the Bushveld and Stillwater Complexes. *Journal of Petrolology*, 24, 133-165.

Capobianco, C. J., Hervig, R. L., & Drake, M. J., 1994. Experiments on crystal/liquid partitioning of Ru, Rh and Pd for magnetite and hematite solid solutions crystallized from silicate melt. *Chemical Geology*, 113(1-2), 23-43.

Cawthorn, R. G., 1996. Models for incompatible trace element abundances in cumulus minerals and their application to plagioclase and pyroxenes in the Bushveld Complex. *Contributions to Mineralogy and Petrology*, 123, 109–115.

Cawthorn, R. G., 2002. The role of magma mixing in the genesis of PGE mineralization in the Bushveld Complex: thermodynamic calculations and new interpretations—a discussion. *Economic Geology*, 97(3), 663-666.

Cawthorn, R. G., 2010. Geological interpretations from the PGE distribution in the Bushveld Merensky and UG2 chromitite reefs. *The 4th International Platinum Conference, Platinum in transition 'Boom or Bust', The Southern African Institute of Mining and Metallurgy.*

Cawthorn, R. G., & Barry, S. D., 1992. The role of intercumulus residua in the formation of pegmatoid associated with the UG2 chromitite, Bushveld Complex. *Australian Journal of Earth Sciences*, 39(3), 263-276.

Cawthorn, R. G., & Boerst, K., 2006. Origin of the pegmatitic pyroxenite in the Merensky unit, Bushveld Complex, South Africa. *Journal of Petrology*, 47(8), 1509-1530.

Cawthorn, R. G., & Walraven, F., 1998. Emplacement and crystallization time for the Bushveld Complex. *Journal of Petrology*, 39(9), 1669-1687.

Cawthorn, R. G., & Webb, S. J., 2013. Cooling of the Bushveld Complex, South Africa: Implications for paleomagnetic reversals. *Geology*, 41(6), 687-690.

Dare, S., Barnes, S.-J., Prichard, H., Fisher, P., 2011. Chalcophile and platinum-group element (PGE) concentrations in the sulfide minerals from the McCreedy East deposit, Sudbury, Canada, and the origin of PGE in pyrite. *Mineralium Deposita*, 46, 381-407.

Drake, M. J., & Weill, D. F., 1975. Partition of Sr, Ba, Ca, Y, Eu 2+, Eu 3+, and other REE between plagioclase feldspar and magmatic liquid: an experimental study. *Geochimica et Cosmochimica Acta*, 39(5), 689-712.

Eales, H. V., 2000. Implications of the chromium budget of the Western Limb of the Bushveld Complex. *South African Journal of Geology*, 103(2), 141-150.

Eales, H. V., & Cawthorn, R. G., 1996. The bushveld complex. *Developments in Petrology*, 15, 181-229.

Eales, H. V., & Costin, G., 2012. Crustally contaminated komatiite: primary source of the chromitites and Marginal, Lower, and Critical Zone magmas in a staging chamber beneath the Bushveld Complex. *Economic Geology*, 107(4), 645-665.

Eales, H. V., De Klerk, W. J., & Teigler, B., 1990. Evidence for magma mixing processes within the Critical and Lower Zones of the northwestern Bushveld Complex, South Africa. *Chemical Geology*, 88(3), 261-278.

Eales, H. V., Maier, W. D., & Teigler, B., 1991. Corroded plagioclase feldspar inclusions in orthopyroxene and olivine of the Lower and Critical Zones, Western Bushveld Complex. *Mineralogical Magazine*, 55, 479-786.

Fleet, M. E., Chryssoulis, S. L., Stone, W. E., & Weisener, C. G., 1993. Partitioning of platinum-group elements and Au in the Fe− Ni− Cu− S system: experiments on the fractional crystallization of sulfide melt. *Contributions to Mineralogy and Petrology*, 115(1), 36-44.

Fleet, M. E., Crocket, J. H., Liu, M., & Stone, W. E., 1999. Laboratory partitioning of platinum-group elements (PGE) and gold with application to magmatic sulfide–PGE deposits. *Lithos*, 47(1), 127-142.

Fleet, M. E., & Stone, W. E., 1991. Partitioning of platinum-group elements in the Fe-Ni-S system and their fractionation in nature. *Geochimica et Cosmochimica Acta*, 55(1), 245-253.

Fleet, M. E., & Wu, T. W., 1993. Volatile transport of platinum-group elements in sulfide-chloride assemblages at 1000 C. *Geochimica et cosmochimica acta*, 57(15), 3519-3531.

Frost, B. R., & Frost, C. D., 2013. Essentials of Igneous and Metamorphic Petrology. *Cambridge University Press*. 118.

Godel, B., Barnes, S. J., & Maier, W. D., 2006. 3-D distribution of sulphide minerals in the Merensky Reef (Bushveld Complex, South Africa) and the JM Reef (Stillwater Complex, USA) and their relationship to microstructures using X-ray computed tomography. *Journal of Petrology*, 47(9), 1853-1872.

Godel, B., Barnes, S. J., & Maier, W. D., 2007. Platinum-group elements in sulphide minerals, platinum-group minerals, and whole-rocks of the Merensky Reef (Bushveld Complex, South Africa): implications for the formation of the reef. *Journal of Petrology*, 48(8), 1569-1604.

Godel, B., Barnes, S. J., Barnes, S. J., & Maier, W. D., 2010. Platinum ore in three dimensions: Insights from high-resolution X-ray computed tomography. *Geology*, 38(12), 1127-1130.

Google Earth 7.1.2.2041., 2015. Eland Platinum Mine, Western Bushveld, 25°38'23.04" S 27°52'57.54" E, 1198m. [26/05/15]. Available from: https://earth.google.com/

Harmer, R. E., & Sharpe, M. R., 1985. Field relations and strontium isotope systematics of the marginal rocks of the eastern Bushveld Complex. *Economic Geology*, 80(4), 813-837.

Harne, D. M., & Von Gruenewaldt, G., 1995. Ore-forming processes in the upper part of the Bushveld complex, South Africa. *Journal of African Earth Sciences*, 20(2), 77-89.

Harris, C., Pronost, J. J., Ashwal, L. D., & Cawthorn, R. G., 2005. Oxygen and hydrogen isotope stratigraphy of the Rustenburg Layered Suite, Bushveld Complex: constraints on crustal contamination. *Journal of Petrology*, 46(3), 579-601.

Helmenstine, T., 2015. Periodic Table With Charges. [ONLINE] Available at: http://sciencenotes.org/periodic-table-with-charges/. [Accessed 01 November 15].

Hiemstra, S. A., 1979. The role of collectors in the formation of the platinum deposits in the Bushveld Complex. *Canadian Mineralogist*, 17, 469–482.

Hutchinson, D., Foster, J., Prichard, H., & Gilbert, S., 2015. Concentration of particulate platinum-group minerals during magma emplacement; a case study from the Merensky Reef, Bushveld Complex. *Journal of Petrology*, 56(1), 113-159.

ICDA., 2015. What is Chrome. [ONLINE]. Available at: http://www.icdacr.com/index.php?option=com_content&view=article&id=105&Itemid=166&lang=en. [Accessed 23 March 15].

Irvine, T. N., 1975. Crystallization sequences in the Muskox intrusion and other layered intrusions—II. Origin of chromitite layers and similar deposits of other magmatic ores. *Geochimica et Cosmochimica Acta*, 39(6), 991-1020.

Irvine, T. N., 1977. Origin of chromitite layers in the Muskox intrusion and other stratiform intrusions: a new interpretation. *Geology*, 5(5), 273-277.

Irvine, T. N., 1980. Magmatic infiltration metasomatism, double-diffusive fractional crystallization, and adcumulus growth in the Muskox intrusion and other layered intrusions. *Physics of magmatic processes*, 325-383.

Kinloch, E. D., 1982. Regional trends in the platinum-group mineralogy of the critical zone of the Bushveld Complex, South Africa. *Economic Geology*, 77(6), 1328-1347.

Kottke-Levin, J., Tredoux, M., & Gräbe, P. J., 2009. An investigation of the geochemistry of the Middle Group of the eastern Bushveld complex, South Africa Part 1–the chromitite layers. *Applied Earth Science: Transactions of the Institutions of Mining and Metallurgy: Section B*, 118(3-4), 111-130.

Kruger, F. J., 2010. The Merensky and Bastard cyclic units and the Platreef of the Bushveld Complex: consequences of Main Zone magma influxes and dynamics. In *The 4th International Platinum Conference, Platinum in Transition 'Boom or Bust', Southern African Institute of Mining and Metallurgy* (pp. 43-46).

Kruger, F. J., & Schoenberg, R., 1998. Isotope evidence for the origin of PGE rich Bushveld chromitites and the Merensky Reef by felsic magma mixing. In: *Proceedings of the eighth international platinum symposium abstracts, GSSA/SAIMM symposium series S,* 18, 185-188.

Largatzis, S.A., 2014. PGE distributions in Merensky wide-reef facies: petrogenetic implications. (Honours dissertation, Rhodes University).

Latypov, R., O'Driscoll, B., & Lavrenchuk, A., 2013. Towards a model for the in situ origin of PGE reefs in layered intrusions: insights from chromitite seams of the Rum Eastern Layered Intrusion, Scotland. *Contributions to Mineralogy and Petrology*, 166(1), 309-327.

Lee, C. A., & Butcher, A. R., 1990. Cyclicity in the Sr isotope stratigraphy through the Merensky and Bastard Reef units, Atok section, eastern Bushveld Complex. *Economic Geology*, 85(4), 877-883.

Li, C., Barnes, S. J., Makovicky, E., Rose-Hansen, J., & Makovicky, M., 1996. Partitioning of nickel, copper, iridium, rhenium, platinum, and palladium between monosulfide solid solution and sulfide liquid: effects of composition and temperature. *Geochimica et Cosmochimica Acta*, 60(7), 1231-1238.

Li, C., Ripley, E. M., Sarkar, A., Shin, D. & Maier, W. D., 2005. Origin of phlogopite–orthopyroxene inclusions in chromites from the Merensky Reef of the Bushveld Complex, South Africa. *Contributions to Mineralogy and Petrology*, 150, 119–130.

Lipin, B.R., 1993. Pressure increases, the formation of chromite seams, and the development of the ultramafic series in the Stillwater Complex, Montana. Journal of Petrology, 34, 955-976.

Maier, W. D., 1995. Olivine oikocrysts in Bushveld anorthosite: some implications for cumulate formation. *Canadian Mineralogist*, 33, 1011-1022.

Maier, W. D., 2005. Platinum-group element (PGE) deposits and occurrences: mineralization styles, genetic concepts, and exploration criteria. *Journal of African Earth Sciences*, 41(3), 165-191.

Maier, W. D., & Barnes, S.-J., 1998. Concentrations of rare earth elements in silicate rocks of the Lower, Critical and Main Zones of the Bushveld Complex. *Chemical Geology*, 150(1), 85-103.

Maier, W. D., Barnes, S. J., & De Waal, S. A., 1998. Exploration for magmatic Ni-Cu-PGE sulphide deposits; a review of recent advances in the use of geochemical tools, and their application to some South African ores. *South African Journal of Geology*, 101(3), 237-253.

Maier, W. D., Li, C., & De Waal, S. A., 2001. Why are there no major Ni–Cu sulfide deposits in large layered mafic-ultramafic intrusions? *The Canadian Mineralogist*, 39(2), 547-556.

Maier, W.D., & Barnes, S.-J., 1999. Platinum-group elements in silicate rocks of the lower, critical, and main zones at Union Section, western Bushveld Complex. *J. Petrol*., 40, 1647–1671.

Maier, W.D., Barnes, S.-J. & Groves, D.I., 2013. The Bushveld Complex, South Africa: formation of platinum-palladium, chrome- and vanadium-rich layers via a hydrodynamic sorting of a mobilized cumulate slurry in a large, relatively slowly cooling, subsiding magma chamber. *Mineral Deposita*, 48, 1-56.

Marsh, B. D., 1996. Solidification fronts and magmatic evolution. *Mineralogical Magazine*, 60(398), 5-40.

Mathez, E. A., 1995. Magmatic metasomatism and formation of the Merensky Reef, Bushveld Complex. *Contributions to Mineralogy and Petrology*, 119(2-3), 277-286.

Mathez, E. A., 1999. On factors controlling the concentrations of platinum-group elements in layered intrusions and chromitites. In*:* Keays, R.R., Eds. *Dynamic processes in magmatic ore deposits and their application in mineral exploration. Geological Association of Canada, short course notes*, 13, 251 – 285.

Mathez, E. A., & Waight, T. E., 2003. Lead isotopic disequilibrium between sulfide and plagioclase in the Bushveld Complex and the chemical evolution of large layered intrusions. *Geochimica et Cosmochimica Acta*, 67(10), 1875-1888.

MINXCON., 2009. An Independent Technical Report on Project Areas 1 and 1a of the Western Bushveld Joint Venture (WBJV) located on the Western Limb of the Bushveld Igneous Complex, South Africa. MINXCON, 10-11.

Mitchell, A. A., & Scoon, R. N., 2007. The Merensky reef at Winnaarshoek, Eastern Bushveld Complex: a primary magmatic hypothesis based on a wide reef facies. *Economic Geology*, 102(5), 971-1009.

Naldrett, A. J., 1997. Key factors in the genesis of Noril'sk, Sudbury, Jinchuan, Voisey's Bay and other world-class Ni-Cu-PGE deposits: Implications for exploration. *Australian Journal of Earth Sciences*, 44(3), 283-315.

Naldrett, A. J., 1999. World-class Ni-Cu-PGE deposits: key factors in their genesis. *Mineralium deposita*, 34(3), 227-240.

Naldrett, A. J., 2004. *Magmatic sulfide deposits: geology, geochemistry and exploration*. Springer. 589.

Naldrett, A. J., & Von Gruenewaldt, G., 1989. Association of platinum-group elements with chromitite in layered intrusions and ophiolite complexes. *Economic Geology*, 84(1), 180-187.

Naldrett, A. J., & Wilson, A. H., 1990. Horizontal and vertical variations in noble-metal distribution in the Great Dyke of Zimbabwe: A model for the origin of the PGE mineralization by fractional segregation of sulfide. *Chemical Geology*, 88(3), 279-300.

Naldrett, A. J., Innes, D. G., Sowa, J., & Gorton, M. P., 1982. Compositional variations within and between five Sudbury ore deposits. *Economic Geology*, 77(6), 1519-1534.

Naldrett, A. J., Wilson, A., Kinnaird, J., & Chunnett, G., 2009. PGE tenor and metal ratios within and below the Merensky Reef, Bushveld Complex: implications for its genesis. *Journal of Petrology*, 50(4), 625-659.

Nicholson, D. M. & Mathez, E.A., 1991. Petrogenesis of the Merensky Reef in the Rustenburg Section of the Bushveld Complex. *Contributions to Mineralogy and Petrology*, 107, 293-309.

Patten, C., Barnes, S. J., Mathez, E. A., & Jenner, F. E., 2013. Partition coefficients of chalcophile elements between sulfide and silicate melts and the early crystallization history of sulfide liquid: LA-ICP-MS analysis of MORB sulfide droplets. *Chemical Geology*, 358, 170-188.

Peach, C. L., Mathez, E. A., & Keays, R. R., 1990. Sulfide melt-silicate melt distribution coefficients for noble metals and other chalcophile elements as deduced from MORB: implications for partial melting. *Geochimica et Cosmochimica Acta*, 54(12), 3379-3389.

Prevec, S. A., Ashwal, L. D., & Mkaza, M. S., 2005. Mineral disequilibrium in the Merensky Reef, western Bushveld Complex, South Africa: new Sm–Nd isotopic evidence. *Contributions to Mineralogy and Petrology*, 149(3), 306-315.

Raines, M. D., 2014. *An Assessment of Equilibrium in the Merensky Reef: A Textural, Geochemical and Nd Isotope Study of Coexisting Plagioclase and Orthopyroxene from Winnaarshoek in the Eastern Bushveld Complex, RSA* (Doctoral dissertation, Rhodes University).

Robb, L., 2005. *Introduction to ore-forming processes*. Blackwell Science Ltd. Oxford, 373.

Sattari, P., Brenan, J. M., Horn, I., & McDonough, W. F., 2002. Experimental constraints on the sulfide- and chromite-silicate melt partitioning behaviour of rhenium and platinum-group elements. *Economic Geology*, 97(2), 385-398.

Savard, D., Barnes, S-J., and Meisel, T., 2010. *Geostandards and Geoanalytical Research*, 3(34), 281-291.

Schoenberg, R., Kruger, F. J., Nägler, T. F., Meisel, T., & Kramers, J. D., 1999. PGE enrichment in chromitite layers and the Merensky Reef of the western Bushveld Complex; a Re–Os and Rb–Sr isotope study. *Earth and Planetary Science Letters*, 172(1), 49-64.

Schouwstra, R. P., Kinloch, E. D., & Lee, C. A., 2000. A short geological review of the Bushveld Complex. *Platinum Metals Review*, 44(1), 33-39.

Seabrook, C. L., Cawthorn, R. G., & Kruger, F. J., 2005. The Merensky Reef, Bushveld Complex: mixing of minerals not mixing of magmas. *Economic Geology*, 100(6), 1191-1206.

Sharpe, M. R., & Irvine, T. N., 1983. Melting relations of two Bushveld chilled margin rocks and implications for the origin of chromitite. *Carnegie Institute Washington Yearbook*, 82, 295-300.

Shcherbakov, V. D., Plechov, P. Y., Izbekov, P. E., & Shipman, J. S., 2011. Plagioclase zoning as an indicator of magma processes at Bezymianny Volcano, Kamchatka. *Contributions to Mineralogy and Petrology*, 162(1), 83-99.

Tredoux, M., Lindsay, N.M., Davies, G. and McDonald, I., 1995. The fractionation of platinum-group elements in magmatic systems, with suggestion of a novel causal mechanism. *South African Journal of Geology*, 98(2), 157-168.

U.S. Geological Survey., 2004. Platinum-Group Metals—World Supply and Demand. U.S. Geological Survey, 10-14.

U.S. Geological Survey., 2015. Mineral commodity summaries 2015: U.S. Geological Survey, 45-46.

Vermaak, C. F., & Hendriks, L. P., 1976. A review of the mineralogy of the Merensky Reef, with specific reference to new data on the precious metal mineralogy. *Economic Geology*, 71(7), 1244-1269.

Vernon, R. H., 2004. *A practical guide to rock microstructure*. Cambridge university press. 139.

Viljoen, M. J., 1999. The nature and origin of the Merensky Reef of the western Bushveld Complex based on geological facies and geological data. *South African Journal of Geology*, 102(3), 221-239.

Von Gruenewaldt, G., Hulbert, L.J., and Naldrett, A.J., 1989. Contrasting platinum-group element concentration patterns in cumulus of the Bushveld Complex. *Mineralium Deposita*, 24, 219-229.

Wagner, P.A., 1929. *The platinum deposits of the Bushveld Complex*. Oliver and Boyd, Edinburgh, 588.

Webb, S. J., Cawthorn, R. G., Nguuri, T., & James, D., 2004. Gravity modelling of Bushveld Complex connectivity supported by Southern African seismic experiment results. *South African Journal of Geology*, 107(1-2), 207-218.

Weill, D. F., & Drake, M. J., 1973. Europium anomaly in plagioclase feldspar: experimental results and semiquantitative model. *Science*, 180(4090), 1059-1060.

Wilson, A., & Chunnett, G., 2006. Trace element and platinum group element distributions and the genesis of the Merensky Reef, Western Bushveld Complex, South Africa. *Journal of Petrology*, 47(12), 2369-2403.

Yudovskaya, M., Kinnaird, J., Naldrett, A. J., Mokhov, A. V., McDonald, I., & Reinke, C., 2011. Facies variation in PGE mineralization in the central Platreef of the Bushveld Complex, South Africa. *The Canadian Mineralogist*, 49(6), 1349-1384.

Appendix 1: Plagioclase Compositions. Oxide data are presented in wt. %. Plagioclases were normalised to 8 oxygens.

Point	Sample	Unit	SiO_2	TiO_2	Al_2O_3	FeO	MnO	MgO	CaO	Na_2O	K_2O	BaO	Total	Total Cations	% An
1	MR02_fsp_1	Anorthosite HW	50.62	0.14	30.49	0.32	0.01	0.01	14.91	2.62	0.16	0.00	**99.26**	**4.97**	75.2
2	MR02_fsp_2	Anorthosite HW	50.76	0.00	30.38	0.36	0.03	0.01	14.73	2.62	0.19	0.00	**99.09**	**4.97**	74.8
3	MR02_fsp_3	Anorthosite HW	51.26	0.21	30.17	0.37	0.09	0.02	14.81	2.69	0.16	0.05	**99.82**	**4.96**	74.5
4	MR02_fsp_4	Anorthosite HW	50.36	0.00	30.69	0.44	0.00	0.03	15.20	2.40	0.19	0.12	**99.42**	**4.97**	76.9
5	MR02_fsp_5	Anorthosite HW	51.30	0.14	30.25	0.32	0.07	0.02	14.58	2.91	0.21	0.00	**99.80**	**4.97**	72.6
6	MR02_fsp_6	Anorthosite HW	50.63	0.03	30.55	0.41	0.00	0.00	15.00	2.66	0.17	0.00	**99.45**	**4.97**	74.9
7	MR02_fsp_incl1	Anorthosite HW	50.80	0.00	30.59	0.40	0.06	0.02	14.90	2.59	0.20	0.18	**99.72**	**4.97**	75.2
8	MR02_fsp_incl2	Anorthosite HW	50.53	0.00	30.34	0.47	0.00	0.00	15.10	2.43	0.17	0.00	**99.02**	**4.96**	76.7
9	MR02_fsp_incl3	Anorthosite HW	50.57	0.00	30.49	0.32	0.03	0.01	15.17	2.36	0.16	0.00	**99.11**	**4.96**	77.3
10	MR02_fsp_incl4	Anorthosite HW	51.32	0.00	30.34	0.34	0.00	0.02	14.46	2.77	0.17	0.14	**99.56**	**4.96**	73.5
11	MR02_fsp7	Anorthosite HW	50.79	0.03	30.43	0.21	0.00	0.03	14.74	2.77	0.14	0.00	**99.14**	**4.97**	74.0
12	MR02_fsp8	Anorthosite HW	50.83	0.12	30.33	0.29	0.00	0.00	14.65	2.77	0.14	0.00	**99.13**	**4.97**	73.9
13	MR02_fsp9	Anorthosite HW	51.05	0.21	30.56	0.25	0.00	0.01	14.76	2.73	0.18	0.01	**99.74**	**4.97**	74.2
14	MR02_fsp10	Anorthosite HW	50.17	0.05	30.95	0.30	0.01	0.02	15.22	2.41	0.12	0.00	**99.25**	**4.97**	77.2
15	MR04_fsp11	Anorthosite HW	51.38	0.18	30.48	0.34	0.00	0.04	14.70	2.74	0.22	0.00	**100.08**	**4.97**	73.8
16	MR04_fsp12	Anorthosite HW	50.23	0.00	30.98	0.45	0.00	0.01	15.24	2.34	0.19	0.06	**99.50**	**4.97**	77.4
17	MR04_fsp_incl5	Anorthosite HW	50.76	0.11	30.72	0.31	0.01	0.02	15.06	2.46	0.18	0.00	**99.63**	**4.96**	76.4
18	MR04_fsp_incl6	Anorthosite HW	50.65	0.30	30.40	0.37	0.05	0.04	14.91	2.52	0.17	0.00	**99.41**	**4.96**	75.7
19	MR04_fsp_incl7	Anorthosite HW	49.81	0.00	30.82	0.41	0.07	0.02	15.11	2.44	0.18	0.02	**98.88**	**4.98**	76.5
20	MR04_fsp_incl8	Anorthosite HW	50.22	0.02	30.86	0.27	0.08	0.03	15.55	2.27	0.19	0.12	**99.59**	**4.97**	78.2
21	MR04_fsp_incl9	Anorthosite HW	50.38	0.00	31.06	0.35	0.00	0.02	15.50	2.24	0.19	0.06	**99.81**	**4.96**	78.4
22	MR04_fsp_incl10	Anorthosite HW	50.23	0.06	30.76	0.31	0.06	0.03	15.30	2.35	0.17	0.02	**99.30**	**4.97**	77.5
23	MR04_fsp_incl11	Anorthosite HW	50.55	0.00	30.89	0.35	0.00	0.01	15.25	2.43	0.16	0.00	**99.64**	**4.97**	76.9
24	MR04_fsp13	Anorthosite HW	51.42	0.00	30.01	0.40	0.00	0.04	14.57	2.82	0.19	0.06	**99.50**	**4.97**	73.3
25	MR04_fsp14	Anorthosite HW	50.72	0.00	30.39	0.26	0.00	0.03	14.74	2.60	0.22	0.05	**99.00**	**4.97**	74.8
26	MR04_fsp16	Anorthosite HW	51.58	0.12	29.83	0.37	0.00	0.03	14.17	2.91	0.25	0.05	**99.31**	**4.96**	71.8
27	MR06_fsp17	Leuconorite HW	51.25	0.00	30.72	0.17	0.03	0.03	14.92	2.55	0.21	0.01	**99.88**	**4.96**	75.4
28	MR06_fsp18	Leuconorite HW	50.44	0.02	30.86	0.32	0.03	0.02	15.25	2.46	0.17	0.00	**99.56**	**4.97**	76.6
29	MR06_fsp19	Leuconorite HW	50.59	0.08	30.63	0.28	0.05	0.03	15.31	2.45	0.19	0.00	**99.60**	**4.97**	76.7
30	MR06_fsp20	Leuconorite HW	50.92	0.00	30.66	0.57	0.05	0.02	14.95	2.53	0.19	0.00	**99.87**	**4.97**	75.7
31	MR06_fsp_incl12	Leuconorite HW	50.39	0.00	30.73	0.27	0.01	0.02	15.10	2.57	0.16	0.00	**99.25**	**4.97**	75.7
32	MR06_fsp_incl13	Leuconorite HW	50.53	0.02	30.57	0.41	0.02	0.02	15.18	2.51	0.16	0.00	**99.42**	**4.97**	76.2

Appendix 1: Plagioclase Compositions. Oxide data are presented in wt. %. Plagioclases were normalised to 8 oxygens.

Point	Sample	Unit	SiO_2	TiO_2	Al_2O_3	FeO	MnO	MgO	CaO	Na_2O	K_2O	BaO	Total	Total Cations	% An
33	MR06_fsp_incl14	Leuconorite HW	50.39	0.12	30.64	0.39	0.06	0.01	15.33	2.44	0.15	0.00	**99.53**	**4.97**	76.9
34	MR06_fsp_incl15	Leuconorite HW	50.72	0.00	30.89	0.32	0.00	0.01	15.23	2.48	0.17	0.18	**99.99**	**4.97**	76.5
35	MR06_fsp_incl16	Leuconorite HW	50.61	0.18	30.60	0.24	0.00	0.03	15.07	2.49	0.20	0.15	**99.56**	**4.96**	76.1
36	MR06_fsp_incl17	Leuconorite HW	51.03	0.08	30.41	0.47	0.06	0.01	14.70	2.63	0.22	0.00	**99.61**	**4.97**	74.6
37	MR06_fsp_incl18	Leuconorite HW	50.99	0.00	30.53	0.32	0.02	0.02	14.95	2.65	0.18	0.09	**99.75**	**4.97**	74.9
38	MR06_fsp21	Leuconorite HW	50.82	0.12	30.54	0.43	0.00	0.01	14.78	2.57	0.19	0.04	**99.49**	**4.96**	75.2
39	MR06_fsp22	Leuconorite HW	51.12	0.17	30.57	0.26	0.00	0.01	15.08	2.60	0.20	0.02	**100.01**	**4.96**	75.3
40	MR06_fsp_incl19	Leuconorite HW	50.39	0.17	30.49	0.31	0.00	0.03	15.18	2.50	0.18	0.15	**99.39**	**4.97**	76.2
41	MR06_fsp_incl20	Leuconorite HW	50.47	0.06	30.64	0.43	0.00	0.02	14.99	2.53	0.15	0.00	**99.29**	**4.97**	75.9
42	MR06_fsp_incl21	Leuconorite HW	50.66	0.03	30.64	0.22	0.08	0.02	15.12	2.53	0.16	0.00	**99.47**	**4.97**	76.0
43	MR06_fsp_incl22	Leuconorite HW	50.43	0.17	30.82	0.47	0.00	0.00	15.37	2.46	0.17	0.11	**99.98**	**4.97**	76.8
44	MR06_fsp_incl23	Leuconorite HW	50.41	0.00	30.20	0.39	0.01	0.02	14.74	2.64	0.18	0.00	**98.59**	**4.97**	74.8
45	MR06_fsp_incl24	Leuconorite HW	50.65	0.03	30.59	0.34	0.09	0.02	14.99	2.51	0.17	0.07	**99.47**	**4.97**	75.9
46	MR07_fsp_incl25	Norite HW	51.03	0.00	30.44	0.33	0.01	0.00	14.67	2.72	0.21	0.00	**99.40**	**4.97**	74.0
47	MR07_fsp_incl26	Norite HW	50.81	0.00	30.83	0.25	0.02	0.03	14.91	2.69	0.22	0.00	**99.76**	**4.97**	74.4
48	MR07_fsp_incl27	Norite HW	50.94	0.00	30.26	0.37	0.00	0.00	14.80	2.73	0.22	0.14	**99.46**	**4.97**	74.0
49	MR07_fsp_incl28	Norite HW	50.94	0.08	30.43	0.37	0.03	0.03	14.78	2.70	0.24	0.02	**99.61**	**4.97**	74.1
50	MR07_fsp_incl29	Norite HW	50.35	0.00	30.75	0.30	0.03	0.00	15.47	2.42	0.18	0.00	**99.49**	**4.97**	77.1
51	MR07_fsp_incl30	Norite HW	50.41	0.00	31.04	0.36	0.00	0.01	15.48	2.46	0.19	0.00	**99.94**	**4.98**	76.9
52	MR07_fsp23	Norite HW	51.35	0.09	30.00	0.21	0.02	0.01	14.23	2.99	0.20	0.04	**99.13**	**4.97**	71.6
53	MR07_fsp24	Norite HW	50.73	0.00	30.36	0.28	0.00	0.02	14.85	2.70	0.21	0.01	**99.17**	**4.97**	74.3
54	MR07_fsp25	Norite HW	51.05	0.08	30.35	0.35	0.01	0.02	14.82	2.68	0.20	0.20	**99.75**	**4.97**	74.5
55	MR07_fsp26	Norite HW	50.37	0.02	30.57	0.26	0.00	0.01	14.97	2.55	0.16	0.00	**98.91**	**4.97**	75.7
56	MR08_fsp_incl31	Pyroxenite Reef	51.19	0.03	30.79	0.19	0.00	0.01	14.70	2.65	0.21	0.00	**99.77**	**4.96**	74.4
57	MR08_fsp_incl32	Pyroxenite Reef	51.25	0.02	30.53	0.36	0.03	0.01	14.85	2.65	0.21	0.00	**99.91**	**4.97**	74.6
58	MR08_fsp_incl33	Pyroxenite Reef	51.51	0.00	30.35	0.28	0.00	0.02	14.40	2.88	0.21	0.00	**99.64**	**4.97**	72.5
59	MR08_fsp_incl34	Pyroxenite Reef	51.96	0.00	30.16	0.38	0.01	0.00	14.16	2.83	0.23	0.08	**99.80**	**4.96**	72.4
60	MR08_fsp27	Pyroxenite Reef	50.91	0.00	30.84	0.34	0.08	0.02	15.14	2.38	0.14	0.00	**99.84**	**4.96**	77.2
61	MR08_fsp28	Pyroxenite Reef	50.85	0.00	31.09	0.25	0.01	0.05	15.39	2.40	0.17	0.00	**100.22**	**4.96**	77.2
62	MR08_fsp_incl35	Pyroxenite Reef	51.06	0.08	30.70	0.45	0.00	0.01	14.93	2.58	0.18	0.00	**99.97**	**4.96**	75.4
63	MR08_fsp_incl36	Pyroxenite Reef	50.89	0.08	30.78	0.21	0.00	0.02	15.13	2.60	0.18	0.00	**99.88**	**4.97**	75.4
64	MR08_fsp_incl37	Pyroxenite Reef	51.13	0.00	31.01	0.55	0.01	0.03	14.76	2.53	0.17	0.02	**100.22**	**4.96**	75.5
65	MR08_fsp29	Pyroxenite Reef	51.19	0.21	30.43	0.32	0.00	0.01	14.80	2.71	0.21	0.01	**99.90**	**4.97**	74.1
66	MR08_fsp30	Pyroxenite Reef	51.47	0.09	30.54	0.27	0.02	0.07	14.77	2.78	0.23	0.00	**100.24**	**4.97**	73.6

Appendix 1: Plagioclase Compositions. Oxide data are presented in wt. %. Plagioclases were normalised to 8 oxygens.

Point	Sample	Unit	SiO_2	TiO_2	Al_2O_3	FeO	MnO	MgO	CaO	Na_2O	K_2O	BaO	Total	Total Cations	% An
67	MR08_fsp31	Pyroxenite Reef	51.26	0.02	30.37	0.33	0.00	0.02	14.61	2.65	0.21	0.00	**99.45**	**4.96**	74.4
68	MR08_fsp32	Pyroxenite Reef	51.40	0.00	30.55	0.18	0.00	0.04	14.84	2.59	0.20	0.00	**99.79**	**4.96**	75.1
69	MR08_fsp_incl38	Pyroxenite Reef	50.92	0.09	30.92	0.26	0.01	0.04	15.12	2.41	0.15	0.05	**99.95**	**4.96**	76.9
70	MR08_fsp_incl39	Pyroxenite Reef	50.78	0.03	30.80	0.39	0.08	0.03	15.11	2.46	0.15	0.00	**99.84**	**4.96**	76.5
71	MR08_fsp_incl40	Pyroxenite Reef	50.60	0.00	30.93	0.25	0.00	0.03	15.06	2.47	0.14	0.00	**99.48**	**4.96**	76.5
72	MR08_fsp_incl41	Pyroxenite Reef	50.51	0.00	30.95	0.33	0.06	0.04	15.34	2.41	0.11	0.06	**99.80**	**4.97**	77.3
73	MR08_fsp_incl42	Pyroxenite Reef	50.38	0.00	31.02	0.29	0.04	0.03	15.33	2.38	0.12	0.11	**99.70**	**4.97**	77.5
74	MR08_fsp33	Pyroxenite Reef	50.46	0.00	30.87	0.34	0.00	0.02	15.45	2.48	0.18	0.08	**99.87**	**4.97**	76.7
75	MR08_fsp34	Pyroxenite Reef	50.51	0.14	30.94	0.27	0.00	0.02	15.47	2.43	0.16	0.04	**99.97**	**4.97**	77.1
76	MR08_fsp35	Pyroxenite Reef	51.34	0.00	30.48	0.18	0.01	0.05	14.75	2.75	0.20	0.00	**99.75**	**4.97**	73.9
77	MR08_fsp36	Pyroxenite Reef	50.00	0.00	31.21	0.20	0.00	0.04	15.46	2.31	0.14	0.08	**99.43**	**4.97**	78.0
78	MR08_fsp37	Pyroxenite Reef	50.50	0.00	30.60	0.21	0.00	0.02	15.25	2.39	0.17	0.00	**99.14**	**4.96**	77.1
79	MR08_fsp38	Pyroxenite Reef	50.80	0.00	31.02	0.31	0.03	0.03	15.14	2.36	0.16	0.00	**99.84**	**4.96**	77.3
80	MR08_fsp39	Pyroxenite Reef	50.31	0.00	30.87	0.22	0.00	0.03	15.24	2.37	0.16	0.00	**99.19**	**4.96**	77.3
81	MR011_fsp40	Pyroxenite Reef	56.50	0.08	27.36	0.27	0.01	0.00	10.86	4.96	0.25	0.00	**100.27**	**4.96**	53.9
82	MR011_fsp41	Pyroxenite Reef	55.14	0.11	27.64	0.07	0.00	0.00	11.09	4.77	0.18	0.00	**99.00**	**4.96**	55.6
83	MR011_fsp42	Pyroxenite Reef	56.31	0.09	27.24	0.30	0.02	0.02	10.68	4.96	0.26	0.02	**99.90**	**4.96**	53.5
84	MR011_fsp43	Pyroxenite Reef	56.15	0.09	27.30	0.35	0.06	0.03	10.89	4.86	0.26	0.13	**100.12**	**4.96**	54.5
85	MR011_fsp44	Pyroxenite Reef	56.04	0.12	27.21	0.02	0.00	0.01	11.00	5.08	0.26	0.00	**99.74**	**4.97**	53.7
86	MR011_fsp45	Pyroxenite Reef	56.57	0.08	27.30	0.15	0.03	0.02	10.69	5.10	0.26	0.07	**100.26**	**4.97**	52.9
87	MR011_fsp46	Pyroxenite Reef	54.02	0.00	28.92	0.22	0.00	0.03	12.74	3.84	0.34	0.00	**100.08**	**4.97**	63.4
88	MR011_fsp47	Pyroxenite Reef	53.43	0.00	28.80	0.16	0.00	0.01	12.90	3.83	0.30	0.00	**99.43**	**4.97**	63.9
89	MR011_fsp48	Pyroxenite Reef	53.77	0.00	29.09	0.22	0.01	0.00	12.96	3.81	0.30	0.00	**100.15**	**4.97**	64.1
90	MR011_fsp49	Pyroxenite Reef	53.70	0.11	29.13	0.26	0.06	0.00	12.85	3.69	0.28	0.04	**100.10**	**4.96**	64.7
91	MR011_fsp50	Pyroxenite Reef	53.44	0.02	28.98	0.21	0.00	0.02	12.78	3.59	0.28	0.06	**99.37**	**4.96**	65.2
92	MR011_fsp51	Pyroxenite Reef	56.11	0.14	27.62	0.17	0.07	0.03	10.80	4.94	0.19	0.00	**100.06**	**4.96**	54.1
93	MR011_fsp52	Pyroxenite Reef	54.54	0.00	28.11	0.21	0.05	0.02	11.75	4.43	0.18	0.08	**99.37**	**4.97**	58.8
94	MR011_fsp53	Pyroxenite Reef	54.61	0.15	28.30	0.01	0.03	0.01	12.11	4.26	0.21	0.09	**99.76**	**4.96**	60.4
95	MR011_fsp54	Pyroxenite Reef	54.13	0.11	28.42	0.10	0.04	0.01	12.16	4.26	0.13	0.08	**99.43**	**4.97**	60.8
96	MR011_fsp55	Pyroxenite Reef	54.38	0.17	28.50	0.19	0.00	0.02	12.22	4.29	0.12	0.06	**99.94**	**4.97**	60.7
97	MR010_fsp62	Pyroxenite Reef	52.19	0.02	30.21	0.27	0.00	0.02	14.22	3.14	0.19	0.00	**100.26**	**4.97**	70.6
98	MR010_fsp63	Pyroxenite Reef	52.31	0.09	30.30	0.25	0.01	0.01	14.28	3.09	0.17	0.00	**100.50**	**4.97**	71.1
99	MR010_fsp64	Pyroxenite Reef	52.26	0.00	30.06	0.23	0.02	0.02	13.96	3.12	0.19	0.01	**99.86**	**4.96**	70.4
100	MR010_fsp65	Pyroxenite Reef	52.97	0.05	29.60	0.18	0.01	0.01	13.28	3.42	0.23	0.00	**99.76**	**4.96**	67.2

Appendix 1: Plagioclase Compositions. Oxide data are presented in wt. %. Plagioclases were normalised to 8 oxygens.

Point	Sample	Unit	SiO_2	TiO_2	Al_2O_3	FeO	MnO	MgO	CaO	Na_2O	K_2O	BaO	Total	Total Cations	% An
101	MR010_fsp66	Pyroxenite Reef	52.14	0.00	30.35	0.14	0.04	0.00	14.35	3.07	0.18	0.13	**100.40**	**4.97**	71.3
102	MR010_fsp67	Pyroxenite Reef	52.27	0.00	29.79	0.05	0.03	0.01	13.99	2.97	0.41	0.00	**99.52**	**4.96**	70.4
103	MR010_fsp68	Pyroxenite Reef	52.11	0.00	30.11	0.33	0.00	0.02	13.86	3.13	0.37	0.05	**99.98**	**4.97**	69.4
104	MR010_fsp69	Pyroxenite Reef	51.76	0.00	30.22	0.09	0.00	0.02	14.46	2.97	0.16	0.02	**99.70**	**4.97**	72.2
105	MR010_fsp70	Pyroxenite Reef	52.49	0.05	29.98	0.16	0.03	0.03	14.04	3.28	0.20	0.00	**100.24**	**4.97**	69.5
106	MR010_fsp71	Pyroxenite Reef	52.58	0.03	30.08	0.09	0.00	0.01	13.95	3.26	0.21	0.12	**100.32**	**4.97**	69.5
107	MR010_fsp72	Pyroxenite Reef	54.35	0.02	28.40	0.25	0.00	0.05	12.40	3.94	0.36	0.00	**99.76**	**4.96**	62.1
108	MR010_fsp73	Pyroxenite Reef	52.67	0.09	29.59	0.21	0.00	0.03	13.87	3.33	0.26	0.12	**100.18**	**4.97**	68.7
109	MR010_fsp74	Pyroxenite Reef	54.33	0.05	28.88	0.03	0.00	0.01	12.79	3.87	0.33	0.11	**100.39**	**4.96**	63.4
110	MR010_fsp75	Pyroxenite Reef	53.95	0.05	28.89	0.27	0.00	0.02	12.70	3.78	0.32	0.00	**99.96**	**4.96**	63.7
111	MR010_fsp76	Pyroxenite Reef	53.75	0.15	29.20	0.15	0.00	0.03	13.00	3.71	0.30	0.08	**100.37**	**4.96**	64.7
112	MR09_fsp_incl46	Anorthosite Reef	53.30	0.00	29.19	0.18	0.01	0.00	12.92	3.76	0.25	0.00	**99.61**	**4.97**	64.5
113	MR09_fsp_incl47	Anorthosite Reef	53.44	0.03	29.10	0.18	0.08	0.01	13.07	3.78	0.22	0.00	**99.91**	**4.97**	64.8
114	MR09_fsp_incl48	Anorthosite Reef	54.72	0.00	28.06	0.25	0.05	0.03	12.15	4.16	0.38	0.06	**99.86**	**4.97**	60.4
115	MR09_fsp_incl49	Anorthosite Reef	54.08	0.20	28.55	0.14	0.00	0.03	12.30	4.00	0.31	0.00	**99.61**	**4.96**	61.8
116	MR09_fsp_incl50	Anorthosite Reef	54.83	0.02	28.22	0.23	0.04	0.01	11.82	4.27	0.36	0.00	**99.78**	**4.96**	59.2
117	MR09_fsp_incl51	Anorthosite Reef	53.97	0.00	29.18	0.20	0.04	0.02	12.69	3.95	0.26	0.01	**100.32**	**4.97**	63.0
118	MR09_fsp_incl52	Anorthosite Reef	51.51	0.09	30.49	0.35	0.00	0.04	14.70	2.79	0.21	0.01	**100.18**	**4.97**	73.5
119	MR09_fsp_incl53	Anorthosite Reef	51.27	0.00	30.26	0.12	0.02	0.02	14.51	2.89	0.27	0.00	**99.34**	**4.97**	72.3
120	MR09_fsp_incl54	Anorthosite Reef	53.76	0.00	29.10	0.38	0.01	0.02	13.02	3.57	0.31	0.00	**100.17**	**4.96**	65.6
121	MR09_fsp_incl55	Anorthosite Reef	53.27	0.00	29.37	0.28	0.04	0.01	13.40	3.59	0.24	0.00	**100.19**	**4.97**	66.4
122	MR09_zoned_fsp 001	Anorthosite Reef	53.43	0.00	28.87	0.39	0.00	0.03	13.01	3.80	0.31	0.00	**99.83**	**4.98**	64.2
123	MR09_zoned_fsp 002	Anorthosite Reef	52.07	0.11	29.75	0.28	0.07	0.02	14.10	3.09	0.22	0.05	**99.76**	**4.97**	70.6
124	MR09_zoned_fsp 003	Anorthosite Reef	50.91	0.08	30.20	0.22	0.07	0.03	14.60	2.82	0.20	0.00	**99.13**	**4.97**	73.2
125	MR09_zoned_fsp 004	Anorthosite Reef	51.71	0.24	29.95	0.21	0.04	0.04	14.02	3.12	0.26	0.00	**99.59**	**4.97**	70.2
126	MR09_zoned_fsp 005	Anorthosite Reef	51.93	0.11	30.15	0.35	0.01	0.03	14.41	2.96	0.21	0.00	**100.16**	**4.97**	72.0
127	MR09_zoned_fsp 006	Anorthosite Reef	54.23	0.06	28.39	0.31	0.00	0.03	12.53	4.00	0.31	0.07	**99.93**	**4.97**	62.2
128	MR09_fsp79	Anorthosite Reef	57.05	0.06	26.83	0.25	0.00	0.04	10.33	5.38	0.34	0.00	**100.28**	**4.97**	50.5
129	MR09_fsp80	Anorthosite Reef	58.34	0.08	26.09	0.15	0.03	0.03	9.59	5.72	0.40	0.00	**100.44**	**4.97**	47.0
130	MR09_zoned_fsp2 001	Anorthosite Reef	56.27	0.03	26.86	0.25	0.00	0.03	10.77	4.97	0.37	0.00	**99.55**	**4.97**	53.3
131	MR09_zoned_fsp2 002	Anorthosite Reef	55.26	0.00	27.67	0.22	0.02	0.07	11.50	4.38	0.40	0.34	**99.87**	**4.96**	57.8
132	MR09_zoned_fsp2 003	Anorthosite Reef	54.92	0.18	27.88	0.29	0.04	0.05	11.85	4.26	0.40	0.00	**99.86**	**4.96**	59.2
133	MR09_zoned_fsp2 004	Anorthosite Reef	52.76	0.08	27.88	0.22	0.00	0.03	12.88	3.74	0.36	0.05	**97.99**	**4.97**	64.2
134	MR09_zoned_fsp2 005	Anorthosite Reef	54.12	0.20	28.59	0.35	0.00	0.02	12.34	3.93	0.41	0.12	**100.07**	**4.97**	61.9

Appendix 1: Plagioclase Compositions. Oxide data are presented in wt. %. Plagioclases were normalised to 8 oxygens.

Point	Sample	Unit	SiO_2	TiO_2	Al_2O_3	FeO	MnO	MgO	CaO	Na_2O	K_2O	BaO	Total	Total Cations	% An
135	MR09_zoned_fsp2 006	Anorthosite Reef	52.72	0.15	27.48	0.34	0.00	0.04	12.00	4.14	0.43	0.15	**97.44**	**4.98**	60.0
136	MR09_zoned_fsp2 007	Anorthosite Reef	57.57	0.00	26.48	0.14	0.03	0.03	10.37	5.15	0.52	0.00	**100.29**	**4.96**	51.1
137	MR09_zoned_fsp2 008	Anorthosite Reef	56.33	0.08	27.25	0.37	0.00	0.04	11.11	4.65	0.36	0.08	**100.27**	**4.96**	55.7
138	MR13_fsp81	Pyroxenite Reef	51.13	0.03	30.20	0.17	0.00	0.01	14.48	2.97	0.11	0.00	**99.10**	**4.97**	72.5
139	MR13_fsp82	Pyroxenite Reef	51.61	0.09	29.67	0.00	0.00	0.02	14.22	3.22	0.06	0.00	**98.89**	**4.97**	70.7
140	MR13_fsp83	Pyroxenite Reef	52.46	0.00	29.31	0.18	0.15	0.02	13.62	3.45	0.14	0.01	**99.33**	**4.97**	68.0
141	MR13_fsp_incl56	Pyroxenite Reef	51.29	0.00	29.46	0.41	0.00	0.38	14.07	3.08	0.08	0.00	**98.76**	**4.98**	71.3
142	MR13_fsp_incl57	Pyroxenite Reef	51.37	0.00	30.07	0.23	0.02	0.00	14.26	3.19	0.06	0.15	**99.36**	**4.98**	70.9
143	MR13_fsp_incl58	Pyroxenite Reef	51.28	0.03	30.16	0.35	0.01	0.01	14.27	3.14	0.07	0.07	**99.40**	**4.98**	71.2
144	MR13_fsp_incl59	Pyroxenite Reef	51.63	0.14	30.31	0.32	0.06	0.02	14.34	3.09	0.08	0.07	**100.04**	**4.97**	71.6
145	MR13_fsp84	Pyroxenite Reef	52.88	0.00	29.11	0.08	0.00	0.01	13.13	3.79	0.17	0.00	**99.18**	**4.97**	65.0
146	MR13_fsp85	Pyroxenite Reef	52.98	0.02	29.10	0.28	0.00	0.01	13.03	3.68	0.16	0.00	**99.25**	**4.97**	65.5
147	MR13_fsp86	Pyroxenite Reef	53.01	0.08	29.00	0.24	0.00	0.03	13.39	3.67	0.15	0.06	**99.63**	**4.97**	66.3
148	MR13_fsp87	Pyroxenite Reef	51.79	0.00	30.16	0.25	0.00	0.01	14.14	3.25	0.12	0.07	**99.80**	**4.98**	70.1
149	MR13_fsp88	Pyroxenite Reef	51.60	0.00	30.15	0.17	0.03	0.01	14.33	3.11	0.12	0.18	**99.70**	**4.97**	71.3
150	MR13_fsp89	Pyroxenite Reef	52.11	0.00	29.60	0.20	0.04	0.02	13.82	3.39	0.20	0.00	**99.38**	**4.98**	68.5
151	MR13_fsp90	Pyroxenite Reef	52.77	0.30	29.30	0.32	0.00	0.02	13.48	3.50	0.20	0.00	**99.90**	**4.97**	67.2
152	MR13_fsp91	Pyroxenite Reef	52.18	0.00	29.45	0.18	0.03	0.02	13.53	3.55	0.08	0.00	**99.02**	**4.97**	67.5
153	MR13_fsp92	Pyroxenite Reef	52.59	0.00	29.42	0.15	0.06	0.01	13.81	3.48	0.10	0.00	**99.60**	**4.97**	68.3
154	MR13_fsp93	Pyroxenite Reef	51.67	0.09	29.72	0.21	0.01	0.03	14.11	3.34	0.08	0.02	**99.27**	**4.98**	69.7
155	MR16_fsp94	Pyroxenite Reef	53.10	0.00	29.33	0.25	0.01	0.00	13.41	3.56	0.20	0.00	**99.86**	**4.97**	66.7
156	MR16_fsp95	Pyroxenite Reef	53.66	0.00	28.84	0.15	0.04	0.01	12.69	4.11	0.29	0.14	**99.93**	**4.98**	62.0
157	MR16_fsp96	Pyroxenite Reef	54.32	0.00	28.38	0.21	0.12	0.03	12.28	4.14	0.28	0.00	**99.76**	**4.97**	61.1
158	MR16_fsp97	Pyroxenite Reef	53.43	0.12	29.11	0.16	0.03	0.02	13.09	3.60	0.28	0.00	**99.84**	**4.96**	65.6
159	MR16_fsp98	Pyroxenite Reef	53.38	0.23	29.18	0.06	0.00	0.02	13.31	3.60	0.28	0.00	**100.06**	**4.96**	66.0
160	MR16_fsp99	Pyroxenite Reef	53.13	0.30	29.41	0.18	0.07	0.03	13.39	3.64	0.28	0.15	**100.57**	**4.97**	65.9
161	MR16_fsp100	Pyroxenite Reef	52.92	0.00	29.18	0.35	0.00	0.01	13.36	3.64	0.26	0.00	**99.72**	**4.98**	65.9
162	MR16_fsp101	Pyroxenite Reef	52.84	0.26	29.14	0.35	0.00	0.03	13.14	3.54	0.25	0.00	**99.54**	**4.96**	66.2
163	MR16_fsp102	Pyroxenite Reef	52.88	0.00	29.16	0.21	0.08	0.03	13.02	3.72	0.27	0.06	**99.43**	**4.98**	64.9
164	MR16_fsp103	Pyroxenite Reef	52.34	0.00	29.21	0.24	0.00	0.02	13.62	3.62	0.23	0.07	**99.35**	**4.98**	66.6
165	MR16_fsp104	Pyroxenite Reef	52.04	0.18	29.84	0.08	0.01	0.02	13.78	3.25	0.22	0.00	**99.41**	**4.97**	69.2
166	MR16_fsp105	Pyroxenite Reef	55.46	0.11	28.02	0.15	0.00	0.02	11.44	4.60	0.44	0.00	**100.24**	**4.97**	56.4
167	MR16_fsp106	Pyroxenite Reef	56.17	0.00	27.42	0.13	0.00	0.01	11.17	4.67	0.38	0.04	**99.98**	**4.96**	55.6

Appendix 1: Plagioclase Compositions. Oxide data are presented in wt. %. Plagioclases were normalised to 8 oxygens.

Point	Sample	Unit	SiO_2	TiO_2	Al_2O_3	FeO	MnO	MgO	CaO	Na_2O	K_2O	BaO	Total	Total Cations	% An
168	MR16_fsp107	Pyroxenite Reef	52.32	0.06	29.65	0.15	0.04	0.03	13.46	3.48	0.23	0.19	**99.59**	**4.97**	67.2
169	MR16_fsp108	Pyroxenite Reef	52.49	0.05	29.55	0.17	0.00	0.01	13.62	3.45	0.22	0.00	**99.55**	**4.97**	67.7
170	MR16_fsp109	Pyroxenite Reef	52.31	0.00	29.32	0.30	0.00	0.02	13.47	3.39	0.22	0.12	**99.16**	**4.97**	67.8
171	MR16_fsp110	Pyroxenite Reef	54.02	0.15	28.80	0.20	0.03	0.04	12.64	4.06	0.27	0.04	**100.24**	**4.97**	62.3
172	MR16_fsp111	Pyroxenite Reef	53.68	0.18	29.25	0.35	0.02	0.01	12.96	3.85	0.25	0.00	**100.54**	**4.97**	64.1
173	MR16_fsp112	Pyroxenite Reef	54.18	0.11	28.56	0.15	0.00	0.02	12.32	4.13	0.30	0.05	**99.80**	**4.97**	61.1
174	MR19_fsp114	Pyroxenite Reef	53.33	0.02	29.00	0.25	0.07	0.01	13.20	3.71	0.26	0.00	**99.84**	**4.97**	65.3
175	MR19_fsp115	Pyroxenite Reef	53.20	0.14	29.07	0.18	0.00	0.01	13.05	3.70	0.26	0.00	**99.61**	**4.97**	65.1
176	MR19_fsp116	Pyroxenite Reef	52.78	0.00	29.20	0.01	0.00	0.02	13.26	3.68	0.23	0.02	**99.20**	**4.97**	65.7
177	MR19_fsp117	Pyroxenite Reef	53.04	0.11	28.97	0.14	0.05	0.01	12.87	3.77	0.30	0.01	**99.26**	**4.97**	64.2
178	MR19_fsp118	Pyroxenite Reef	58.89	0.00	26.32	0.26	0.01	0.02	9.25	6.13	0.32	0.00	**101.20**	**4.98**	44.6
179	MR19_fsp119	Pyroxenite Reef	58.28	0.14	25.79	0.21	0.06	0.02	9.40	6.13	0.31	0.05	**100.37**	**4.98**	45.1
180	MR21_fsp128	Pyroxenite Reef	55.45	0.12	27.81	0.15	0.00	0.01	11.51	4.72	0.30	0.06	**100.13**	**4.97**	56.4
181	MR21_fsp129	Pyroxenite Reef	55.67	0.09	27.51	0.03	0.03	0.00	11.19	4.81	0.29	0.00	**99.61**	**4.97**	55.3
182	MR21_fsp130	Pyroxenite Reef	56.15	0.00	27.39	0.13	0.00	0.02	10.63	5.03	0.27	0.05	**99.67**	**4.97**	53.0
183	MR21_fsp131	Pyroxenite Reef	55.90	0.15	27.51	0.15	0.04	0.00	11.17	4.97	0.26	0.00	**100.16**	**4.97**	54.5
184	MR21_fsp132	Pyroxenite Reef	56.16	0.06	27.06	0.11	0.01	0.00	10.62	5.16	0.25	0.01	**99.44**	**4.97**	52.4
185	MR21_fsp133	Pyroxenite Reef	56.64	0.14	26.97	0.25	0.01	0.03	10.62	5.39	0.29	0.04	**100.38**	**4.98**	51.3
186	MR21_fsp134	Pyroxenite Reef	56.75	0.18	26.88	0.10	0.00	0.01	10.31	5.42	0.29	0.00	**99.94**	**4.97**	50.3
187	MR21_fsp135	Pyroxenite Reef	58.52	0.00	25.76	0.15	0.04	0.01	9.12	6.05	0.33	0.00	**99.96**	**4.97**	44.6
188	MR21_fsp136	Pyroxenite Reef	58.27	0.00	25.93	0.20	0.03	0.02	9.42	5.99	0.29	0.11	**100.25**	**4.98**	45.7
189	MR21_fsp137	Pyroxenite Reef	58.20	0.12	25.84	0.21	0.02	0.00	9.41	6.07	0.32	0.05	**100.24**	**4.98**	45.3
190	MR21_fsp138	Pyroxenite Reef	58.13	0.14	25.84	0.12	0.00	0.01	9.24	6.01	0.33	0.00	**99.82**	**4.97**	45.1
191	MR22_fsp143	Pyroxenite Reef	53.79	0.00	29.04	0.22	0.01	0.00	13.01	3.84	0.30	0.06	**100.27**	**4.97**	64.0
192	MR22_fsp144	Pyroxenite Reef	53.93	0.06	28.83	0.35	0.00	0.02	12.69	3.95	0.29	0.05	**100.17**	**4.97**	62.9
193	MR22_fsp145	Pyroxenite Reef	54.13	0.00	28.76	0.17	0.00	0.03	12.74	4.02	0.31	0.00	**100.15**	**4.97**	62.5
194	MR22_fsp146	Pyroxenite Reef	50.20	0.11	31.00	0.26	0.04	0.01	15.27	2.43	0.14	0.00	**99.45**	**4.97**	77.0
195	MR22_fsp147	Pyroxenite Reef	50.67	0.15	30.72	0.25	0.00	0.03	15.17	2.60	0.15	0.04	**99.77**	**4.97**	75.6
196	MR23_fsp148	Chromitite	51.15	0.11	30.25	0.29	0.01	0.03	14.65	2.94	0.19	0.04	**99.66**	**4.98**	72.6
197	MR23_fsp149	Chromitite	51.13	0.00	30.53	0.35	0.02	0.01	14.61	2.95	0.18	0.05	**99.82**	**4.98**	72.4
198	MR23_fsp150	Chromitite	51.46	0.05	30.10	0.33	0.06	0.02	14.68	2.88	0.18	0.00	**99.74**	**4.97**	73.1
199	MR23_fsp151	Chromitite	51.29	0.08	30.67	0.42	0.05	0.01	14.70	2.91	0.19	0.08	**100.40**	**4.98**	72.8
200	MR23_fsp152	Chromitite	51.67	0.09	30.10	0.49	0.03	0.03	14.52	2.87	0.24	0.00	**100.04**	**4.97**	72.6
201	MR23_fsp153	Chromitite	52.29	0.17	30.16	0.21	0.00	0.02	14.48	3.08	0.21	0.00	**100.62**	**4.97**	71.3

Appendix 1: Plagioclase Compositions. Oxide data are presented in wt. %. Plagioclases were normalised to 8 oxygens.

Point	Sample	Unit	SiO_2	TiO_2	Al_2O_3	FeO	MnO	MgO	CaO	Na_2O	K_2O	BaO	Total	Total Cations	% An
202	MR23_fsp154	Chromitite	50.69	0.03	30.73	0.42	0.01	0.05	15.32	2.49	0.17	0.00	**99.89**	**4.97**	76.5
203	MR23_fsp155	Chromitite	50.66	0.00	30.86	0.35	0.07	0.02	15.49	2.53	0.18	0.00	**100.17**	**4.98**	76.3
204	MR23_fsp156	Chromitite	50.70	0.11	30.69	0.32	0.00	0.01	15.02	2.62	0.19	0.00	**99.66**	**4.97**	75.2
205	MR23_fsp157	Chromitite	50.30	0.00	30.87	0.33	0.00	0.02	15.32	2.50	0.20	0.01	**99.54**	**4.98**	76.3
206	MR23_fsp158	Chromitite	50.69	0.00	30.98	0.56	0.08	0.01	15.28	2.56	0.16	0.00	**100.32**	**4.98**	76.0
207	MR23_fsp159	Chromitite	50.43	0.00	30.66	0.38	0.06	0.01	15.30	2.51	0.14	0.00	**99.48**	**4.97**	76.5
208	MR23_fsp160	Chromitite	50.29	0.12	30.86	0.37	0.00	0.02	15.22	2.55	0.20	0.00	**99.63**	**4.98**	75.8
209	MR23_fsp161	Chromitite	50.52	0.00	30.58	0.26	0.00	0.02	15.15	2.63	0.18	0.04	**99.38**	**4.98**	75.3
210	MR23_fsp162	Chromitite	51.12	0.00	30.34	0.53	0.07	0.02	14.83	2.74	0.20	0.00	**99.83**	**4.97**	74.1
211	MR23_fsp163	Chromitite	50.79	0.00	30.99	0.33	0.03	0.00	15.61	2.54	0.16	0.15	**100.60**	**4.98**	76.5
212	MR23_fsp164	Chromitite	50.66	0.00	30.68	0.20	0.01	0.03	15.24	2.54	0.17	0.06	**99.59**	**4.97**	76.0
213	MR24_fsp165 001	Anorthosite FW	50.75	0.00	30.72	0.49	0.00	0.01	15.18	2.63	0.16	0.12	**100.05**	**4.98**	75.4
214	MR24_fsp165 002	Anorthosite FW	50.96	0.03	30.59	0.49	0.00	0.05	14.96	2.55	0.20	0.11	**99.92**	**4.97**	75.5
215	MR24_fsp165 003	Anorthosite FW	51.29	0.00	30.30	0.42	0.01	0.05	15.07	2.69	0.17	0.09	**100.08**	**4.97**	74.9
216	MR24_fsp165 004	Anorthosite FW	51.56	0.11	30.04	0.56	0.00	0.04	14.67	2.79	0.21	0.08	**100.06**	**4.97**	73.5
217	MR24_fsp165 005	Anorthosite FW	51.13	0.14	30.53	0.49	0.07	0.05	15.13	2.57	0.18	0.00	**100.28**	**4.97**	75.7
218	MR24_fsp165 006	Anorthosite FW	51.01	0.00	30.63	0.44	0.02	0.04	15.02	2.54	0.16	0.06	**99.92**	**4.97**	75.8
219	MR24_fsp166	Anorthosite FW	50.68	0.12	30.29	0.37	0.07	0.03	14.98	2.71	0.19	0.07	**99.51**	**4.98**	74.5
220	MR24_fsp167	Anorthosite FW	51.22	0.14	30.31	0.49	0.01	0.04	14.74	2.67	0.18	0.14	**99.93**	**4.97**	74.5
221	MR24_fsp168	Anorthosite FW	50.69	0.06	30.34	0.47	0.00	0.03	15.17	2.51	0.18	0.00	**99.44**	**4.97**	76.1
222	MR24_fsp169	Anorthosite FW	50.64	0.00	30.87	0.42	0.06	0.02	15.36	2.44	0.18	0.00	**99.97**	**4.97**	76.9
223	MR24_fsp170	Anorthosite FW	49.98	0.00	30.70	0.57	0.00	0.04	15.34	2.40	0.17	0.00	**99.21**	**4.98**	77.1
224	MR24_fsp171	Anorthosite FW	50.81	0.02	30.51	0.45	0.00	0.04	15.19	2.49	0.18	0.06	**99.74**	**4.97**	76.2
225	MR24_fsp172	Anorthosite FW	50.63	0.05	30.39	0.61	0.00	0.04	14.66	2.61	0.17	0.00	**99.15**	**4.97**	74.8
226	MR24_fsp173	Anorthosite FW	51.30	0.05	30.18	0.39	0.00	0.03	14.71	2.94	0.24	0.01	**99.85**	**4.98**	72.4
227	MR24_fsp174	Anorthosite FW	51.56	0.00	30.07	0.53	0.01	0.01	14.55	2.88	0.18	0.00	**99.78**	**4.97**	72.9
228	MR24_fsp175	Anorthosite FW	50.97	0.00	30.28	0.27	0.05	0.02	15.10	2.66	0.18	0.00	**99.51**	**4.97**	75.0
229	MR24_fsp176	Anorthosite FW	49.74	0.09	31.05	0.31	0.01	0.02	15.67	2.19	0.14	0.07	**99.28**	**4.97**	79.1
230	MR24_fsp178	Anorthosite FW	50.81	0.00	30.43	0.42	0.04	0.02	15.15	2.75	0.18	0.01	**99.80**	**4.98**	74.5
231	MR24_fsp_incl72	Anorthosite FW	50.69	0.00	30.75	0.49	0.02	0.03	15.41	2.50	0.14	0.08	**100.13**	**4.97**	76.7
232	MR24_fsp_incl73	Anorthosite FW	50.71	0.08	30.73	0.29	0.00	0.02	15.06	2.49	0.16	0.00	**99.53**	**4.96**	76.2
233	MR24_fsp179	Anorthosite FW	50.77	0.00	30.97	0.41	0.09	0.04	15.49	2.49	0.15	0.00	**100.41**	**4.97**	76.8
234	MR24_fsp180	Anorthosite FW	51.79	0.02	30.25	0.22	0.01	0.03	14.62	2.89	0.21	0.04	**100.06**	**4.97**	72.8
235	MR24_fsp181	Anorthosite FW	50.72	0.06	30.51	0.49	0.08	0.06	15.00	2.55	0.20	0.00	**99.66**	**4.97**	75.6

Appendix 1: Plagioclase Compositions. Oxide data are presented in wt. %. Plagioclases were normalised to 8 oxygens.

Point	Sample	Unit	SiO_2	TiO_2	Al_2O_3	FeO	MnO	MgO	CaO	Na_2O	K_2O	BaO	Total	Total Cations	% An
236	MR24_fsp182	Anorthosite FW	50.85	0.05	30.73	0.70	0.00	0.02	15.23	2.65	0.15	0.00	**100.36**	**4.98**	75.4
237	MR25_fsp183	Anorthosite FW	51.29	0.00	30.32	0.66	0.00	0.05	14.74	2.66	0.19	0.00	**99.92**	**4.97**	74.5
238	MR25_fsp184	Anorthosite FW	50.95	0.02	30.53	0.47	0.02	0.04	15.22	2.57	0.17	0.00	**99.99**	**4.97**	75.8
239	MR25_fsp185	Anorthosite FW	51.33	0.00	30.49	0.55	0.00	0.05	14.96	2.70	0.20	0.00	**100.28**	**4.97**	74.5
240	MR25_fsp186	Anorthosite FW	50.86	0.20	30.74	0.52	0.00	0.05	15.50	2.52	0.19	0.00	**100.58**	**4.98**	76.4
241	MR25_fsp187	Anorthosite FW	51.14	0.00	30.24	0.55	0.08	0.04	14.92	2.66	0.19	0.05	**99.86**	**4.97**	74.7
242	MR25_fsp188	Anorthosite FW	50.75	0.14	30.45	0.57	0.00	0.03	14.87	2.63	0.17	0.00	**99.61**	**4.97**	75.0
243	MR25_fsp189	Anorthosite FW	51.39	0.18	30.14	0.49	0.00	0.03	14.89	2.72	0.19	0.01	**100.04**	**4.97**	74.3
244	MR25_fsp190	Anorthosite FW	51.37	0.08	30.34	0.52	0.00	0.04	14.96	2.82	0.19	0.00	**100.32**	**4.98**	73.7
245	MR25_fsp191	Anorthosite FW	51.16	0.06	30.43	0.54	0.03	0.03	15.07	2.62	0.18	0.00	**100.12**	**4.97**	75.2

Appendix 2: Clinopyroxene Compositions. Oxide data are presented in wt. %. Pyroxenes were normalised to 6 oxygens.

Point	Sample	Unit	SiO_2	TiO_2	Al_2O_3	Cr_2O_3	Fe_2O_3	FeO	MnO	NiO	MgO	CaO	Na_2O	Total	Total Cations	Mg#	En
1	MR02_cpx1	Anorthosite HW	51.73	0.31	1.28	0.22	0.38	11.70	0.27	0.00	11.98	21.58	0.17	**99.62**	**4.00**	**76.6**	41.01
2	MR02_cpx2	Anorthosite HW	49.07	0.27	1.50	0.07	0.00	13.35	0.31	0.00	11.19	20.99	0.14	**96.89**	**4.01**	**76.5**	40.60
3	MR02_cpx3	Anorthosite HW	52.08	0.46	1.41	0.13	0.87	7.16	0.22	0.00	14.22	22.53	0.24	**99.31**	**4.01**	**76.1**	40.63
4	MR02_cpx4	Anorthosite HW	52.46	0.39	1.29	0.13	0.00	7.57	0.17	0.00	14.32	22.32	0.24	**98.89**	**4.00**	**77.1**	41.25
5	MR02_cpx5	Anorthosite HW	52.96	0.26	1.13	0.15	0.38	7.43	0.21	0.00	14.16	23.08	0.24	**100.00**	**4.00**	**76.4**	40.18
6	MR04_cpx6	Anorthosite HW	52.90	0.36	1.51	0.51	0.03	6.04	0.17	0.00	14.87	23.16	0.26	**99.80**	**4.00**	**81.4**	42.47
7	MR04_cpx7	Anorthosite HW	52.55	0.42	1.61	0.48	1.03	5.64	0.14	0.00	14.96	23.05	0.27	**100.13**	**4.01**	**80.2**	42.40
8	MR04_opx1	Anorthosite HW	53.94	0.17	1.13	0.33	0.00	16.27	0.42	0.00	24.50	2.24	0.03	**99.03**	**3.99**	**72.9**	69.06
9	MR04_opx2	Anorthosite HW	53.70	0.16	0.96	0.21	0.00	17.02	0.37	0.00	24.96	1.12	0.01	**98.50**	**3.99**	**72.3**	70.26
10	MR04_cpx_incl3	Anorthosite HW	52.34	0.32	1.68	0.50	0.46	5.54	0.14	0.00	14.95	22.71	0.32	**98.95**	**4.00**	**81.7**	43.11
11	MR04_cpx_incl4	Anorthosite HW	52.83	0.33	1.68	0.57	0.59	5.98	0.18	0.00	15.05	22.73	0.29	**100.24**	**4.01**	**80.5**	42.82
12	MR04_cpx8	Anorthosite HW	52.83	0.40	1.55	0.40	0.22	6.25	0.21	0.00	14.85	22.79	0.31	**99.80**	**4.00**	**80.4**	42.46
13	MR04_cpx9	Anorthosite HW	52.58	0.41	1.54	0.45	0.30	6.48	0.18	0.00	14.69	22.80	0.26	**99.69**	**4.00**	**79.5**	42.00
14	MR04_cpx10	Anorthosite HW	52.86	0.40	1.51	0.40	0.23	7.31	0.22	0.00	15.33	21.49	0.26	**99.99**	**4.00**	**78.4**	43.65
15	MR04_cpx11	Anorthosite HW	52.69	0.38	1.72	0.46	0.00	6.01	0.13	0.00	14.84	22.76	0.29	**99.27**	**4.00**	**81.5**	42.84
16	MR04_cpx12	Anorthosite HW	53.01	0.42	1.47	0.30	0.28	6.75	0.21	0.00	14.98	22.54	0.27	**100.22**	**4.00**	**79.2**	42.53
17	MR04_cpx13	Anorthosite HW	52.58	0.38	1.41	0.26	0.00	6.87	0.23	0.00	15.43	21.35	0.26	**98.75**	**4.00**	**80.0**	44.39
18	MR04_cpx14	Anorthosite HW	52.68	0.42	1.52	0.41	1.21	5.84	0.36	0.00	14.99	22.80	0.27	**100.51**	**4.01**	**79.4**	42.26
19	MR04_cpx15	Anorthosite HW	52.78	0.39	1.43	0.34	0.00	8.69	0.21	0.00	16.00	19.42	0.24	**99.49**	**4.00**	**76.7**	45.77
20	MR04_cpx16	Anorthosite HW	52.96	0.41	1.50	0.49	0.10	6.27	0.18	0.00	14.99	22.96	0.24	**100.12**	**4.00**	**80.8**	42.63
21	MR04_cpx17	Anorthosite HW	52.81	0.37	1.49	0.46	0.39	6.74	0.15	0.00	15.21	22.03	0.27	**99.94**	**4.00**	**79.2**	43.31
22	MR06_cpx3	Leuconorite HW	52.59	0.39	1.63	0.44	0.66	6.57	0.18	0.00	14.56	22.77	0.29	**100.07**	**4.01**	**78.4**	41.54
23	MR06_cpx4	Leuconorite HW	52.72	0.44	1.65	0.45	0.13	7.39	0.13	0.00	14.67	22.34	0.25	**100.14**	**4.00**	**77.7**	41.90
24	MR06_cpx5	Leuconorite HW	52.88	0.33	1.43	0.36	0.60	6.63	0.27	0.00	14.57	23.00	0.26	**100.33**	**4.01**	**78.4**	41.29
25	MR06_cpx6	Leuconorite HW	52.62	0.36	1.68	0.56	0.69	6.77	0.35	0.00	14.51	22.59	0.28	**100.42**	**4.01**	**77.8**	41.35
26	MR06_cpx7	Leuconorite HW	52.50	0.44	1.57	0.39	1.30	6.10	0.25	0.00	14.46	23.07	0.32	**100.41**	**4.01**	**78.0**	41.00
27	MR06_cpx8	Leuconorite HW	52.75	0.45	1.48	0.30	0.09	7.15	0.17	0.00	14.70	22.47	0.26	**99.79**	**4.00**	**78.4**	41.99
28	MR06_cpx18	Leuconorite HW	52.61	0.45	1.51	0.28	0.23	7.10	0.24	0.00	14.34	22.86	0.24	**99.87**	**4.00**	**77.8**	40.96
29	MR06_cpx19	Leuconorite HW	52.53	0.51	1.62	0.23	0.63	7.75	0.24	0.00	14.65	21.80	0.27	**100.23**	**4.01**	**75.9**	41.72
30	MR06_cpx20	Leuconorite HW	52.59	0.48	1.49	0.27	0.97	6.52	0.24	0.00	14.43	23.06	0.28	**100.33**	**4.01**	**77.7**	40.88
31	MR06_cpx21	Leuconorite HW	52.73	0.50	1.49	0.24	0.64	7.35	0.18	0.00	14.58	22.47	0.26	**100.43**	**4.01**	**76.6**	41.32
32	MR06_cpx23	Leuconorite HW	53.13	0.28	1.30	0.33	0.00	6.31	0.20	0.00	14.61	23.15	0.24	**99.54**	**4.00**	**80.5**	41.85
33	MR06_cpx24	Leuconorite HW	52.70	0.46	1.78	0.43	0.09	6.56	0.29	0.00	14.55	22.98	0.26	**100.09**	**4.00**	**79.6**	41.63

Appendix 2: Clinopyroxene Compositions. Oxide data are presented in wt. %. Pyroxenes were normalised to 6 oxygens.

Point	Sample	Unit	SiO_2	TiO_2	Al_2O_3	Cr_2O_3	Fe_2O_3	FeO	MnO	NiO	MgO	CaO	Na_2O	Total	Total Cations	Mg#	En
34	MR06_cpx25	Leuconorite HW	52.87	0.36	1.40	0.39	0.34	6.54	0.35	0.00	14.41	23.23	0.26	**100.15**	**4.00**	**78.9**	41.01
35	MR07_cpx26	Norite HW	53.15	0.44	1.90	0.65	0.26	6.21	0.12	0.00	15.00	22.86	0.34	**100.92**	**4.00**	**80.6**	42.72
36	MR07_cpx27	Norite HW	53.24	0.26	1.82	0.54	0.00	7.26	0.21	0.00	15.96	20.05	0.28	**99.62**	**3.99**	**79.7**	46.17
37	MR07_cpx28	Norite HW	53.58	0.33	1.67	0.58	0.00	6.23	0.17	0.00	15.20	22.81	0.34	**100.90**	**4.00**	**81.3**	43.20
38	MR07_cpx29	Norite HW	51.73	0.31	1.28	0.60	0.51	11.70	0.27	0.00	11.98	21.58	0.17	**100.14**	**4.00**	**80.2**	44.30
39	MR07_cpx30	Norite HW	49.07	0.27	1.50	0.07	0.00	13.35	0.31	0.00	11.19	20.99	0.14	**96.89**	**4.00**	**79.9**	41.96
40	MR07_cpx31	Norite HW	52.90	0.43	1.37	0.41	0.96	6.17	0.22	0.00	15.27	22.49	0.27	**100.47**	**4.01**	**79.5**	43.00
41	MR07_cpx32	Norite HW	53.04	0.50	1.59	0.40	0.85	7.33	0.24	0.00	15.46	21.27	0.32	**101.00**	**4.01**	**77.3**	43.64
42	MR07_cpx33	Norite HW	52.91	0.54	1.55	0.41	0.04	6.35	0.16	0.00	14.85	23.10	0.25	**100.18**	**4.00**	**80.6**	42.27
43	MR07_cpx_rim?	Norite HW	53.03	0.44	1.36	0.29	0.00	6.65	0.16	0.00	14.90	22.40	0.25	**99.49**	**3.99**	**80.0**	42.78
44	MR07_cpx_rim?	Norite HW	54.44	0.07	0.74	0.19	0.00	6.50	0.22	0.00	15.03	23.59	0.20	**100.97**	**3.99**	**80.5**	42.03
45	MR07_cpx_incl5	Norite HW	53.28	0.32	2.10	0.64	0.00	6.18	0.19	0.00	14.53	22.98	0.42	**100.65**	**4.00**	**80.7**	41.96
46	MR07_cpx_incl6	Norite HW	52.96	0.33	2.12	0.63	0.37	6.65	0.20	0.00	14.67	22.48	0.39	**100.81**	**4.00**	**78.9**	42.09
47	MR08_cpx35	Pyroxenite Reef	54.16	0.45	1.73	0.67	0.00	5.17	0.15	0.00	15.84	23.08	0.27	**101.50**	**3.99**	**84.5**	44.73
48	MR08_cpx36	Pyroxenite Reef	54.01	0.40	1.75	0.79	0.00	5.10	0.10	0.00	15.68	23.38	0.25	**101.45**	**3.99**	**84.6**	44.29
49	MR08_cpx_incl9	Pyroxenite Reef	54.53	0.28	1.59	0.82	0.00	4.67	0.16	0.00	15.83	22.93	0.32	**101.12**	**3.98**	**85.8**	45.19
50	MR08_cpx38	Pyroxenite Reef	53.59	0.39	2.03	0.72	0.00	5.56	0.12	0.00	15.41	23.20	0.30	**101.33**	**4.00**	**83.1**	43.67
51	MR08_cpx39	Pyroxenite Reef	53.79	0.37	2.14	0.73	0.00	5.57	0.12	0.00	15.24	23.14	0.33	**101.43**	**3.99**	**83.0**	43.46
52	MR08_cpx40	Pyroxenite Reef	54.21	0.30	1.87	0.61	0.00	8.49	0.25	0.00	19.18	15.49	0.22	**100.59**	**3.99**	**80.1**	54.46
53	MR08_cpx_incl14	Pyroxenite Reef	54.44	0.35	1.57	0.73	0.00	4.55	0.01	0.00	16.09	23.34	0.30	**101.37**	**3.99**	**86.3**	45.42
54	MR08_cpx_incl15	Pyroxenite Reef	54.23	0.34	1.83	0.77	0.00	4.39	0.01	0.00	15.80	23.43	0.26	**101.06**	**3.99**	**86.5**	44.99
55	MR08_cpx_incl17	Pyroxenite Reef	51.94	0.37	1.69	0.76	2.30	2.57	0.11	0.00	15.91	23.63	0.24	**99.53**	**4.02**	**85.9**	44.74
56	MR11_cpx_incl18	Pyroxenite Reef	54.29	0.40	1.49	0.78	0.00	4.71	0.15	0.00	15.82	23.37	0.37	**101.38**	**3.99**	**85.7**	44.75
57	MR11_cpx_incl19	Pyroxenite Reef	53.87	0.40	1.55	0.80	0.00	4.66	0.10	0.00	15.82	22.98	0.37	**100.54**	**3.99**	**85.8**	45.20
58	MR11_cpx_incl22	Pyroxenite Reef	54.06	0.33	1.81	1.04	0.00	4.87	0.10	0.00	15.94	22.50	0.35	**101.01**	**3.99**	**85.4**	45.67
59	MR11_cpx_incl23	Pyroxenite Reef	54.26	0.28	1.89	0.98	0.00	5.58	0.04	0.00	15.58	22.88	0.35	**101.83**	**3.99**	**83.3**	44.29
60	MR11_cpx43	Pyroxenite Reef	55.41	0.17	3.36	0.50	0.00	6.43	0.13	0.00	20.12	12.68	0.41	**99.22**	**3.94**	**84.8**	61.13
61	MR10_cpx44	Pyroxenite Reef	53.52	0.46	1.93	0.36	0.71	5.02	0.16	0.00	16.60	22.22	0.25	**101.22**	**4.01**	**83.9**	46.32
62	MR10_cpx45	Pyroxenite Reef	53.76	0.58	1.79	0.38	0.00	4.81	0.12	0.00	15.69	23.54	0.30	**100.96**	**4.00**	**85.3**	44.35
63	MR10_cpx46	Pyroxenite Reef	54.20	0.51	1.65	0.35	0.00	4.89	0.12	0.00	16.14	23.27	0.29	**101.41**	**4.00**	**85.5**	45.23
64	MR10_cpx47	Pyroxenite Reef	54.23	0.60	1.51	0.39	0.00	5.15	0.19	0.00	15.96	22.91	0.27	**101.21**	**3.99**	**84.7**	45.05
65	MR10_cpx48	Pyroxenite Reef	54.16	0.67	1.74	0.36	0.00	4.91	0.13	0.00	15.72	23.52	0.31	**101.51**	**3.99**	**85.1**	44.33
66	MR10_cpx49	Pyroxenite Reef	54.07	0.57	1.56	0.38	0.00	5.33	0.10	0.00	16.08	22.96	0.27	**101.33**	**4.00**	**84.3**	45.13
67	MR10_cpx50	Pyroxenite Reef	53.57	0.44	1.76	0.61	0.28	5.01	0.17	0.00	16.06	22.81	0.31	**101.01**	**4.00**	**84.5**	45.24

Appendix 2: Clinopyroxene Compositions. Oxide data are presented in wt. %. Pyroxenes were normalised to 6 oxygens.

Point	Sample	Unit	SiO_2	TiO_2	Al_2O_3	Cr_2O_3	Fe_2O_3	FeO	MnO	NiO	MgO	CaO	Na_2O	Total	Total Cations	Mg#	En
68	MR10_cpx51	Pyroxenite Reef	54.13	0.47	1.80	0.59	0.00	5.94	0.17	0.00	16.64	21.67	0.28	**101.70**	**4.00**	**83.3**	46.68
69	MR09_cpx52	Anorthosite Reef	53.88	0.65	1.67	0.52	0.00	5.57	0.07	0.00	15.72	22.70	0.32	**101.11**	**3.99**	**83.4**	44.66
70	MR09_cpx53	Anorthosite Reef	53.47	0.59	1.69	0.50	0.00	5.45	0.13	0.00	15.49	22.97	0.35	**100.63**	**4.00**	**83.5**	44.09
71	MR09_cpx54	Anorthosite Reef	54.13	0.48	1.44	0.50	0.00	5.47	0.19	0.00	15.59	23.29	0.30	**101.38**	**3.99**	**83.5**	43.90
72	MR09_cpx55	Anorthosite Reef	54.04	0.56	1.65	0.44	0.00	5.44	0.08	0.00	15.79	22.74	0.36	**101.11**	**3.99**	**83.8**	44.81
73	MR09_cpx56	Anorthosite Reef	52.75	0.56	1.65	0.46	1.55	4.21	0.15	0.00	15.67	23.13	0.36	**100.48**	**4.01**	**83.3**	44.10
74	MR09_cpx58	Anorthosite Reef	53.76	0.48	1.62	0.74	0.00	5.00	0.14	0.00	15.39	23.01	0.36	**100.49**	**3.99**	**84.6**	44.21
75	MR09_cpx60	Anorthosite Reef	52.38	2.15	1.63	0.71	0.00	6.20	0.18	0.00	15.66	21.86	0.29	**101.05**	**3.99**	**81.8**	44.81
76	MR13_cpx_incl24	Pyroxenite Reef	52.38	0.39	3.06	1.15	0.00	4.89	0.04	0.00	15.13	22.64	0.45	**100.11**	**4.00**	**84.6**	44.27
77	MR13_cpx_incl25	Pyroxenite Reef	52.58	0.43	3.03	1.15	0.45	4.21	0.17	0.00	15.26	23.07	0.46	**100.80**	**4.00**	**85.5**	44.20
78	MR13_cpx_incl26	Pyroxenite Reef	53.88	0.25	1.85	0.79	0.00	4.02	0.15	0.00	16.01	23.21	0.37	**100.53**	**4.00**	**87.6**	45.70
79	MR13_cpx_incl27	Pyroxenite Reef	54.02	0.28	1.84	0.83	0.00	4.28	0.21	0.00	15.97	23.34	0.37	**101.14**	**4.00**	**86.9**	45.28
80	MR13_cpx_incl28	Pyroxenite Reef	52.90	0.40	2.79	1.10	0.51	3.88	0.15	0.00	15.39	23.28	0.51	**100.88**	**4.00**	**86.3**	44.42
81	MR13_cpx_incl29	Pyroxenite Reef	52.80	0.41	2.69	1.04	1.15	3.82	0.16	0.00	15.43	23.26	0.48	**101.24**	**4.01**	**85.0**	44.13
82	MR13_cpx_rim	Pyroxenite Reef	53.72	0.29	2.05	1.01	0.00	5.27	0.21	0.00	15.99	21.99	0.34	**100.87**	**3.99**	**84.4**	45.85
83	MR13_cpx_rim	Pyroxenite Reef	53.57	0.36	1.87	1.03	0.29	5.04	0.15	0.00	16.62	21.83	0.35	**101.11**	**4.00**	**84.8**	47.00
84	MR13_cpx_rim	Pyroxenite Reef	53.30	0.32	2.02	0.97	1.08	3.71	0.22	0.00	16.19	23.01	0.38	**101.19**	**4.01**	**86.0**	45.63
85	MR16_cpx_incl30	Pyroxenite Reef	53.04	0.56	2.24	0.88	0.78	4.68	0.17	0.00	15.30	23.10	0.48	**101.22**	**4.01**	**83.5**	43.69
86	MR16_cpx_incl31	Pyroxenite Reef	53.34	0.62	1.88	0.72	0.00	6.18	0.07	0.00	16.69	20.70	0.38	**100.57**	**4.00**	**82.8**	47.57
87	MR16_cpx_incl32	Pyroxenite Reef	52.80	0.60	1.98	0.80	1.07	4.58	0.10	0.00	15.98	22.48	0.37	**100.75**	**4.01**	**83.7**	45.25
88	MR16_cpx_incl33	Pyroxenite Reef	53.14	0.28	2.12	0.93	0.46	4.20	0.19	0.00	15.54	23.14	0.44	**100.44**	**4.00**	**85.7**	44.55
89	MR16_cpx_incl34	Pyroxenite Reef	53.15	0.24	2.11	0.98	1.13	4.13	0.18	0.00	15.64	23.06	0.44	**101.05**	**4.01**	**84.4**	44.42
90	MR16_cpx_incl35	Pyroxenite Reef	53.90	0.13	1.49	0.55	0.91	4.05	0.18	0.00	15.64	24.35	0.28	**101.48**	**4.01**	**85.1**	43.47
91	MR16_cpx73	Pyroxenite Reef	53.56	0.35	2.05	1.04	0.00	6.61	0.15	0.00	16.71	20.40	0.36	**101.23**	**4.00**	**81.8**	47.52
92	MR16_cpx74	Pyroxenite Reef	53.24	0.36	1.94	1.08	0.16	4.60	0.14	0.00	15.68	22.97	0.41	**100.57**	**4.00**	**85.5**	44.88
93	MR16_cpx75	Pyroxenite Reef	53.31	0.35	2.07	1.12	0.01	4.85	0.12	0.00	15.88	22.73	0.36	**100.79**	**4.00**	**85.3**	45.35
94	MR16_cpx76	Pyroxenite Reef	53.65	0.39	2.02	1.03	0.00	4.70	0.21	0.00	15.53	22.86	0.41	**100.80**	**3.99**	**85.5**	44.73
95	MR19_cpx_incl39	Pyroxenite Reef	53.71	0.26	1.62	0.90	0.83	4.62	0.18	0.00	15.77	23.21	0.39	**101.49**	**4.01**	**84.0**	44.33
96	MR19_cpx_incl40	Pyroxenite Reef	53.30	0.28	1.59	0.86	0.16	4.65	0.19	0.00	15.63	22.96	0.40	**100.03**	**4.00**	**85.3**	44.74
97	MR19_cpx_incl41	Pyroxenite Reef	53.10	0.33	1.82	0.93	1.64	4.57	0.16	0.00	15.79	22.57	0.43	**101.34**	**4.02**	**82.3**	44.47
98	MR19_cpx_incl42	Pyroxenite Reef	53.11	0.32	1.86	1.05	0.55	4.60	0.14	0.00	15.72	22.71	0.42	**100.47**	**4.01**	**84.6**	44.94
99	MR19_cpx_rim1	Pyroxenite Reef	53.66	0.35	1.40	0.86	0.53	4.62	0.06	0.00	15.91	23.21	0.37	**100.97**	**4.00**	**84.8**	44.83
100	MR19_cpx_rim2	Pyroxenite Reef	53.94	0.33	1.31	0.81	0.30	4.52	0.13	0.00	15.96	23.26	0.41	**100.96**	**4.00**	**85.6**	45.04
101	MR19_cpx_rim3	Pyroxenite Reef	54.08	0.28	1.31	0.86	0.37	4.29	0.13	0.00	16.09	23.41	0.39	**101.21**	**4.00**	**86.1**	45.22

Appendix 2: Clinopyroxene Compositions. Oxide data are presented in wt. %. Pyroxenes were normalised to 6 oxygens.

Point	Sample	Unit	SiO_2	TiO_2	Al_2O_3	Cr_2O_3	Fe_2O_3	FeO	MnO	NiO	MgO	CaO	Na_2O	Total	Total Cations	Mg#	En
102	MR19_cpx_rim4	Pyroxenite Reef	54.18	0.37	1.42	0.90	0.05	4.56	0.12	0.00	15.85	23.65	0.41	**101.50**	**4.00**	**86.0**	44.64
103	MR19_cpx77	Pyroxenite Reef	52.97	0.49	2.27	0.81	0.00	5.46	0.21	0.00	15.71	22.33	0.30	**100.55**	**4.00**	**83.7**	44.95
104	MR19_cpx78	Pyroxenite Reef	53.29	0.39	2.05	0.70	0.00	6.37	0.00	0.00	16.35	21.02	0.34	**100.50**	**4.00**	**82.1**	46.67
105	MR19_cpx80	Pyroxenite Reef	53.58	0.41	1.92	0.64	0.00	8.21	0.27	0.00	18.05	16.98	0.26	**100.32**	**3.99**	**79.7**	51.56
106	MR21_cpx82	Pyroxenite Reef	53.35	0.64	1.72	0.68	0.63	4.91	0.13	0.00	15.55	23.19	0.41	**101.21**	**4.01**	**83.5**	43.97
107	MR21_cpx84	Pyroxenite Reef	52.98	0.54	1.83	0.75	0.58	4.70	0.12	0.00	15.56	22.92	0.42	**100.38**	**4.01**	**84.1**	44.42
108	MR21_cpx85	Pyroxenite Reef	53.31	0.67	1.67	0.75	0.84	5.12	0.18	0.00	15.70	22.63	0.44	**101.30**	**4.01**	**82.7**	44.40
109	MR21_cpx92	Pyroxenite Reef	52.82	0.61	1.93	0.68	0.96	5.14	0.02	0.00	15.86	22.10	0.43	**100.54**	**4.01**	**82.5**	45.14
110	MR21_cpx93	Pyroxenite Reef	53.30	0.60	1.91	0.73	0.33	5.07	0.17	0.00	15.98	22.28	0.44	**100.79**	**4.00**	**84.1**	45.52
111	MR21_cpx94	Pyroxenite Reef	52.98	0.67	1.96	0.74	0.87	4.79	0.14	0.00	15.35	23.11	0.44	**101.06**	**4.01**	**83.1**	43.64
112	MR21_cpx95	Pyroxenite Reef	53.91	0.48	1.63	0.58	0.00	7.25	0.14	0.00	17.62	18.20	0.37	**100.18**	**3.99**	**81.2**	50.57
113	MR22_cpx96	Pyroxenite Reef	54.83	0.23	1.81	0.64	0.00	9.24	0.27	0.00	20.55	12.45	0.19	**100.23**	**3.97**	**79.9**	58.98
114	MR22_cpx99	Pyroxenite Reef	56.56	0.23	2.62	0.48	0.00	5.04	0.14	0.00	20.95	12.71	0.38	**99.09**	**3.93**	**88.1**	63.51
115	MR22_cpx101	Pyroxenite Reef	53.09	0.62	5.00	0.66	0.00	6.35	0.00	0.00	19.40	12.56	0.81	**98.47**	**3.97**	**84.5**	60.66
116	MR22_cpx_incl54	Pyroxenite Reef	54.05	0.50	2.05	0.92	0.00	5.45	0.13	0.00	15.43	23.21	0.45	**102.18**	**4.00**	**83.5**	43.79
117	MR23_cpx104	Chromitite	53.46	0.53	1.90	0.77	0.12	5.00	0.08	0.00	15.71	23.08	0.38	**101.03**	**4.00**	**84.6**	44.61
118	MR23_cpx106	Chromitite	53.31	0.47	2.14	0.08	0.00	9.62	0.31	0.00	13.85	21.05	0.26	**101.09**	**3.99**	**72.0**	40.08
119	MR23_cpx108	Chromitite	53.40	0.41	1.93	0.18	0.00	7.13	0.27	0.00	14.99	22.12	0.27	**100.69**	**3.99**	**78.9**	42.77
120	MR23_cpx113	Chromitite	53.40	0.49	1.54	0.16	0.54	7.13	0.17	0.00	14.98	22.69	0.27	**101.35**	**4.00**	**77.8**	42.01
121	MR23_cpx114	Chromitite	53.64	0.50	1.43	0.15	0.12	7.34	0.24	0.00	15.04	22.72	0.23	**101.40**	**4.00**	**78.3**	42.14
122	MR23_cpx115	Chromitite	53.66	0.47	1.46	0.10	0.00	7.37	0.21	0.00	14.90	22.83	0.26	**101.27**	**4.00**	**78.3**	41.90
123	MR23_cpx116	Chromitite	53.67	0.35	1.43	0.11	0.36	6.72	0.29	0.00	14.61	23.60	0.26	**101.39**	**4.00**	**78.7**	40.94
124	MR24_cpx119	Anorthosite FW	53.91	0.41	1.22	0.05	0.00	7.99	0.22	0.00	14.86	22.50	0.22	**101.36**	**4.00**	**76.8**	41.69
125	MR24_cpx120	Anorthosite FW	53.58	0.54	1.53	0.09	0.00	9.98	0.24	0.00	15.48	19.69	0.23	**101.36**	**4.00**	**73.5**	43.77
126	MR24_cpx124	Anorthosite FW	53.55	0.50	1.51	0.12	0.00	8.09	0.19	0.00	14.68	22.28	0.24	**101.16**	**4.00**	**76.4**	41.53
127	MR24_cpx126	Anorthosite FW	53.41	0.36	1.35	0.10	0.68	6.93	0.27	0.00	14.54	23.43	0.23	**101.28**	**4.01**	**77.5**	40.66
128	MR24_cpx127	Anorthosite FW	53.50	0.57	1.53	0.13	0.00	7.87	0.21	0.00	14.51	22.79	0.26	**101.37**	**4.00**	**76.7**	40.95
129	MR24_cpx128	Anorthosite FW	53.48	0.53	1.53	0.10	0.00	8.09	0.22	0.00	14.54	22.74	0.22	**101.44**	**4.00**	**76.2**	40.89
130	MR24_cpx_incl63	Anorthosite FW	53.63	0.52	1.27	0.03	0.49	7.43	0.35	0.00	15.17	22.50	0.21	**101.60**	**4.00**	**77.4**	42.18
131	MR24_cpx_incl64	Anorthosite FW	53.42	0.63	1.24	0.00	0.88	6.60	0.28	0.00	15.60	22.48	0.21	**101.34**	**4.01**	**79.0**	43.25
132	MR24_cpx_incl65	Anorthosite FW	53.52	0.55	1.31	0.00	0.00	6.78	0.38	0.00	15.15	22.67	0.21	**100.57**	**4.00**	**79.9**	42.72
133	MR24_cpx_incl66	Anorthosite FW	53.76	0.59	1.36	0.00	0.00	7.56	0.18	0.00	15.06	22.51	0.26	**101.27**	**4.00**	**78.0**	42.32

Appendix 3: Orthopyroxene Compositions. Oxide data are presented in wt. %. Pyroxenes were normalised to 6 oxygens.

Point	Sample	Unit	SiO_2	TiO_2	Al_2O_3	Cr_2O_3	Fe_2O_3	FeO	MnO	NiO	MgO	CaO	Na_2O	Total	Total Cations	Mg#	En
1	MR04_opx1	Anorthosite HW	53.94	0.17	1.13	0.33	0.00	16.27	0.42	0.00	24.50	2.24	0.03	**99.03**	**3.99**	**72.9**	69.06
2	MR04_opx2	Anorthosite HW	53.70	0.16	0.96	0.21	0.00	17.02	0.37	0.00	24.96	1.12	0.01	**98.50**	**3.99**	**72.3**	70.26
3	MR07_opx_incl4	Norite HW	54.53	0.18	0.99	0.27	0.00	17.16	0.34	0.00	26.01	0.92	0.00	**100.41**	**4.00**	**73.0**	71.27
4	MR07_opx_incl5	Norite HW	54.28	0.25	1.03	0.26	0.00	16.22	0.37	0.00	25.74	1.54	0.00	**99.70**	**3.99**	**73.9**	71.19
5	MR07_opx_incl6	Norite HW	54.56	0.20	1.09	0.29	0.00	16.54	0.38	0.00	25.75	0.95	0.01	**99.78**	**3.99**	**73.5**	71.67
6	MR07_opx_incl7	Norite HW	54.18	0.17	1.22	0.27	0.00	16.07	0.32	0.00	25.28	1.53	0.01	**99.06**	**3.98**	**73.7**	71.06
7	MR07_opx_incl7	Norite HW	53.89	0.10	1.35	0.39	0.00	17.74	0.42	0.00	24.84	0.49	0.00	**99.22**	**3.98**	**71.4**	70.20
8	MR08_opx13	Pyroxenite Reef	56.47	0.13	0.96	0.30	0.00	12.95	0.38	0.00	28.48	0.84	0.02	**100.53**	**3.98**	**79.7**	77.90
9	MR08_opx14	Pyroxenite Reef	56.27	0.15	1.04	0.38	0.00	12.61	0.24	0.00	27.49	2.27	0.03	**100.49**	**3.98**	**79.5**	75.66
10	MR08_opx15	Pyroxenite Reef	55.87	0.17	1.08	0.46	0.00	12.58	0.31	0.00	27.26	3.15	0.09	**100.95**	**3.99**	**79.4**	74.17
11	MR08_opx16	Pyroxenite Reef	56.38	0.16	0.93	0.41	0.00	13.10	0.31	0.00	28.44	0.75	0.03	**100.50**	**3.98**	**79.5**	77.90
12	MR08_opx17	Pyroxenite Reef	55.79	0.16	0.98	0.31	0.00	14.53	0.35	0.00	27.50	0.82	0.01	**100.46**	**3.98**	**77.1**	75.46
13	MR08_opx18	Pyroxenite Reef	55.80	0.12	0.97	0.37	0.00	13.49	0.35	0.00	26.64	2.23	0.02	**99.97**	**3.97**	**77.9**	73.98
14	MR08_opx19	Pyroxenite Reef	55.40	0.21	1.06	0.34	0.00	14.21	0.36	0.00	26.80	1.90	0.01	**100.30**	**3.98**	**77.1**	73.73
15	MR08_opx20	Pyroxenite Reef	55.46	0.20	1.24	0.44	0.00	13.32	0.21	0.00	26.58	2.01	0.02	**99.49**	**3.97**	**78.1**	74.63
16	MR08_opx21	Pyroxenite Reef	55.54	0.21	1.24	0.38	0.00	14.84	0.30	0.00	27.16	0.82	0.01	**100.50**	**3.98**	**76.5**	74.94
17	MR08_opx22	Pyroxenite Reef	55.09	0.18	1.14	0.39	0.00	14.73	0.00	0.00	27.29	0.82	0.02	**99.67**	**3.98**	**76.8**	75.50
18	MR08_opx23	Pyroxenite Reef	56.35	0.17	0.96	0.45	0.00	11.91	0.26	0.00	28.50	0.88	0.03	**99.50**	**3.97**	**81.0**	79.25
19	MR08_opx24	Pyroxenite Reef	56.10	0.15	1.10	0.48	0.00	12.00	0.26	0.00	28.38	0.77	0.01	**99.24**	**3.97**	**80.8**	79.25
20	MR08_opx25	Pyroxenite Reef	56.12	0.16	1.01	0.47	0.00	12.61	0.00	0.00	28.20	1.63	0.01	**100.21**	**3.98**	**79.9**	77.37
21	MR11_opx26	Pyroxenite Reef	56.18	0.25	0.97	0.26	0.00	13.13	0.02	0.00	27.23	1.87	0.02	**99.93**	**3.97**	**78.7**	75.74
22	MR11_opx27	Pyroxenite Reef	55.39	0.24	0.92	0.30	0.00	13.74	0.00	0.00	27.63	1.46	0.01	**99.69**	**3.98**	**78.2**	75.93
23	MR11_opx28	Pyroxenite Reef	55.85	0.28	0.63	0.16	0.00	13.69	0.28	0.00	28.05	0.99	0.01	**99.93**	**3.98**	**78.5**	76.63
24	MR11_opx29	Pyroxenite Reef	55.98	0.21	0.97	0.37	0.00	12.21	0.00	0.00	28.20	0.86	0.02	**98.81**	**3.97**	**80.5**	79.07
25	MR11_opx30	Pyroxenite Reef	56.00	0.26	0.91	0.37	0.00	12.76	0.00	0.00	28.05	0.84	0.00	**99.19**	**3.97**	**79.7**	78.32
26	MR11_opx31	Pyroxenite Reef	56.31	0.25	0.76	0.32	0.00	12.64	0.34	0.00	27.91	1.53	0.02	**100.09**	**3.97**	**79.7**	76.90
27	MR11_opx32	Pyroxenite Reef	51.73	0.31	1.28	0.32	0.00	11.70	0.27	0.00	11.98	21.58	0.17	**99.34**	**3.98**	**78.9**	77.41
28	MR11_opx33	Pyroxenite Reef	49.07	0.27	1.50	0.07	0.00	13.35	0.31	0.00	11.19	20.99	0.14	**96.89**	**3.98**	**80.3**	75.01
29	MR11_opx34	Pyroxenite Reef	55.90	0.15	0.82	0.33	0.00	12.30	0.23	0.00	28.25	0.85	0.01	**98.84**	**3.97**	**80.4**	78.71
30	MR11_opx35	Pyroxenite Reef	56.20	0.23	0.99	0.39	0.00	12.39	0.34	0.00	28.35	1.02	0.02	**99.92**	**3.97**	**80.3**	78.26
31	MR11_opx36	Pyroxenite Reef	56.01	0.19	0.96	0.42	0.00	12.80	0.13	0.00	28.39	1.00	0.00	**99.91**	**3.98**	**79.8**	78.07
32	MR11_opx37	Pyroxenite Reef	55.84	0.22	0.91	0.39	0.00	12.63	0.20	0.00	28.28	1.10	0.01	**99.56**	**3.98**	**80.0**	77.98

Appendix 3: Orthopyroxene Compositions. Oxide data are presented in wt. %. Pyroxenes were normalised to 6 oxygens.

Point	Sample	Unit	SiO_2	TiO_2	Al_2O_3	Cr_2O_3	Fe_2O_3	FeO	MnO	NiO	MgO	CaO	Na_2O	Total	Total Cations	Mg#	En
33	MR11_opx38	Pyroxenite Reef	55.96	0.12	0.99	0.37	0.00	12.83	0.21	0.00	28.39	0.76	0.02	**99.65**	**3.98**	**79.8**	78.30
34	MR11_opx39	Pyroxenite Reef	56.08	0.13	1.03	0.42	0.00	12.54	0.26	0.00	28.56	0.92	0.00	**99.93**	**3.98**	**80.2**	78.46
35	MR10_opx40	Pyroxenite Reef	56.07	0.28	1.00	0.40	0.00	13.18	0.29	0.00	28.41	0.92	0.00	**100.55**	**3.98**	**79.3**	77.55
36	MR10_opx41	Pyroxenite Reef	55.88	0.26	1.01	0.41	0.00	12.24	0.23	0.00	27.73	2.00	0.04	**99.80**	**3.98**	**80.1**	76.66
37	MR10_opx42	Pyroxenite Reef	55.77	0.28	1.11	0.45	0.00	12.99	0.33	0.00	28.00	1.19	0.02	**100.13**	**3.98**	**79.3**	77.07
38	MR10_opx44	Pyroxenite Reef	55.81	0.34	1.10	0.51	0.00	12.89	0.29	0.00	27.95	1.19	0.01	**100.08**	**3.98**	**79.4**	77.20
39	MR10_opx45	Pyroxenite Reef	56.06	0.31	1.04	0.45	0.00	12.70	0.14	0.00	27.91	1.22	0.01	**99.85**	**3.97**	**79.7**	77.54
40	MR10_opx46	Pyroxenite Reef	55.50	0.31	1.02	0.41	0.00	13.32	0.31	0.00	27.97	1.08	0.01	**99.92**	**3.98**	**78.9**	76.85
41	MR10_opx47	Pyroxenite Reef	56.21	0.34	1.07	0.44	0.00	12.62	0.26	0.00	28.10	0.94	0.03	**100.00**	**3.97**	**79.9**	78.05
42	MR10_opx49	Pyroxenite Reef	56.15	0.20	1.11	0.39	0.00	12.53	0.16	0.00	27.79	2.38	0.04	**100.74**	**3.98**	**79.8**	75.89
43	MR10_opx50	Pyroxenite Reef	55.56	0.28	1.14	0.45	0.00	11.77	0.36	0.00	28.01	1.64	0.02	**99.22**	**3.98**	**80.9**	77.82
44	MR10_opx51	Pyroxenite Reef	55.91	0.28	1.13	0.40	0.00	13.16	0.29	0.00	28.35	1.18	0.01	**100.70**	**3.98**	**79.3**	77.16
45	MR10_opx52	Pyroxenite Reef	55.83	0.27	1.16	0.44	0.00	13.16	0.34	0.00	27.93	1.31	0.03	**100.48**	**3.98**	**79.1**	76.62
46	MR10_opx53	Pyroxenite Reef	56.27	0.26	1.10	0.45	0.00	12.29	0.25	0.00	28.37	1.18	0.03	**100.19**	**3.97**	**80.4**	78.24
47	MR10_opx54	Pyroxenite Reef	56.03	0.26	0.96	0.41	0.00	12.33	0.31	0.00	28.35	0.99	0.03	**99.66**	**3.97**	**80.4**	78.41
48	MR10_opx55	Pyroxenite Reef	55.89	0.28	0.96	0.52	0.00	12.44	0.29	0.00	28.68	1.11	0.02	**100.18**	**3.98**	**80.4**	78.32
49	MR10_opx56	Pyroxenite Reef	55.88	0.21	1.29	0.45	0.00	13.03	0.23	0.00	28.51	0.97	0.00	**100.55**	**3.98**	**79.6**	77.80
50	MR10_opx57	Pyroxenite Reef	54.73	0.20	1.09	0.96	0.00	13.04	0.20	0.00	27.38	1.78	0.04	**99.41**	**3.99**	**78.9**	75.88
51	MR10_opx58	Pyroxenite Reef	55.79	0.21	1.13	0.47	0.00	12.54	0.16	0.00	27.79	2.64	0.05	**100.76**	**3.99**	**79.8**	75.49
52	MR10_opx59	Pyroxenite Reef	55.43	0.30	1.02	0.38	0.00	13.11	0.28	0.00	28.23	1.00	0.03	**99.77**	**3.99**	**79.3**	77.42
53	MR10_opx60	Pyroxenite Reef	55.96	0.31	1.00	0.35	0.00	13.30	0.32	0.00	28.29	1.05	0.01	**100.59**	**3.98**	**79.1**	77.11
54	MR10_opx61	Pyroxenite Reef	55.44	0.27	1.07	0.38	0.00	12.75	0.28	0.00	27.93	0.99	0.00	**99.12**	**3.98**	**79.6**	77.67
55	MR10_opx62	Pyroxenite Reef	55.44	0.29	1.06	0.34	0.00	12.89	0.25	0.00	27.94	0.82	0.03	**99.04**	**3.98**	**79.4**	77.83
56	MR10_opx63?	Pyroxenite Reef	51.73	0.31	1.28	0.44	0.00	11.70	0.27	0.00	11.98	21.58	0.17	**99.46**	**3.97**	**81.4**	78.38
57	MR10_opx63?	Pyroxenite Reef	49.07	0.27	1.50	0.07	0.00	13.35	0.31	0.00	11.19	20.99	0.14	**96.89**	**3.98**	**81.2**	76.24
58	MR13_opx64	Pyroxenite Reef	55.79	0.16	1.16	0.55	0.00	10.80	0.24	0.00	29.10	0.88	0.01	**98.68**	**3.97**	**82.8**	81.00
59	MR13_opx65	Pyroxenite Reef	55.92	0.12	1.12	0.49	0.00	12.72	0.35	0.00	29.26	0.59	0.01	**100.58**	**3.99**	**80.4**	79.03
60	MR13_opx66	Pyroxenite Reef	55.73	0.14	1.09	0.51	0.00	12.59	0.34	0.00	29.15	0.90	0.01	**100.45**	**3.99**	**80.5**	78.67
61	MR13_opx67	Pyroxenite Reef	55.69	0.10	1.27	0.52	0.00	11.75	0.31	0.00	28.84	0.89	0.04	**99.40**	**3.98**	**81.4**	79.57
62	MR13_opx68	Pyroxenite Reef	55.29	0.11	1.45	0.56	0.00	10.74	0.23	0.00	27.82	2.57	0.05	**98.81**	**3.98**	**82.2**	77.66
63	MR13_opx69	Pyroxenite Reef	55.81	0.12	1.37	0.46	0.00	11.72	0.32	0.00	28.97	0.87	0.01	**99.66**	**3.98**	**81.5**	79.68
64	MR13_opx70	Pyroxenite Reef	55.91	0.13	1.24	0.50	0.00	11.79	0.39	0.00	28.87	1.17	0.03	**100.02**	**3.98**	**81.4**	78.99
65	MR13_opx72	Pyroxenite Reef	55.11	0.15	1.57	0.51	0.00	11.33	0.27	0.00	27.92	2.96	0.06	**99.88**	**3.99**	**81.4**	76.36
66	MR13_opx73	Pyroxenite Reef	55.47	0.11	1.40	0.49	0.00	11.71	0.20	0.00	29.17	0.90	0.02	**99.47**	**3.99**	**81.6**	79.92

Appendix 3: Orthopyroxene Compositions. Oxide data are presented in wt. %. Pyroxenes were normalised to 6 oxygens.

Point	Sample	Unit	SiO_2	TiO_2	Al_2O_3	Cr_2O_3	Fe_2O_3	FeO	MnO	NiO	MgO	CaO	Na_2O	Total	Total Cations	Mg#	En
67	MR13_opx74	Pyroxenite Reef	55.60	0.10	1.40	0.54	0.00	11.59	0.38	0.00	28.65	1.86	0.02	**100.14**	**3.99**	**81.5**	78.05
68	MR16_opx76	Pyroxenite Reef	55.18	0.29	1.10	0.40	0.00	12.84	0.30	0.00	27.76	1.44	0.05	**99.36**	**3.98**	**79.4**	76.74
69	MR16_opx77	Pyroxenite Reef	55.40	0.22	1.06	0.38	0.00	12.52	0.34	0.00	28.51	0.99	0.01	**99.43**	**3.99**	**80.2**	78.23
70	MR16_opx78	Pyroxenite Reef	55.35	0.12	1.12	0.40	0.00	12.78	0.20	0.00	28.46	0.86	0.00	**99.28**	**3.99**	**79.9**	78.28
71	MR16_opx79	Pyroxenite Reef	55.30	0.11	1.21	0.45	0.00	12.94	0.34	0.00	28.26	1.05	0.02	**99.67**	**3.99**	**79.6**	77.49
72	MR16_opx80	Pyroxenite Reef	55.66	0.18	1.14	0.47	0.00	11.32	0.42	0.00	28.15	3.42	0.01	**100.78**	**4.00**	**81.6**	75.67
73	MR16_opx81	Pyroxenite Reef	55.62	0.17	1.20	0.43	0.00	12.62	0.31	0.00	28.76	0.96	0.00	**100.06**	**3.99**	**80.2**	78.36
74	MR16_opx82	Pyroxenite Reef	55.63	0.13	1.29	0.50	0.00	11.51	0.34	0.00	27.93	2.71	0.05	**100.07**	**3.99**	**81.2**	76.46
75	MR16_opx83	Pyroxenite Reef	55.42	0.18	1.15	0.49	0.00	12.51	0.34	0.00	28.50	1.40	0.00	**99.98**	**3.99**	**80.2**	77.61
76	MR16_opx84	Pyroxenite Reef	51.73	0.31	1.28	0.48	0.00	11.70	0.27	0.00	11.98	21.58	0.17	**99.50**	**3.99**	**80.6**	75.51
77	MR16_opx85	Pyroxenite Reef	49.07	0.27	1.50	0.07	0.00	13.35	0.31	0.00	11.19	20.99	0.14	**96.89**	**3.99**	**80.1**	78.25
78	MR16_opx86	Pyroxenite Reef	55.99	0.13	1.19	0.47	0.00	12.84	0.28	0.00	28.87	1.02	0.02	**100.80**	**3.99**	**80.0**	78.10
79	MR16_opx87	Pyroxenite Reef	55.62	0.19	1.11	0.49	0.00	12.23	0.30	0.00	28.08	2.24	0.02	**100.28**	**3.99**	**80.4**	76.46
80	MR16_opx88	Pyroxenite Reef	55.68	0.13	1.25	0.54	0.00	12.15	0.25	0.00	27.78	1.58	0.03	**99.38**	**3.97**	**80.3**	77.44
81	MR16_opx89	Pyroxenite Reef	55.94	0.14	1.15	0.56	0.00	12.56	0.28	0.00	29.07	0.94	0.00	**100.65**	**3.99**	**80.5**	78.66
82	MR16_opx90	Pyroxenite Reef	55.82	0.17	1.25	0.56	0.00	12.34	0.30	0.00	29.18	0.65	0.00	**100.27**	**3.99**	**80.8**	79.41
83	MR16_opx91	Pyroxenite Reef	55.67	0.16	1.20	0.55	0.00	12.27	0.35	0.00	28.54	1.11	0.04	**99.88**	**3.98**	**80.6**	78.36
84	MR16_cpx_incl37	Pyroxenite Reef	54.01	0.28	1.85	0.99	0.00	4.55	0.18	0.00	16.01	23.29	0.36	**101.51**	**4.00**	**86.2**	45.21
85	MR16_opx92	Pyroxenite Reef	55.39	0.27	1.14	0.46	0.00	12.37	0.24	0.00	28.57	1.15	0.02	**99.59**	**3.99**	**80.4**	78.34
86	MR16_opx94	Pyroxenite Reef	56.60	0.26	1.08	0.46	0.00	12.31	0.30	0.00	28.22	1.13	0.01	**100.37**	**3.97**	**80.3**	78.15
87	MR16_opx95	Pyroxenite Reef	55.26	0.22	1.23	0.51	0.00	12.59	0.24	0.00	28.74	0.98	0.00	**99.77**	**3.99**	**80.3**	78.43
88	MR16_opx96	Pyroxenite Reef	55.06	0.18	1.18	0.50	0.00	11.73	0.41	0.00	28.53	0.91	0.01	**98.52**	**3.98**	**81.3**	79.26
89	MR16_opx97	Pyroxenite Reef	54.80	0.22	1.33	0.49	0.00	9.64	0.32	0.00	25.28	6.29	0.13	**98.50**	**3.98**	**82.4**	71.43
90	MR16_opx98	Pyroxenite Reef	55.49	0.21	1.12	0.50	0.00	12.67	0.37	0.00	28.74	0.62	0.00	**99.73**	**3.99**	**80.2**	78.73
91	MR19_opx100	Pyroxenite Reef	55.78	0.14	0.94	0.38	0.00	13.85	0.44	0.00	28.29	0.80	0.01	**100.62**	**3.99**	**78.4**	76.70
92	MR19_opx101	Pyroxenite Reef	55.28	0.15	1.14	0.42	0.00	14.01	0.31	0.00	28.24	0.77	0.00	**100.33**	**3.99**	**78.2**	76.67
93	MR19_opx102	Pyroxenite Reef	55.48	0.16	1.08	0.47	0.00	13.29	0.39	0.00	27.91	0.91	0.02	**99.71**	**3.98**	**78.9**	77.01
94	MR19_opx103	Pyroxenite Reef	55.46	0.15	1.08	0.48	0.00	14.04	0.36	0.00	28.03	1.11	0.02	**100.71**	**3.99**	**78.1**	75.95
95	MR19_opx104	Pyroxenite Reef	55.21	0.16	1.25	0.48	0.00	13.27	0.26	0.00	28.16	1.21	0.01	**99.99**	**3.99**	**79.1**	76.90
96	MR19_opx105	Pyroxenite Reef	55.38	0.19	1.24	0.50	0.00	12.14	0.22	0.00	26.89	4.00	0.05	**100.60**	**3.99**	**79.8**	73.27
97	MR19_opx106	Pyroxenite Reef	55.46	0.23	1.08	0.37	0.00	13.51	0.33	0.00	28.39	0.95	0.00	**100.31**	**3.99**	**78.9**	77.07
98	MR19_opx107	Pyroxenite Reef	55.16	0.23	1.01	0.44	0.00	12.30	0.39	0.00	28.17	1.00	0.00	**98.70**	**3.98**	**80.3**	78.23
99	MR19_opx108	Pyroxenite Reef	55.48	0.21	1.11	0.42	0.00	12.93	0.41	0.00	28.39	1.34	0.00	**100.29**	**3.99**	**79.6**	77.06
100	MR19_opx109	Pyroxenite Reef	55.40	0.16	1.25	0.49	0.00	13.15	0.31	0.00	27.95	1.66	0.03	**100.40**	**3.99**	**79.1**	76.17

Appendix 3: Orthopyroxene Compositions. Oxide data are presented in wt. %. Pyroxenes were normalised to 6 oxygens.

Point	Sample	Unit	SiO_2	TiO_2	Al_2O_3	Cr_2O_3	Fe_2O_3	FeO	MnO	NiO	MgO	CaO	Na_2O	Total	Total Cations	Mg#	En
101	MR19_opx110	Pyroxenite Reef	55.53	0.13	1.15	0.44	0.00	13.37	0.20	0.00	27.02	2.10	0.01	**99.94**	**3.98**	**78.3**	74.76
102	MR19_opx111	Pyroxenite Reef	55.52	0.11	1.07	0.46	0.00	13.21	0.22	0.00	26.75	3.48	0.06	**100.88**	**3.99**	**78.3**	72.72
103	MR19_opx112	Pyroxenite Reef	55.33	0.15	1.15	0.55	0.00	10.96	0.19	0.00	23.13	8.58	0.22	**100.26**	**3.98**	**79.0**	65.06
104	MR19_opx113	Pyroxenite Reef	55.38	0.14	1.05	0.48	0.00	13.58	0.28	0.00	27.35	1.98	0.05	**100.29**	**3.99**	**78.2**	74.83
105	MR19_cpx_incl43	Pyroxenite Reef	54.02	0.14	1.38	0.64	0.53	4.66	0.15	0.00	15.61	23.98	0.30	**101.39**	**4.00**	**84.4**	43.58
106	MR19_opx114	Pyroxenite Reef	51.73	0.31	1.28	0.31	0.00	11.70	0.27	0.00	11.98	21.58	0.17	**99.33**	**3.99**	**77.6**	75.99
107	MR19_opx117	Pyroxenite Reef	49.07	0.27	1.50	0.07	0.00	13.35	0.31	0.00	11.19	20.99	0.14	**96.89**	**3.98**	**78.9**	74.96
108	MR19_opx118	Pyroxenite Reef	55.89	0.19	0.70	0.29	0.00	14.29	0.38	0.00	28.43	0.55	0.01	**100.71**	**3.99**	**78.0**	76.71
109	MR19_opx119	Pyroxenite Reef	56.18	0.13	0.68	0.23	0.00	13.90	0.30	0.00	28.30	0.54	0.02	**100.29**	**3.98**	**78.4**	77.20
110	MR19_opx81	Pyroxenite Reef	55.03	0.22	1.30	0.33	0.00	13.99	0.38	0.00	24.87	4.36	0.07	**100.55**	**3.99**	**76.0**	68.95
111	MR21_opx86	Pyroxenite Reef	55.60	0.28	0.75	0.28	0.00	12.86	0.00	0.00	27.14	2.17	0.02	**99.11**	**3.97**	**79.0**	75.56
112	MR21_opx87	Pyroxenite Reef	55.61	0.24	0.73	0.25	0.00	13.43	0.34	0.00	27.14	2.26	0.05	**100.05**	**3.99**	**78.3**	74.37
113	MR21_opx88	Pyroxenite Reef	55.71	0.29	0.99	0.31	0.00	13.40	0.35	0.00	26.95	2.36	0.05	**100.39**	**3.98**	**78.2**	74.12
114	MR21_opx89	Pyroxenite Reef	55.37	0.27	0.89	0.36	0.00	12.87	0.03	0.00	27.11	2.64	0.03	**99.57**	**3.98**	**79.0**	74.80
115	MR21_opx90	Pyroxenite Reef	55.24	0.25	0.95	0.39	0.00	13.80	0.36	0.00	27.69	1.16	0.01	**99.84**	**3.99**	**78.2**	75.93
116	MR21_opx91	Pyroxenite Reef	55.17	0.28	1.00	0.44	0.00	13.59	0.40	0.00	26.97	3.10	0.03	**100.96**	**4.00**	**78.0**	72.80
117	MR21_opx114	Pyroxenite Reef	55.51	0.26	0.84	0.32	0.00	14.60	0.25	0.00	27.80	0.84	0.00	**100.41**	**3.99**	**77.2**	75.67
118	MR21_opx115	Pyroxenite Reef	56.51	0.02	0.37	0.07	0.00	14.99	0.36	0.00	28.35	0.59	0.02	**101.27**	**3.99**	**77.1**	75.82
119	MR22_opx/ol?116	Pyroxenite Reef	56.29	0.14	1.06	0.37	0.00	13.42	0.40	0.00	28.08	1.04	0.01	**100.81**	**3.98**	**78.9**	76.74
120	MR22_opx/ol?117	Pyroxenite Reef	56.10	0.20	0.97	0.35	0.00	13.54	0.35	0.00	27.51	2.20	0.03	**101.26**	**3.99**	**78.4**	74.57
121	MR22_opx/ol?118	Pyroxenite Reef	56.55	0.12	1.11	0.38	0.00	13.14	0.46	0.00	28.08	1.25	0.00	**101.08**	**3.98**	**79.2**	76.70
122	MR22_opx/ol?119	Pyroxenite Reef	55.94	0.18	1.03	0.41	0.00	12.91	0.29	0.00	27.58	2.41	0.04	**100.79**	**3.99**	**79.2**	75.12
123	MR22_opx/ol?120	Pyroxenite Reef	56.47	0.20	1.04	0.41	0.00	13.23	0.38	0.00	27.46	2.02	0.02	**101.22**	**3.98**	**78.7**	75.13
124	MR22_opx/ol?121	Pyroxenite Reef	56.51	0.20	1.01	0.35	0.00	13.49	0.32	0.00	27.91	0.97	0.01	**100.75**	**3.97**	**78.7**	76.76
125	MR22_opx122	Pyroxenite Reef	56.55	0.14	1.21	0.48	0.00	13.71	0.30	0.00	27.99	0.92	0.00	**101.29**	**3.97**	**78.4**	76.67
126	MR22_opx123	Pyroxenite Reef	56.30	0.16	1.19	0.50	0.00	12.92	0.29	0.00	27.51	2.09	0.03	**100.99**	**3.98**	**79.1**	75.53
127	MR22_opx124	Pyroxenite Reef	56.19	0.18	1.26	0.54	0.00	12.29	0.17	0.00	27.83	2.00	0.02	**100.48**	**3.97**	**80.1**	76.75
128	MR22_opx125	Pyroxenite Reef	56.39	0.17	1.16	0.54	0.00	12.96	0.32	0.00	27.40	1.41	0.05	**100.39**	**3.97**	**79.0**	76.40
129	MR22_opx126	Pyroxenite Reef	56.40	0.18	1.14	0.46	0.00	13.11	0.36	0.00	28.22	0.99	0.00	**100.85**	**3.97**	**79.3**	77.34
130	MR22_opx130	Pyroxenite Reef	55.67	0.25	1.07	0.42	0.00	13.41	0.35	0.00	26.59	3.07	0.04	**100.87**	**3.99**	**78.0**	72.81
131	MR22_opx131	Pyroxenite Reef	56.19	0.22	1.03	0.43	0.00	13.32	0.36	0.00	27.41	2.31	0.02	**101.28**	**3.98**	**78.6**	74.59
132	MR22_opx132	Pyroxenite Reef	56.02	0.22	1.01	0.36	0.00	13.67	0.37	0.00	27.89	0.96	0.00	**100.50**	**3.98**	**78.4**	76.50
133	MR22_opx133	Pyroxenite Reef	55.83	0.24	1.16	0.41	0.00	12.50	0.35	0.00	26.84	3.15	0.07	**100.54**	**3.98**	**79.3**	73.91
134	MR22_opx135	Pyroxenite Reef	51.73	0.31	1.28	0.45	0.00	11.70	0.27	0.00	11.98	21.58	0.17	**99.47**	**3.98**	**78.5**	74.84

Appendix 3: Orthopyroxene Compositions. Oxide data are presented in wt. %. Pyroxenes were normalised to 6 oxygens.

Point	Sample	Unit	SiO_2	TiO_2	Al_2O_3	Cr_2O_3	Fe_2O_3	FeO	MnO	NiO	MgO	CaO	Na_2O	Total	Total Cations	Mg#	En
135	MR23_opx136	Chromitite	49.07	0.27	1.50	0.07	0.00	13.35	0.31	0.00	11.19	20.99	0.14	**96.89**	**3.98**	**78.7**	76.71
136	MR23_opx137	Chromitite	55.93	0.19	1.20	0.54	0.00	12.06	0.38	0.00	27.17	3.00	0.02	**100.49**	**3.98**	**80.1**	74.83
137	MR23_opx138	Chromitite	56.35	0.18	1.11	0.47	0.00	13.74	0.27	0.00	27.94	1.29	0.01	**101.36**	**3.98**	**78.4**	76.07
138	MR23_opx139	Chromitite	55.58	0.13	1.23	0.52	0.00	12.96	0.36	0.00	27.91	0.95	0.01	**99.66**	**3.98**	**79.3**	77.38
139	MR23_opx140	Chromitite	55.74	0.19	1.39	0.59	0.00	12.49	0.31	0.00	26.56	3.58	0.06	**100.91**	**3.98**	**79.1**	73.13
140	MR23_opx141	Chromitite	55.42	0.18	1.26	0.57	0.00	13.16	0.35	0.00	27.69	1.81	0.02	**100.44**	**3.99**	**78.9**	75.72
141	MR23_opx142	Chromitite	56.22	0.16	1.13	0.53	0.00	14.16	0.26	0.00	28.20	0.72	0.02	**101.39**	**3.98**	**78.0**	76.62

Appendix 4: Base Metal Sulphide Compositions. Data are presented in wt. %.

Point	Sample	Unit	S	Ni	Cu	Zn	Fe	Pb	Total	Mineral
1	MR02_BMS2	Anorthosite HW	54.65	0.02	0.00	0.00	42.85	0.19	**97.71**	Pyrite
2	MR04_BMS7	Anorthosite HW	54.21	0.14	0.00	0.00	43.39	0.20	**97.94**	Pyrite
3	MR04_BMS8	Anorthosite HW	54.36	0.33	0.10	0.00	43.03	0.16	**97.98**	Pyrite
4	MR04_BMS14	Anorthosite HW	54.48	0.00	0.00	0.00	43.90	0.14	**98.52**	Pyrite
5	MR04_BMS15	Anorthosite HW	54.59	0.00	0.10	0.00	44.22	0.15	**99.05**	Pyrite
6	MR04_BMS16	Anorthosite HW	54.11	0.01	0.00	0.00	44.15	0.24	**98.52**	Pyrite
7	MR04_BMS17	Anorthosite HW	54.40	0.02	0.06	0.02	44.29	0.23	**99.04**	Pyrite
8	MR06_BMS18	Leuconorite HW	54.47	0.46	0.00	0.00	43.22	0.12	**98.26**	Pyrite
9	MR06_BMS19	Leuconorite HW	54.48	0.04	0.00	0.00	44.75	0.10	**99.37**	Pyrite
10	MR06_BMS20	Leuconorite HW	33.38	41.39	0.00	0.03	22.81	0.16	**97.77**	Pentlandite
11	MR06_BMS21	Leuconorite HW	40.16	0.78	0.12	0.03	57.49	0.08	**98.66**	Pyrrhotite
12	MR06_BMS22	Leuconorite HW	33.30	37.64	0.00	0.00	27.70	0.12	**98.76**	Pentlandite
13	MR06_BMS23	Leuconorite HW	55.35	0.86	0.00	0.00	42.79	0.26	**99.27**	Pyrite
14	MR06_BMS24	Leuconorite HW	54.86	0.15	0.00	0.08	44.34	0.24	**99.67**	Pyrite
15	MR06_BMS28	Leuconorite HW	35.65	0.00	33.76	0.00	28.63	0.17	**98.21**	Chalcopyrite
16	MR06_BMS39	Leuconorite HW	33.73	35.18	0.00	0.00	29.04	0.12	**98.07**	Pentlandite
17	MR06_BMS40	Leuconorite HW	40.44	0.78	0.07	0.00	57.87	0.24	**99.39**	Pyrrhotite
18	MR07_BMS43	Norite HW	54.67	0.10	0.01	0.00	47.54	0.24	**102.55**	Pyrite
19	MR07_BMS44	Norite HW	54.48	0.09	0.00	0.00	46.68	0.04	**101.28**	Pyrite
20	MR07_BMS45	Norite HW	54.65	0.25	0.00	0.04	46.47	0.32	**101.74**	Pyrite
21	MR07_BMS47	Norite HW	34.01	36.80	0.00	0.00	28.09	0.03	**98.92**	Pentlandite
22	MR07_BMS48	Norite HW	54.60	0.79	0.05	0.06	45.22	0.15	**100.87**	Pyrite
23	MR07_BMS49	Norite HW	54.33	0.78	0.00	0.02	44.99	0.17	**100.28**	Pyrite
24	MR11_BMS75	Pyroxenite Reef	54.56	0.15	0.00	0.02	43.25	0.25	**98.24**	Pyrite
25	MR11_BMS76	Pyroxenite Reef	54.93	0.00	0.14	0.00	42.73	0.14	**97.95**	Pyrite
26	MR11_BMS79	Pyroxenite Reef	34.34	35.42	0.00	0.03	27.96	0.10	**97.83**	Pentlandite
27	MR11_BMS80	Pyroxenite Reef	33.97	35.80	0.00	0.00	28.65	0.23	**98.64**	Pentlandite
28	MR11_BMS83	Pyroxenite Reef	40.04	0.39	0.10	0.07	57.34	0.28	**98.21**	Pyrrhotite
29	MR11_BMS84	Pyroxenite Reef	40.35	0.25	0.22	0.06	57.34	0.05	**98.25**	Pyrrhotite
30	MR11_BMS85	Pyroxenite Reef	40.34	0.37	0.08	0.07	58.22	0.18	**99.25**	Pyrrhotite
31	MR10_BMS98	Pyroxenite Reef	54.63	0.06	0.10	0.03	43.08	0.17	**98.06**	Pyrite
32	MR10_BMS105	Pyroxenite Reef	34.23	35.65	0.21	0.00	27.80	0.17	**98.06**	Pentlandite
33	MR10_BMS106	Pyroxenite Reef	34.27	35.76	0.00	0.00	28.97	0.16	**99.16**	Pentlandite
34	MR13_BMS121	Pyroxenite Reef	34.13	35.73	0.00	0.00	31.72	0.09	**101.67**	Pentlandite

Appendix 4: Base Metal Sulphide Compositions. Data are presented in wt. %.

Point	Sample	Unit	S	Ni	Cu	Zn	Fe	Pb	Total	Mineral
35	MR13_BMS122	Pyroxenite Reef	33.67	35.88	0.00	0.00	31.74	0.14	**101.43**	Pentlandite
36	MR13_BMS123	Pyroxenite Reef	33.31	35.48	0.00	0.00	31.74	0.00	**100.52**	Pentlandite
37	MR13_BMS124	Pyroxenite Reef	33.98	35.10	0.00	0.00	32.02	0.24	**101.33**	Pentlandite
38	MR13_BMS125	Pyroxenite Reef	33.13	35.74	0.00	0.00	30.30	0.20	**99.37**	Pentlandite
39	MR13_BMS126	Pyroxenite Reef	34.27	36.16	0.00	0.08	31.77	0.14	**102.42**	Pentlandite
40	MR13_BMS127	Pyroxenite Reef	40.45	0.50	0.00	0.02	61.38	0.23	**102.58**	Pyrrhotite
41	MR13_BMS128	Pyroxenite Reef	40.05	0.39	0.00	0.02	60.33	0.05	**100.84**	Pyrrhotite
42	MR13_BMS129	Pyroxenite Reef	35.40	0.00	32.47	0.04	31.38	0.04	**99.33**	Chalcopyrite
43	MR13_BMS130	Pyroxenite Reef	35.27	0.00	33.69	0.39	30.79	0.08	**100.22**	Chalcopyrite
44	MR13_BMS131	Pyroxenite Reef	35.51	0.03	34.43	0.25	30.48	0.17	**100.87**	Chalcopyrite
45	MR19_BMS133	Pyroxenite Reef	55.22	0.01	0.11	0.09	43.16	0.08	**98.66**	Pyrite
46	MR19_BMS134	Pyroxenite Reef	54.86	0.13	0.00	0.00	46.16	0.16	**101.31**	Pyrite
47	MR19_BMS135	Pyroxenite Reef	35.64	0.05	34.01	0.00	30.78	0.05	**100.53**	Chalcopyrite
48	MR19_BMS136	Pyroxenite Reef	35.30	0.11	33.86	0.11	30.35	0.16	**99.89**	Chalcopyrite
49	MR19_BMS137	Pyroxenite Reef	35.33	0.00	33.20	0.02	31.19	0.10	**99.83**	Chalcopyrite
50	MR19_BMS138	Pyroxenite Reef	35.76	0.01	33.40	0.04	30.61	0.11	**99.94**	Chalcopyrite
51	MR19_BMS139	Pyroxenite Reef	35.21	0.00	33.25	0.09	30.00	0.13	**98.68**	Chalcopyrite
52	MR19_BMS143	Pyroxenite Reef	35.37	0.00	33.31	0.17	32.06	0.08	**100.99**	Chalcopyrite
53	MR19_BMS144	Pyroxenite Reef	35.83	0.01	32.32	0.00	31.64	0.17	**99.96**	Chalcopyrite
54	MR21_BMS147	Pyroxenite Reef	33.89	41.56	0.00	0.00	26.80	0.10	**102.34**	Pentlandite
55	MR21_BMS148	Pyroxenite Reef	33.65	39.89	0.00	0.04	26.09	0.33	**100.01**	Pentlandite
56	MR21_BMS150	Pyroxenite Reef	34.09	40.09	0.02	0.00	25.22	0.07	**99.49**	Pentlandite
57	MR21_BMS151	Pyroxenite Reef	34.11	39.60	0.00	0.02	24.65	0.09	**98.46**	Pentlandite

Appendix 5: Oxide Compositions. Oxide data are presented in wt. %. Rutiles were normalised to 2 oxygens, ilmenites to 3 oxygens and chromites to 4 oxygens.

Point	Unit	Comment	SiO_2	TiO_2	Al_2O_3	FeO	MnO	MgO	CaO	ZnO	Cr_2O_3	V_2O_3	Total	Total Cations	Mineral
1	Anorthosite HW	MR02_Rut/Ilm5	0.03	94.94	0.08	2.01	0.15	0.00	0.58	0.02	0.08	1.45	**99.34**	**1.01**	Rutile
2	Anorthosite HW	MR02_Rut/Ilm6	2.84	89.78	0.47	1.39	0.05	0.01	2.97	0.03	0.11	1.17	**98.80**	**1.03**	Rutile
3	Anorthosite HW	MR02_ox2	0.03	44.57	0.05	49.31	2.87	0.02	0.03	0.13	0.06	0.53	**97.60**	**2.09**	Ilmenite
4	Anorthosite HW	MR02_Rut/Ilm3	0.07	50.81	0.04	40.89	4.81	0.03	0.19	0.00	0.04	0.61	**97.48**	**2.00**	Ilmenite
5	Anorthosite HW	MR02_Rut/Ilm4	0.02	52.25	0.05	41.18	5.23	0.00	0.28	0.03	0.01	0.41	**99.46**	**1.99**	Ilmenite
6	Anorthosite HW	MR04_ox3	0.02	46.81	0.06	44.08	5.04	0.06	0.07	0.00	0.96	0.88	**97.98**	**2.04**	Ilmenite
7	Anorthosite HW	MR04_ox4	0.04	47.08	0.04	43.57	5.00	0.04	0.07	0.00	0.70	0.60	**97.14**	**2.04**	Ilmenite
8	Anorthosite HW	MR04_ox5	0.04	47.43	0.02	44.55	5.29	0.04	0.04	0.03	0.68	0.63	**98.76**	**2.05**	Ilmenite
9	Norite HW	MR07_ox14	0.04	52.04	0.04	40.05	6.20	0.05	0.06	0.00	0.15	0.29	**98.91**	**1.99**	Ilmenite
10	Norite HW	MR07_ox15	0.01	46.67	0.06	44.46	5.82	0.05	0.04	0.02	0.42	0.49	**98.03**	**2.06**	Ilmenite
11	Anorthosite Reef	MR09_ox38	0.02	47.18	0.03	47.60	1.16	1.02	0.00	0.06	0.67	0.43	**98.18**	**2.05**	Ilmenite
12	Anorthosite Reef	MR09_ox39	0.02	47.25	0.04	45.38	1.06	1.15	0.00	0.06	0.63	0.37	**95.97**	**2.04**	Ilmenite
13	Anorthosite Reef	MR09_ox40	0.04	46.72	0.06	46.26	1.28	1.05	0.01	0.00	0.76	0.56	**96.73**	**2.05**	Ilmenite
14	Anorthosite Reef	MR09_ox41	0.03	47.34	0.04	44.27	3.62	0.47	0.01	0.09	0.70	0.53	**97.11**	**2.04**	Ilmenite
15	Pyroxenite Reef	MR10_ox16	0.03	1.82	9.71	37.57	0.42	5.45	0.00	0.21	40.38	0.32	**95.90**	**3.14**	Chromite
16	Pyroxenite Reef	MR10_ox17	0.00	1.74	9.91	38.02	0.27	5.48	0.00	0.16	40.65	0.35	**96.58**	**3.14**	Chromite
17	Pyroxenite Reef	MR10_ox18	0.05	1.92	9.70	37.64	0.45	5.35	0.00	0.00	40.84	0.47	**96.43**	**3.13**	Chromite
18	Pyroxenite Reef	MR10_ox19	0.08	1.85	9.92	37.88	0.27	5.46	0.00	0.24	41.52	0.43	**97.65**	**3.13**	Chromite
19	Pyroxenite Reef	MR10_ox20	0.02	1.89	9.74	37.38	0.44	5.40	0.02	0.22	40.00	0.48	**95.58**	**3.13**	Chromite
20	Pyroxenite Reef	MR10_ox21	0.02	1.91	9.89	38.03	0.37	5.32	0.00	0.18	40.66	0.37	**96.74**	**3.13**	Chromite
21	Pyroxenite Reef	MR10_ox22	0.03	1.79	9.80	35.54	0.36	5.31	0.00	0.06	43.48	0.47	**96.83**	**3.10**	Chromite
22	Pyroxenite Reef	MR10_ox23	0.03	1.72	9.78	35.81	0.36	5.32	0.00	0.18	45.50	0.42	**99.12**	**3.10**	Chromite
23	Pyroxenite Reef	MR10_ox24	0.06	1.67	10.36	36.62	0.38	5.97	0.03	0.06	45.03	0.36	**100.53**	**3.11**	Chromite
24	Pyroxenite Reef	MR10_ox25	0.02	1.81	9.98	35.78	0.47	5.35	0.00	0.11	43.22	0.41	**97.13**	**3.11**	Chromite
25	Pyroxenite Reef	MR10_ox26	0.02	1.73	9.64	37.05	0.40	5.27	0.00	0.15	43.02	0.46	**97.73**	**3.12**	Chromite
26	Pyroxenite Reef	MR10_ox27	0.03	1.63	9.66	35.52	0.42	5.22	0.03	0.10	41.65	0.43	**94.68**	**3.11**	Chromite
27	Pyroxenite Reef	MR10_ox28	0.03	1.66	9.51	36.65	0.38	5.15	0.00	0.00	42.32	0.31	**96.00**	**3.12**	Chromite
28	Pyroxenite Reef	MR10_ox29	0.04	1.76	9.43	37.62	0.39	5.16	0.01	0.06	44.39	0.37	**99.22**	**3.11**	Chromite
29	Pyroxenite Reef	MR10_ox30	0.03	1.61	9.65	35.97	0.34	5.09	0.00	0.14	46.32	0.43	**99.59**	**3.09**	Chromite
30	Pyroxenite Reef	MR10_ox31	0.03	1.55	9.58	36.94	0.39	5.16	0.00	0.10	45.86	0.39	**100.01**	**3.11**	Chromite
31	Pyroxenite Reef	MR10_ox32	0.03	1.72	8.68	38.59	0.48	4.39	0.01	0.17	43.14	0.29	**97.50**	**3.13**	Chromite

Appendix 5: Oxide Compositions. Oxide data are presented in wt. %. Rutiles were normalised to 2 oxygens, ilmenites to 3 oxygens and chromites to 4 oxygens.

Point	Unit	Comment	SiO_2	TiO_2	Al_2O_3	FeO	MnO	MgO	CaO	ZnO	Cr_2O_3	V_2O_3	Total	Total Cations	Mineral
32	Pyroxenite Reef	MR10_ox33	0.01	1.71	8.63	38.80	0.37	4.47	0.04	0.06	41.14	0.41	**95.63**	**3.14**	Chromite
33	Pyroxenite Reef	MR10_ox34	0.04	1.63	8.60	37.41	0.42	4.52	0.01	0.00	40.43	0.35	**93.40**	**3.13**	Chromite
34	Pyroxenite Reef	MR10_ox35	0.02	1.86	9.03	36.23	0.37	5.05	0.00	0.15	41.62	0.35	**94.67**	**3.12**	Chromite
35	Pyroxenite Reef	MR10_ox36	0.03	1.76	9.07	37.94	0.49	5.04	0.00	0.15	41.52	0.41	**96.40**	**3.13**	Chromite
36	Pyroxenite Reef	MR10_ox37	0.04	1.86	9.21	36.41	0.56	5.12	0.00	0.00	40.56	0.34	**94.08**	**3.13**	Chromite
37	Pyroxenite Reef	MR13_ox43	0.00	0.70	5.76	50.31	0.68	0.64	0.00	0.43	37.17	0.50	**96.20**	**3.24**	Chromite
38	Pyroxenite Reef	MR13_ox44	0.02	0.85	5.15	49.37	0.74	0.59	0.00	0.39	37.76	0.67	**95.54**	**3.22**	Chromite
39	Pyroxenite Reef	MR13_ox45	0.04	0.98	5.06	50.56	0.82	0.55	0.01	0.37	40.08	0.57	**99.04**	**3.22**	Chromite
40	Pyroxenite Reef	MR13_ox46	0.01	0.92	5.19	49.59	0.95	0.52	0.02	0.33	41.91	0.46	**99.89**	**3.20**	Chromite
41	Pyroxenite Reef	MR13_ox47	0.03	0.89	5.45	50.52	0.79	0.58	0.02	0.30	40.80	0.55	**99.93**	**3.21**	Chromite
42	Pyroxenite Reef	MR13_ox48	0.01	0.72	5.89	49.08	0.94	0.46	0.02	0.44	39.93	0.50	**97.97**	**3.21**	Chromite
43	Pyroxenite Reef	MR13_ox49	0.03	0.79	6.05	49.71	1.01	0.53	0.03	0.59	39.84	0.47	**99.05**	**3.21**	Chromite
44	Pyroxenite Reef	MR13_ox50	0.01	0.64	3.59	53.25	1.11	0.39	0.11	0.36	38.98	0.56	**98.98**	**3.26**	Chromite
45	Pyroxenite Reef	MR13_ox51	0.00	0.76	3.77	51.69	1.28	0.40	0.03	0.31	40.82	0.75	**99.81**	**3.23**	Chromite
46	Pyroxenite Reef	MR13_ox52	0.04	0.57	3.30	54.09	1.56	0.21	1.99	1.84	35.25	0.60	**99.45**	**3.32**	Chromite
47	Pyroxenite Reef	MR13_ox53	0.05	0.60	3.18	55.69	1.62	0.23	0.21	0.62	37.70	0.57	**100.47**	**3.30**	Chromite
48	Pyroxenite Reef	MR13_ox54	0.05	0.79	5.05	51.41	0.67	0.88	0.01	0.36	41.51	0.44	**101.17**	**3.22**	Chromite
49	Pyroxenite Reef	MR13_ox55	0.02	0.68	5.59	49.32	0.71	0.79	0.02	0.60	41.87	0.45	**100.06**	**3.21**	Chromite
50	Pyroxenite Reef	MR13_ox56	0.04	1.33	6.61	45.40	0.59	1.14	0.01	0.59	43.85	0.70	**100.24**	**3.15**	Chromite
51	Pyroxenite Reef	MR13_ox57	0.00	1.41	6.94	45.60	0.67	1.37	0.01	0.54	45.20	0.62	**102.37**	**3.14**	Chromite
52	Pyroxenite Reef	MR16_ox58	0.01	2.27	7.35	42.39	0.48	3.77	0.01	0.09	44.36	0.64	**101.36**	**3.13**	Chromite
53	Pyroxenite Reef	MR16_ox59	0.01	2.28	7.42	42.96	0.51	3.87	0.00	0.11	44.17	0.48	**101.81**	**3.14**	Chromite
54	Pyroxenite Reef	MR16_ox60	0.02	2.05	7.33	42.97	0.44	3.92	0.00	0.12	45.32	0.47	**102.66**	**3.14**	Chromite
55	Pyroxenite Reef	MR16_ox61	0.01	2.10	7.44	42.15	0.35	3.93	0.00	0.03	44.69	0.59	**101.29**	**3.13**	Chromite
56	Pyroxenite Reef	MR16_ox62	0.00	1.98	7.61	42.35	0.35	3.90	0.00	0.19	44.18	0.58	**101.14**	**3.14**	Chromite
57	Pyroxenite Reef	MR19_ox63	0.05	0.22	6.78	48.42	0.59	1.45	0.01	0.27	41.25	0.71	**99.73**	**3.20**	Chromite
58	Pyroxenite Reef	MR19_ox64	0.07	0.18	6.75	47.76	0.57	1.42	0.00	0.28	42.13	0.77	**99.92**	**3.19**	Chromite
59	Pyroxenite Reef	MR19_ox65	1.34	0.93	4.26	48.26	0.71	1.61	0.10	0.26	39.02	1.00	**97.48**	**3.19**	Chromite
60	Pyroxenite Reef	MR19_ox66	4.05	0.90	4.33	47.96	0.67	2.64	0.10	0.42	35.78	1.00	**97.85**	**3.16**	Chromite
61	Pyroxenite Reef	MR19_ox67	0.02	1.46	4.40	49.71	0.44	1.65	0.00	0.16	40.78	0.97	**99.58**	**3.20**	Chromite
62	Pyroxenite Reef	MR19_ox68	0.00	1.45	4.38	49.85	0.54	1.62	0.01	0.33	39.95	0.67	**98.79**	**3.22**	Chromite
63	Pyroxenite Reef	MR19_ox69	0.02	1.42	4.56	49.43	0.51	1.57	0.01	0.18	38.48	0.73	**96.90**	**3.22**	Chromite
64	Pyroxenite Reef	MR19_ox70	0.03	0.52	4.73	48.85	0.54	1.45	0.01	0.28	41.71	0.68	**98.80**	**3.21**	Chromite
65	Pyroxenite Reef	MR19_ox71	0.01	0.50	4.62	50.51	0.66	1.41	0.01	0.00	41.73	0.57	**100.01**	**3.23**	Chromite

Appendix 5: Oxide Compositions. Oxide data are presented in wt. %. Rutiles were normalised to 2 oxygens, ilmenites to 3 oxygens and chromites to 4 oxygens.

Point	Unit	Comment	SiO_2	TiO_2	Al_2O_3	FeO	MnO	MgO	CaO	ZnO	Cr_2O_3	V_2O_3	Total	Total Cations	Mineral
66	Pyroxenite Reef	MR19_ox72	0.03	0.40	4.69	49.13	0.71	1.01	0.04	0.35	41.69	0.66	**98.70**	**3.21**	Chromite
67	Pyroxenite Reef	MR19_ox73	0.11	0.43	4.81	49.71	0.58	1.15	0.02	0.48	41.86	0.66	**99.80**	**3.21**	Chromite
68	Pyroxenite Reef	MR19_ox74	0.03	0.98	3.69	49.79	0.57	1.01	0.00	0.35	41.34	0.86	**98.63**	**3.21**	Chromite
69	Pyroxenite Reef	MR19_ox75	0.02	1.01	3.52	50.92	0.70	1.00	0.00	0.33	39.25	0.92	**97.67**	**3.23**	Chromite
70	Pyroxenite Reef	MR19_ox76	0.05	1.11	3.93	49.67	0.58	1.16	0.00	0.35	42.10	0.92	**99.88**	**3.20**	Chromite
71	Pyroxenite Reef	MR19_ox77	0.06	1.15	3.79	49.42	0.66	1.14	0.01	0.23	43.69	0.89	**101.04**	**3.19**	Chromite
72	Pyroxenite Reef	MR21_ox78	0.01	0.67	4.74	50.36	0.49	1.87	0.02	0.30	43.78	0.47	**102.71**	**3.22**	Chromite
73	Pyroxenite Reef	MR21_ox79	0.00	0.69	4.54	51.80	0.41	1.74	0.00	0.18	43.28	0.58	**103.21**	**3.22**	Chromite
74	Pyroxenite Reef	MR21_ox80	0.01	0.64	4.58	49.57	0.52	1.70	0.00	0.24	41.23	0.44	**98.92**	**3.23**	Chromite
75	Pyroxenite Reef	MR21_ox81	0.02	0.63	4.75	50.92	0.56	1.72	0.00	0.23	40.89	0.46	**100.19**	**3.24**	Chromite
76	Pyroxenite Reef	MR21_ox82	0.03	0.65	4.66	49.43	0.56	1.75	0.03	0.11	43.58	0.52	**101.31**	**3.21**	Chromite
77	Pyroxenite Reef	MR21_ox83	2.33	0.45	3.89	34.11	0.50	2.74	8.13	0.16	28.11	0.26	**80.68**	**3.26**	Chromite
78	Pyroxenite Reef	MR21_ox84	0.01	0.64	4.57	50.31	0.48	1.64	0.00	0.16	46.13	0.38	**104.32**	**3.20**	Chromite
79	Pyroxenite Reef	MR21_ox85	0.04	0.66	4.60	48.86	0.56	1.61	0.01	0.20	47.16	0.37	**104.06**	**3.19**	Chromite
80	Pyroxenite Reef	MR22_ox86	0.01	0.59	6.11	48.61	0.47	1.23	0.00	0.55	42.16	0.63	**100.36**	**3.19**	Chromite
81	Pyroxenite Reef	MR22_ox87	0.00	0.56	6.00	48.37	0.61	1.24	0.00	0.35	42.48	0.54	**100.15**	**3.20**	Chromite
82	Pyroxenite Reef	MR22_ox88	0.01	0.58	6.13	46.77	0.57	1.23	0.01	0.44	44.76	0.53	**101.03**	**3.17**	Chromite
83	Pyroxenite Reef	MR22_ox89	0.03	0.58	6.10	47.49	0.53	1.27	0.00	0.22	46.36	0.73	**103.30**	**3.16**	Chromite
84	Pyroxenite Reef	MR22_ox90	0.03	0.57	5.94	48.79	0.47	1.18	0.00	0.32	45.19	0.59	**103.08**	**3.18**	Chromite
85	Chromitite	MR23_chr1	0.04	1.30	11.69	37.06	0.49	5.93	0.00	0.03	45.56	0.39	**102.48**	**3.11**	Chromite
86	Chromitite	MR23_chr2	0.04	1.14	11.62	36.35	0.42	5.99	0.00	0.00	43.68	0.36	**99.61**	**3.11**	Chromite
87	Chromitite	MR23_chr3	0.04	1.01	11.59	36.04	0.52	6.17	0.00	0.05	46.41	0.34	**102.15**	**3.10**	Chromite
88	Chromitite	MR23_chr4	0.06	0.90	11.33	34.84	0.45	5.91	0.00	0.15	48.77	0.39	**102.79**	**3.09**	Chromite
89	Chromitite	MR23_chr5	0.02	1.31	10.57	35.47	0.52	5.82	0.00	0.01	48.97	0.38	**103.09**	**3.09**	Chromite
90	Chromitite	MR23_chr6	0.00	1.35	10.58	35.94	0.46	5.83	0.00	0.07	49.04	0.36	**103.63**	**3.09**	Chromite
91	Chromitite	MR23_chr7	0.02	1.34	10.74	36.17	0.54	5.89	0.00	0.08	50.54	0.40	**105.72**	**3.08**	Chromite
92	Chromitite	MR23_chr8	0.02	1.35	10.86	35.33	0.54	5.68	0.01	0.02	49.84	0.38	**104.04**	**3.08**	Chromite
93	Chromitite	MR23_chr9	0.01	1.19	11.06	35.83	0.57	5.68	0.02	0.05	49.57	0.59	**104.56**	**3.08**	Chromite
94	Chromitite	MR23_chr10	0.01	1.29	10.91	35.22	0.48	5.58	0.00	0.03	48.94	0.35	**102.79**	**3.08**	Chromite
95	Chromitite	MR23_chr11	0.02	1.24	11.78	30.10	0.37	5.75	0.00	0.04	48.27	0.43	**97.99**	**3.05**	Chromite
96	Chromitite	MR23_chr12	0.01	1.14	11.76	36.68	0.40	5.91	0.00	0.11	48.75	0.39	**105.15**	**3.09**	Chromite
97	Chromitite	MR23_chr13	0.04	2.18	10.99	35.31	0.61	5.54	0.00	0.06	50.47	0.43	**105.62**	**3.06**	Chromite
98	Chromitite	MR23_chr14	0.09	1.67	10.98	36.33	0.51	5.60	0.01	0.04	50.07	0.42	**105.73**	**3.08**	Chromite

Appendix 5: Oxide Compositions. Oxide data are presented in wt. %. Rutiles were normalised to 2 oxygens, ilmenites to 3 oxygens and chromites to 4 oxygens.

Point	Unit	Comment	SiO_2	TiO_2	Al_2O_3	FeO	MnO	MgO	CaO	ZnO	Cr_2O_3	V_2O_3	Total	Total Cations	Mineral
99	Chromitite	MR23_chr15	0.00	0.98	11.29	34.87	0.54	5.88	0.00	0.09	49.01	0.40	**103.05**	**3.08**	Chromite
100	Chromitite	MR23_chr16	0.04	0.97	11.65	35.62	0.49	5.73	0.00	0.31	48.70	0.35	**103.86**	**3.09**	Chromite
101	Chromitite	MR23_chr17	0.00	1.07	10.90	37.37	0.47	5.52	0.00	0.07	47.33	0.47	**103.19**	**3.10**	Chromite
102	Chromitite	MR23_chr18	0.03	1.06	10.92	36.14	0.51	5.53	0.00	0.19	47.15	0.35	**101.87**	**3.10**	Chromite
103	Chromitite	MR23_chr19	0.00	0.94	12.80	33.20	0.50	6.67	0.00	0.11	48.22	0.37	**102.80**	**3.08**	Chromite
104	Chromitite	MR23_chr20	0.00	1.06	12.79	35.21	0.49	6.82	0.01	0.06	50.01	0.32	**106.76**	**3.08**	Chromite
105	Chromitite	MR23_chr21	0.00	0.98	13.02	34.47	0.43	6.89	0.00	0.01	49.54	0.33	**105.67**	**3.08**	Chromite
106	Chromitite	MR23_chr22	0.02	0.95	13.12	34.66	0.54	6.86	0.00	0.10	46.88	0.38	**103.49**	**3.09**	Chromite
107	Chromitite	MR23_chr23	0.02	1.08	13.21	33.82	0.40	6.75	0.00	0.15	45.49	0.37	**101.29**	**3.09**	Chromite
108	Chromitite	MR23_chr24	0.02	1.00	13.35	33.57	0.47	6.88	0.00	0.12	45.85	0.36	**101.59**	**3.09**	Chromite
109	Chromitite	MR23_chr25	0.04	1.00	13.30	35.08	0.47	7.02	0.00	0.05	46.92	0.42	**104.32**	**3.09**	Chromite
110	Chromitite	MR23_chr26	0.02	0.99	13.19	31.98	0.38	6.75	0.00	0.11	46.89	0.49	**100.80**	**3.07**	Chromite
111	Chromitite	MR23_chr27	0.03	0.99	13.32	32.77	0.48	6.88	0.00	0.05	48.00	0.44	**102.95**	**3.07**	Chromite
112	Chromitite	MR23_chr28	0.01	1.14	13.42	33.96	0.47	7.02	0.00	0.10	47.18	0.38	**103.67**	**3.08**	Chromite
113	Chromitite	MR23_chr29	0.05	1.08	13.54	33.28	0.52	7.00	0.01	0.15	45.62	0.24	**101.48**	**3.09**	Chromite
114	Chromitite	MR23_chr30	0.00	1.17	12.92	33.72	0.43	6.81	0.01	0.20	45.31	0.32	**100.88**	**3.09**	Chromite
115	Chromitite	MR23_chr31	0.03	1.11	12.84	33.49	0.45	6.64	0.01	0.00	44.59	0.38	**99.53**	**3.09**	Chromite
116	Chromitite	MR23_chr32	0.05	1.12	12.77	34.58	0.45	6.74	0.00	0.01	45.25	0.34	**101.30**	**3.10**	Chromite
117	Chromitite	MR23_chr33	0.00	1.08	12.77	34.20	0.40	6.88	0.00	0.13	46.02	0.25	**101.72**	**3.10**	Chromite
118	Chromitite	MR23_chr34	0.00	1.14	12.74	33.29	0.45	6.81	0.02	0.16	48.39	0.41	**103.42**	**3.08**	Chromite
119	Chromitite	MR23_chr35	0.03	1.10	12.92	34.22	0.53	6.80	0.02	0.07	47.84	0.28	**103.79**	**3.09**	Chromite
120	Chromitite	MR23_chr36	0.01	1.07	12.66	32.89	0.44	6.66	0.00	0.16	44.99	0.37	**99.24**	**3.09**	Chromite
121	Chromitite	MR23_chr37	0.01	1.06	12.91	32.74	0.46	6.80	0.00	0.11	45.69	0.36	**100.13**	**3.08**	Chromite

Appendix 6: Biotite Compositions. Oxide data are presented in wt. %. Data was normalised to 11 oxygens.

Point	Unit	Sample	SiO_2	TiO_2	Al_2O_3	FeO	MnO	MgO	CaO	Na_2O	K_2O	F	Cl	Cr_2O_3	H_2O*	O=F,Cl	Total	Total Cations
1	Anorthosite HW	MR02_bt1	37.42	3.79	13.64	12.11	0.09	16.22	0.07	0.05	8.70	0.26	0.23	0.11	3.76	0.16	**96.29**	**7.78**
2	Anorthosite HW	MR02_bt3	36.81	3.09	13.86	12.53	0.05	16.21	0.09	0.11	8.65	0.30	0.25	0.23	3.70	0.18	**95.69**	**7.83**
3	Anorthosite HW	MR02_bt4	37.66	3.92	13.47	11.25	0.10	15.04	0.10	0.06	9.96	0.58	0.27	0.21	3.57	0.30	**95.87**	**7.82**
4	Pyroxenite Reef	MR08_bt7	39.71	4.39	13.29	7.10	0.01	18.57	0.02	0.11	9.30	0.34	0.33	1.37	3.87	0.22	**98.18**	**7.73**
5	Pyroxenite Reef	MR08_bt8	39.49	5.61	13.25	8.11	0.06	17.92	0.03	0.10	8.86	0.45	0.29	1.29	3.85	0.25	**99.03**	**7.69**
6	Pyroxenite Reef	MR08_bt9	39.74	4.38	13.15	7.57	0.07	18.82	0.01	0.08	8.46	0.34	0.31	1.22	3.87	0.21	**97.80**	**7.69**
7	Pyroxenite Reef	MR08_bt10	39.26	4.44	13.26	7.81	0.07	18.60	0.00	0.10	9.11	0.44	0.33	1.33	3.81	0.26	**98.29**	**7.75**
8	Pyroxenite Reef	MR11_bt15	39.44	3.72	13.79	7.77	0.03	19.01	0.01	0.13	8.63	0.17	0.32	1.52	3.96	0.14	**98.35**	**7.72**
9	Pyroxenite Reef	MR11_bt16	39.27	3.75	13.63	7.79	0.00	18.63	0.02	0.08	9.18	0.04	0.33	1.48	3.99	0.09	**98.09**	**7.74**
10	Pyroxenite Reef	MR11_bt17	38.89	3.99	13.64	7.44	0.06	18.56	0.00	0.08	9.15	0.00	0.34	1.38	3.99	0.08	**97.44**	**7.73**
11	Pyroxenite Reef	MR11_bt18	39.28	3.58	13.81	7.91	0.00	18.84	0.00	0.07	9.04	0.14	0.32	1.55	3.96	0.13	**98.37**	**7.75**
12	Pyroxenite Reef	MR10_bt19	38.45	5.20	13.04	9.43	0.05	16.90	0.00	0.09	9.33	0.54	0.32	0.34	3.68	0.30	**97.06**	**7.75**
13	Pyroxenite Reef	MR10_bt20	38.72	5.46	12.79	9.88	0.10	16.72	0.00	0.09	9.38	0.53	0.32	0.38	3.70	0.29	**97.77**	**7.75**
14	Pyroxenite Reef	MR10_bt21	38.04	3.09	13.05	11.50	0.15	17.03	0.04	0.08	8.91	0.15	0.49	0.54	3.77	0.17	**96.66**	**7.81**
15	Anorthosite Reef	MR09_bt22	38.27	5.66	12.82	10.81	0.14	15.68	0.05	0.12	9.42	0.28	0.34	0.46	3.78	0.20	**97.63**	**7.73**
16	Anorthosite Reef	MR09_bt23	38.52	5.73	12.70	10.99	0.04	16.00	0.00	0.09	10.24	0.36	0.33	0.48	3.79	0.23	**99.05**	**7.78**
17	Anorthosite Reef	MR09_bt24	38.31	5.34	12.81	11.21	0.06	15.91	0.01	0.08	10.02	0.52	0.30	0.50	3.70	0.29	**98.48**	**7.79**
18	Anorthosite Reef	MR09_bt25	38.27	5.14	12.89	10.98	0.09	15.96	0.02	0.07	9.51	0.44	0.33	0.60	3.71	0.26	**97.74**	**7.76**
19	Anorthosite Reef	MR09_bt26	37.70	4.80	13.08	10.88	0.11	16.13	0.04	0.06	9.24	0.36	0.32	0.54	3.72	0.22	**96.77**	**7.77**
20	Anorthosite Reef	MR09_bt27	38.04	4.85	13.01	10.60	0.18	16.05	0.01	0.06	9.14	0.25	0.36	0.48	3.76	0.19	**96.59**	**7.74**
21	Anorthosite Reef	MR09_bt28	38.34	5.16	13.23	9.80	0.01	17.11	0.02	0.10	10.28	0.44	0.31	0.50	3.77	0.26	**98.81**	**7.82**
22	Anorthosite Reef	MR09_bt29	38.46	5.42	13.08	9.45	0.06	16.95	0.00	0.08	10.07	0.20	0.31	0.46	3.87	0.15	**98.25**	**7.77**
23	Anorthosite Reef	MR09_bt30	37.94	5.26	12.98	9.43	0.08	16.76	0.05	0.10	9.03	0.43	0.27	0.54	3.71	0.24	**96.35**	**7.74**
24	Pyroxenite Reef	MR19_bt38	39.29	5.33	12.82	7.55	0.00	18.69	0.00	0.20	9.20	0.14	0.26	0.62	3.96	0.12	**97.94**	**7.72**
25	Pyroxenite Reef	MR19_bt39	39.67	5.27	12.82	8.63	0.06	18.86	0.03	0.16	9.65	0.17	0.26	0.64	4.01	0.13	**100.08**	**7.76**
26	Pyroxenite Reef	MR19_bt40	39.77	4.90	12.99	7.67	0.04	18.87	0.00	0.17	9.71	0.41	0.25	0.51	3.87	0.23	**98.92**	**7.77**
27	Pyroxenite Reef	MR19_bt41	38.95	5.18	12.54	8.38	0.06	18.36	0.01	0.24	10.36	0.26	0.26	0.58	3.90	0.17	**98.91**	**7.82**
28	Pyroxenite Reef	MR19_bt42	39.39	5.21	12.66	8.50	0.10	18.56	0.04	0.21	10.13	0.40	0.24	0.65	3.87	0.22	**99.72**	**7.81**
29	Pyroxenite Reef	MR19_bt43	39.67	2.57	13.39	8.71	0.08	19.98	0.06	0.20	9.97	0.51	0.37	0.68	3.79	0.30	**99.68**	**7.91**
30	Pyroxenite Reef	MR19_bt44	40.18	3.13	13.49	8.25	0.03	19.64	0.02	0.16	9.56	0.27	0.35	0.64	3.93	0.19	**99.45**	**7.81**
31	Pyroxenite Reef	MR19_bt45	40.17	3.14	13.29	8.06	0.07	19.80	0.03	0.34	8.96	0.51	0.24	1.38	3.85	0.27	**99.58**	**7.81**
32	Pyroxenite Reef	MR19_bt46	40.14	3.13	13.40	8.38	0.03	19.34	0.02	0.33	9.28	0.62	0.27	1.40	3.79	0.32	**99.81**	**7.82**
33	Pyroxenite Reef	MR19_bt47	39.98	3.23	13.31	8.53	0.09	19.24	0.03	0.35	9.23	0.46	0.25	1.48	3.87	0.25	**99.81**	**7.82**

Appendix 6: Biotite Compositions. Oxide data are presented in wt. %. Data was normalised to 11 oxygens.

Point	Unit	Sample	SiO_2	TiO_2	Al_2O_3	FeO	MnO	MgO	CaO	Na_2O	K_2O	F	Cl	Cr_2O_3	H_2O*	O=F,Cl	Total	Total Cations
34	Pyroxenite Reef	MR19_bt48	40.02	3.81	13.59	7.65	0.00	19.57	0.01	0.20	9.64	0.52	0.36	0.89	3.83	0.30	**99.79**	**7.81**
35	Pyroxenite Reef	MR19_bt49	39.98	3.76	13.60	7.97	0.04	19.78	0.03	0.21	9.62	0.36	0.34	0.92	3.92	0.23	**100.27**	**7.82**
36	Pyroxenite Reef	MR19_bt50	39.79	3.87	13.52	7.56	0.04	19.36	0.02	0.21	9.25	0.24	0.32	0.93	3.94	0.17	**98.88**	**7.77**
37	Pyroxenite Reef	MR19_bt51	40.00	3.82	13.40	7.89	0.03	19.58	0.00	0.19	9.89	0.52	0.31	0.98	3.84	0.29	**100.17**	**7.83**
38	Pyroxenite Reef	MR21_bt52	39.66	2.90	13.32	9.33	0.03	19.56	0.02	0.09	9.07	0.21	0.39	0.56	3.91	0.17	**98.88**	**7.81**
39	Pyroxenite Reef	MR21_bt53	39.67	2.98	13.08	9.13	0.08	19.58	0.03	0.09	9.47	0.09	0.42	0.53	3.96	0.13	**98.97**	**7.83**
40	Pyroxenite Reef	MR21_bt54	39.55	2.98	13.17	8.41	0.07	19.29	0.03	0.11	8.82	0.23	0.35	0.53	3.87	0.18	**97.23**	**7.78**
41	Pyroxenite Reef	MR21_bt55	39.86	2.58	13.43	8.62	0.16	20.08	0.04	0.11	8.86	0.33	0.40	0.88	3.87	0.23	**98.98**	**7.82**
42	Pyroxenite Reef	MR21_bt56	39.92	2.55	13.45	8.82	0.11	19.76	0.10	0.15	8.25	0.27	0.41	0.84	3.88	0.21	**98.31**	**7.78**
43	Pyroxenite Reef	MR21_bt57	44.19	1.82	10.03	9.78	0.05	20.23	0.08	0.14	6.34	0.07	0.28	0.63	4.04	0.09	**97.59**	**7.58**
44	Pyroxenite Reef	MR21_bt58	38.14	0.54	14.00	10.44	0.13	20.89	0.07	0.11	7.90	0.40	0.46	0.23	3.71	0.27	**96.75**	**7.93**
45	Pyroxenite Reef	MR21_bt59	39.64	2.69	13.24	8.49	0.04	19.72	0.03	0.14	9.63	0.26	0.40	0.93	3.88	0.20	**98.89**	**7.85**
46	Pyroxenite Reef	MR21_bt60	39.98	2.68	13.46	8.17	0.07	19.87	0.06	0.13	9.45	0.51	0.43	1.07	3.79	0.31	**99.36**	**7.85**
47	Pyroxenite Reef	MR21_bt61	39.92	2.65	13.30	9.05	0.04	20.01	0.04	0.11	8.66	0.32	0.33	0.76	3.89	0.21	**98.87**	**7.80**
48	Pyroxenite Reef	MR21_bt62	39.84	2.82	13.44	7.95	0.00	19.85	0.00	0.14	8.93	0.41	0.35	0.74	3.83	0.25	**98.03**	**7.80**
49	Pyroxenite Reef	MR21_bt63	39.80	2.68	13.54	8.72	0.08	19.56	0.04	0.12	9.25	0.49	0.42	1.27	3.79	0.30	**99.45**	**7.83**
50	Pyroxenite Reef	MR21_bt64	40.04	2.80	13.38	8.24	0.04	19.56	0.02	0.12	8.99	0.38	0.40	1.25	3.85	0.25	**98.81**	**7.79**

Appendix 7: Major Element Geochemistry. Data are presented in wt. %. *S is included here although it was calculated using a HH-XRF.

Sample	Lithology	Stratigraphic Depth (m)	Al_2O_3	BaO	CaO	Cr_2O_3	Fe_2O_3	K_2O	LOI	MgO	MnO	Na_2O	P_2O_5	*S	SiO_2	TiO_2	Total
MR-01	Anorthosite HW	55.07	29.20	0.01	14.30	0.02	2.19	0.23	0.62	1.56	0.06	2.37	0.00	0.97	49.07	0.10	**99.72**
MR-02	Anorthosite HW	55.31	28.64	0.01	13.82	0.02	2.87	0.20	0.29	2.21	0.06	2.32	0.00	0.04	49.57	0.11	**100.10**
MR-03	Anorthosite HW	56.09	31.73	0.01	14.97	<LOD	1.08	0.24	0.34	0.24	0.02	2.48	0.00	0.00	48.87	0.05	**100.04**
MR-04	Anorthosite HW	56.38	28.31	0.01	13.90	0.02	2.97	0.17	0.17	2.81	0.05	2.17	0.00	0.03	49.32	0.09	**99.99**
MR-05	Anorthosite HW	56.89	29.47	0.02	13.22	0.02	1.99	0.53	1.75	1.57	0.04	2.72	0.01	0.03	48.66	0.07	**100.05**
MR-06	Leuconorite HW	57.05	29.12	0.01	14.04	0.02	2.40	0.30	0.35	1.95	0.04	2.34	0.01	0.05	49.22	0.08	**99.88**
MR-07	Norite HW	57.27	19.58	0.01	10.95	0.13	7.77	0.17	0.20	9.07	0.13	1.62	0.01	0.37	50.11	0.14	**99.90**
MR-08	Pyroxenite Reef	57.80	12.91	0.01	6.99	0.25	9.95	0.09	-0.16	17.16	0.18	0.98	0.00	0.11	52.05	0.12	**100.54**
MR-09a	Anorthosite Reef	57.97	24.89	0.03	11.97	0.07	2.44	0.51	1.26	2.54	0.06	3.60	0.12	0.22	52.06	0.21	**99.76**
MR-09b	Anorthosite Reef	58.01	16.95	0.03	8.00	0.13	7.46	0.55	1.19	10.11	0.12	2.38	0.10	1.13	52.53	0.32	**99.87**
MR-10	Pyroxenite Reef	58.04	12.64	0.01	6.18	0.21	15.63	0.21	2.07	13.45	0.14	1.37	0.01	5.22	46.40	0.14	**98.47**
MR-11	Pyroxenite Reef	58.13	5.46	0.01	4.31	0.33	13.71	0.15	0.43	21.75	0.22	0.64	0.04	1.23	52.60	0.22	**99.87**
MR-12	Pyroxenite Reef	58.88	3.94	0.02	4.99	0.37	12.54	0.30	0.69	22.46	0.26	0.49	0.01	0.20	53.85	0.38	**100.29**
MR-13	Pyroxenite Reef	59.60	5.63	0.01	3.77	0.39	12.79	0.09	0.38	23.21	0.23	0.55	<LOD	0.55	52.75	0.20	**99.99**
MR-14	Pyroxenite Reef	60.43	2.17	0.01	3.36	0.44	13.01	0.56	1.24	23.98	0.23	0.16	0.01	0.15	54.91	0.42	**100.50**
MR-15	Pyroxenite Reef	62.48	4.82	0.01	5.20	0.41	12.32	0.20	-0.20	22.57	0.23	0.62	0.00	0.05	54.31	0.26	**100.76**
MR-16	Pyroxenite Reef	63.30	5.71	0.01	3.46	0.33	12.58	0.36	-0.10	22.17	0.23	0.75	0.01	0.05	54.77	0.24	**100.54**
MR-17	Pyroxenite Reef	63.95	4.65	0.01	6.19	0.41	12.12	0.15	-0.08	22.25	0.23	0.59	0.00	0.03	54.02	0.25	**100.78**
MR-18	Pyroxenite Reef	65.50	3.34	0.01	4.33	0.38	13.32	0.28	-0.08	23.32	0.24	0.43	0.00	0.05	54.33	0.37	**100.27**
MR-19	Pyroxenite Reef	66.63	4.08	0.01	4.11	0.36	13.10	0.30	-0.21	22.81	0.24	0.56	0.00	0.07	54.57	0.32	**100.24**
MR-20	Pyroxenite Reef	67.63	4.83	0.01	4.39	0.35	12.70	0.29	0.25	22.26	0.23	0.58	0.01	0.03	54.22	0.24	**100.36**
MR-21	Pyroxenite Reef	68.14	6.99	0.01	4.70	0.34	11.77	0.14	0.05	22.16	0.22	0.73	0.00	0.02	53.78	0.19	**101.07**
MR-22	Pyroxenite Reef	68.61	5.49	0.01	3.85	0.33	12.92	0.23	0.25	22.34	0.24	0.54	0.00	0.03	53.90	0.24	**100.33**
MR-23	Chromitite Reef	68.64	12.27	0.01	6.48	2.61	11.56	0.14	0.05	16.69	0.19	0.99	0.01	0.02	49.34	0.21	**100.55**
MR-24	Anorthosite FW	68.68	31.27	0.01	15.12	<LOD	1.21	0.25	0.38	0.42	0.02	2.47	0.00	<LOD	48.74	0.05	**99.95**
MR-25	Anorthosite FW	68.79	31.71	0.01	15.03	<LOD	1.07	0.33	0.41	0.23	0.02	2.50	0.00	<LOD	49.02	0.04	**100.37**
MR-26	Anorthosite FW	69.00	31.33	0.01	14.96	<LOD	1.07	0.40	0.51	0.36	0.02	2.45	0.01	<LOD	48.77	0.05	**99.95**
MR-27	Anorthosite FW	70.73	30.73	0.01	14.78	0.01	1.50	0.20	0.24	0.86	0.03	2.41	0.01	<LOD	49.36	0.07	**100.19**
MR-28	Anorthosite FW	71.17	29.3	0.01	14.36	0.01	2.26	0.19	0.13	1.85	0.04	2.33	0.01	<LOD	49.44	0.08	**100.01**

Appendix 8: Trace Element Geochemistry for ELF-395. Data are presented in ppm. Limits of detection are given for each element.

Element	**Ba**	**Be**	**Bi**	**Cd**	**Ce**	**Co**	**Cr**	**Cs**	**Cu**	**Dy**	**Er**	**Eu**	**Ga**	**Gd**	**Hf**
Units	ppm	ppm	ppm	ppm	ppm	ppm	ppm	ppm	ppm	ppm	ppm	ppm	ppm	ppm	ppm
Detection Limit	0.8	0.04	0.47	0.013	0.12	0.13	3	0.013	1.4	0.009	0.007	0.0031	0.04	0.009	0.14
Sample															
MR-01	74.7	0.29	<0.47	0.03	4.42	10.78	93	0.22	54.0	0.32	0.18	0.34	19.11	0.32	0.41
MR-02	75.1	0.36	<0.47	0.04	4.92	15.10	122	0.13	65.8	0.34	0.19	0.36	19.11	0.35	0.39
MR-03	79.8	0.32	<0.47	0.03	3.60	3.43	11	0.21	15.5	0.12	0.06	0.39	20.86	0.17	<0.14
MR-04	66.1	0.27	<0.47	0.04	3.02	17.14	178	0.09	68.9	0.21	0.14	0.31	18.59	0.21	0.19
MR-05	98.7	0.36	<0.47	0.05	3.49	11.79	103	1.29	108.7	0.13	0.07	0.33	19.29	0.17	0.25
MR-06	76.2	0.32	<0.47	0.03	3.45	14.43	116	0.19	136.3	0.20	0.12	0.31	19.23	0.23	0.24
MR-07	79.2	0.22	<0.47	0.09	4.93	59.38	888	0.13	556.3	0.71	0.47	0.35	13.85	0.62	0.31
MR-08	45.2	0.14	<0.47	0.09	2.41	74.37	1783	0.10	353.8	0.39	0.30	0.22	10.16	0.29	<0.14
MR-09A	216.1	0.77	<0.47	0.07	21.49	21.22	468	0.80	624.7	1.24	0.58	0.81	20.31	1.63	0.63
MR-09B	224.9	0.59	<0.47	0.26	15.62	108.60	951	0.55	2454.0	1.08	0.54	0.64	14.56	1.32	0.85
MR-10	90.6	0.28	0.94	0.29	4.53	>187	1501	0.20	2097.6	0.51	0.33	0.37	10.34	0.45	0.26
MR-11	59.7	0.22	0.57	0.17	10.21	141.33	2461	0.29	1529.8	1.30	0.86	0.26	6.58	1.17	0.58
MR-12	176.8	0.27	<0.47	0.21	9.49	99.59	2699	0.67	533.6	1.62	1.03	0.26	5.45	1.41	1.08
MR-13	52.0	0.18	<0.47	0.11	3.43	117.74	2866	0.26	753.2	0.65	0.50	0.18	6.15	0.51	0.27
MR-14	60.0	0.22	<0.47	0.10	13.81	93.25	3221	1.23	103.1	1.86	1.23	0.18	4.72	1.60	1.83
MR-15	58.8	0.32	<0.47	0.08	7.99	90.32	3050	0.24	50.3	1.48	0.96	0.30	6.50	1.32	0.64
MR-16	115.6	0.35	<0.47	0.12	7.55	92.66	2507	0.41	43.1	1.11	0.81	0.27	7.05	0.92	0.84
MR-17	58.7	0.28	<0.47	0.10	8.03	90.43	3139	0.32	42.2	1.72	1.07	0.32	6.35	1.59	0.65
MR-18	51.7	0.27	<0.47	0.08	7.92	93.52	2739	0.57	45.9	1.64	1.07	0.23	5.20	1.39	1.30
MR-19	63.1	0.30	<0.47	0.04	8.48	96.57	2664	0.49	70.9	1.59	1.03	0.25	6.09	1.32	0.92
MR-20	61.5	0.21	<0.47	0.07	9.59	90.59	2576	0.46	39.9	1.38	0.93	0.25	6.40	1.18	0.73
MR-21	51.0	0.17	<0.47	0.05	4.67	89.15	2435	0.31	28.6	0.70	0.51	0.23	6.72	0.59	0.33
MR-22	53.2	0.22	<0.47	0.06	6.57	94.87	2357	0.39	24.4	1.00	0.70	0.20	6.18	0.84	1.00
MR-23	57.2	0.23	<0.47	0.09	4.42	89.43	>4500	0.19	41.3	0.59	0.41	0.21	13.45	0.50	0.36
MR-24	86.3	0.27	<0.47	0.29	2.86	3.51	23	0.51	7.9	0.13	0.07	0.26	21.35	0.14	0.14
MR-25	113.1	0.30	<0.47	0.02	3.53	2.74	11	0.82	6.2	0.12	0.06	0.31	21.27	0.19	<0.14
MR-26	97.8	0.30	<0.47	0.02	3.65	3.31	17	0.51	7.4	0.14	0.08	0.30	20.87	0.19	0.20
MR-27	75.5	0.35	<0.47	0.02	4.11	5.66	55	0.08	10.2	0.19	0.11	0.31	20.69	0.24	0.20
MR-28	74.3	0.23	<0.47	0.03	4.36	10.84	102	0.07	13.3	0.28	0.18	0.34	19.53	0.29	0.36

Appendix 8: Trace Element Geochemistry for ELF-395. Data are presented in ppm. Limits of detection are given for each element.

Element	**Ho**	**In**	**La**	**Li**	**Lu**	**Mo**	**Nb**	**Nd**	**Ni**	**Pb**	**Pr**	**Rb**	**Sb**	**Sc**	**Sm**
Units	ppm	ppm	ppm	ppm	ppm	ppm	ppm	ppm	ppm	ppm	ppm	ppm	ppm	ppm	ppm
Detection Limit	0.0025	0.0018	0.1	0.4	0.002	0.08	0.028	0.06	0.7	0.18	0.014	0.11	0.04	1.1	0.026
Sample															
MR-01	0.06	0.01	2.38	2.7	0.02	0.55	0.54	2.00	115.0	2.0	0.51	4.02	0.18	3.4	0.39
MR-02	0.07	0.01	2.70	1.5	0.03	0.70	0.61	2.04	147.6	3.8	0.57	2.88	0.10	4.0	0.39
MR-03	0.02	0.00	2.16	1.7	0.01	0.53	0.22	1.41	25.3	1.4	0.41	4.01	0.09	<1.1	0.24
MR-04	0.04	0.01	1.68	1.5	0.02	0.70	0.23	1.34	149.7	2.8	0.36	2.10	0.09	4.5	0.25
MR-05	0.02	0.00	1.93	5.5	0.01	0.49	0.30	1.29	156.3	2.7	0.39	18.73	0.20	3.1	0.23
MR-06	0.04	0.01	1.95	1.6	0.02	0.41	0.31	1.53	190.7	2.0	0.40	4.93	0.10	3.4	0.28
MR-07	0.15	0.02	2.60	3.9	0.08	0.69	0.31	2.60	1116.4	3.4	0.62	2.54	0.10	18.7	0.58
MR-08	0.09	0.02	1.41	3.7	0.07	0.64	0.12	1.13	706.8	1.7	0.30	1.31	0.09	21.6	0.23
MR-09A	0.22	0.01	10.07	4.0	0.05	1.10	2.88	10.52	704.5	12.7	2.68	12.09	0.21	9.8	1.92
MR-09B	0.20	0.03	7.30	4.7	0.08	1.25	3.21	7.85	2591.6	10.2	2.03	16.73	0.18	15.5	1.46
MR-10	0.11	0.02	2.38	5.0	0.06	2.59	0.45	2.07	>4100	7.5	0.53	4.43	0.18	15.4	0.43
MR-11	0.28	0.05	5.40	5.4	0.14	1.01	0.87	5.01	3140.7	3.8	1.25	5.29	0.17	30.3	1.10
MR-12	0.35	0.04	5.05	5.3	0.16	0.40	5.83	4.79	1106.2	8.4	1.16	14.08	0.17	36.1	1.21
MR-13	0.15	0.03	1.83	4.6	0.09	0.51	0.32	1.64	1870.3	3.3	0.41	2.02	0.15	18.3	0.41
MR-14	0.40	0.04	7.93	5.9	0.19	0.44	3.11	6.19	692.1	1.8	1.59	28.47	0.19	36.3	1.47
MR-15	0.32	0.03	4.04	4.8	0.15	0.65	1.05	4.81	571.5	1.9	1.07	6.74	0.12	35.6	1.24
MR-16	0.25	0.03	3.73	5.3	0.13	0.73	1.58	3.60	564.0	2.7	0.94	12.70	0.14	21.3	0.81
MR-17	0.37	0.04	3.61	6.7	0.16	0.64	0.68	5.08	562.2	3.1	1.13	6.17	0.13	41.0	1.38
MR-18	0.35	0.04	3.87	4.2	0.16	0.64	2.24	4.44	585.5	1.2	1.05	14.63	0.12	34.2	1.19
MR-19	0.34	0.03	4.24	4.6	0.16	0.80	1.61	4.49	614.0	1.5	1.06	13.42	0.14	33.4	1.14
MR-20	0.29	0.03	4.70	5.9	0.15	0.75	1.42	4.41	545.1	1.9	1.12	11.76	0.14	33.8	1.07
MR-21	0.16	0.03	2.51	4.2	0.08	0.67	0.69	2.15	541.7	2.0	0.57	4.40	0.11	23.9	0.49
MR-22	0.22	0.03	3.63	5.1	0.12	0.69	1.32	3.20	571.8	3.4	0.80	8.86	0.10	19.1	0.77
MR-23	0.13	0.02	2.30	4.6	0.07	0.61	0.48	2.17	506.8	3.0	0.51	3.85	0.28	13.8	0.46
MR-24	0.03	0.00	1.66	2.2	0.01	0.48	0.20	1.22	14.0	1.3	0.32	6.26	0.09	1.7	0.19
MR-25	0.02	0.00	2.12	1.5	0.01	0.50	0.21	1.30	8.6	1.2	0.38	10.46	0.09	<1.1	0.21
MR-26	0.03	0.00	2.08	1.7	0.01	0.39	0.25	1.37	10.2	1.2	0.39	9.62	0.07	1.5	0.24
MR-27	0.03	0.00	2.37	4.6	0.01	0.56	0.41	1.68	22.3	1.3	0.46	3.32	0.10	2.3	0.28
MR-28	0.06	0.01	2.41	4.1	0.02	0.56	0.53	1.81	41.1	1.4	0.50	2.82	0.09	4.5	0.34

Appendix 8: Trace Element Geochemistry for ELF-395. Data are presented in ppm. Limits of detection are given for each element.

Element	**Sn**	**Sr**	**Ta**	**Tb**	**Th**	**Ti**	**Tl**	**Tm**	**U**	**V**	**W**	**Y**	**Yb**	**Zn**	**Zr**
Units	ppm	ppm	ppm	ppm	ppm	ppm	ppm	ppm	ppm	ppm	ppm	ppm	ppm	ppm	ppm
Detection Limit	0.16	0.6	0.007	0.0023	0.018	7	0.002	0.0019	0.011	0.8	0.05	0.05	0.009	1.8	6
Sample															
MR-01	0.36	361.2	0.03	0.05	0.34	519	0.03	0.02	0.12	30.5	0.32	1.64	0.17	16	16
MR-02	0.44	374.8	0.04	0.06	0.46	596	0.02	0.03	0.14	34.2	0.42	1.91	0.19	20	16
MR-03	0.36	418.0	0.01	0.02	0.14	243	0.02	0.01	0.04	8.5	0.31	0.59	0.04	8	<6
MR-04	0.36	368.3	0.01	0.03	0.14	397	0.01	0.02	0.04	34.0	0.39	1.22	0.12	21	8
MR-05	0.26	386.5	0.02	0.02	0.19	403	0.11	0.01	0.08	21.7	0.32	0.78	0.08	20	10
MR-06	0.26	370.6	0.02	0.03	0.16	432	0.03	0.02	0.06	26.2	0.23	1.07	0.12	17	9
MR-07	0.48	267.8	0.02	0.11	0.22	798	0.03	0.07	0.06	90.4	0.36	4.24	0.51	50	12
MR-08	0.49	174.7	<0.007	0.05	0.08	682	0.02	0.05	0.02	<0.8	0.34	2.67	0.38	76	<6
MR-09A	1.14	391.3	0.24	0.22	0.85	1212	0.05	0.07	0.26	57.3	0.58	6.21	0.42	16	21
MR-09B	0.83	273.1	0.19	0.18	1.11	1746	0.10	0.08	0.16	83.4	0.47	5.69	0.51	104	30
MR-10	0.63	193.1	0.02	0.07	0.31	776	0.14	0.05	0.04	<0.8	0.46	2.99	0.37	120	9
MR-11	0.58	74.1	0.06	0.19	0.89	1354	0.08	0.13	0.44	<0.9	0.30	7.92	0.91	127	22
MR-12	0.81	63.2	0.26	0.23	1.64	2661	0.07	0.16	0.58	<0.10	0.76	9.38	1.03	132	40
MR-13	0.36	77.0	0.02	0.10	0.14	1198	0.04	0.08	0.09	<0.11	0.22	4.14	0.55	117	10
MR-14	0.72	10.6	0.23	0.27	3.52	2535	0.17	0.19	1.51	<0.12	0.34	11.11	1.28	134	67
MR-15	0.58	68.5	0.06	0.22	0.84	1589	0.04	0.15	0.26	<0.13	0.35	8.84	0.96	89	23
MR-16	0.64	84.2	0.11	0.16	1.22	1530	0.06	0.12	0.25	<0.14	0.46	6.90	0.85	118	31
MR-17	0.61	66.9	0.04	0.26	0.69	1543	0.03	0.16	0.22	<0.15	0.36	9.99	1.09	89	23
MR-18	0.66	38.0	0.14	0.24	1.22	2212	0.07	0.16	0.34	<0.16	0.35	9.52	1.04	97	51
MR-19	0.66	51.0	0.12	0.24	1.47	1789	0.06	0.15	0.44	<0.17	0.46	9.26	1.07	93	37
MR-20	0.72	67.2	0.11	0.20	1.64	1466	0.06	0.13	0.44	<0.18	0.43	8.46	0.95	88	27
MR-21	0.40	93.7	0.04	0.10	0.39	1130	0.03	0.08	0.12	<0.19	0.38	4.40	0.53	85	12
MR-22	0.45	67.3	0.10	0.15	0.98	1514	0.04	0.11	0.49	<0.20	0.39	6.02	0.73	90	41
MR-23	0.40	171.6	0.03	0.09	0.31	1327	0.02	0.06	0.12	<0.21	0.37	3.51	0.46	130	14
MR-24	0.30	438.9	0.01	0.02	0.11	268	0.02	0.01	0.04	12.0	0.31	0.67	0.06	120	6
MR-25	0.36	484.3	0.01	0.02	0.13	246	0.04	0.01	0.04	8.5	0.29	0.67	0.05	8	6
MR-26	0.33	460.5	0.01	0.03	0.16	275	0.04	0.01	0.06	10.7	0.25	0.81	0.07	8.	8
MR-27	0.39	428.7	0.02	0.03	0.19	411	0.02	0.01	0.07	17.8	0.35	1.07	0.10	10	9
MR-28	0.37	411.2	0.03	0.05	0.37	488	0.01	0.03	0.11	26.7	0.32	1.67	0.17	16	14

Appendix 9: Trace Element Geochemistry for ELF-393. Data are presented in ppm. Limits of detection are given for each element.

Element	**Ba**	**Be**	**Bi**	**Cd**	**Ce**	**Co**	**Cr**	**Cs**	**Cu**	**Dy**	**Er**	**Eu**	**Ga**	**Gd**	**Hf**
Units	ppm	ppm	ppm	ppm	ppm	ppm	ppm	ppm	ppm	ppm	ppm	ppm	ppm	ppm	ppm
Detection Limit	0.8	0.04	0.47	0.013	0.12	0.13	3	0.013	1.4	0.009	0.007	0.0031	0.04	0.009	0.14
Sample															
ELF-393-1	60.5	0.28	<0.47	0.04	4.15	9.04	123	0.06	75.5	0.25	0.15	0.37	19.72	0.30	0.22
ELF-393-2	63.7	0.29	<0.47	0.03	4.19	14.49	155	0.16	139.2	0.23	0.13	0.35	19.25	0.25	0.16
ELF-393-3	71.6	0.25	<0.47	0.12	4.78	36.33	527	0.25	328.0	0.66	0.40	0.34	15.59	0.64	0.41
ELF-393-4A	62.3	0.23	<0.47	0.08	4.65	48.11	947	0.13	359.3	0.73	0.46	0.38	14.48	0.62	0.46
ELF-393-4B	51.3	0.15	<0.47	0.38	5.48	117.05	1851	0.25	985.2	1.10	0.80	0.23	7.07	0.89	0.68
ELF-393-4C	25.1	0.15	0.67	0.28	4.45	126.90	2301	0.17	1502.8	0.92	0.68	0.16	5.63	0.71	0.53
ELF-393-14	40.3	0.20	<0.47	0.19	5.14	122.60	2284	0.18	1508.1	0.88	0.63	0.21	6.65	0.69	0.45
ELF-393-5	22.6	0.18	<0.47	0.20	5.12	141.50	2259	0.20	1487.3	1.15	0.79	0.19	5.48	0.92	0.56
ELF-393-6	56.1	0.19	<0.47	0.09	8.27	86.38	2334	0.50	56.7	1.24	0.85	0.20	6.19	0.99	0.86
ELF-393-7	44.0	0.21	<0.47	0.10	3.80	86.06	2822	0.24	124.3	0.75	0.53	0.22	6.47	0.58	0.35
ELF-393-8	43.2	0.29	<0.47	0.07	10.23	84.73	2417	0.29	38.4	1.45	0.97	0.28	6.70	1.24	1.07
ELF-393-9	26.3	0.31	<0.47	0.10	12.58	88.46	2574	0.58	35.6	1.86	1.23	0.23	5.43	1.71	1.37
ELF-393-10	36.0	0.33	<0.47	0.07	6.89	88.33	2301	0.20	44.4	1.28	0.85	0.27	6.87	1.11	0.80
ELF-393-11	31.4	0.23	<0.47	0.06	4.18	83.35	2250	0.11	44.4	0.71	0.51	0.21	6.83	0.59	0.32
ELF-393-12	33.6	0.26	<0.47	0.05	5.56	85.04	2285	0.13	40.8	0.82	0.58	0.23	6.74	0.69	0.43
ELF-393-13	28.8	0.20	<0.47	0.05	3.31	85.34	2367	0.09	52.1	0.66	0.48	0.19	6.71	0.53	0.31
ELF-393-15	41.2	0.36	<0.47	0.06	11.52	84.24	2242	0.26	45.0	1.46	0.95	0.31	7.11	1.27	0.95
ELF-393-16	49.7	0.64	<0.47	0.05	18.94	70.06	1563	0.54	85.0	1.31	0.79	0.30	8.52	1.38	1.62
ELF-393-17	30.0	0.21	<0.47	0.07	3.64	87.06	1858	0.10	39.8	0.64	0.49	0.22	6.75	0.45	0.33
ELF-393-18	29.1	0.20	<0.47	0.06	2.97	93.43	1969	0.08	44.3	0.64	0.49	0.21	6.34	0.49	0.27
ELF-393-19	25.9	0.10	<0.47	0.05	2.23	96.91	2149	0.11	48.8	0.54	0.43	0.17	5.93	0.39	0.33
ELF-393-20	30.6	0.17	<0.47	0.05	2.56	91.91	2054	0.13	40.4	0.56	0.44	0.20	6.53	0.41	0.40
ELF-393-21	86.9	0.43	<0.47	0.04	3.43	11.41	102	0.43	296.2	0.15	0.08	0.55	20.02	0.20	<0.14
ELF-393-22	135.0	0.40	<0.47	0.02	3.13	4.88	42	0.71	28.5	0.17	0.09	0.56	21.35	0.21	<0.14
ELF-393-23	73.8	0.51	<0.47	0.02	3.68	8.41	66	0.12	24.6	0.23	0.12	0.47	21.81	0.23	0.21

Appendix 9: Trace Element Geochemistry for ELF-393. Data are presented in ppm. Limits of detection are given for each element.

Element	**Ho**	**In**	**La**	**Li**	**Lu**	**Mo**	**Nb**	**Nd**	**Ni**	**Pb**	**Pr**	**Rb**	**Sb**	**Sc**	**Sm**
Units	ppm	ppm	ppm	ppm	ppm	ppm	ppm	ppm	ppm	ppm	ppm	ppm	ppm	ppm	ppm
Detection Limit	0.0025	0.0018	0.1	0.4	0.002	0.08	0.028	0.06	1.6	0.18	0.014	0.11	0.04	1.1	0.026
Sample															
ELF-393-1	0.05	0.01	2.25	2.7	0.02	0.26	0.21	1.79	111.5	1.5	0.47	1.67	0.04	4.1	0.35
ELF-393-2	0.05	0.01	2.36	1.7	0.02	0.30	0.23	1.63	164.4	1.7	0.47	2.35	0.05	4.5	0.29
ELF-393-3	0.14	0.02	2.39	1.8	0.06	0.30	0.36	2.52	620.6	5.4	0.63	1.80	0.10	14.3	0.59
ELF-393-4A	0.15	0.02	2.39	3.4	0.07	0.27	0.23	2.49	601.0	3.6	0.59	1.04	0.07	18.1	0.60
ELF-393-4B	0.25	0.04	2.46	4.0	0.15	0.52	0.82	3.31	2279.7	4.4	0.76	4.19	0.16	32.2	0.79
ELF-393-4C	0.21	0.04	2.25	4.4	0.12	0.61	0.62	2.23	2945.2	15.2	0.52	2.32	0.09	29.1	0.56
ELF-393-14	0.20	0.04	2.64	5.0	0.12	0.49	0.69	2.40	2878.5	8.4	0.60	2.41	0.09	28.2	0.61
ELF-393-5	0.25	0.05	2.25	4.0	0.14	0.64	0.82	2.92	3496.8	3.9	0.68	2.69	0.09	32.4	0.79
ELF-393-6	0.27	0.03	4.36	4.4	0.15	0.48	1.61	3.71	625.7	2.8	1.01	9.72	0.11	29.5	0.87
ELF-393-7	0.17	0.03	1.86	4.8	0.09	0.25	0.30	2.03	697.2	3.5	0.50	2.55	0.08	24.7	0.51
ELF-393-8	0.32	0.04	5.09	4.4	0.16	0.43	1.51	4.96	497.4	1.8	1.23	6.94	0.07	31.4	1.13
ELF-393-9	0.39	0.04	5.85	8.6	0.19	0.47	3.52	6.78	522.7	2.3	1.67	15.11	0.09	38.7	1.58
ELF-393-10	0.27	0.04	3.17	4.7	0.14	0.47	1.85	4.01	503.8	1.3	0.93	4.60	0.08	33.1	1.01
ELF-393-11	0.16	0.03	2.03	5.0	0.09	0.30	0.23	2.23	495.2	1.2	0.55	1.10	0.05	26.0	0.50
ELF-393-12	0.18	0.03	2.78	5.4	0.10	0.34	0.56	2.85	500.2	1.7	0.68	2.52	0.05	27.1	0.65
ELF-393-13	0.14	0.03	1.67	4.3	0.09	0.33	0.27	1.74	515.6	1.0	0.42	1.31	0.05	26.8	0.42
ELF-393-15	0.32	0.04	6.13	6.2	0.16	0.49	1.74	5.13	484.8	1.7	1.31	8.93	0.11	34.6	1.21
ELF-393-16	0.26	0.03	8.16	6.5	0.12	0.82	7.67	8.60	392.7	3.2	2.35	15.31	0.10	24.9	1.57
ELF-393-17	0.15	0.03	1.80	3.9	0.10	0.35	0.46	1.79	475.9	1.2	0.44	1.60	0.04	27.0	0.40
ELF-393-18	0.15	0.03	1.65	3.6	0.09	0.24	0.23	1.50	515.2	1.4	0.38	0.71	0.05	29.3	0.39
ELF-393-19	0.12	0.03	1.20	4.9	0.08	0.33	0.29	1.20	601.9	2.4	0.29	1.15	0.07	29.6	0.31
ELF-393-20	0.13	0.02	1.33	4.8	0.08	0.36	0.31	1.30	543.9	2.2	0.33	1.53	0.05	28.5	0.35
ELF-393-21	0.03	0.01	2.13	1.8	0.01	0.27	0.10	1.40	204.7	4.1	0.40	4.12	0.06	2.7	0.25
ELF-393-22	0.03	0.00	1.93	1.5	0.01	0.19	0.11	1.33	30.0	1.1	0.35	8.88	<0.04	3.0	0.23
ELF-393-23	0.04	0.01	2.12	3.0	0.02	0.32	0.23	1.63	31.0	1.5	0.43	2.49	0.05	4.0	0.28

Appendix 9: Trace Element Geochemistry for ELF-393. Data are presented in ppm. Limits of detection are given for each element.

Element	**Sn**	**Sr**	**Ta**	**Tb**	**Th**	**Ti**	**Tl**	**Tm**	**U**	**V**	**W**	**Y**	**Yb**	**Zn**	**Zr**
Units	ppm	ppm	ppm	ppm	ppm	ppm	ppm	ppm	ppm	ppm	ppm	ppm	ppm	ppm	ppm
Detection Limit	0.16	0.6	0.007	0.0023	0.018	7	0.002	0.0019	0.011	0.8	0.05	0.05	0.009	1.8	6
Sample															
ELF-393-1	0.16	367.7	0.01	0.04	0.12	392	0.01	0.02	0.04	23.9	0.14	1.41	0.13	13	8
ELF-393-2	0.19	364.1	0.01	0.03	0.11	437	0.01	0.02	0.04	23.8	0.17	1.36	0.14	19	6
ELF-393-3	0.49	301.2	0.03	0.10	0.46	778	0.02	0.06	0.07	70.4	0.19	3.61	0.40	54	14
ELF-393-4A	0.27	280.2	0.01	0.11	0.19	815	0.01	0.07	0.05	76.8	0.15	4.15	0.47	48	20
ELF-393-4B	0.65	83.2	0.05	0.16	0.62	1335	0.08	0.13	0.14	120.1	0.33	6.61	0.90	97	26
ELF-393-4C	0.55	59.8	0.04	0.13	0.50	1306	0.06	0.11	0.15	112.1	0.27	5.96	0.78	123	20
ELF-393-14	0.55	93.1	0.05	0.12	0.59	1183	0.04	0.10	0.18	118.4	0.23	5.67	0.69	99	18
ELF-393-5	0.56	53.7	0.06	0.16	0.67	1325	0.05	0.13	0.23	121.7	0.30	6.83	0.85	98	19
ELF-393-6	0.61	59.8	0.12	0.18	1.52	1436	0.06	0.14	0.51	100.2	0.28	7.11	0.94	94	30
ELF-393-7	0.26	74.6	0.02	0.11	0.24	1049	0.02	0.09	0.07	80.0	0.11	4.57	0.63	97	12
ELF-393-8	0.44	61.2	0.10	0.22	1.22	1650	0.03	0.15	0.45	112.5	0.20	8.24	1.03	98	38
ELF-393-9	0.66	13.2	0.23	0.28	2.58	2363	0.08	0.19	0.54	152.6	0.25	10.75	1.24	106	46
ELF-393-10	0.44	67.5	0.11	0.18	0.75	1839	0.02	0.13	0.13	132.2	0.24	7.43	0.89	92	27
ELF-393-11	0.19	87.4	0.02	0.10	0.23	919	0.01	0.08	0.06	97.2	0.16	4.50	0.58	89	11
ELF-393-12	0.27	89.3	0.04	0.12	0.43	1120	0.01	0.09	0.13	107.9	0.17	5.18	0.64	91	16
ELF-393-13	0.21	93.9	0.02	0.09	0.21	936	0.01	0.08	0.06	103.1	0.16	4.31	0.55	91	12
ELF-393-15	0.57	73.2	0.10	0.21	1.34	1671	0.04	0.15	0.46	146.7	0.32	8.88	0.97	91	37
ELF-393-16	1.53	86.3	0.49	0.21	6.20	2027	0.07	0.12	0.59	100.4	0.57	7.67	0.80	75	51
ELF-393-17	0.27	95.4	0.03	0.08	0.40	926	0.01	0.08	0.08	112.1	0.17	4.24	0.59	95	11
ELF-393-18	0.17	88.1	0.01	0.09	0.17	994	0.01	0.08	0.07	145.9	0.12	4.00	0.56	100	10
ELF-393-19	0.18	77.2	0.02	0.07	0.19	938	0.01	0.07	0.05	135.5	0.20	3.49	0.48	99	12
ELF-393-20	0.22	95.2	0.02	0.07	0.24	955	0.01	0.07	0.06	137.2	0.22	3.60	0.48	98	14
ELF-393-21	0.21	392.9	<0.007	0.03	0.05	303	0.02	0.01	0.02	20.5	0.16	0.86	0.07	16	<6
ELF-393-22	<0.16	428.0	<0.007	0.03	0.06	302	0.05	0.01	0.02	20.2	0.12	0.88	0.08	13	<6
ELF-393-23	0.27	390.9	0.01	0.04	0.14	406	0.01	0.02	0.05	24.5	0.17	1.27	0.13	17	8

Appendix 10: Platinum-Group Element Geochemistry. Data are presented in ppb. Limits of detection (LOD) for each element are given as well as the relative standard deviation (RSD) for each sample.

	99 Ru		103 Rh		105 Pd		190 Os		193 Ir		195 Pt		197 Au	
LOD	**0.120**		**0.082**		**0.471**		**0.065**		**0.025**		**0.084**		**0.484**	
Sample	**Conc.**	RSD	**Conc.**	RSD	**Conc.**	RSD	**Conc.**	RSD	**Conc.**	RSD	**Conc.**	RSD	**Conc.**	RSD
MR-1	**2.18**	9.93	**1.77**	1.15	**4.27**	6.79	**2.21**	31.86	**0.61**	5.20	**21.99**	2.79	**12.78**	0.46
MR-2	**0.39**	11.37	**0.40**	2.43	**5.18**	1.43	**0.09**	2.27	**0.19**	2.83	**4.33**	0.23	**19.00**	1.33
MR-3	**2.13**	3.90	**1.34**	0.63	**2.00**	1.73	**0.82**	4.63	**0.37**	2.80	**28.74**	0.58	**4.19**	1.07
MR-4	**1.21**	2.34	**0.53**	4.66	**5.69**	2.08	**0.25**	8.50	**0.21**	1.61	**10.13**	0.93	**9.50**	0.84
MR-5	**2.60**	2.68	**2.10**	0.51	**6.19**	0.66	**1.04**	9.04	**0.58**	1.31	**39.31**	0.49	**4.12**	0.99
MR-6	**0.62**	7.19	**0.36**	1.51	**5.80**	2.53	**0.17**	5.58	**0.17**	3.23	**9.70**	0.59	**18.40**	1.49
MR-7	**6.62**	3.29	**2.38**	0.98	**29.45**	0.73	**0.98**	2.66	**1.49**	1.41	**65.59**	0.73	**96.90**	0.62
MR-8	**34.41**	0.58	**19.86**	0.36	**109.07**	0.22	**5.31**	2.07	**5.45**	0.97	**161.58**	0.48	**39.95**	0.28
MR-9A	**27.68**	0.67	**9.23**	0.64	**276.28**	0.17	**6.60**	1.59	**4.19**	0.35	**343.29**	0.32	**173.03**	0.80
MR-9B	**129.16**	0.27	**43.98**	0.62	**1158.56**	0.22	**34.89**	1.20	**19.20**	0.50	**2809.13**	0.47	**221.52**	1.04
MR-10	**422.01**	0.19	**146.88**	0.46	**3339.70**	0.30	**168.12**	0.27	**65.25**	0.29	**2297.29**	0.35	**92.75**	0.18
MR-11	**526.66**	0.28	**159.62**	0.97	**1690.11**	0.66	**87.77**	1.31	**69.47**	0.50	**2885.38**	0.44	**289.45**	0.59
MR-12	**143.72**	0.53	**41.79**	0.05	**411.27**	0.87	**22.79**	0.51	**20.25**	0.50	**494.97**	0.80	**179.98**	0.61
MR-13	**60.22**	0.72	**40.26**	0.57	**468.69**	0.55	**9.05**	1.70	**10.45**	0.58	**587.57**	0.54	**290.87**	0.23
MR-14	**4.02**	2.60	**4.30**	0.08	**33.04**	0.28	**0.82**	2.48	**0.99**	1.10	**138.11**	0.35	**29.84**	0.77
MR-15	**1.98**	2.22	**0.91**	1.96	**11.47**	1.93	**0.58**	10.91	**0.35**	1.50	**26.79**	1.09	**4.50**	1.34
MR-16	**2.21**	2.38	**0.96**	0.26	**2.40**	1.07	**0.35**	12.21	**0.34**	4.84	**9.69**	0.68	**2.44**	1.01
MR-17	**2.47**	3.08	**1.07**	1.53	**2.53**	1.44	**0.33**	2.80	**0.42**	2.56	**8.74**	1.28	**3.45**	1.24
MR-18	**7.11**	0.43	**0.98**	2.50	**2.79**	0.70	**0.97**	4.06	**0.59**	1.42	**10.08**	0.62	**1.95**	1.07
MR-19	**7.84**	5.69	**4.32**	2.52	**3.90**	6.99	**7.07**	31.57	**1.40**	4.75	**28.68**	4.73	**1.99**	2.72

Appendix 10: Platinum-Group Element Geochemistry. Data are presented in ppb. Limits of detection (LOD) for each element are given as well as the relative standard deviation (RSD) for each sample.

	99 Ru		**103 Rh**		**105 Pd**		**190 Os**		**193 Ir**		**195 Pt**		**197 Au**	
LOD	**0.120**		**0.082**		**0.471**		**0.065**		**0.025**		**0.084**		**0.484**	
Sample	**Conc.**	RSD	**Conc.**	RSD	**Conc.**	RSD	**Conc.**	RSD	**Conc.**	RSD	**Conc.**	RSD	**Conc.**	RSD
MR-20	**13.74**	0.93	**2.17**	1.19	**3.68**	2.35	**1.51**	1.00	**1.21**	1.57	**20.56**	1.02	**5.69**	0.32
MR-21	**13.07**	0.94	**1.64**	1.80	**15.66**	0.81	**1.62**	3.15	**1.01**	1.65	**19.77**	0.30	**3.91**	1.64
MR-22	**21.02**	0.98	**5.25**	0.13	**55.05**	0.42	**3.23**	2.76	**2.36**	0.58	**64.64**	0.32	**6.21**	1.85
MR-23	**3803.03**	0.31	**1291.91**	0.41	**2082.71**	0.43	**460.71**	0.40	**434.93**	0.50	**10615.92**	0.74	**14.61**	0.51
MR-24	**2.85**	4.42	**0.12**	4.40	**3.36**	1.08	**0.32**	1.97	**0.34**	4.88	**1.13**	2.01	**0.86**	2.39
MR-25	**1.85**	3.56	**0.19**	2.17	**0.51**	5.72	**0.14**	7.37	**0.19**	2.76	**1.07**	1.44	**1.04**	2.24
MR-26	**1.65**	0.77	**1.47**	0.78	**0.40**	0.71	**0.35**	3.85	**0.40**	2.75	**6.26**	1.74	**<LOD**	2.83
MR-27	**0.81**	2.61	**0.46**	1.03	**0.72**	6.29	**0.23**	4.12	**0.28**	4.73	**1.91**	2.12	**1.49**	1.92
MR-28	**2.01**	3.75	**0.17**	3.23	**1.26**	1.24	**0.14**	6.58	**0.22**	4.71	**0.96**	2.63	**<LOD**	1.63